



12-2023

## **Additive Manufacturing of Magnetic Materials for Electric Motor and Generator Applications**

Haobo Wang

*University of Tennessee, Knoxville, [hwang109@vols.utk.edu](mailto:hwang109@vols.utk.edu)*

Follow this and additional works at: [https://trace.tennessee.edu/utk\\_graddiss](https://trace.tennessee.edu/utk_graddiss)



Part of the [Automotive Engineering Commons](#), [Electromagnetics and Photonics Commons](#), and the [Other Materials Science and Engineering Commons](#)

---

### **Recommended Citation**

Wang, Haobo, "Additive Manufacturing of Magnetic Materials for Electric Motor and Generator Applications." PhD diss., University of Tennessee, 2023.  
[https://trace.tennessee.edu/utk\\_graddiss/9009](https://trace.tennessee.edu/utk_graddiss/9009)

This Dissertation is brought to you for free and open access by the Graduate School at TRACE: Tennessee Research and Creative Exchange. It has been accepted for inclusion in Doctoral Dissertations by an authorized administrator of TRACE: Tennessee Research and Creative Exchange. For more information, please contact [trace@utk.edu](mailto:trace@utk.edu).

To the Graduate Council:

I am submitting herewith a dissertation written by Haobo Wang entitled "Additive Manufacturing of Magnetic Materials for Electric Motor and Generator Applications." I have examined the final electronic copy of this dissertation for form and content and recommend that it be accepted in partial fulfillment of the requirements for the degree of Doctor of Philosophy, with a major in Energy Science and Engineering.

Parans Paranthaman, Major Professor

We have read this dissertation and recommend its acceptance:

Parans Paranthaman, Suresh Babu, Uday Vaidya, David Mandrus

Accepted for the Council:

Dixie L. Thompson

Vice Provost and Dean of the Graduate School

(Original signatures are on file with official student records.)

# **Additive Manufacturing of Magnetic Materials for Electric Motor and Generator Applications**

A Dissertation Presented for the  
Doctor of Philosophy  
Degree  
The University of Tennessee, Knoxville

Haobo Wang  
December 2023

Copyright © 2023 by Haobo Wang  
All rights reserved.



## ACKNOWLEDGMENTS

Five years ago, when I first joined the Bredesen Center program, I was supposed to be paired with another mentor, with the goal of working on the Big Area Additive Manufacturing project. However, because of the national security concerns of that mentor's work, I could not work with him. With the generous assistance of Dr. Lee Riedinger, the previous Bredesen head, I was introduced to Dr. Parans Paranthaman, who graciously took me in and became my mentor. Studying as a Chinese national in the United States, especially in a national laboratory, has been extraordinarily difficult owing to recent global events. Dr. Riedinger and Dr. Parans went through a lot of hoops and troubles for me to make my doctorate possible. Despite the chaos caused by COVID-19 for almost 3 years, including many months of laboratory shutdowns, I still managed to complete a great amount of research. This accomplishment is again thanks to the efforts of my mentor, Dr. Parans. Thus, I would like to thank Dr. Parans for guiding, advising, and mentoring me all this time. I would also like to thank Dr. Riedinger for helping me immensely by getting me started in the program.

Next, I would like to thank Dr. Suresh Babu, Dr. David Mandrus, and Dr. Uday Vaidya for being my doctoral committee members. Their suggestions and thoughts on my dissertation are greatly appreciated. I have expanded my knowledge horizon and see things in brand new ways thanks to you.

With luck, I was able to work with some great people in the lab during my time. Thank you to Dr. Tej Lamichhane for improving my lab skills and proficiency in writing scientific literature. Thank you, Kaustubh, for our fun times with the extruder and compression molder. Thank you to Dr. Willie Kemp for being a pleasant coworker to work with. Thank you to the office staff at Bredesen Center as well as Elizabeth of the University International Office for all their help. Thank you to

Devin and Annabelle for being great lab interns. I have made many great and life-changing friends during my time here in the United States. Thank you, Nate, Max, Eric, and Greg, for all the fun times we've had and for always being there when I need you—in good times and bad.

Lastly, I would like to thank my family for their love and support throughout my life. Words fail to describe my gratitude and love for my parents, grandparents, and my extended family for all their support and love.

## **ABSTRACT**

This work details research into the 3D printing, also known as additive manufacturing (AM), of both impermanent and permanent magnets. This work also details research toward enabling 3D printed magnets in electrical machine applications—primarily motors and generators. The AM processes of many types of magnets are described in detail. The material properties of these 3D printed magnets are also described. The two main types of 3D printed magnets that are discussed in detail are NdFeB and silicon steel. Discussed in detail are the implementation of NdFeB as rotor magnets and the implementation of silicon steel as rotor and stator cores. The construction of a working electrical motor made with 3D printed magnets is described. Lastly, future research directions are discussed.

## TABLE OF CONTENTS

<b>CHAPTER 1 : INTRODUCTION AND BACKGROUND .....</b>	<b>1</b>
1.1 Research Background.....	2
1.2 Objective .....	2
1.3 On the Importance of Electric Vehicles and Wind Turbine Generators .....	4
1.4 On the Criticality of Vital Strategic Materials (Critical Materials) .....	5
<b>CHAPTER 2 : REVIEW OF FUNDAMENTAL CONCEPTS OF MAGNETS.....</b>	<b>32</b>
2.1 On the Fundamental Concepts of Magnets .....	33
2.2 On the Classification of Soft and Hard Magnets.....	39
2.3 On the Conventional Manufacturing Processes of Magnets .....	45
2.3.1 Powder Metallurgy, or Pressing and Sintering.....	45
2.3.2 Bonded Magnets, or Injection Molding and Compression Molding .....	47
2.3.3 Other Conventional Hard Magnet Manufacturing Processes .....	51
2.3.4 Conventional Soft Magnet Manufacturing Processes.....	53
2.3.5 Conventional Soft Magnet Lamination Manufacturing Process .....	54
2.4 On the Additive Manufacturing Processes of Magnets .....	55
2.4.1 Binder Jetting.....	56
2.4.2 Directed Energy Deposition .....	58
2.4.3 Material Extrusion, or Fused Deposition Modeling .....	60
2.4.4 Powder Bed Fusion .....	65
<b>CHAPTER 3 : MATERIALS CHARACTERIZATION AND TESTING .....</b>	<b>70</b>
3.1 Material Characterization and Testing.....	71
3.2 Mechanical Testing .....	71
3.3 Thermogravimetric Analysis.....	72
3.4 Differential Scanning Calorimetry.....	75
3.5 Scanning Electron Microscopy.....	78
3.6 X-Ray Powder Diffraction .....	80
3.7 Superconducting Quantum Interference Device Magnetometer.....	82
<b>CHAPTER 4 : SOFT MAGNETS .....</b>	<b>86</b>
4.1 On the Important Material Properties Concerning Soft Magnets.....	87
4.2 Important Soft Magnets and their Properties .....	87
4.3 On the Additive Manufacturing of Soft Magnets and the Material Properties of these Magnets .....	89

4.3.1	<b>Binder Jetting Fe-6.5Si</b> .....	89
4.3.2	<b>Selective Laser Melting Fe-3Si</b> .....	91
4.3.3	<b>Selective Laser Melting FeCoV (Hiperco 50)</b> .....	93
4.4	Comparison of the Materials Properties of 3D printed Soft Magnets and their Baseline Counterparts.....	94
<b>CHAPTER 5 : HARD OR PERMANENT MAGNETS</b> .....		<b>98</b>
5.1	On Important Material Properties Concerning Hard Magnets.....	99
5.2	List of Important Hard Magnets and their Properties .....	99
5.3	On the Additive Manufacturing of Hard Magnets and the Material Properties of these Magnets .....	101
5.3.1	Beginning Steps .....	101
5.3.2	Initial BAAM Permanent Magnets.....	103
5.3.3	Binder Jetting NdFeB Magnets with Low Melting Point Eutectic Alloy Infiltration .....	103
5.3.4	Initial Experiments on Bimodal Powder BAAM Magnets.....	105
5.3.5	Initial Anisotropic BAAM Magnets.....	107
5.3.6	Recycling of BAAM Magnets.....	108
5.3.7	High Mechanical Strength PPS BAAM Magnets .....	110
5.3.8	Anisotropic BAAM Magnets with Magnetic Field Alignment.....	111
5.3.9	Printing Bimodal and Recycled Magnets with Magnetic Field Alignment .....	113
5.3.10	Mathematical Model on Degree of Alignment of the Magnetic Field Alignment of 3D Printed Magnets .....	115
5.3.11	BAAM Halbach Arrays.....	116
5.3.12	Optimizing Feedstock: Increased Magnetic Material Loading via Premixing.....	117
5.3.13	Optimizing Feedstock: Bimodal Powder Mixing for Higher Packing Density.....	118
5.4	The Eddy Current Behavior, Working Temperatures, and Material Properties Summary of the 3D Printed Permanent Magnets .....	118
5.4.1	On Electrical Resistivity and Eddy Current Behavior of 3D Printed Permanent Magnets .....	118
5.4.2	On Flux Loss Behavior of 3D Printed Permanent Magnets and the Influence of Coatings .....	124
5.4.3	On the Mechanical Properties of 3D Printed Permanent Magnets.....	129
5.5	Comparison of the Materials Properties of 3D Printed Hard Magnets and their Baseline Counterparts.....	136
<b>CHAPTER 6 : ON THE EVOLUTION AND IMPROVEMENT OF THE ENERGY PRODUCT OF 3D PRINTED HARD MAGNETS</b> .....		<b>139</b>
6.1	On Utilizing Sacrificial Polymers for 3D Printed Permanent Magnets.....	140

6.2 History of the Development of Energy Products of 3D Printed Permanent Magnets.....	151
<b>CHAPTER 7 : THE IMPLEMENTATION OF 3D PRINTED SOFT AND HARD MAGNETS IN ELECTRIC MACHINES .....</b>	<b>157</b>
7.1 On the Design and Fabrication of an Electric Motor Incorporating 3D Printed Soft and Hard Magnets.....	158
7.2 On the Material Characterization of 3D Printed Stator Laminates.....	167
<b>CHAPTER 8 : FUTURE RESEARCH DIRECTIONS.....</b>	<b>191</b>
8.0 Future Research Directions for 3D Printed Magnetic Materials.....	192
8.1 On the Additive Manufacturing of Multimaterial Stators for Electrical Machines .....	192
8.1.1 Premixing Aluminum Alloy with Fe-3Si and made via SLM.....	192
8.1.2 Premixing Alumina with FeSi and Made via BJT.....	193
8.1.3 On the Layer-by-Layer Dual-Feed Approach.....	196
8.2 Future Direction of the Additive Manufacturing of Permanent Magnets .....	196
8.2.1 Magnetic Alignment of 3D Printed Permanent Magnet to Further Improve their Magnetic Properties.....	198
8.2.2 The 3D Printed Permanent Magnet with Tailorable Gradient Concentrations of Critical Materials.....	200
8.3 On the Additive Manufacturing of Cu Coils for Electric Motors and Generators .....	204
8.4 Concluding Remarks on the Implementation of Future Research on Electric Motors and Generators .....	204
<b>REFERENCES: .....</b>	<b>209</b>
<b>APPENDIX:.....</b>	<b>228</b>
<b>VITA:.....</b>	<b>231</b>

## LIST OF TABLES

TABLE 1.1: MARKET PRICES OF VARIOUS RAW MATERIALS AS OF OCTOBER 2022.....	12
TABLE 1.2: RECYCLING RATES OF VARIOUS RAW MATERIALS.....	14
TABLE 1.3: US WIND POWER GENERATION CAPACITY IN 2022.....	18
TABLE 1.4: ESTIMATED LOWER AND UPPER LIMITS FOR WIND TURBINE RAW MATERIAL USAGE.....	18
TABLE 1.5: DOE WIND VISION TARGETS AND NET CHANGES.....	18
TABLE 1.6: CALCULATED PROJECTED DEMAND OF RAW MATERIALS FOR WIND VISION 2030 TARGET.....	18
TABLE 1.7: CALCULATED PROJECTED DEMAND OF RAW MATERIALS FOR WIND VISION 2050 TARGET.....	19
TABLE 1.8: MATERIAL COMPOSITION OF A TYPICAL NDFEB PERMANENT MAGNET.....	19
TABLE 1.9: CALCULATED COBALT DEMAND FOR WIND VISION WIND GENERATION TARGETS.....	19
TABLE 1.10: IEA STEPS PROJECTED MATERIAL DEMAND FOR EV AND BATTERY STORAGE.....	22
TABLE 1.11: IEA SDS PROJECTED MATERIAL DEMAND FOR EV AND BATTERY STORAGE.....	23
TABLE 1.12: IEA STEPS PROJECTED CRITICAL MATERIAL DEMAND GROWTH FROM EV AND BATTERY STORAGE IN MULTIPLES OF 2020 CRITICAL MATERIALS DEMAND.....	25
TABLE 1.13: IEA SDS PROJECTED CRITICAL MATERIAL DEMAND GROWTH FROM EV AND BATTERY STORAGE IN MULTIPLES OF 2020 CRITICAL MATERIALS DEMAND.....	26
TABLE 1.14: IEA STEPS PROJECTED MATERIAL DEMAND FOR WIND POWER GENERATION.....	29
TABLE 1.15: IEA SDS PROJECTED MATERIAL DEMAND FOR WIND POWER GENERATION.....	29
TABLE 1.16: IEA STEPS PROJECTED SECTORIAL DEMAND BY CRITICAL MATERIAL.....	30
TABLE 1.17: IEA SDS PROJECTED SECTORIAL DEMAND BY CRITICAL MATERIAL.....	31
TABLE 2.1: CONCEPTS AND TERMS ASSOCIATED WITH MAGNETIC HYSTERESIS.....	46
TABLE 2.2: SI AND CGS-EMU UNITS FOR MAGNETIC PROPERTIES.....	46
TABLE 2.3: ADVANTAGES AND DISADVANTAGES OF THE PRESSING AND SINTERING CONVENTIONAL MAGNET MANUFACTURING PROCESS.....	48
TABLE 2.4: ADVANTAGES AND DISADVANTAGES OF THE BONDED MAGNET MANUFACTURING PROCESSES.....	50
TABLE 4.1: SOFT MAGNETIC MATERIAL FAMILIES AND THEIR MAGNETIC PROPERTIES.....	88
TABLE 4.2: DENSITIES OF BJT SILICON STEEL.....	92
TABLE 4.3: MATERIAL PROPERTIES OF THE BJT Fe-6.5Si SOFT MAGNETIC MATERIAL.....	92
TABLE 4.4: MATERIAL PROPERTIES OF THE CONVENTIONAL AND SLM Fe-3Si STEEL.....	92
TABLE 4.5: MATERIAL PROPERTIES OF THE SLM HIPERCO 50 STATOR.....	95
TABLE 4.6: MATERIAL PROPERTIES OF CONVENTIONAL AND 3D PRINTED SOFT MAGNETIC MATERIAL.....	95
TABLE 5.1: TABLE OF HARD MAGNETIC MATERIAL FAMILIES AND PROPERTIES.....	102
TABLE 5.2: MATERIAL PROPERTIES OF THE BAAM BONDED NDFEB MAGNETS.....	104
TABLE 5.3: MATERIAL PROPERTIES OF THE BJT NDFEB AND ITS ALLOY-INFILTRATED VARIANTS.....	106
TABLE 5.4: MAGNETIC PROPERTIES OF AS-PRINTED AND POST-ALIGNED BAAM NDFEB AND SMFEN HYBRID BONDED MAGNETS.....	106
TABLE 5.5: MATERIAL PROPERTIES OF THE STARTING BAAM MAGNETS, THE CRYOMILLED POWDER, AND THE RECYCLED BONDED MAGNET.....	109
TABLE 5.6: MATERIAL PROPERTIES OF THE BAAM NDFEB-PPS BONDED PERMANENT MAGNET.....	112
TABLE 5.7: MECHANICAL PROPERTIES OF BAAM NDFEB PPS PERMANENT MAGNETS.....	112
TABLE 5.8: MAGNETIC PROPERTIES OF THE AS-PRINTED MAGNET AND THE 2.0 T ALIGNED MAGNET.....	114
TABLE 5.9: MAGNETIC PROPERTIES OF THE HIGH-DENSITY ALIGNED BAAM MAGNETS AND ITS INJECTION-MOLDED COMMERCIAL EQUIVALENT.....	114
TABLE 5.10: MECHANICAL PROPERTIES OF THE HIGH-DENSITY BAAM NDFEB MAGNET.....	114
TABLE 5.11: MODEL PREDICTION AND EXPERIMENTAL DATA OF THE DEGREE OF ALIGNMENT OF 3D PRINTED BONDED MAGNETS.....	119

TABLE 5.12: MATERIAL PROPERTIES OF 95 WT% NdFeB COMPRESSION-MOLDED MAGNET .....	119
TABLE 5.13: ELECTRICAL RESISTIVITY OF CONVENTIONAL AND 3D PRINTED MAGNETS.....	125
TABLE 5.14: THERMAL STABILITY OF BAAM NdFeB MAGNET AND COMMERCIAL INJECTION-MOLDED NdFeB MAGNET. ....	131
TABLE 5.15: DIMENSIONS FOR THE TYPE V VARIANT OF THE ASTM D638-22 SPECIMEN.....	134
TABLE 5.16: MECHANICAL PROPERTIES OF 3D PRINTED AND CM MAGNETS.....	135
TABLE 5.17: MAGNETIC PROPERTIES OF 3D PRINTED AND CM MAGNETS. ....	137
TABLE 5.18: MAGNETIC PROPERTIES OF COMMERCIAL AND 3D PRINTED PERMANENT MAGNETS.....	138
TABLE 6.1: PERMANENT AND SACRIFICIAL POLYMERS.....	142
TABLE 6.2: NdFeB WITH NYLON-ABS SAMPLE TESTING CONDITIONS AND MAGNETIC PROPERTIES. ....	145
TABLE 6.3: NdFeB WITH PPS-ABS SAMPLE TESTING CONDITIONS AND MAGNETIC PROPERTIES. ....	145
TABLE 6.4: NdFeB WITH NYLON-ABS SAMPLE TESTING CONDITIONS AND MAGNETIC PROPERTIES. ....	148
TABLE 6.5: MQA-ABS SAMPLE TESTING CONDITIONS AND MAGNETIC PROPERTIES. ....	150
TABLE 6.6: STA RESULTS OF POSSIBLE NEW SACRIFICIAL POLYMERS.....	154
TABLE 7.1: DATA SHEET OF THE ARNOLD MOTOR. ....	160
TABLE 7.2: NOMINAL PROCESS PARAMETERS FOR THE PRINTING OF THE Fe <sub>3</sub> Si STATOR AND INDUCTION RINGS FOR MAGNETIC PROPERTY MEASUREMENTS. ....	165
TABLE 7.3: MAGNETIC PROPERTIES OF THE 3D PRINTED PERMANENT MAGNET ROTOR CORE. ....	173
TABLE 7.4: MEASURED MECHANICAL PROPERTIES OF THE 3D PRINTED Fe-3Si ALLOY USING ORNL SS-3 STANDARD SAMPLES. .....	180
TABLE 7.5: AC MAGNETIC PROPERTIES OF AS-PRINTED AND 4% HYDROGEN-ARGON ATMOSPHERE ANNEALED 3D PRINTED Fe- 3Si RINGS. ....	186
TABLE 7.6: COMPARISON OF MAGNETIC AND ELECTRICAL PROPERTIES OF CONVENTIONALLY PROCESSED ELECTRICAL STEEL AND SLM 3D PRINTED Fe <sub>3</sub> Si LAMINATES. ....	187
TABLE 8.1: MATERIAL PROPERTIES OF THE FOUR 3D PRINTED FeSi SAMPLES.....	197
TABLE 8.2: THE FIVE STEPS OF THE MAGNETIC ALIGNMENT EXPERIMENT.....	201
TABLE 8.3: KEY MAGNETIC PROPERTIES OF THE ALIGNED 3D PRINTED PERMANENT MAGNET AT THE VARIOUS STEPS.....	203



## LIST OF FIGURES

FIGURE 1.1: RARE EARTH ELEMENTS (BLUE) AND COBALT (GOLD) ON THE PERIODIC TABLE. <sup>19</sup> .....	8
FIGURE 1.2: THE RELATIVE ABUNDANCE OF ELEMENTS WITHIN EARTH’S UPPER CRUST. <sup>22</sup> .....	10
FIGURE 1.3: MARKET PRICES OF CRITICAL AND NONCRITICAL MATERIALS. <sup>24–30</sup> .....	12
FIGURE 1.4: MARKET PRICES OF CRITICAL AND NONCRITICAL MATERIALS IN LOGARITHMIC SCALE. <sup>24–30</sup> .....	13
FIGURE 1.5: THE PRICE HISTORY OF NEODYMIUM, PRASEODYMIUM, DYSPROSIUM, AND COBALT (2010–2022). <sup>13,31,32</sup> .....	13
FIGURE 2.1: MAGNETIZATION HYSTERESIS CURVE (LEFT); MAGNETIC INDUCTION HYSTERESIS CURVE (RIGHT). <sup>61</sup> .....	35
FIGURE 2.2: HYSTERESIS CURVE, SHOWING THE MAGNETIC INDUCTION ( $B$ ) VS. THE MAGNETIZING FIELD ( $H$ )......	42
FIGURE 2.3: PRESSING AND SINTERING (POWDER METALLURGY) MANUFACTURING PROCESS. <sup>9</sup> .....	48
FIGURE 2.4: THE BONDED MAGNET MANUFACTURING PROCESSES. <sup>9</sup> .....	52
FIGURE 2.5: THE BINDER JETTING AM PROCESS. <sup>113</sup> .....	57
FIGURE 2.6: THE LASER ENGINEERED NET SHAPING (LENS) AM PROCESS. <sup>113</sup> .....	59
FIGURE 2.7: THE FUSED DEPOSITION MODELING AM PROCESS. ....	62
FIGURE 2.8: THE BIG AREA ADDITIVE MANUFACTURING (BAAM) PROCESS. <sup>113</sup> .....	63
FIGURE 2.9: THE POWDER BED FUSION AM PROCESSES. <sup>113</sup> .....	68
FIGURE 3.1: EXAMPLE OF THE STRESS–STRAIN CURVE RESULTING FROM MECHANICAL TESTING. ....	73
FIGURE 3.2: SCREENSHOT OF ORIGIN’S USER INTERFACE.....	73
FIGURE 3.3: SCREENSHOT OF EXCEL’S USER INTERFACE.....	74
FIGURE 3.4: EXAMPLE OF TDG/DSC CURVES.....	76
FIGURE 3.5: EXAMPLE OF TGA CURVE MADE VIA ORIGIN USING DATA FROM 3D PRINTED SLM HIPERCO. ....	77
FIGURE 3.6: EXAMPLE OF AN IDEALIZED DSC CURVE. <sup>137</sup> .....	79
FIGURE 3.7: DSC GRAPH MADE WITH ORIGIN, USING DATA FROM NdCuCo AND PrCuCo, ALLOYS USED TO INFILTRATE 3D PRINTED NdFeB MAGNETS. <sup>140</sup> .....	79
FIGURE 3.8: SEM IMAGE OF 3D PRINTED SmFeN MAGNET.....	81
FIGURE 3.9: SIMULATED Nd <sub>2</sub> Fe <sub>14</sub> B XRPD PATTERN.....	83
FIGURE 3.10: XRPD RESULTS OF A 3D PRINTED SmFeN MAGNET. <sup>148</sup> .....	83
FIGURE 3.11: HYSTERESIS GRAPH GENERATED WITH ORIGIN USING DATA FROM SQUID OF 3D PRINTED NdFeB. ....	85
FIGURE 3.12: $B$ AND $(BH)_{\text{MAX}}$ VS. $H$ CURVES GENERATED WITH ORIGIN USING DATA FROM SQUID OF 3D PRINTED NdFeB. ....	85
FIGURE 4.1: SOFT MAGNETIC MATERIALS AND THEIR PROPERTIES.....	88
FIGURE 4.2: MATERIAL PROPERTIES OF CONVENTIONAL AND 3D PRINTED SOFT MAGNETIC MATERIAL.....	96
FIGURE 5.1: PLOT OF HARD MAGNETIC MATERIALS AND THEIR MATERIAL PROPERTIES. ....	102
FIGURE 5.2. SAMPLE 66: MQA-PC, SURFACE.....	120
FIGURE 5.3. SAMPLE 66: MQA-PC, SURFACE.....	120
FIGURE 5.4. SAMPLE 67: MQA-PC, CROSS SECTION.....	121
FIGURE 5.5. SAMPLE 67: MQA-PC, CROSS SECTION.....	121
FIGURE 5.6: AC LOSS FRACTION OF SINTERED AND 3D PRINTED MAGNETS. <sup>125</sup> .....	125
FIGURE 5.7: FLUX LOSS BEHAVIOR OF BAAM NdFeB NYLON 12 BONDED MAGNETS. <sup>123</sup> .....	127
FIGURE 5.8: FLUX LOSS BEHAVIOR OF BAAM NdFeB NYLON 12 BONDED MAGNETS.....	130
FIGURE 5.9: FLUX LOSS BEHAVIOR OF BAAM NdFeB PPS BONDED MAGNETS WITH AND WITHOUT PROTECTIVE COATING. <sup>125</sup> .....	130
FIGURE 5.10: SPECIMEN BLUEPRINT FOR THE ASTM D638-22, “STANDARD TEST METHOD FOR TENSILE PROPERTIES.” <sup>210</sup>	134
FIGURE 6.1: HYSTERESIS CURVE OF NdFeB WITH PC–POM.....	143
FIGURE 6.2: HYSTERESIS CURVES OF NYLON–ABS NdFeB SAMPLES UNDER VARIOUS HEAT-TREATMENT CONDITIONS.....	145
FIGURE 6.3: HYSTERESIS CURVES OF PPS–ABS NdFeB SAMPLES UNDER VARIOUS HEAT-TREATMENT CONDITIONS. ....	146
FIGURE 6.4: HYSTERESIS CURVES OF BAAM NYLON–ABS NdFeB SAMPLES UNDER VARIOUS HEAT-TREATMENT CONDITIONS. .....	148

FIGURE 6.5: HYSTERESIS CURVES OF THE BAAM MQA-ABS SAMPLES WITH AND WITHOUT HEAT TREATMENT UNDER AN APPLIED MAGNETIC FIELD.....	150
FIGURE 6.6: MAGNETIZATION ( $M$ ), ENERGY PRODUCT ( $(I)_{MAX}$ ), MAGNETIC INDUCTION ( $B$ ) OF THE 97% MQA 3% ABS MAGNET. ....	152
FIGURE 6.7. SAMPLE 68: MQA-ABS, SURFACE, LOW MAGNIFICATION.....	152
FIGURE 6.8. SAMPLE 68: MQA-ABS, SURFACE, HIGH MAGNIFICATION.....	153
FIGURE 6.9: SAMPLE 69: MQA-ABS, CROSS SECTION, LOW MAGNIFICATION.....	153
FIGURE 6.10. SAMPLE 69: MQA-ABS, CROSS SECTION, HIGH MAGNIFICATION.....	154
FIGURE 6.11: HISTORY OF THE DEVELOPMENT OF THE ENERGY PRODUCT OF 3D PRINTED NDFEB MAGNETS. <sup>123,124,188</sup> .....	156
FIGURE 7.1: STATOR DESIGN OF THE MOTOR. ....	159
FIGURE 7.2: ROTOR SHAPE OF THE MOTOR. ....	159
FIGURE 7.3: SCREENSHOT OF THE CAD MODEL OF THE ARNOLD MOTOR. ....	160
FIGURE 7.4: SCREENSHOT OF THE CAD MODEL OF THE ARNOLD MOTOR, CROSS-SECTIONAL VIEW.....	161
FIGURE 7.5:THE 3D PRINTED ROTOR MAGNET CYLINDER IN MAGNET HOUSING.....	162
FIGURE 7.6: RENISHAW AM250 SLM PRINTER. <sup>221</sup> .....	162
FIGURE 7.7: PHOTO OF THE FIRST LAYER BEING PRINTED DURING THE SLM PROCESS (LEFT); COMPLETED BUILD OF THE SEVEN FE-3SI STATOR SAMPLES IN A SINGLE RUN (RIGHT).....	165
FIGURE 7.8: STACKED EDM SLICED 3D PRINTED FE3SI LAMINATES. ....	168
FIGURE 7.9: THE MOTOR UNDERGOING THE WINDING PROCESS. ....	169
FIGURE 7.10: ILLUSTRATION OF THE WINDING OF A SINGLE PHASE OF THE THREE-PHASE 3D PRINTED MOTOR. ....	170
FIGURE 7.11: THE STATOR ASSEMBLY SUBMERGED IN VARNISH (LEFT); THE STATOR ASSEMBLY COATED IN VARNISH.....	171
FIGURE 7.12: STATOR ASSEMBLY WITHIN ITS HOUSING.....	171
FIGURE 7.13: CROSS SECTION OF THE PERMANENT MAGNET ROTOR CORE.....	172
FIGURE 7.14: THE COMPLETED ROTOR ASSEMBLY. ....	172
FIGURE 7.15: THE FULLY ASSEMBLED ELECTRIC MOTOR.....	173
FIGURE 7.16: SIDE VIEW OF THE FULLY ASSEMBLED ELECTRIC MOTOR.....	174
FIGURE 7.17: TOP VIEW OF THE FULLY ASSEMBLED ELECTRIC MOTOR.....	174
FIGURE 7.18: OPTICAL MICROSCOPE IMAGES OF THE 3D PRINTED FE3SI LAMINATE SAMPLES.....	177
FIGURE 7.19: SEM/EDX RESULTS OF 3D PRINTED SILICON STEEL LAMINATE.....	178
FIGURE 7.20: (A) ORNL SS-3 STANDARD SAMPLE SPECIFICATION; (B) TENSILE CURVE CHART AND PICTURE OF THE TENSILE SAMPLES. ....	178
FIGURE 7.21: MEASURING DC PROPERTIES OF A PRINTED FE3SI CYLINDER.....	180
FIGURE 7.22: RESISTIVITY OF AM FE-3Si VS. TEMPERATURE (LEFT) ; HYSTERESIS LOOP OF AM FE-3Si, UNDER DC MAGNETIZATION UP TO A HIGH MAGNITUDE OF 6 T (RIGHT); SATURATION INDUCTION OF APPROXIMATELY 2.1 T IS ACHIEVABLE AT HIGH MAGNETIZING FIELD VALUES.....	182
FIGURE 7.23: LOW DC MAGNETIC FIELD HYSTERESIS CURVE OF 3D PRINTED FE-3Si INDUCTION RING (LEFT); RELATIVE PERMEABILITY OF THE RING ACROSS INITIAL MAGNETIZATION $H$ FIELD VALUES.....	182
FIGURE 7.24: EFFECT OF HEAT TREATMENT ON THE MAGNETIC INDUCTION (LEFT) AND RELATIVE PERMEABILITY (RIGHT) OF THE AS PRINTED AND HEAT-TREATED FE-3Si LAMINATES; HIGHER THE ANNEALING TEMPERATURE, HIGHER THE B OR PERMEABILITY VALUES.....	184
FIGURE 7.25: COMPARISON OF 3D PRINTED FE3Si VS. 3D PRINTED FE6Si. <sup>160</sup> .....	184
FIGURE 7.26: THE LABORATORIO ELETTFISICO AMH-200K-S PERMEAMETER SYSTEM. <sup>227</sup> .....	186
FIGURE 7.27: CORE LOSS VS. INDUCTION OF THE 3D PRINTED FE3Si AT 60 HZ.....	187
FIGURE 7.28: MEASURED BACK EMF FOR THE 3D PRINTED MOTOR AT VARIOUS RPMS.....	189
FIGURE 8.1: MULTIMATERIAL 3D PRINTED STATORS; FeSi PREMIXED WITH 1-2 WT% ALSi10MG AND PRINTED VIA SLM..	194
FIGURE 8.2: ELLINGHAM DIAGRAM OF VARIOUS MATERIALS.....	194
FIGURE 8.3: SEVERAL 3D PRINTED MULTIMATERIAL STATOR SAMPLES UNDERWENT ANNEALING.....	195
FIGURE 8.4: COMPARING MAGNETIC PROPERTIES OF THE FOUR SAMPLES.....	197

FIGURE 8.5: MAGNETIC ALIGNMENT OF 3D PRINTED PERMANENT MAGNETS .....	201
FIGURE 8.6: MAGNETIC ALIGNMENT EXPERIMENT RESULTS.....	202
FIGURE 8.7: SECOND QUADRANT OF THE STEP III HYSTERESIS LOOP.....	202
FIGURE 8.8: A FILM THAT MANIFESTS THE MAGNETIC FIELD OF OBJECTS COVERING 3D PRINTED NdFeB MAGNETS. ....	205
FIGURE 8.9: A PAIR OF ADVANCED COPPER MOTOR WINDING DESIGNS.....	206
FIGURE 8.10: A 3D PRINTED COPPER WINDING COMPONENT. ....	206
FIGURE 8.11: THE TECHNOLOGIES OF CHAPTER 8 IN AN ELECTRIC INTERIOR PERMANENT MAGNET MOTOR. <sup>233</sup> .....	208

# **CHAPTER 1 : INTRODUCTION AND BACKGROUND**

## **1.1 Research Background**

Renewable technologies such as electric vehicles and wind turbine generators do not consume fossil fuels and are vital for nations to achieve energy independence and self-sufficiency. However, such technologies require critical materials, especially rare earth-based magnets, to operate at the highest efficiency. The United States lacks domestic deposits of these critical materials as well as internal refining infrastructure and capability to process these critical materials. Control over the supply chain of critical material mining and the supply chain of critical material refining are both currently out of reach for the United States. Thus, it is vital to conserve the usage and reduce the waste of critical materials. Additive manufacturing (AM) is a promising avenue for achieving this goal and for reducing the criticality of these materials, thereby enabling a greater deployment of critical material-dependent technologies such as electric vehicles and wind generators at a more optimal efficiency. This dissertation addresses the additive manufacturing of critical material-based magnets for electrical machine applications.

## **1.2 Objective**

Is it possible to create additively manufactured (3D printed) magnets with properties that are competitive with conventionally made magnets, with the intent of reducing the criticality of strategic materials by reducing usage and waste? The primary goal of this project is to answer this question. Chapter 1 provides motivation and objective of this study. The importance of electric vehicles and wind power generators is discussed. The criticality of vital strategic materials is reviewed, including the rare earth elements.

Chapter 2 reviews the fundamental concepts of magnets. The classification of magnets is reviewed. The conventional manufacturing processes of both soft and hard magnets are discussed. The AM processes that have been used to produce magnets are explored.

Chapter 3 reviews the material characterization and testing techniques used in this project to investigate the properties of 3D printed magnets. Material testing includes mechanical testing such as tensile testing and magnetic field testing via a superconducting quantum interference device (SQUID). Material characterization includes thermogravimetric analysis (TGA), differential scanning calorimetry (DSC), scanning electron microscopy (SEM), and X-ray powder diffraction (XRPD).

Chapter 4 reviews soft magnets. Important material properties concerning soft magnets are discussed. A list of the important conventional soft magnets and their magnetic properties is provided. A comparison of these properties is provided. The work that this project has done on the AM of soft magnets is reviewed, and the magnetic properties of these 3D printed soft magnets is provided. A comparison of the material properties of conventional and 3D printed soft magnets is provided and discussed.

Chapter 5 reviews hard (permanent) magnets is provided. Important material properties concerning permanent magnets (PMs) are discussed. A list of the important conventional hard magnets and their magnetic properties is provided. The magnetic properties of the conventional magnets are compared and discussed. The work that this project has done on the AM of hard magnets is reviewed, and the magnetic properties of these 3D printed PMs is provided. The eddy current behavior and working temperatures of the 3D printed magnets are discussed in detail. The material properties of the 3D printed PMs are then summarized. A comparison of the material properties of conventional and 3D printed hard magnets is provided and discussed.

Chapter 6 describes the evolution and improvement of the energy product of 3D printed PMs. First, the utilization of sacrificial polymers on such magnets is described. These temporary polymers exist within the 3D printed magnet after print but gets removed by heat-based postprocessing. This

process yields a magnet that has a higher composition of magnetic materials. This process also improves magnetic performance. The second part of this chapter recounts the historical development of energy products of 3D printed hard magnets. During the past few years, magnet strength has increased from less than 6 MGOe to more than 18 MGOe by 2020. Current research continues to improve energy products.

Chapter 7 describes the implementation of soft and hard 3D printed magnets in electrical machine applications. First, the construction of an electrical motor with 3D printed FeSi stator laminations and 3D printed NdFeB rotor components is described. Second, in-depth material characterization of the 3D printed soft magnetic laminate material is provided.

Chapter 8 describes future directions of research on 3D printed magnets. The first part addresses 3D printed multimaterial stators. The second part addresses future research directions for 3D printed PMs, with possible ways to further improve the energy product of 3D printed hard magnets. The third part addresses 3D printed copper windings for electrical machines. Although copper windings are not magnets, their function is closely interwoven with that of magnets. These 3D printed copper windings are another step toward a full 3D printed motor, which will use 3D printed soft and hard magnets. The fourth part provides concluding remarks on the chapter and describes a possible motor with the technology mentioned in this chapter.

### **1.3 On the Importance of Electric Vehicles and Wind Turbine Generators**

An Electric Vehicle (EV) uses an electric motor to power its wheels. Traditionally, this description has been applied to trains and trams that are powered by an electrical third rail or power cables. Motorized wheelchairs, golf carts, and the like are also EVs. However, the term EV now mainly refers to cars powered by rechargeable batteries whose speed and range rivals that of the conventional combustion engine-based cars powered by fossil fuels.<sup>1</sup> Wind power is the

harnessing of winds to drive machinery, such as a mill or an electrical generator. Such generators are known as wind generators or aerogenerators.<sup>2</sup> Most wind generators are wind turbines, which use airfoils attached to an electrical generator. The winds lift the blades, providing kinetic energy to the generator for conversion into electrical energy.<sup>3</sup> An electric motor is a machine that converts electrical energy into mechanical energy.<sup>4</sup> An electric generator is the opposite: a machine that converts mechanical energy into electrical power.<sup>5</sup> Fossil fuels play no part in energy conversion in either of these machines, which is why EVs and wind generation are important.

Energy powers a nation's economy, and a nation cannot truly achieve self-sufficiency without energy independence. This fact is illustrated by the recent Russia–Ukraine war. Russia, in retaliation to Western sanctions and support for Ukraine, shut off its natural gas pipelines, such as the Nord Stream I, to Europe, resulting in a severe energy crisis and a devastating economic blow to the West. Consequently, Europe is on the brink of recession, and many of its industries may incur permanent damage and never reopen.<sup>6</sup> Europe relied too heavily on Russian supplied fossil fuels instead of more domestic alternative power sources, such as nuclear, wind, or solar. This issue highlights the necessity to dramatically expand the infrastructure of power sources that are less vulnerable to foreign intervention. An EV fleet can help accomplish this goal by reducing the need for foreign gasoline, and wind turbines can reduce the reliance on imported natural gas. Both technologies are vital to building a nation's capacity for energy independence and economic freedom. Furthermore, EVs and wind turbines pollute less than carbon-based power sources and use renewable resources.

#### **1.4 On the Criticality of Vital Strategic Materials (Critical Materials)**

Electric motors and generators are known as electrical machines—devices that can convert mechanical energy to electrical energy or vice versa. Any electrical machine can convert power in



either direction; therefore, any electrical machine can be used as either a generator or a motor.<sup>7</sup> Electrical machine designs that employ PMs are characterized by high efficiency, good controllability, and superior torque and power density.<sup>8</sup> Not all PMs contain rare earth elements, but the ones with the highest magnetic strength do. The strongest rare earth PM is NdFeB, and thus it is the most commonly used PM for electric machine applications, such as wind turbines and automotive electric motors.<sup>9-11</sup> Other less powerful and thus less widely used PMs include SmCo and AlNiCo. The US government designates aluminum, cobalt, neodymium, nickel, and samarium (also a rare earth element) as critical materials.<sup>9,12</sup>

Rare earth elements are a group of 17 elements comprising scandium, yttrium, and the lanthanides. Figure 1.1 highlights the rare earth elements in blue on the periodic table and highlights cobalt, another critical material, in gold. The principal economic sources of rare earth elements are from the minerals monazite, bastnasite, and loparite along with the lateritic ion-adsorption clays. Rare earth elements are relatively abundant in the Earth's crust, but are distributed unevenly; therefore, mineable concentrations are less common than most other mineral commodities.<sup>13</sup> Rare earth elements also tend to occur together in nature and are difficult to separate from one another and thus are difficult to extract. The lack of economically mineable deposits as well as the difficulty in refining rare earth elements contributes to their rarity and material criticality.<sup>11,13,14</sup> Only one rare earth mine is within the United States, located at Mountain Pass, California. This facility mines the mineral bastnaesite. Monazite, another rare earth mineral, is produced as a byproduct of heavy mineral mining in the southeastern United States. The United States has very meager rare earth reserves, and rare earth mining production is modest compared with the countries that are leading rare earth mining producers.<sup>13,15</sup> The United States also has very little domestic rare earth refining capacity, and most of the rare earth ores it produces from mining are exported abroad for separation

and refining.<sup>13,15</sup> By contrast, China is the world's leading producer and refiner of rare earth elements. Conservative estimates suggest that China controls more than 50% of the global rare earth mining capacity as well as over 80% of the global rare earth refining capacity. China dominates the global rare earth supply chain. Creating a domestic rare earth supply chain within the United States faces significant economic, political, and technical challenges.<sup>15-18</sup> Therefore, the US government considers rare earth elements critical materials.<sup>15</sup>

The United States government defines critical materials as nonfuel minerals that are essential to US economic or national security and that have a supply chain vulnerable to disruption. Critical materials are also characterized as serving an essential function in the manufacturing of a product, the absence of which would have significant consequences for the economy or national security.<sup>12,15,20,21</sup> The United States Geological Survey (USGS) publishes annual lists of the 50 most critical materials to the United States. A copy of the 2022 USGS list is provided in Table S1 in the Supplemental Section. This list is ordered alphabetically and not in order of criticality. The four most common commercial PMs are NdFeB, SmCo, AlNiCo, and hard ferrites; the names of the former three describe their composition.<sup>9</sup> In addition to the rare earth elements neodymium and samarium, aluminum, cobalt, and nickel all appears on the 2022 USGS critical materials list.<sup>12</sup> Hard ferrites are typically ceramic materials created by mixing and firing large portions of Fe<sub>2</sub>O<sub>3</sub> with other constituents such as barium or strontium carbonates at high temperatures. Barite is composed of barium and is on the 2022 critical materials list, and strontium appeared on a previous version of the critical materials list.<sup>12</sup> Hard ferrites are the magnetically weakest and have the lowest energy product of these four PMs, whereas NdFeB is the strongest and has the highest energy density.<sup>9</sup> Therefore, hard ferrites are rarely used for electric machines, and NdFeB is the

### Periodic Table of the Elements

1 <b>H</b> Hydrogen 1.0079																	2 <b>He</b> Helium 4.0026
3 <b>Li</b> Lithium 6.941	4 <b>Be</b> Beryllium 9.0122											5 <b>B</b> Boron 10.81	6 <b>C</b> Carbon 12.011	7 <b>N</b> Nitrogen 14.007	8 <b>O</b> Oxygen 15.999	9 <b>F</b> Fluorine 18.998	10 <b>Ne</b> Neon 20.179
11 <b>Na</b> Sodium 22.99	12 <b>Mg</b> Magnesium 24.305											13 <b>Al</b> Aluminium 26.982	14 <b>Si</b> Silicon 28.086	15 <b>P</b> Phosphorus 30.974	16 <b>S</b> Sulfur 32.06	17 <b>Cl</b> Chlorine 35.453	18 <b>Ar</b> Argon 39.948
19 <b>K</b> Potassium 39.098	20 <b>Ca</b> Calcium 40.08	21 <b>Sc</b> Scandium 44.956	22 <b>Ti</b> Titanium 47.9	23 <b>V</b> Vanadium 50.941	24 <b>Cr</b> Chromium 51.996	25 <b>Mn</b> Manganese 54.938	26 <b>Fe</b> Iron 55.847	27 <b>Co</b> Cobalt 58.933	28 <b>Ni</b> Nickel 58.71	29 <b>Cu</b> Copper 63.546	30 <b>Zn</b> Zinc 65.38	31 <b>Ga</b> Gallium 69.72	32 <b>Ge</b> Germanium 72.59	33 <b>As</b> Arsenic 74.922	34 <b>Se</b> Selenium 78.96	35 <b>Br</b> Bromine 79.904	36 <b>Kr</b> Krypton 83.8
37 <b>Rb</b> Rubidium 85.468	38 <b>Sr</b> Strontium 87.62	39 <b>Y</b> Yttrium 88.906	40 <b>Zr</b> Zirconium 91.22	41 <b>Nb</b> Niobium 92.906	42 <b>Mo</b> Molybdenum 95.94	43 <b>Tc</b> Technetium (98)	44 <b>Ru</b> Ruthenium 101.07	45 <b>Rh</b> Rhodium 102.91	46 <b>Pd</b> Palladium 106.4	47 <b>Ag</b> Silver 107.87	48 <b>Cd</b> Cadmium 112.41	49 <b>In</b> Indium 114.82	50 <b>Sn</b> Tin 118.69	51 <b>Sb</b> Antimony 121.75	52 <b>Te</b> Tellurium 127.6	53 <b>I</b> Iodine 126.9	54 <b>Xe</b> Xenon 131.3
55 <b>Cs</b> Caesium 132.91	56 <b>Ba</b> Barium 137.33	57 <b>*La</b> Lanthanum 138.91	72 <b>Hf</b> Hafnium 178.49	73 <b>Ta</b> Tantalum 180.95	74 <b>W</b> Tungsten 183.85	75 <b>Re</b> Rhenium 186.21	76 <b>Os</b> Osmium 190.2	77 <b>Ir</b> Iridium 192.22	78 <b>Pt</b> Platinum 195.09	79 <b>Au</b> Gold 196.97	80 <b>Hg</b> Mercury 200.59	81 <b>Tl</b> Thallium 204.37	82 <b>Pb</b> Lead 207.2	83 <b>Bi</b> Bismuth 208.98	84 <b>Po</b> Polonium (209)	85 <b>At</b> Astatine (210)	86 <b>Rn</b> Radon (222)
87 <b>Fr</b> Francium (223)	88 <b>Ra</b> Radium (226)	89 <b>†Ac</b> Actinium (227)	104 <b>Rf</b> Rutherfordium (267)	105 <b>Db</b> Dubnium (268)	106 <b>Sg</b> Seaborgium (271)	107 <b>Bh</b> Bohrium (272)	108 <b>Hs</b> Hassium (270)	109 <b>Mt</b> Meitnerium (276)	110 <b>Ds</b> Darmstadtium (281)	111 <b>Rg</b> Roentgenium (280)	112 <b>Cn</b> Copernicium (285)	113 <b>Nh</b> Nihonium (284)	114 <b>Fl</b> Flerovium (289)	115 <b>Mc</b> Moscovium (288)	116 <b>Lv</b> Livermorium (293)	117 <b>Ts</b> Tennessine (294)	118 <b>Og</b> Oganesson (294)
* Lanthanides		58 <b>Ce</b> Cerium 140.12	59 <b>Pr</b> Praseodymium 140.91	60 <b>Nd</b> Neodymium 144.24	61 <b>Pm</b> Promethium [145]	62 <b>Sm</b> Samarium 150.4	63 <b>Eu</b> Europium 151.96	64 <b>Gd</b> Gadolinium 157.25	65 <b>Tb</b> Terbium 158.93	66 <b>Dy</b> Dysprosium 162.5	67 <b>Ho</b> Holmium 164.93	68 <b>Er</b> Erbium 167.26	69 <b>Tm</b> Thulium 168.93	70 <b>Yb</b> Ytterbium 173.04	71 <b>Lu</b> Lutetium 174.97		
† Actinides		90 <b>Th</b> Thorium 232.04	91 <b>Pa</b> Protactinium 231.04	92 <b>U</b> Uranium 238.03	93 <b>Np</b> Neptunium (237)	94 <b>Pu</b> Plutonium (244)	95 <b>Am</b> Americium (243)	96 <b>Cm</b> Curium (247)	97 <b>Bk</b> Berkelium (247)	98 <b>Cf</b> Californium (251)	99 <b>Es</b> Einsteinium (252)	100 <b>Fm</b> Fermium (257)	101 <b>Md</b> Mendelevium (258)	102 <b>No</b> Nobelium (259)	103 <b>Lr</b> Lawrencium (262)		

Figure 1.1: Rare earth elements (blue) and cobalt (gold) on the periodic table.<sup>19</sup>

most common PM used for such an application.<sup>11</sup> PMs used by electrical machines found in EVs and wind generators comprise critical materials and are vulnerable to supply-chain disruptions. Figure 1.2 illustrates the relative abundance of elements within the Earth's upper crust. The rare earth elements are not the scarcest elements, and crustal abundance alone does not determine the material's criticality.

Material criticality is also illustrated by market prices: demand typically far exceeds supply, resulting in extremely high prices. Table 1.1 lists the market prices of certain materials on a US dollar (\$) per metric ton (t) basis. These prices are further illustrated by Figures 1.3 and 1.4. The price histories of certain critical materials are illustrated by Figures 1.5.

Critical materials such as the rare earth elements neodymium or dysprosium can have market prices that are orders of magnitude higher than noncritical commodities such as steel. All the materials in the aforementioned table and figures are critical materials, except for steel and copper.<sup>12</sup> Manganese illustrates that not all critical materials have a high market price. Manganese has a low market price primarily because of its low demand. Its primary purpose is as an additive in steel manufacturing, and it is not used in large quantities. Manganese's criticality is due to its lack of US domestic production as the result of low demand.<sup>23</sup> Even within critical materials, market price can vary significantly. A few, such as manganese, are actually quite inexpensive and their market price does not reflect their criticality. Critical metals such as nickel and cobalt, have high market prices, albeit much less than rare earth critical materials such as neodymium and dysprosium. The critical heavy rare earth material dysprosium is much more expensive than the light rare earth material neodymium. Many factors influence the market price and the criticality of materials; one such important factor is recyclability, or more accurately, the current recycling rate. Table 1.2 and

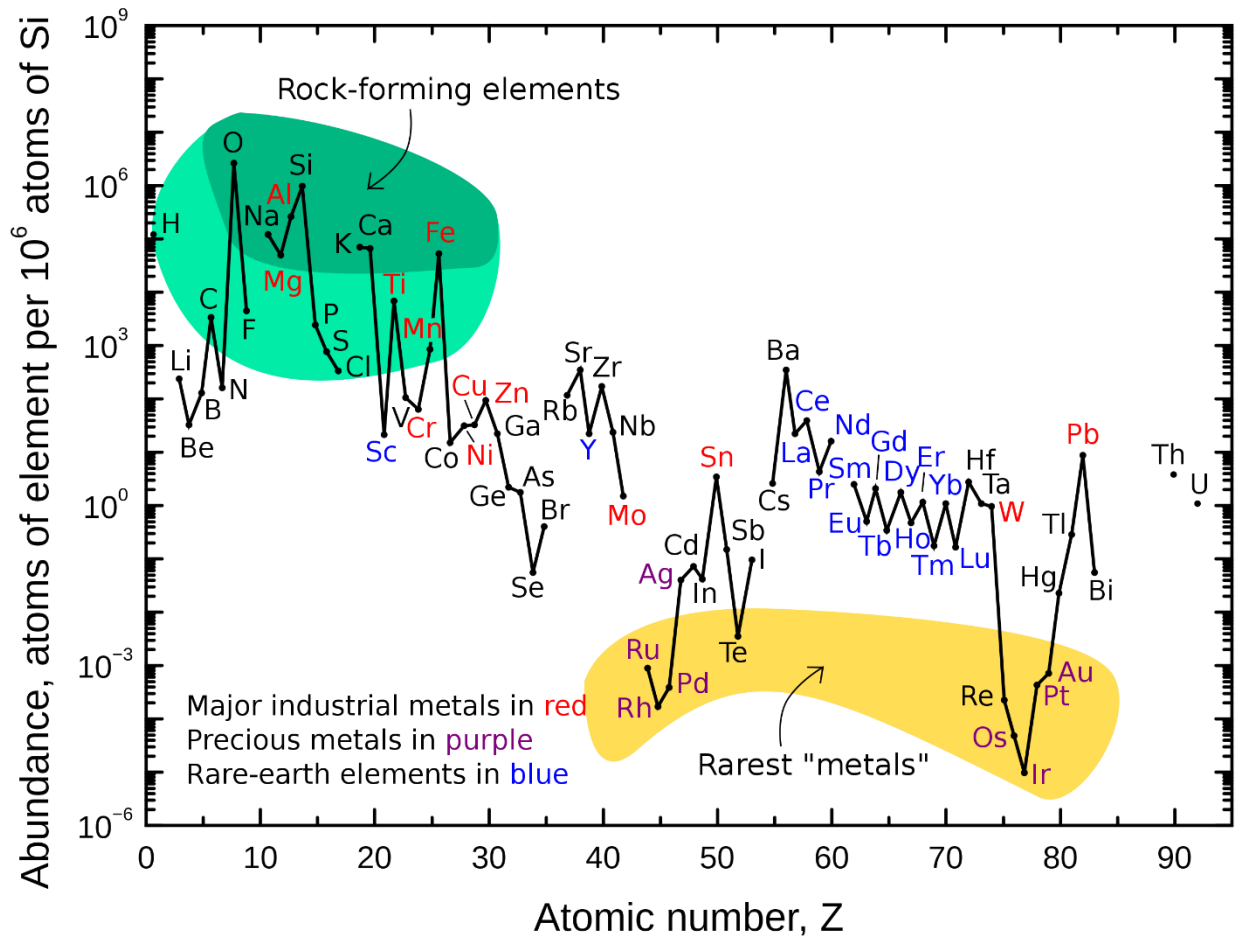


Figure 1.2: The relative abundance of elements within Earth's upper crust.<sup>22</sup>

Figure 1.6 illustrate the recycling rate of critical and noncritical materials important to EVs and wind generators.

Table 1.2 and Figure 1.6 show that the recycling rates of these materials varies greatly. The recycling rates of the non-rare earth metals are higher than that of the rare earth metals. Current recycling rates of rare earth metals are negligible and are estimated to be less than 2%.<sup>10,13</sup> The most common and critical uses for neodymium and dysprosium are for high-performance PMs.<sup>10,12,13</sup> Dysprosium is commonly added in minute quantities to increase the working temperature of the NdFeB PM.<sup>11,35</sup> The most common applications for such rare earth PMs are for electrical machine-related applications.<sup>36</sup> Rare earth elements in general are difficult to substitute in their applications without compromising effectiveness.<sup>13</sup> Rare earth magnets are especially difficult to replace with non-rare earth magnets without sacrificing performance quality.<sup>35,37</sup> Thus, neodymium and dysprosium are extremely valuable and critical. Nevertheless, recycling rates of rare earth elements such as neodymium and dysprosium are extremely low. The main factor contributing to these low recycling rates is technical. Rare earth chemical compounds are especially difficult to decompose to extract the rare earth elements from the waste in a usable form. Common consumer products containing rare earth elements often have low concentrations of these elements, further complicating technical and efficiency issues surrounding rare earth recycling. Several rare earth recycling processes have been proposed, but they are all currently in the research phase and are not fully developed for practical applications. Thus, no widely adopted rare earth recycling process nor infrastructure currently exists. Consequently, collection rates of rare earth elements for recycling are abysmal.<sup>8,10,33</sup> By contrast, the recycling rates of the other materials in Table 1.2 and Figure 1.6 are higher for several reasons. Often, the cheapest materials by market

Table 1.1: Market prices of various raw materials as of October 2022.

Raw material	Price (\$/t)	Source
Neodymium	127,000.96	SMM <sup>24</sup>
Dysprosium	411,706.4	SMM <sup>25</sup>
Cobalt	51,955	LME <sup>26</sup>
Nickel	22,412	LME <sup>27</sup>
Copper	7,578.5	LME <sup>28</sup>
Manganese	2,246.88	SMM <sup>29</sup>
Steel	582.5	LME <sup>30</sup>

Note: SMM = Shanghai Metals Market; LME = London Metal Exchange; \$/t = United States Dollar per metric ton; 1 metric ton = 1,000 kilograms

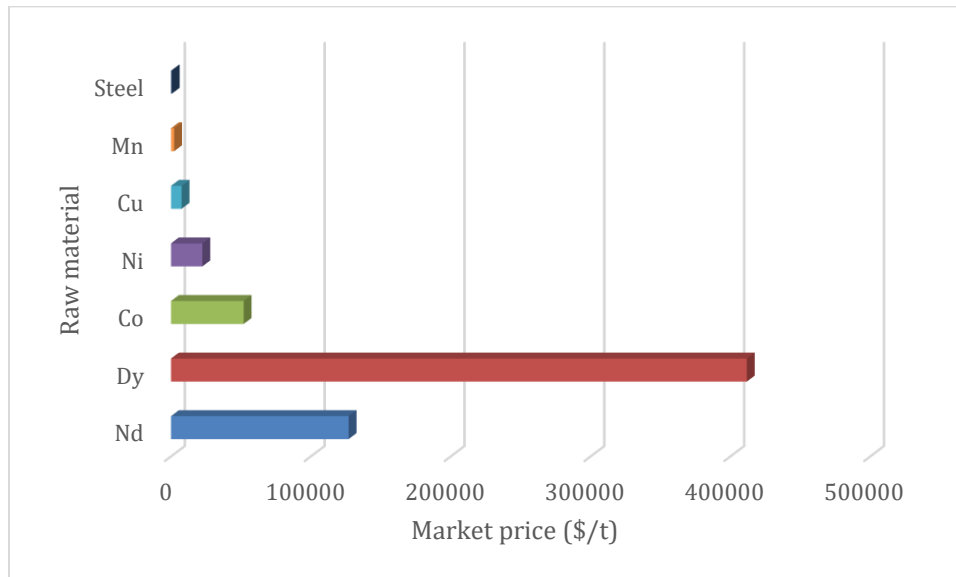


Figure 1.3: Market prices of critical and noncritical materials.<sup>24-30</sup>

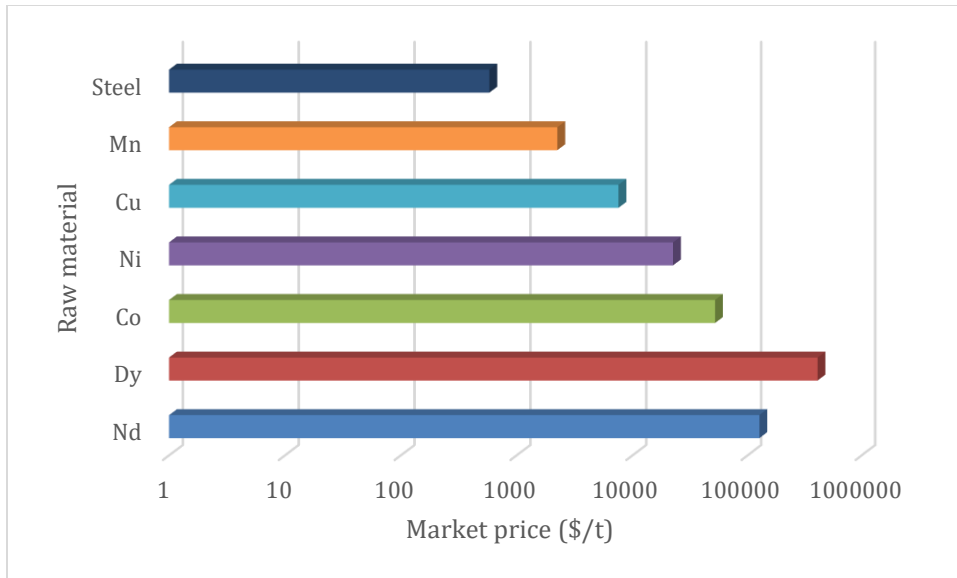


Figure 1.4: Market prices of critical and noncritical materials in logarithmic scale.<sup>24-30</sup>

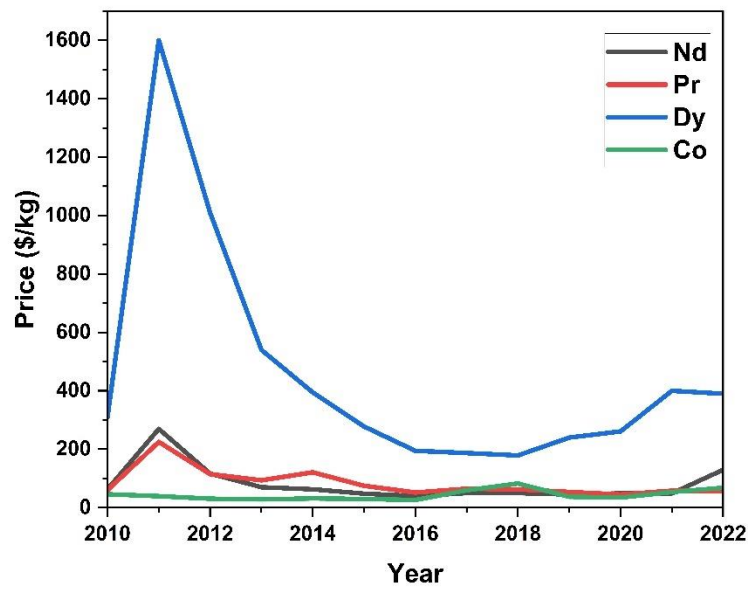


Figure 1.5: The price history of neodymium, praseodymium, dysprosium, and cobalt (2010–2022).<sup>13,31,32</sup>



Table 1.2: Recycling rates of various raw materials.

Raw materials	End-of-life recycling rate (%)	Source
Neodymium	2	10
Dysprosium	2	10
Cobalt	32	33
Nickel	60	33
Copper	50	33
Manganese	53	33
Steel	85	34

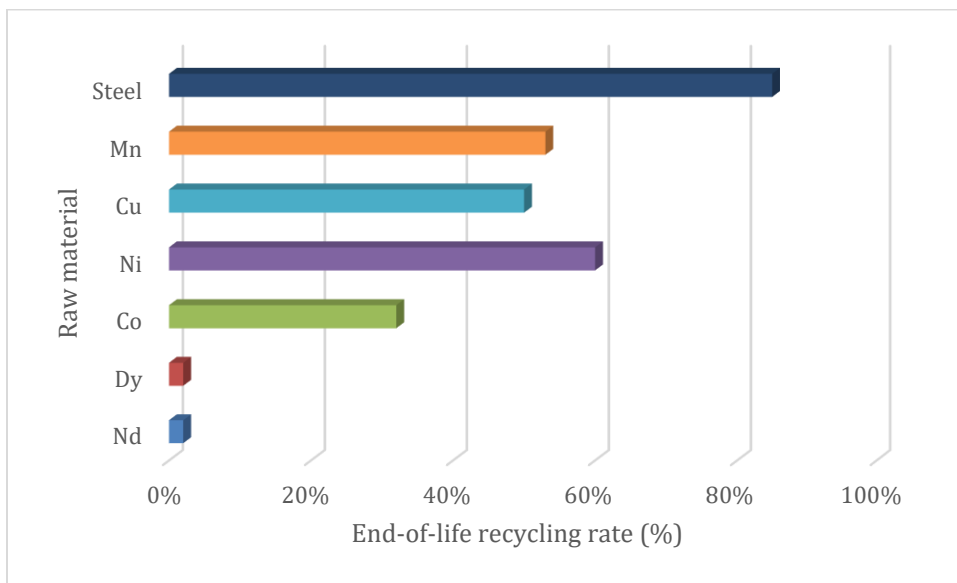


Figure 1.6: Recycling rates of various materials.<sup>10,33,34</sup>

price, such as steel and manganese, have the highest recycling rates. Steel, being one of the most widely used materials in existence, has both high demand and high supply. Partially because of its high demand, steel has a mature and highly developed recycling infrastructure. This infrastructure leads to a high waste collection rate. A large percentage (estimated to be 40% in Organization for Economic Co-Operation and Development [OECD] countries) of recycled steel is used to produce new steel. In the United States, the average annual recycling rate of steel is nearly 90%. Steel's excellent recycling capabilities increase its supply, partially leading to its low cost.<sup>11,33,34</sup> By contrast, manganese's lack of demand in sufficient volume hampers dedicated recycling efforts. Manganese is critical to steel manufacture because of its alloying, deoxidizing, and sulfur-fixing properties. Manganese steels exhibit excellent strength and high ductility despite low quantities of manganese within the alloy. Medium-manganese steel, one of the most common and in-demand types of manganese steel, is classified as steel with only 3–10 wt% manganese. Steelmaking is the primary and dominant application and demand for manganese. Up to 90% of the manganese within the United States is used for steelmaking alone, but steelmaking does not consume manganese in high quantities, so demand for it is not high. World reserves and therefore supply of manganese is high. Thus, its market price is very low—so low, in fact, that the United States has not mined manganese-rich ores domestically since 1970. Even with no domestic production, the United States imports less than 500,000 t of manganese per year. Consequently, negligible dedicated scrap recovery exists for manganese, and it is recycled incidentally as a constituent of ferrous and nonferrous scrap. Nevertheless, the recycling rate of manganese in OECD countries is an impressively high 53%,<sup>23,33,38</sup> demonstrating that it is possible for the incidental recycling of low-quantity constituent materials to have a high recycling rate if the main material being recycled has a high recycling rate and mature recycling infrastructure. Dysprosium within NdFeB is like

manganese within steel: it is an important low-quantity constituent material within a main host material. Recycling could concurrently increase the supply of both neodymium and dysprosium and allow both to become more sustainable, thereby becoming less critical. As discussed in detail in section 5.3.6 of this paper, AM is a potential highly efficient avenue of recycling and reducing the waste of neodymium and dysprosium.<sup>39</sup>

Cobalt also has a relatively low recycling rate despite a having high material cost. Cobalt is used in many diverse industrial, commercial, and military applications; many of these are highly critical and strategic. Of the cobalt consumed within the United States, 42% was used in superalloys in aircraft gas turbine engines. Globally, the leading use of cobalt is in rechargeable battery electrodes, especially in lithium-ion batteries, which are widely used in electric vehicles. Cobalt is also used in SmCo and AlNiCo PMs as well as in small quantities in NdFeB magnets. PMs are important in EVs and in wind power generation. For certain applications, another material can be substituted for cobalt. However, this substitution often results in reduced product performance or increased cost. Global distribution of cobalt deposits is extremely uneven, and most of these deposits are concentrated within the Democratic Republic of the Congo. The United States has very low cobalt resources within its borders. Consequently, cobalt is a highly critical and expensive material. The difficulty in recycling cobalt further exacerbates its criticality and price. The OECD cobalt recycling rate is only 32%. In 2021, cobalt contained in purchased scrap represented 24% of the cobalt consumed within the United States. Currently, technical challenges and limitations hinder cobalt recycling processes, and more research is needed to improve the efficiency and economic viability of cobalt recycling.<sup>12,31,33,40-42</sup> Again, AM could be a potential method to recycle and reduce the waste of cobalt and help alleviate its criticality. This possibility will be discussed in section 5.3.9 of the paper.

Market share for Wind power generation and for EVs is projected to grow significantly in the near future.<sup>43-48</sup> Table 1.3 summarizes the US wind power generation capacity in 2022. The US Department of Energy (DOE) published a report called *Wind Vision: A New Era for Wind Power in the United States*, which lists DOE's future wind capacity goals.<sup>43</sup> Table 1.5 lists the 2030 and 2050 Wind Vision target wind generation capacities and the next change from the 2022 wind generation power capacity. Table 1.4 lists the estimated raw materials usage for wind turbine generators. The projected demand of raw materials for the Wind Vision 2030 target was calculated using the data from Tables 1.4 and 1.5, and the result is presented in Table 1.6. Likewise, the projected demand of raw materials for the Wind Vision 2050 target was calculated, and the result is summarized in Table 1.7. Table 1.8 lists the material composition of a typical NdFeB PM. By using data from Tables 1.6, 1.7, and 1.8, the projected demand for cobalt for the Wind Vision targets was calculated, and the result is presented in Table 1.9. Tables 1.6, 1.7, and 1.9 indicate that large quantities of critical materials are needed to accomplish the DOE Wind Vision 2030 and 2050 wind generation target capacities, particularly the extremely large values for neodymium and dysprosium. The highest projected material demand for neodymium exceeds the total rare earth production within the United States in 2022.<sup>13</sup> Furthermore, calculations indicate that the deployment of wind turbines according to European Union plans alone will require most of the neodymium and dysprosium currently available globally,<sup>46</sup> not including the critical materials that will be used in EVs. These facts illustrate the extreme criticality of rare earth materials and highlight the necessity to reduce this criticality. This reduction can be accomplished by increasing the supply of these critical materials available for use; waste reduction and recycling can both help achieve this goal. AM's ability to reduce waste and recycle feedstock, which can be critical materials, will be discussed in detail in section 5.3.6 of this paper.

Table 1.3: US wind power generation capacity in 2022.

Type	Capacity (MW)	Average capacity per turbine (MW)
Land-based wind	135,886	3
Offshore wind	42	7
Distributed wind	1,075	0.012078652
Total	137,003	N/A

Source: DOE<sup>44</sup>

Table 1.4: Estimated lower and upper limits for wind turbine raw material usage.

Material	Lower limit (t/GW)	Upper limit (t/GW)
Steel	107,000	132,000
Copper	950	5000
Dysprosium	2	17
Manganese	780	800
Neodymium	12	180
Nickel	240	440

Source: European Commission, Joint Research Centre<sup>46</sup>

Table 1.5: DOE Wind Vision targets and net changes.

Year	DOE Wind Vision target (GW)	Net gain from 2022 capacity (GW)
2030	224	86.997
2050	404	266.997

Source: DOE<sup>43</sup>

Table 1.6: Calculated projected demand of raw materials for Wind Vision 2030 target.

Material	Projected demand for 2030 target (low) (t)	Projected demand for 2030 target (high) (t)
Steel	9,308,679	11,483,604
Copper	82,647.15	434,985
Dysprosium	173.994	1,478.949
Manganese	67,857.66	69,597.6
Neodymium	1,043.964	15,659.46
Nickel	2,0879.28	38,278.68

Table 1.7: Calculated projected demand of raw materials for Wind Vision 2050 target.

<b>Material</b>	<b>Projected demand for 2050 target (low) (t)</b>	<b>Projected demand for 2050 target (high) (t)</b>
Steel	28,568,679	35,243,604
Copper	253,647.15	1,334,985
Dysprosium	533.994	4,538.949
Manganese	208,257.66	213,597.6
Neodymium	3,203.964	48,059.46
Nickel	64,079.28	117,478.68

Table 1.8: Material composition of a typical NdFeB permanent magnet.

<b>Material</b>	<b>Concentration (mg/L)</b>	<b>Composition (wt.%)</b>
Boron	278	0.13
Cobalt	245	0.11
Chromium	1	0.00
Copper	32.6	0.01
Dysprosium	210	0.10
Iron	210,000	95.16
Molybdenum	1	0.00
Neodymium	7,580	3.43
Nickel	1	0.00
Praseodymium	2,340	1.06
Total	220,688.6	100.00

Source: Emil et al.<sup>41</sup>

Table 1.9: Calculated cobalt demand for Wind Vision wind generation targets.

<b>Cobalt demand</b>	<b>Low</b>	<b>High</b>
2030 target (t)	33.7	506.1
2050 target (t)	103.6	1,553.4

Wind turbine generators are not the only electrical machines that will soon face massive expansion in deployment and use. In September 2022, the White House published a fact sheet regarding the near-term economic plan for EVs in the United States. One of the goals of this plan is for EVs to make up 50% of all vehicles sold in the United States by 2030. The Bipartisan Infrastructure Law invests \$7.5 billion to build a national network of 500,000 EV chargers across the United States. Another \$7 billion is set aside to ensure domestic manufacturers have the critical materials and other components necessary to make batteries. Since 2020, the private sector has announced investments of more than \$36 billion in EV manufacturing and \$48 billion in batteries within the United States. Another goal of the plan calls for 100% of new light-duty federal vehicles to be zero emission by 2027.<sup>49</sup> In February 2023, European Union lawmakers voted to ban the sale of new gasoline-powered cars from 2035. This aggressive move will accelerate the transition to EVs.<sup>50</sup> These facts indicate that EV manufacturing is facing massive growth and will continue grow for the foreseeable future.

According to a 2021 International Energy Agency (IEA) report, the global expansion of EV manufacturing will cause dramatic increases in the demand for critical materials.<sup>48</sup> The IEA provides two scenarios in this report: the Sustainable Development Scenario (SDS) and the Stated Policies Scenario (STEPS). SDS and STEPS are both global projections. In the SDS scenario, global net-zero carbon emissions are mostly achieved by 2050. This scenario necessitates increased commitment to renewable technologies, and thus SDS is the high material demand scenario. The STEPS scenario is based on the current policy measures and plans. STEPS falls far short of the world sustainability goals but is the more realistic project unless policy regarding commitment to sustainable technology changes. Therefore, STEPS results in a lower commitment to renewable technologies and is the low material demand scenario. Nevertheless, STEPS and SDS

both increase in global demand for critical materials because they increase demand for new EVs. The difference between SDS and STEPS is that SDS projects more extreme increases in the demand for critical materials from EV sales.<sup>48</sup> Table 1.10 lists the IEA STEPS projected material demand for EV and battery storage for 2020, 2030, and 2040, in thousand metric tons. Table 1.11 lists the IEA SDS projected material demand for EV and battery storage, for the years 2020, 2030, and 2040, in thousand metric tons.

The data in Table 1.10 and Table 1.11 indicate massive and dramatic increases in the demand for critical materials, even for the more conservative STEPS estimate, which represents the stated policy goals of various national governments and multinational corporations and is the theoretical minimum material demand of those stated policies. By 2040, the global EV demand for neodymium will be between 11,000 and 28,000 t, and the global EV demand for other rare earth elements will be between 3,000 and 7,000 t. By comparison, the 2021 US total rare earth production is only 43,000 t, and all of it is refined overseas. The global rare earth mine production in 2021 was estimated to be around 280,000 t of rare earth oxide equivalent.<sup>13</sup> The rare earth demand from EVs alone in 2040 will consume a significant portion of the global supply of rare earth elements. Unless the United States starts refining rare earth elements domestically, it will be reliant on imports for refined rare earth elements. The lack of domestic refining as well as the increase in demand will further increase the criticality of rare earth elements.

Several critical materials have been selected from many to construct the following tables and figures. Table 1.12 lists the STEPS projected critical material demand growth from EV and battery storage. Figure 1.7 illustrates the STEPS projected critical material demand growth from EV manufacturing. Figure 1.8 illustrates the STEPS projected critical material demand growth from battery storage.



Table 1.10: IEA STEPS projected material demand for EV and battery storage.

<b>Demand</b>	<b>2020</b>	<b>2030</b>	<b>2040</b>
<b>EV and battery storage (total)</b>	<b>426</b>	<b>2,992</b>	<b>3,994</b>
<b>EVs (total)</b>	<b>401</b>	<b>2,809</b>	<b>3,459</b>
Copper	110	717	951
Cobalt	21	106	127
Graphite	141	1,065	1,027
Lithium	20	152	248
Manganese	25	102	117
Nickel	80	647	950
Silicon	0	8	26
Neodymium	2	9	11
Other rare earth elements	0	2	3
<b>Battery storage (total)</b>	<b>26</b>	<b>183</b>	<b>535</b>
Copper	8	55	133
Cobalt	0	3	9
Graphite	15	86	177
Lithium	2	12	28
Manganese	0	4	9
Nickel	0	10	36
Silicon	0	1	4
Vanadium	—	11	139

Note: in thousand metric tons (kt); Source: International Energy Agency. <sup>48</sup>

Table 1.11: IEA SDS projected material demand for EV and battery storage.

<b>Demand</b>	<b>2020</b>	<b>2030</b>	<b>2040</b>
<b>EV and battery storage (total)</b>	<b>426</b>	<b>6,905</b>	<b>12,650</b>
<b>EVs (total)</b>	<b>401</b>	<b>6,603</b>	<b>11,803</b>
Copper	110	1,633	3,119
Cobalt	21	257	441
Graphite	141	2,499	3,569
Lithium	20	358	859
Manganese	25	246	404
Nickel	80	1,567	3,287
Silicon	0	20	90
Neodymium	2	18	28
Other rare earth elements	0	5	7
<b>Battery storage (total)</b>	<b>26</b>	<b>302</b>	<b>847</b>
Copper	8	90	211
Cobalt	0	6	14
Graphite	15	142	280
Lithium	2	20	45
Manganese	0	7	14
Nickel	0	17	57
Silicon	0	1	7
Vanadium	—	19	219

Note: in thousand metric tons (kt); Source: International Energy Agency. <sup>48</sup>

Table 1.12 and Figures 1.7 and 1.8 reveal that even in the more conservative STEPS projection, neodymium and other rare earth element demand from EVs alone will increase fourfold by 2030 and sixfold by 2040. EV demand for cobalt, a highly critical metal, will increase sixfold, and its battery storage demand will increase 44-fold by 2040. The STEPS projections indicate dramatic increases in the demand for critical materials from EV and battery storage applications.

Table 1.13 lists the SDS projected critical material demand growth from EV manufacturing and battery storage. Figure 1.9 illustrates the SDS projected critical material demand growth from EV manufacturing. Figure 1.10 illustrates the SDS projected critical material demand growth from battery storage.

Table 1.13 and Figures 1.9 and 1.10 reveal that, in the more radical SDS projection, neodymium and other rare earth element demand from EVs alone will increase 10-fold by 2030 and 15-fold by 2040. EV demand for cobalt, a highly critical metal, will increase sixfold, and its battery storage demand will increase an astounding 44-fold by 2040. The SDS projections indicate the dramatic increases in the demand of critical materials from EV and battery storage applications that are required for a sustainable net-zero carbon emission future, and the SDS increases are even more massive than the already high STEPS increases.

The IEA report also included projected global material demands for wind power generation. Table 1.14 lists the IEA STEPS projected material demand for wind power generation, and Table 1.15 lists the SDS version.

Tables 1.14 and 1.15 reveal that the projected global material demand for neodymium from wind power generation is 6,100–8,500 t by 2030 and 6,100–9,000 t by 2040. The earlier Wind Vision calculated that US material demand for neodymium is around 1,000–15,600 t for 2030 and 3,200–48,000 t for 2050. In the Wind Vision calculations, the high and low material demand per gigawatt

Table 1.12: IEA STEPS projected critical material demand growth from EV and battery storage in multiples of 2020 critical materials demand.

EV				Battery storage			
Demand	2020	2030	2040	Demand	2020	2030	2040
Copper	1	6.503	8.619	Copper	1	6.575	15.980
Cobalt	1	5.027	6.033	Cobalt	1	16.986	44.362
Manganese	1	4.020	4.602	Manganese	1	16.703	36.512
Nickel	1	8.044	11.803	Nickel	1	26.082	90.945
Neodymium	1	4.787	6.073				
Other rare earth elements	1	4.787	6.073				

Note: STEPS material demand for 2020 EV/Other rare earth elements = 0.45 kt; 2020 battery storage/cobalt = 0.20 kt; 2020 battery storage/manganese = 0.25 kt; 2020 battery storage/nickel = 0.40 kt; Source: International Energy Agency.<sup>48</sup>

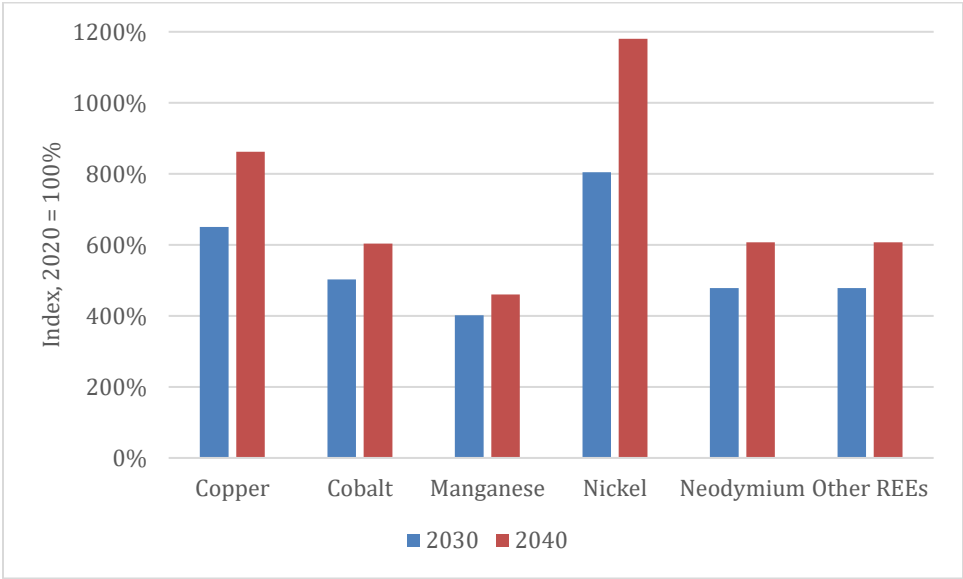


Figure 1.7: STEPS projected growth in critical material demand from EV manufacturing.

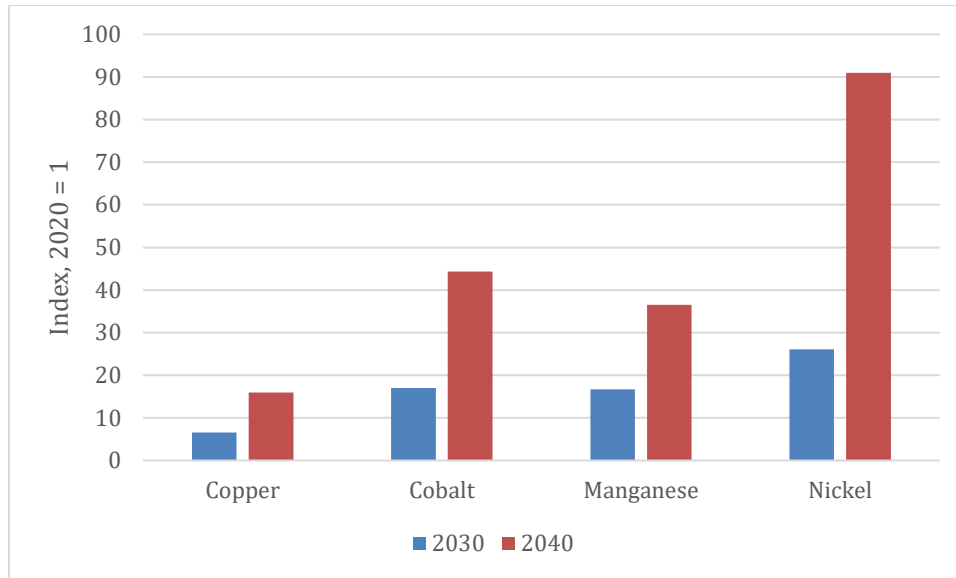


Figure 1.8: STEPS projected growth in critical material demand from battery storage.

Table 1.13: IEA SDS projected critical material demand growth from EV and battery storage in multiples of 2020 critical materials demand.

EV				Battery storage			
Demand	2020	2030	2040	Demand	2020	2030	2040
Copper	1	14.799	28.276	Copper	1	10.853	25.282
Cobalt	1	12.150	20.885	Cobalt	1	28.037	70.188
Manganese	1	9.717	15.931	Manganese	1	27.571	57.767
Nickel	1	19.473	40.844	Nickel	1	43.052	143.889
Neodymium	1	10.200	15.383				
Other rare earth elements	1	10.200	15.383				

Note: SDS material demand for: 2020 EV/other rare earth elements = 0.45 kt; 2020 battery storage/cobalt = 0.20 kt; 2020 battery storage/manganese = 0.25 kt; 2020 battery storage/nickel = 0.40 kt; Source: IEA.<sup>48</sup>

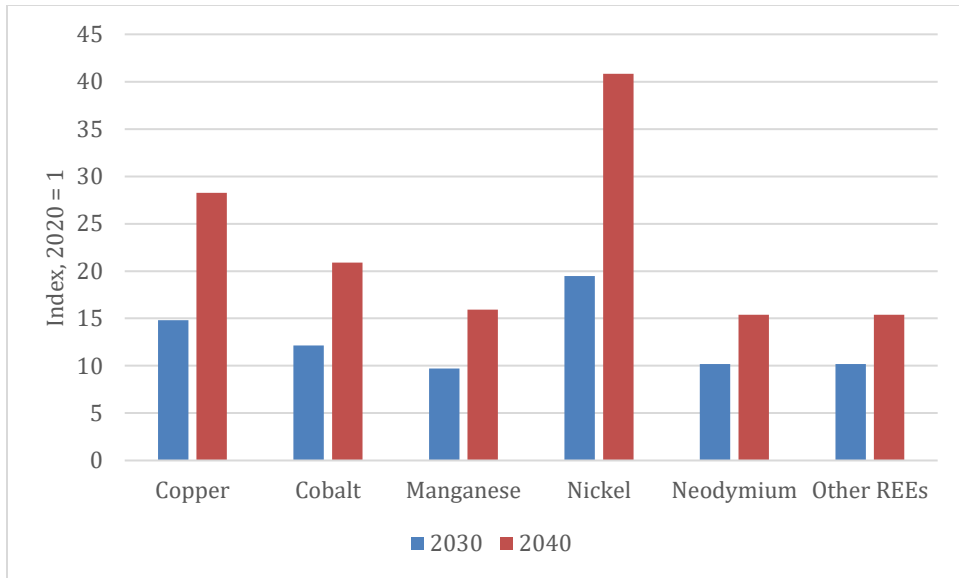


Figure 1.9: SDS projected growth in critical material demand from EV manufacturing.

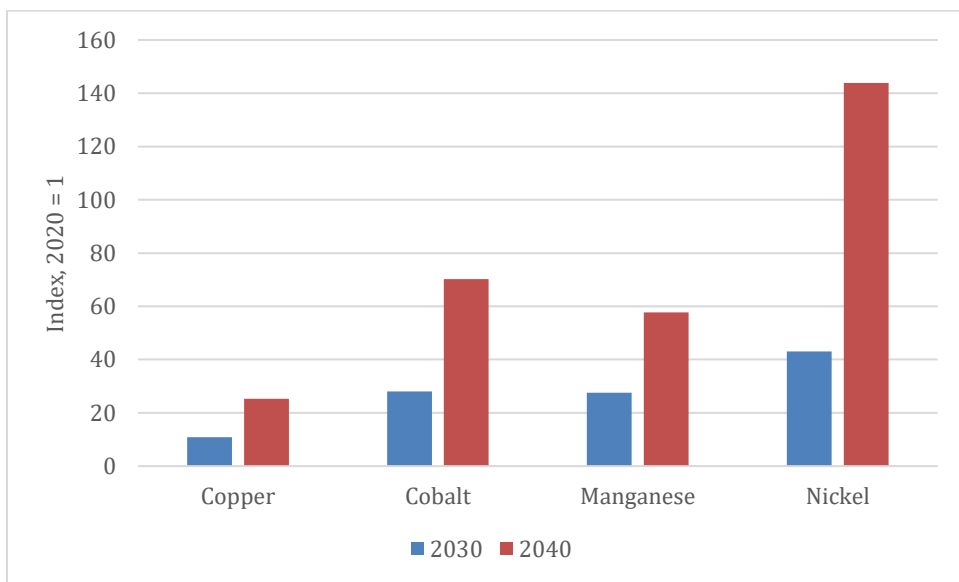


Figure 1.10: SDS projected growth in critical material demand from battery storage.

is based on different wind turbine designs, which vary in material consumption per energy capacity, and thus vary greatly in efficiency. Assuming the most material-efficient wind turbine design is adopted, the low values of the Wind Vision related tables are the most accurate projection of the material demand for wind generation. This aligns well with the IEA global projections, together indicating a US demand of 1,000 t of neodymium out of a global neodymium demand of 6,000–8,500 t for wind power generation by the year 2030. Together with the earlier 9,000–18,000 t of neodymium by 2030 and 11,000–28,000 t of neodymium by 2040 from EV manufacturing demand, the total demand for neodymium increases to 15,000–26,500 t by 2030 and 17,100–37,000 t by 2040. These high projected demands illustrates the high criticality of materials such as neodymium and the high quantities of critical materials needed for clean energy technologies.

IEA also projected the sectoral demand of clean technologies by critical material. Many materials are listed, and cobalt and rare earth elements are selected for Tables 1.116 and 1.117 because these materials are the most critical and relevant to this paper. Tables 1.16 and 1.17, respectively, list the STEPS and SDS projected sectoral demand of clean technologies by critical material.

Tables 1.16 and 1.17 illustrate the massive near-term demands for critical materials such as cobalt and rare earth elements from clean energy applications. The United States lacks control over the mining and refining supply chains of these critical materials. This criticality can be alleviated by procuring domestic mining and refining production or securing such production in allied countries. Numerous economic, political, and technological challenges are involved with this goal. Another way to attenuate such criticality is by reducing manufacturing waste and by creating recycling capability for these materials. This goal can be accomplished via AM of magnets for electrical machine applications, which is the focus of this thesis.

Table 1.14: IEA STEPS projected material demand for wind power generation.

<b>Demand (total)</b>	<b>2020</b>	<b>2030</b>	<b>2040</b>
<b>Wind</b>	<b>644</b>	<b>1,015</b>	<b>1,195</b>
Chromium	29	43	53
Copper	217	387	415
Manganese	46	67	84
Molybdenum	6	9	11
Nickel	21	29	38
Zinc	321	472	587
Neodymium	3.1	6.1	6.1
Dysprosium	0.3	0.6	0.7
Praseodymium	0.5	1.1	1.1
Terbium	0.1	0.2	0.3
Others	0.1	0.2	0.2

Note: in thousand metric tons (kt); Source: International Energy Agency.<sup>48</sup>

Table 1.15: IEA SDS projected material demand for wind power generation.

<b>Demand (total)</b>	<b>2020</b>	<b>2030</b>	<b>2040</b>
<b>Wind</b>	<b>644</b>	<b>1,602</b>	<b>1,705</b>
Chromium	29	70	75
Copper	217	577	610
Manganese	46	110	117
Molybdenum	6	15	16
Nickel	21	49	52
Zinc	321	770	822
Neodymium	3.1	8.5	9.0
Dysprosium	0.3	0.9	1.0
Praseodymium	0.5	1.5	1.6
Terbium	0.1	0.3	0.4
Others	0.1	0.3	0.3

Note: in thousand metric tons (kt); Source International Energy Agency.<sup>48</sup>



Table 1.16: IEA STEPS projected sectorial demand by critical material.

<b>Demand</b>	<b>2020</b>	<b>2030</b>	<b>2040</b>
<b>Cobalt</b>	<b>21</b>	<b>110</b>	<b>136</b>
Low-carbon generation	0	0	0
Solar photovoltaics	—	—	—
Wind	—	—	—
Other renewables	0	0	0
Nuclear	—	—	—
EV and battery storage	21	110	136
EVs	21	106	127
Battery storage	0	3	9
Electricity networks	—	—	—
Hydrogen	0	0	0
<b>Rare earth elements</b>	<b>6</b>	<b>19</b>	<b>22</b>
Low-carbon generation	4	8	8
Solar photovoltaics	—	—	—
Wind	4	8	8
Other renewables	—	—	—
Nuclear	0	0	0
EV and battery storage	2	11	14
EVs	2	11	14
Battery storage	—	—	—
Electricity networks	—	—	—
Hydrogen	—	—	0

Note: in thousand metric tons (kt); Source International Energy Agency.<sup>48</sup>

Table 1.17: IEA SDS Projected Sectorial Demand by Critical Material

<b>Demand</b>	<b>2020</b>	<b>2030</b>	<b>2040</b>
<b>Cobalt</b>	<b>21</b>	<b>262</b>	<b>455</b>
Low-carbon generation	0	0	0
Solar photovoltaics	—	—	—
Wind	—	—	—
Other renewables	0	0	0
Nuclear	—	—	—
EV and battery storage	21	262	455
EVs	21	257	441
Battery storage	0	6	14
Electricity networks	—	—	—
Hydrogen	0	0	0
<b>Rare earth elements</b>	<b>6</b>	<b>34</b>	<b>47</b>
Low-carbon generation	4	11	12
Solar photovoltaics	—	—	—
Wind	4	11	12
Other renewables	—	—	—
Nuclear	0	0	0
EV and battery storage	2	23	35
EVs	2	23	35
Battery storage	—	—	—
Electricity networks	—	—	—
Hydrogen	—	—	0

Note: in thousand metric tons (kt); Source International Energy Agency.<sup>48</sup>

## **CHAPTER 2 : REVIEW OF FUNDAMENTAL CONCEPTS OF MAGNETS**

## 2.1 On the Fundamental Concepts of Magnets

A magnet is a body that possesses the property of magnetism and can produce an appreciable magnetic field external to itself. Magnets can produce this field either temporarily or permanently.<sup>51</sup> The term *magnet* derives from the Latin for the Greek term for lodestone, *magnes lithos* and was originally used to describe only natural magnets.<sup>52</sup> Dictionary definitions also states that magnets are objects that acquired the property of attracting iron and of aligning roughly north–south when freely suspended.<sup>53</sup>

A dipole is a pair of noncoincident equal and opposite electric charges or magnetic poles, which are usually but not necessarily close together. A dipole can also be an object, especially a molecule or atomic particle, that has such charges or poles. The dipole moment is the product of the distance between the two charges or poles of a dipole and the magnitude of either of them. The magnetic version of the dipole is the magnetic dipole, and its associated dipole moment is the magnetic dipole moment.<sup>54</sup> The magnetic dipole moment, or just magnetic moment, is a measure of the strength of a magnet.<sup>55</sup>

Induce comes from the Latin *inducere*, meaning to lead into. To induce is to lead something (or someone) to do something.<sup>56</sup> The noun of induce is induction, and the scientific definition of induction derives from this meaning. In the natural sciences, induction is the action of inducing or bringing about an electric or magnetic state in a body by the proximity, without actual contact, of an electrified or magnetized body. Therefore, magnetic induction is the production of magnetic properties in substances when they are placed in a magnetic field, such as when a piece of iron is magnetized by a neighboring magnet.<sup>57</sup>

Vector, in Latin, means a carrier or one who carries. In the natural sciences, a vector is a quantity that has direction as well as magnitude.<sup>58</sup> The vector is often the carrier of a scientific phenomenon.

Flux comes from the Latin word *fluxus*, meaning flow. Flux, in modern English, means flow, or a flowing. In physics and many other scientific fields, flux refers to the lines or the number of lines of magnetic induction or electric displacement. In the latter case it is known as electric flux, and in the former, magnetic flux.<sup>59</sup> The term magnetic induction can also refer to the vector of such an action, which is the magnetic flux or the magnetic flux density.<sup>57</sup> The magnetic flux density will be further discussed in the next paragraph.

The magnetic field is a field of force that exists around a magnetic body (the magnet) or a current-carrying conductor. Within a magnetic field, a magnetic dipole may experience a torque, and a moving charge may experience a force. The strength and direction of the magnetic field is primarily described in two ways. It can be given in the terms of magnetic flux density, also known as magnetic induction, which has the symbol  $B$ . It can also be given in the terms of magnetic field strength, also known as magnetizing force or magnetic intensity, all of which are represented by the symbol  $H$ . The magnetic flux density,  $B$ , and the magnetic field strength,  $H$ , possesses different units. The SI unit for  $B$  is tesla (T). The SI unit for  $H$  is ampere per meter (A/m). The magnetic flux density  $B$  is a vector quantity and is the magnetic flux per area of a magnetic field at right angles to the magnetic force. The magnetic field strength  $H$  is related to  $B$  in that  $H = B/\mu$ , where  $\mu$  is permeability.<sup>60</sup> Figure 2.1 presents the two main forms of the hysteresis curves, the magnetization ( $M$ ) vs. magnetizing field ( $H$ ) hysteresis curve, and the magnetic induction ( $B$ ) vs. magnetizing field ( $H$ ) hysteresis curve. The second curve does not flatten out, but the first curve does. Magnetization saturates, while magnetic induction does not, with increasing magnetizing field, because the magnetizing field is a component of the magnetic induction.

To permeate is to diffuse, pass, or spread throughout.<sup>62</sup> Therefore, to be permeable is to be capable of being permeated: to be capable of being diffused, passed, or spread throughout.<sup>63</sup> Thus,

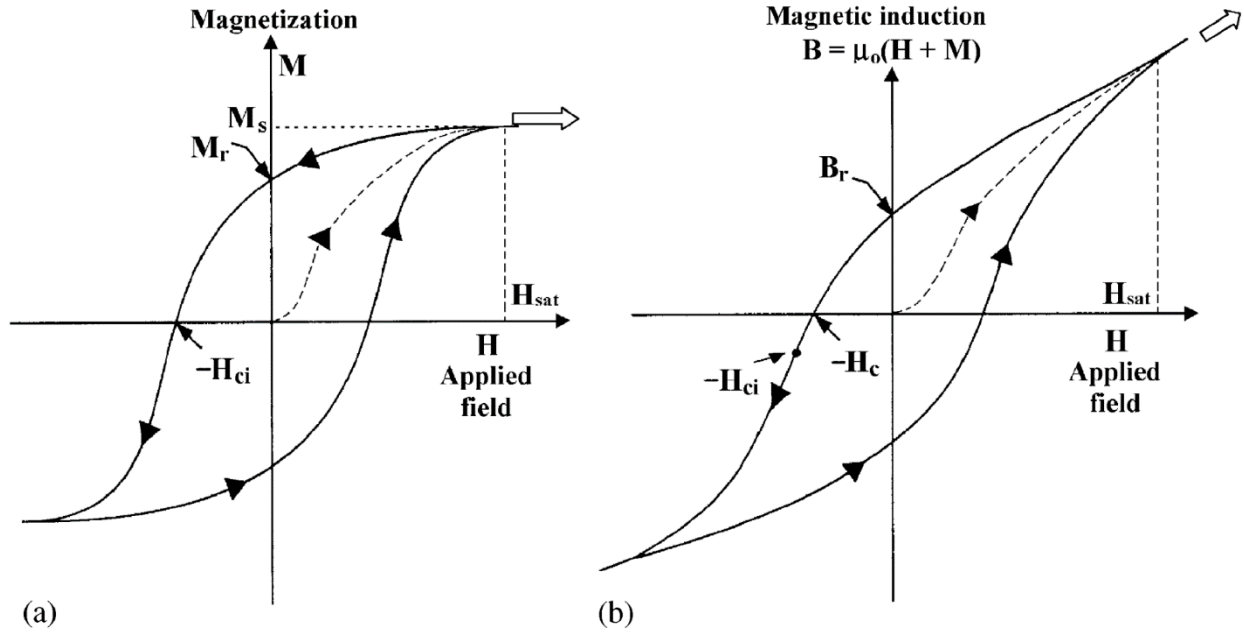


Figure 2.1: Magnetization hysteresis curve (left); magnetic induction hysteresis curve (right).<sup>61</sup>

permeability is the quality or condition of being permeable, and the ability to be permeated: the capability of being diffused, passed, or spread throughout. In science, permeability came to mean the degree to which a solid allows the passage through it of liquid or gas. This concept developed into the coefficient of permeability, which is the volume of fluid flowing through a unit cross section under a unit pressure or concentration gradient. From this meaning, permeability became more general and now means the degree to which a medium allows the passage through it of a fluid. If the fluid is the magnetic flux, then the degree to which a medium allows the passage through it of the magnetic flux is the magnetic permeability of the medium. Magnetic permeability is the ratio of the magnetic flux density  $B$  in a body to the external magnetic field strength  $H$  inducing it. Magnetic permeability describes the capability of the medium to let pass through magnetic flux. Thus, the magnetic flux and the magnetic field are related to and altered by the presence of the substance it surrounds. Therefore, different magnetic permeabilities apply to different types of bodies. Free space has a magnetic permeability, which is a constant known as the permeability of free space ( $\mu_0$ ), or the magnetic constant. The relative permeability ( $\mu_r$ ) of a substance is the ratio of its magnetic permeability to the permeability of free space. The unit for magnetic permeability is henry per meter (H/m), and the permeability of free space has the value of  $4\pi \times 10^{-7}$  H/m.<sup>64,65</sup> All further mentions of permeability in this paper refer to magnetic permeability.

Magnetism refers to the characteristic properties of a magnet, which are attributed to the motion of electric charge. Magnetism is the property of producing or being affected by magnetic flux. Magnetism is also the quality of being magnetic and the phenomena produced by magnetic materials. It is also the branch of science that deals with said magnetic phenomena.<sup>66,67</sup> Magnetism is a group of phenomena associated with magnetic fields. Magnetism and electricity are two sides

of the same coin. Whenever an electric current flows, a magnetic field is produced. The orbital motion and the spin of atomic electrons are equivalent to tiny current loops. When the orbital electrons of individual atoms possess a net magnet moment as a result of their angular momentum, magnetic fields form around said atoms. The magnetic moment of an atom is the vector sum of the magnetic moments of the spins and the orbital motions of all the electrons in the atom. The macroscopic magnetic properties of a substance arise from the interactions of the magnetic moments of its component molecules and atoms. Because these interactions have different results between different materials, different materials have different characteristics and behavior in an applied magnetic field. The four main types of magnetic behavior, or four main types of magnetism are diamagnetism, paramagnetism, ferromagnetism, and antiferromagnetism.<sup>68</sup>

In diamagnetism, the magnetism is in the opposite direction to that of the applied field. All substances are diamagnetic, but diamagnetism is a weak form of magnetism that is often masked by other stronger forms of magnetism. Diamagnetism results from changes induced in the orbits of electrons in the atoms of the substance by the applied field, the direction of the change opposing the applied flux. Diamagnetic materials do not retain magnetization in the absence of an applied magnetic field.<sup>68,69</sup>

In paramagnetism, the molecules or atoms of the substance have net spin or orbital magnetic moments that are capable of being aligned in the direction of the applied field. Therefore, paramagnetism occurs in all molecules and atoms with unpaired electrons. These unpaired electrons can be free atoms, free radicals, or compounds of transition metals containing ions with unfilled electron shells. Paramagnetism can also occur in metals because of magnetic moments associated with the spins of the conducting electrons. Paramagnetic materials do not retain magnetization in the absence of an applied magnetic field.<sup>68,69</sup>



Within ferromagnetic substances, in a certain temperature range, net atomic magnetic moments align such that magnetization persists after the applied field is removed. The Curie temperature, or Curie point, is the upper bound and limit of this temperature range. Below the Curie temperature, an increasing magnetic field applied to a ferromagnetic substance increases magnetization to a high value, called the saturation magnetization, because a ferromagnetic substance consists of magnetized regions called magnetic domains, or domains for short. A magnetic domain is a volume of a ferromagnetic material—typically about  $1\mu$  in diameter—in which all electron spins align in the same direction. Magnetic domains are separated by domain walls. The domain itself can be thought of as a single tiny magnet with a magnetic direction. The total macro magnetic moment of a ferromagnetic substance is the vector sum of the magnetic moments of its constituent component domains. When the ferromagnetic substance is yet to be magnetized by a magnetic field, its constituent magnetic domains are not aligned and are random in their magnetic orientation. When an external magnetic field is applied, the magnetic domains begin to align to the direction of the field. In a sufficiently strong magnetic field, all the domains align in the direction of the field and together provide the highest observed magnetization, the saturation magnetization. Many metals such as iron, cobalt, nickel, and their alloys are ferromagnetic. Many commercial magnets are also ferromagnets, and their unique magnetic properties are especially suited for PMs. Above the Curie temperature, all ferromagnetic materials become paramagnetic materials and lose their ferromagnetic properties.<sup>68,70,71</sup> The forces that cause magnetic ordering in ferromagnetic materials can be overcome by increasing the material's temperature. The higher temperature changes the intermolecular spacing, thereby weakening the forces holding the molecules together. The Curie temperature is the temperature at which thermal vibrations prevent quantum-mechanical coupling between atoms, thereby destroying any ferromagnetism.<sup>69,72,73</sup>

The fourth type of magnetism is antiferromagnetism, which is exhibited by certain metals, alloys, and transition-element salts. This type of magnetism is very similar to, and yet different from, ferromagnetism. The Curie temperature equivalent in this type of magnetism is known as the Neel temperature. Below the Neel temperature, antiferromagnetic materials' constituent atomic magnetic moments spontaneously form an ordered array in which alternate moments have opposite directions with the same magnitudes, therefore resulting in no net magnetic moment in the absence of an applied magnetic field. This spontaneous ordering opposes the normal tendency of the magnetic moments to align with the applied field. Similar to ferromagnetism, the antiferromagnetic substance becomes paramagnetic above the Neel temperature.<sup>68,72</sup>

A special form of antiferromagnetism is ferrimagnetism, which is the type of magnetism exhibited by ferrites. Not all commercial magnets are ferromagnets; some, such as soft and hard ferrite magnets, are ferrimagnetic materials. In ferrimagnetic materials, the magnetic moments of adjacent ions are antiparallel and of unequal strength. Thus the sum magnetic moment in one direction is greater than those in the opposite direction, yielding a net magnet moment in the antiferromagnetic material.<sup>68</sup>

## **2.2 On the Classification of Soft and Hard Magnets**

Magnetic materials are materials in which the magnetic moment of adjacent atoms can adopt either parallel or antiparallel alignment. Ferromagnetism occurs when magnetic moments adopt parallel alignment. Antiferromagnetism occurs when the magnetic moments nullify because of antiparallel alignment. Ferrimagnetism arises when magnetic moments adopt antiparallel alignment without the cancellation caused by unequal magnitudes the opposing magnetic moments. Ferromagnetic and ferrimagnetic materials can both be magnetized and obtain a high degree of magnetization in magnetic fields. These magnetic materials can be classified as either hard magnets or soft magnets.

Hard magnets retain large magnetization in the absence of an applied magnetic field and are also known and used as PMs. Soft magnets are easy to magnetize or demagnetize. When subjected to an alternating magnetic field, a soft magnet loses little energy from hysteresis. PMs include magnet steels, hard ferrites, AlNiCo, rare earth magnets, and many others. Magnet steels are usually steels alloyed with tungsten and cobalt. Rare earth magnets are made of alloys containing rare earth elements. These magnets produce the strongest magnetic fields. The most common rare earth magnets are neodymium–iron–boron (NdFeB) PMs and samarium–cobalt (SmCo) PMs. The most common applications for PMs are electric machine related. In addition to EV motors and wind turbine generators, other PM applications include hard drives, cordless tools, headphones, and toys. Common soft magnet materials include silicon–iron alloys, nickel–iron alloys, soft ferrites, and amorphous nanocrystalline alloys. Silicon–iron alloys are also known as silicon steels or electrical steels. A common example of a nickel–iron soft alloy magnet is permalloy. One of the most common nanocrystalline soft magnetic materials is FINEMET from Hitachi Metals. Soft magnets enhance the magnetic flux produced by an electric current. These soft magnetic materials, especially electrical steels, are used to manufacture parts that are exposed to rapid changes of magnetic flux, such as the cores of electromagnets, transformers, motors, and generators.<sup>9,69,74–78</sup>

In an electromagnet, the magnetic force is produced by an electric current. Electromagnets comprise a soft magnetic core with a coil of insulated wire—the *field coil*—wound round it. When an electric current—the *field current*—flows through the wire, the core becomes magnetized. When the current stops, the core loses its magnetization.<sup>79–81</sup> Soft magnetic materials’ function as electromagnets is their dominant application in electric machines such as EVs and wind turbine generators. Soft magnet electromagnets are the stators in electric motors and generators.<sup>9,77</sup>

Soft and hard magnets have very different magnetic hysteresis behavior.<sup>69</sup> Hysteresis comes from the Greek word *husteros*, meaning late. Hysteresis is a phenomenon in which changes in a property lag behind changes in the agent or influence that causes them. Because of the hysteresis phenomenon, the property response depends not only on the current state of the system but also on the states it has previously occupied. In magnetic hysteresis, increases in a material's magnetic field lag behind increases in the magnetizing field.<sup>82</sup> Ferromagnetic and ferrimagnetic materials can both manifest magnetic hysteresis behavior. The magnetic flux density,  $B$ , represents the magnetic field produced around the magnetic material that is being magnetized. Here,  $B$  includes the material's intrinsic magnetization and the applied magnetic field. Magnetization,  $M$ , is a measure of the magnetic polarization that occurs when a material is placed in a magnetic flux. It is defined as magnetic moment per unit volume. Magnetism relates to magnetic flux density:  $B = \mu_0(H + M)$  (in the SI system). Here,  $\mu_0$  is the permeability of free space (vacuum). Changes in  $M$  and  $B$  both lag behind changes in the applied magnetic field,  $H$ , also known as the magnetizing field. When magnetic hysteresis is present,  $B$  (or  $M$ ) increases as  $H$  increases, but  $B$  (or  $M$ ) does not return to zero when the magnetizing field is removed. A plot of  $B$  (or  $M$ ) vs.  $H$  as  $H$  increases, decreases, and then increases again results in a characteristic curve that is known as a hysteresis loop. The area enclosed within this loop represents the energy (heat) dissipated per cycle per unit volume of material. The magnetic hysteresis phenomenon originates from the resistance to the motion of magnetic domain walls.<sup>60,61,83-85</sup> Figure 2.2 illustrates the hysteresis curves of typical hard and soft magnets, contrasting and highlighting their differences.

Several important terms are associated with magnetic hysteresis. One such term is coercivity. Coercivity, or coercive force, is the strength of the applied magnetic field that is needed to bring the magnetic induction back to zero. It is given by the  $y$ -intercepts on the  $B$ - $H$  magnetic hysteresis

## MAGNETIC HYSTERESIS FOR SOFT AND HARD MAGNETS

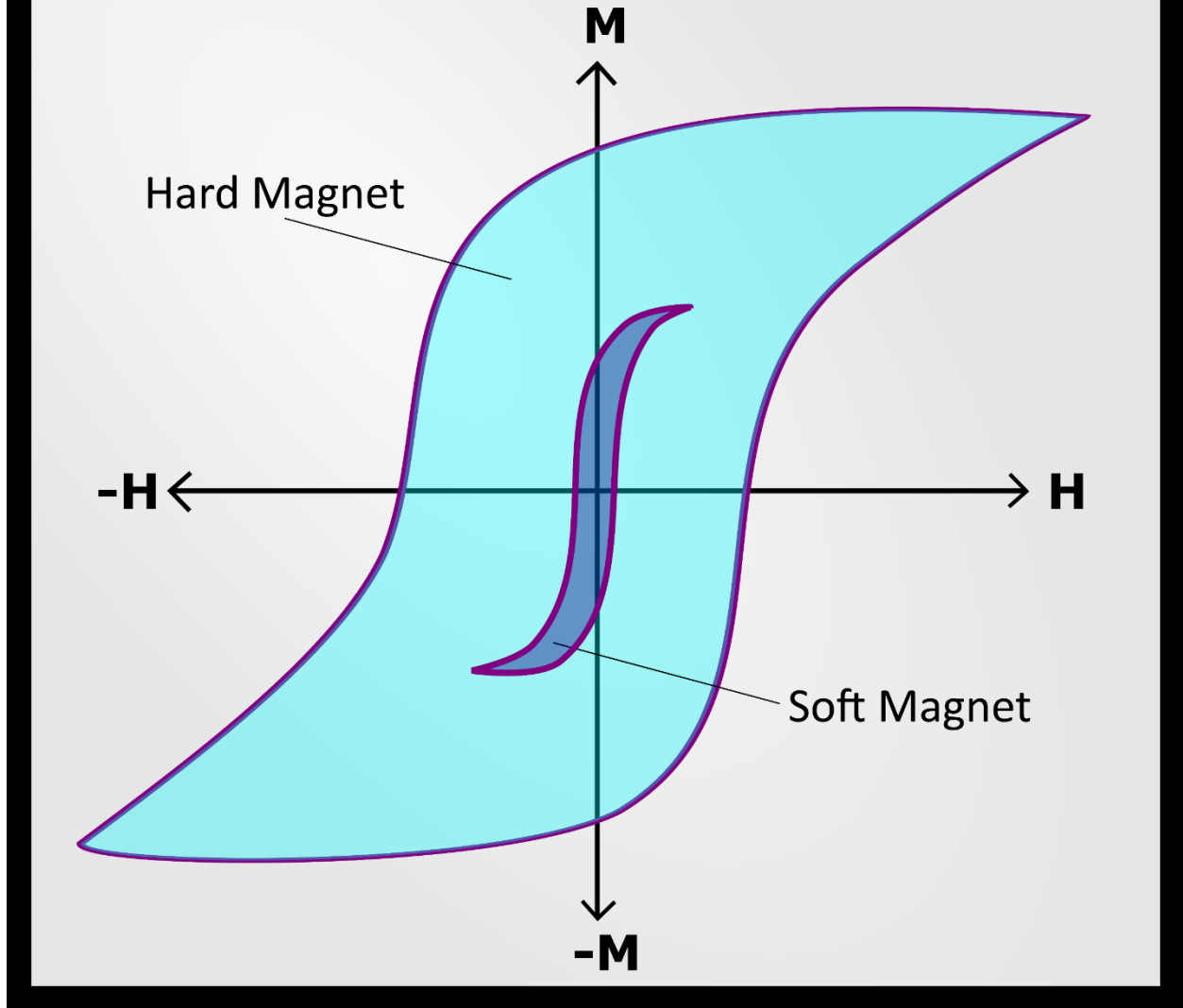


Figure 2.2: Hysteresis curve, showing the magnetization ( $M$ ) vs. the magnetizing field ( $H$ ). Typical curves of hard and soft magnets are contrasted to highlight their differences.<sup>86</sup>

curves. The positive  $y$ -intercept is  $H_c$ , and the negative  $y$ -intercept is  $-H_c$ . The symbol  $H_c$  represents coercivity. The  $M$ – $H$  magnetic hysteresis curves also have  $y$ -intercepts. The positive  $y$ -intercept is  $H_{ci}$ , and the negative  $y$ -intercept is  $-H_{ci}$ . The symbol  $H_{ci}$  represents intrinsic coercivity. Coercivity and intrinsic coercivity are not the same. This difference is usually pronounced for soft magnets and subtle for hard magnets.<sup>61</sup>

Another important concept in magnetic hysteresis is the saturation magnetization  $M_s$ . A key difference between magnetization and magnetic flux density, or the induction, is that induction does not saturate. In magnetization, an upper limit exists at which increasing the magnitude of the applied magnetic field no longer increases the magnitude of the magnetization. The value of  $M$  at this point is  $M_s$ , the saturation magnetization. Saturation magnetization exists when all the magnetic domains have completed orientation and have aligned to the direction of the applied field. Saturation magnetization exists because not all of the magnetic domains within a magnetic material orient to the direction of the applied field. However, magnetic flux density is a combination of magnetization and applied field. At some point,  $M$  no longer increases with  $H$ , but  $B$  (which is partially comprised of  $H$ ) will always increase with  $H$  and will never saturate. Therefore, the  $B$ – $H$  hysteresis curves are significantly different from the  $M$ – $H$  hysteresis curves. The  $M$ – $H$  curve slope tends toward zero (i.e., horizontal) beyond the saturation point of the magnetic material. The  $B$ – $H$  curve slope tends toward  $\mu_0 H$  (i.e., not horizontal) beyond the saturation point of the magnetic material.<sup>61,68</sup>

A key concept in magnetic hysteresis is the remanent magnetization,  $M_r$ . Remanent magnetization is closely associated with the term known as remanence. The curve that tracks the magnetization of the magnetic material from the initial unmagnetized state to saturation is known as the magnetization curve. This curve is sometimes shown on hysteresis plots but is not considered a

part of the hysteresis loop. It is the genesis of the loop but not a repeating component of it. Owing to magnetic hysteresis, after the initial magnetization,  $M$  (or  $B$ ) does not return to zero when  $H$  returns to zero. The value of  $M$  at this point is the remanent magnetization ( $M_r$ ). Its equivalent on the  $B$ – $H$  curve is the remanent induction, retentivity, or remanence ( $B_r$ ). These terms represent the magnetism remaining in the material after the inducing field has been removed.<sup>61,85,87</sup>

One additional concept closely associated with magnetic hysteresis is magnetic susceptibility. Susceptibility is the quality or condition of being susceptible. It is the capability of being affected by something. In the case of magnetism, it is the capacity of a substance to be affected by magnetism, becoming magnetized. It is the ratio of the magnetization to the magnetizing force, or  $M/H$ . The symbol of susceptibility is  $\kappa$ . It is a dimensionless quantity relating to the relative permeability  $\mu_r$  via the equation  $\kappa = \mu_r - 1$ . The symbol of mass susceptibility is  $\chi$  or  $\chi_m$ . It has units of cubic centimeters per gram. Different types of magnetic materials have vastly different magnetic susceptibilities. Diamagnetic materials have a negative susceptibility value. Paramagnetic materials have a positive susceptibility value of small magnitude. Ferromagnetic (and ferrimagnetic) materials have the potential for a very high susceptibility value, depending on the exact strength of the applied magnetic field. Magnetic permeability ( $\mu$ ) is the ratio of the magnetic flux density ( $B$ ) in a medium to the external magnetic field strength ( $H$ ), or  $\mu = B/H$ . This is very similar to the definition of susceptibility, which is  $M/H$ . Permeability is the slope of the  $B$ – $H$  hysteresis curve, and susceptibility is the slope of the  $M$ – $H$  curve. Because they are similar, magnetic permeability manifests itself in a similar fashion on magnetic materials as magnetic susceptibility. The relative permeability of diamagnetic materials is less than unity. Paramagnetic materials have values of relative permeability just greater than unity. Ferromagnetic (and ferrimagnetic) materials have the potential to have relative permeability at values much greater

than unity, depending on the magnetic flux density.<sup>61,88-91</sup> The terms associated with magnetic hysteresis, along with their relationship to the  $B-H$  and  $M-H$  curves, are listed in Table 2.1. SI system units and CGS-EMU units for common magnetic properties are listed in Table 2.2.

### **2.3 On the Conventional Manufacturing Processes of Magnets**

Because a great variety of magnet types are used in various applications, a great multitude of conventional manufacturing processes produce magnets. The processes, just like the magnets themselves, are split into two categories. Some manufacturing methods are primarily used to produce hard magnets, whereas others are primarily used to produce soft magnets.

The conventional manufacturing methods for hard magnets comprise many techniques, including powder metallurgy, injection molding (IM), compression molding (CM), metal injection molding (MIM), casting, extrusion and calendaring (E&C), and hot deforming. These methods are not all common, nor have they all been successfully commercialized. Powder metallurgy, in the context of magnet manufacturing, is also known as pressing and sintering (P&S). IM and CM are collectively known as the bonded magnet manufacturing processes. P&S, bonded, casting, and E&C have been successfully commercialized. Of these, only P&S and the bonded processes have found widespread use; the rest are limited to niche applications.<sup>9</sup>

#### **2.3.1 Powder Metallurgy, or Pressing and Sintering**

In the powder metallurgy process, powdered metals or alloys are pressed into a variety of shapes at high temperature. This process is used to fabricate components by compacting metal powders in a die and subsequently densifying them by sintering or hot pressing. In magnet manufacturing, sintering is the most common, whereas hot pressing is mostly in the R&D phase. Sintering differs from melting: it is the process of heating and compacting a powdered material at a temperature below the melting point to meld the particles into a single rigid shape. Melting occurs only above



Table 2.1: Concepts and terms associated with magnetic hysteresis.

	<b>Magnetic hysteresis curve types</b>	
	<b><i>B-H</i></b>	<b><i>M-H</i></b>
<b>x-axis</b>	<i>H</i> (magnetizing force)	<i>H</i> (magnetizing force)
<b>y-axis</b>	<i>B</i> (magnetic induction)	<i>M</i> (magnetization)
<b>Slope</b>	$\mu$ (permeability)	$\chi$ or $\kappa$ (susceptibility)
<b>Fate of Slope</b>	Remains nonzero	Becomes zero after saturation
<b>x-intercept</b>	$H_c$ (coercivity)	$H_{ci}$ (intrinsic coercivity)
<b>y-intercept</b>	$B_r$ (remanence)	$M_r$ (remanent magnetization)

Source: Sung et al.; American Society for Metals<sup>61,91</sup>

Table 2.2: SI and CGS-EMU units for magnetic properties.

<b>Magnetic properties</b>		<b>SI units</b>	<b>CGS-EMU units</b>
Magnetic field strength ( <i>H</i> )		A/m	Oe
Magnetic induction ( <i>B</i> )		T	G
Magnetic permeability ( $\mu$ )		H/m	Unitless
Relative permeability ( $\mu_r$ )		Unitless	Unitless
Susceptibility ( $\kappa$ )		Unitless	Unitless
Mass susceptibility ( $\chi$ or $\chi_m$ )		cm <sup>3</sup> /g	cm <sup>3</sup> /g
Coercivity ( $H_c$ )		A/m	Oe
Intrinsic coercivity ( $H_{ci}$ )		A/m	Oe
Remanence ( $B_r$ )		T	G
Magnetization ( <i>M</i> )	Volume ( <i>M</i> )	A/m	emu/cm <sup>3</sup>
	Volume ( $4\pi M$ )	A/m	G
	Intensity ( <i>J</i> , <i>I</i> )	T	emu/cm <sup>3</sup>
	Mass ( $\sigma$ , <i>M</i> )	A·m <sup>2</sup> /kg	emu/g
Remanent magnetization ( $M_r$ )		Same as all variants of <i>M</i>	Same as all variants of <i>M</i>

Note: in SI,  $B = \mu_0 (H + M)$  ; in CGS-EMU,  $B = H + 4\pi M$

Source: American Society for Metals; National Institute of Standards and Technology<sup>91,92</sup>

the melting temperature. Powder production can be done via gas atomization, crushing and grinding, or chemical decomposition. In magnet manufacturing, a suitable composition is pulverized into a fine powder, compacted via pressing, and densified via sintering. This process is also known as P&S.<sup>9,93-95</sup> Figure 2.1 illustrates the main steps in the P&S conventional manufacturing method.

P&S is by far the most popular method to create magnets of the highest density, quality, and magnetic properties. This method creates magnets with higher density than any other manufacturing method, and thus the magnets have the best magnetic properties. Although powder metallurgy can produce near-net components (i.e., initial production is very close to the final shape) that have high dimensional precision and intricate features, this capability is extremely limited in the case of magnet manufacturing. P&S achieves limited shape complexity when producing magnets. Features such as holes, slots, and large chamfers are expensive and difficult to produce. Tolerances are more difficult to maintain with increasing shape complexity. Because of the limited shaped complexity, more machining is needed as postprocessing to finalize the part's shape. This additional machining results in increased waste. This method of magnet production produces scrap averaging as much as 25% to 30% of the total raw material intake and allows little opportunity to capture and reuse these expensive materials. Most hard magnets, such as NdFeB, SmCo, AlNiCo, and hard ferrites, can be manufactured via the P&S method.<sup>9,93</sup> Table 2.3 summarizes the pros and cons of the P&S magnet manufacturing method.

### **2.3.2 Bonded Magnets, or Injection Molding and Compression Molding**

Bonded magnet manufacturing processes are a family of magnet manufacturing methods that create magnets by mixing powders of the magnet material with a polymer that acts as the carrier matrix. These processes allow much greater shape complexity owing to the high moldability of

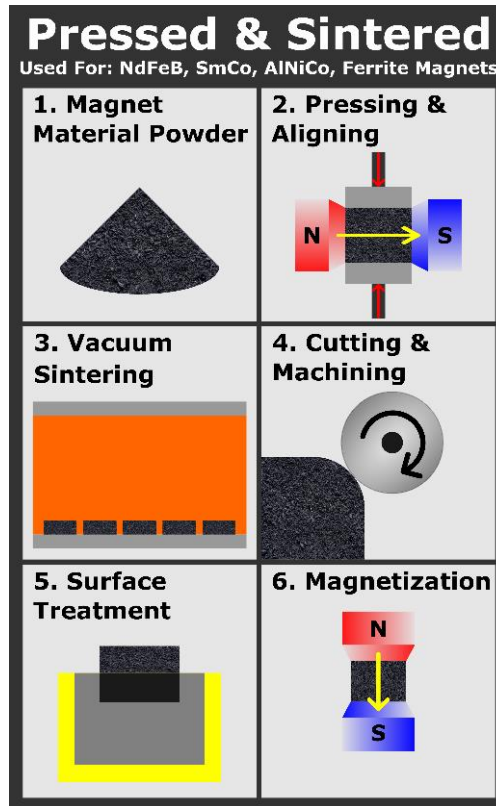


Figure 2.3: Pressing and sintering (powder metallurgy) manufacturing process.<sup>9</sup>

Table 2.3: Advantages and disadvantages of the pressing and sintering conventional magnet manufacturing process.

<b>Advantages:</b>	<b>Disadvantages:</b>
Most mature and widespread manufacturing method for sintered magnets	The pressing step severely limits shape complexity
Unrivaled at producing magnets with the highest density	Significant cutting and machining are needed for intricate features and complexity
Creates magnets with the best magnetic properties	Significant waste of raw critical materials
	High cost of critical materials and significant waste of raw materials results in a relatively high production cost

Source: Wang et al.<sup>9</sup>

the polymer. However, because the polymer is not magnetic, magnetic properties are reduced. The two main commercialized bonded magnet processes are IM and CM. In IM, the raw materials powder mixture is compounded with a thermoplastic polymer into pellets and injected into a mold. In CM, the raw material powder mixture is compressed in a press mold using a thermoset polymer. The primary difference between the two methods is that IM injects the material into a mold, and CM presses the material in a mold. IM offers greater shape complexity but less magnetic strength in the resulting product. CM offers greater density and thus greater magnetic properties than IM but has lower shape complexity. MIM is another member of this family. It is similar to IM, but a special polymer binder is used and additional postprocessing steps occur after IM. The postprocessing removes the polymer binder via chemical or thermal debinding, thereby increasing the material density and thus the magnetic properties. MIM has never been commercialized. It remains in R&D, and little research has been published on the subject in recent years. Most hard magnets, such as NdFeB, SmCo, and hard ferrites, can be manufactured via the bonded magnet production methods.<sup>9</sup> Table 2.4 summarizes the advantages and disadvantages of the bonded magnet manufacturing processes.

Figure 2.2 illustrates the main steps in the bonded magnet conventional manufacturing processes. IM and CM are both represented in the figure, each following a different path. IM is represented via the route with steps 1, 2a, 3a, 4, 5, and 6. CM is represented via the route with steps 1, 2b, 3b, 4, 5, and 6. Both processes begin by mixing magnet and polymer powder into the desired mixture. In IM, the mixture is granulated into pellets and fed into a screw extruder to be squeezed into the mold. In CM, the mixture is loaded into the mold and compressed and then subjected to curing. Then, both processes undergo the cutting and machining, surface treatment, and magnetization steps.

Table 2.4: Advantages and disadvantages of the bonded magnet manufacturing processes.

<b>Advantages</b>	<b>Disadvantages</b>
Minimal to no machining post processing required	Much higher shape complexity than P&S
Much less raw material waste than P&S	Bonded magnets have lower magnetic properties than sintered magnets owing to the nonmagnetic polymer component
Bonded magnets have higher resistivity because of the polymer component	IM offers the greatest shape complexity but the least in magnetic strength
Bonded magnets have lower eddy current losses because they have lower resistivity	CM is a compromise between P&S and IM; shape complexity and magnetic strength are between the two
Bonded magnets have improved corrosion resistance owing to the polymer component	IM requires molds of high shape complexity for products of high shape complexity, and thus very high tooling costs for these molds

Source: Wang et al.<sup>9</sup>

Although the bonded magnet processes use less critical rare earth materials and offer the capability of higher shape complexity with less material waste, these advantages come at the cost of reduced magnetic performance. AM seeks to address this tradeoff by retaining the advantages of the bonded magnets without the associated dramatic reduction in magnetic properties.

### **2.3.3 Other Conventional Hard Magnet Manufacturing Processes**

The other manufacturing methods for hard magnets are much more niche or have never been successfully commercialized; brief overviews are given as follows.

Casting is the process of pouring molten metal into a mold to obtain, after cooling, a component that has the shape of the mold. In casting, the magnet raw material powders are mixed in the desired portions, melted, poured into the mold, and allowed to cool. Casting is used to produce AlNiCo magnets, especially the high-end versions with the strongest magnetic properties. A variant of casting, strip casting, is also used to produce the magnetic powder material that is the input material for many magnet manufacturing processes. It differs from casting in that the mold is the container for the molten metal and does not shape the final product. Strip casting is a preprocess, not a magnet manufacturing method. Although casting is used to produce AlNiCo magnets, AlNiCo has low demand compared with NdFeB and hard ferrites. Casting is only used to produce a relatively niche type of magnet. Potential problems with casting include contamination, porosity, and dimensional inaccuracy.<sup>9,36,96-100</sup>

E&C is a family of two closely related magnet production methods: the extrusion method and the calendaring method. Both methods start with mixing the flexible polymer carrier matrix powder and the magnet material powder. Then the mixed powder is melted. In the extrusion process, the melt is fed through a screw extruder, which pushes the melt through a die into flexible magnet strips or tapes. In the calendaring process, the melt is fed into mechanical rollers that compress

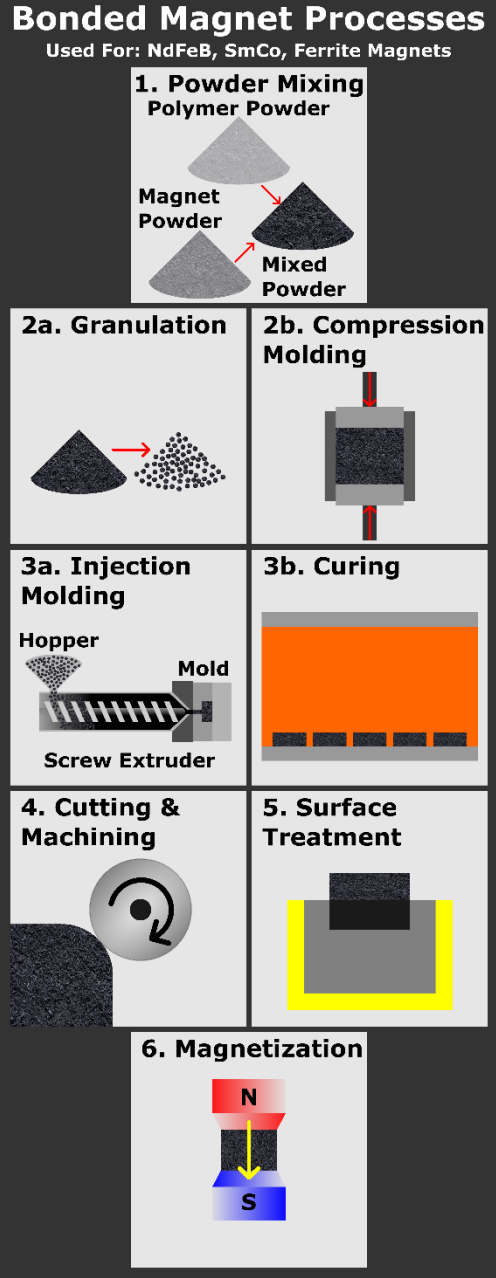


Figure 2.4: The bonded magnet manufacturing processes.<sup>9</sup>

and calendar the melt into flexible magnet sheets. E&C has been commercialized to fabricate flexible hard ferrites, which are used in niche consumer products. Rarely, E&C has also been used to fabricate NdFeB for niche applications.<sup>9,101</sup>

Hot deforming is very similar to the P&S process. Just like in P&S, in the hot deforming process, the magnet raw material powder is mixed with a polymer powder, fed into a die, and pressed for compaction. Hot deforming has the following differences from P&S. In hot deforming, the polymer powder is a thermoplastic. In hot deforming, the material is pressed at high temperatures. After pressing, the product is hot deformed into shape at even higher temperatures to further densify and improve the shape of the magnet. Hot deformation of magnets has not been commercialized and is still mostly in the research stage.<sup>9</sup>

### **2.3.4 Conventional Soft Magnet Manufacturing Processes**

Soft magnets use different manufacturing methods from hard magnets.

An alloy is a metal made by combining two or more metals or metal and nonmetallic elements, typically to improve a material property. To alloy is to combine metals to form an alloy. To alloy is also to combine one or more metals and one or more nonmetallic elements to form an alloy. Alloying is mostly done by melting the base metal and then adding the alloying agents. Most of the commonly used soft magnets are alloys made via the conventional alloying process. Soft magnetic materials are often alloyed with other materials and heat-treated to optimize microstructures. A significant drawback of this production method is the introduction of defects, impurities, and grain boundaries that hinder magnetic domain wall movement and significantly impair magnetic properties.<sup>77,102–105</sup>

Not all soft magnets are typical alloys. FINEMET is a nanocrystalline iron-based soft magnetic material, the precursor of which is an amorphous ribbon obtained by rapid quenching at  $1 \times 10^6$ °C/s from a molten alloy mixture. FINEMET is a crystallized alloy ribbon composed mainly of iron,



with certain amounts of silicon and boron and trace amounts of copper and neodymium.<sup>76</sup> The amorphous precursor ribbon is cast by rapid quenching via the single-roll method, and then this ribbon is wound into a toroidal core. Next, the core undergoes heat treatment for nanocrystallization to obtain the excellent soft magnetic properties of FINEMET. The grain size of FINEMET is around 10 nm.

Alloys are not the end product for most soft magnetic applications. For electrical machines, the dominant soft magnet application, soft magnets become the magnetic core of a motor or generator. For this type of application, the typical soft magnetic materials are ferrosilicon (Fe–Si) alloys, also known as electrical steel or silicon steel.<sup>77,106</sup>

### **2.3.5 Conventional Soft Magnet Lamination Manufacturing Process**

The typical soft magnets for electrical machines undergo the following process. First, the design of the electrical machine is developed into a detailed computer-aided design (CAD) file of the machine core. This design is carefully analyzed to identify and develop special precision tooling for the production and machining of dies for mold forming and stamping. The soft magnet alloy sheets are then cold rolled into the required thickness for lamination and stamped and/or punched into the required dimensions for the electrical machine application. These soft magnet sheets are then coated with insulating material to insulate against the flow of eddy currents. Next, the cut sheets are stacked on an aligning fixture by welding or pinning. These manufacturing process steps may introduce defects into the product via stresses, which can cause deterioration. Thus, the stacks are post-machined and heat-treated as quality assurance to prevent this deterioration. The conventional machine core soft magnet manufacturing process has a few drawbacks. One such drawback is the difficulty in streamlining and consolidating the separated process steps, and thus labor and production times remain high. AM could help alleviate this issue by part count reduction and automation. Another drawback of the conventional method is the lower limitation in the

thickness of the laminations. Core loss, or iron loss, refers to the various frequency-dependent magnetic losses when the magnetic components dissipate energy to the environment in the form of heat. Core losses include hysteresis losses and eddy current losses. Hysteresis loss results from the hysteresis effect resulting from the cycling of the magnetic field. This type of loss is directly related to the texture, grain size, and structural disorder of the magnetic material. Eddy current loss occurs in the electrical machine core by induction currents. This type of loss is determined by the specific electric resistivity of the material and electric path length. Therefore, thinner lamination can minimize the core loss of the electrical machine. However, thinner material requires more processing, such as rolling and stress-relief annealing, thereby increasing fabrication costs. Furthermore, excessive rolling increases the alloy's brittleness, imposing a practical lower limit on the available thickness for laminations. Thinner laminations require more stamping and stacking operations, which can introduce dimensional inaccuracy into the final product. High silicon content silicon steel has increased resistivity for lower core losses but becomes more brittle and limited in ductility and thermal conductivity. AM can facilitate printing of thin-walled hollow structures with high electrical resistivity. AM also allows the mixing of different types of metal and alloy powders and the inclusion of binding agents. Improved material properties are possible by controlling grain texture and the grade of soft magnetic materials in specific sections of the machine parts. AM can process both soft magnet and insulation materials, and it may be possible to realize the fabrication of electrical machine cores via multimaterial printing.<sup>77,107–111</sup>

#### **2.4 On the Additive Manufacturing Processes of Magnets**

AM is the process of joining materials to make parts from 3D model data, usually layer by layer, as opposed to subtractive manufacturing and formative manufacturing mythologies. Manufacturing processes shape materials into objects by one or a combination of three basic

principles: the formative shaping principle, the subtractive shaping principle, and the additive shaping principle. Formative shaping acquires the desired shape by applying pressure into a body of raw material. Manufacturing processes employing this type of shaping principle include bending, forging, and casting. Subtractive shaping acquires the desired shape is acquired by selectively removing material. Examples include cutting, drilling, and milling. Additive shaping acquires the desired shape by successive addition of material. AM applies the additive shaping principle, building physical 3D geometries by successive addition of material. A synonym for AM is 3D printing. A 3D printer is a machine used for 3D printing and is synonymous with an AM machine.<sup>112-116</sup>

AM processes include many different techniques. Not all techniques are relevant to magnet manufacturing. AM processes that have been used to fabricate magnets include binder jetting (BJT), directed energy deposition (DED), material extrusion (MEX), and powder bed fusion (PBF).<sup>112,113</sup>

#### **2.4.1 Binder Jetting**

BJT is an AM process in which a liquid bonding agent is selectively deposited to join powder materials. BJT has been used to fabricate near-net shaped isotropic NdFeB bonded magnets with a density of  $3.47 \text{ g/cm}^3$ , which is approximately 46% of a sintered equivalent. The BJT magnet process involves depositing the liquid bonding agent to selectively join magnet powder materials. The printer's 3D print head moves over the build platform and deposits binder droplets on each new layer of powder. When a layer is complete, the powder bed moves downward, and a new layer of powder is spread onto the build area. The process repeats layer by layer until all parts are completed. After this step, the parts are in the so-called green unfinished state. The green parts are postprocessed via sintering for densification, yielding optimal magnetic performance. Figure 2.3 illustrates the BJT process.<sup>112,113,117</sup>

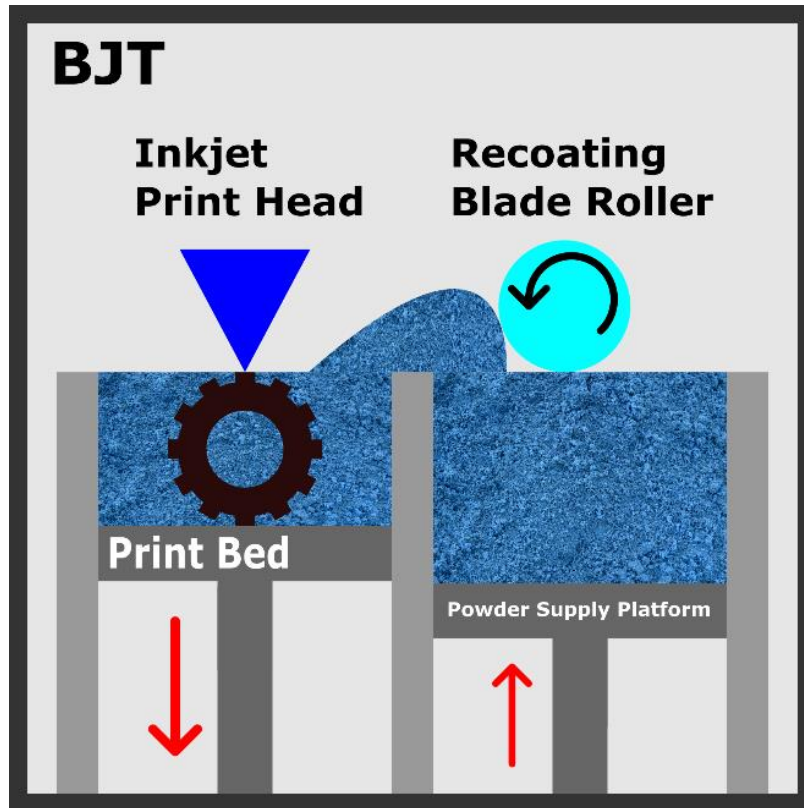


Figure 2.5: The binder jetting AM process.<sup>113</sup>

### 2.4.2 Directed Energy Deposition

DED is a family of AM processes in which focused thermal energy is used to melt and fuse materials as they are being deposited. The focused thermal energy can be a laser, an electron beam, or a plasma arc, depending on the specific AM process. DED print nozzles often have high degrees of freedom: some can move along five different axes. DED systems are often large and operate in closed and controlled environments. In AM, feedstock refers to the bulk raw material supplied to the AM processes. Feedstock is an AM process's starting, source, base, and original material. Common forms of feedstock include filaments, powders, and liquids. For DED, magnet powders are the feedstock relevant to magnet production. Laser-engineered net shaping (LENS) is a type of DED AM process that has been used to produce magnets. In the LENS process, the magnet powders are blown through a nozzle onto a melt pool—created by the heat from lasers—on the substrate to make a deposition. The substrate acts as the print surface. Figure 2.4 illustrates the LENS AM process.<sup>112,113,118</sup>

LENS has been used to create AlNiCo PMs using high-pressure gas-atomized AlNiCo pre-alloyed metal powder. The LENS process followed by heat treatment has been used to create net-shaped AlNiCo 8 PMs. These LENS AlNiCo magnets exceed sintered AlNiCo 8 in remanence and energy product, and they exceed cast AlNiCo 9 in coercivity. However, the LENS printing process alters the microstructure of the desired solidification texture. The result is a loss of copper and aluminum, which can impair the magnetic properties, rendering these magnets less suitable for electrical machine applications. Stainless steel and AlNiCo 9 have been used as metal substrates, suggesting the possibility of printing multiple materials for hybrid magnets. However, because AlNiCo is a niche magnet with low demand, especially compared with NdFeB and hard ferrites, LENS manufacturing of magnets should have limited adoption and use.<sup>98,112,113,118</sup>

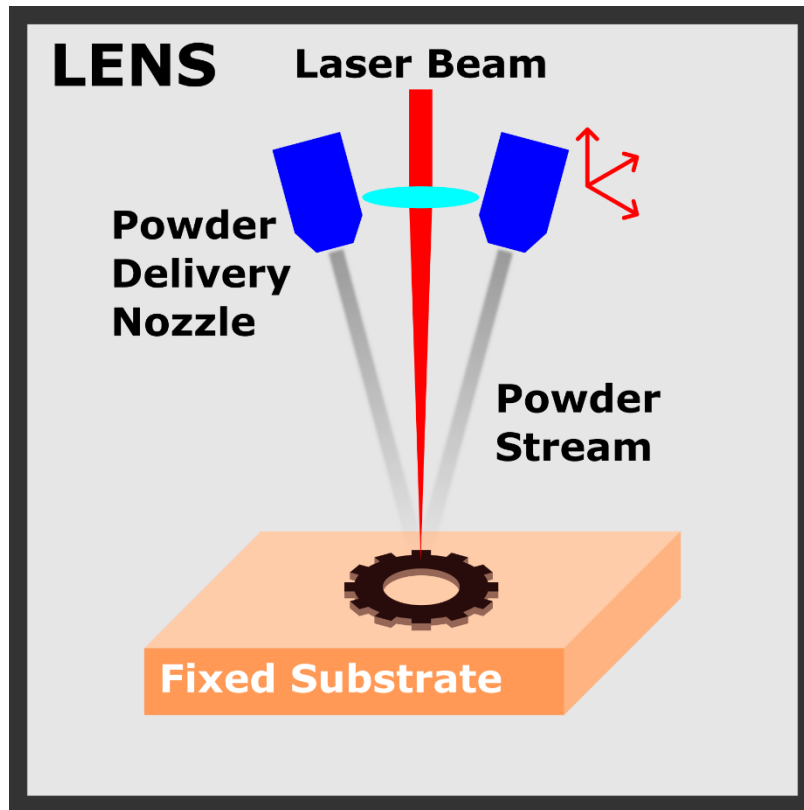


Figure 2.6: The laser engineered net shaping (LENS) AM process.<sup>113</sup>

### **2.4.3 Material Extrusion, or Fused Deposition Modeling**

MEX is any AM process in which material is selectively dispensed through a nozzle or orifice. The feedstock material is forced out of the printer's extruder nozzle and deposited onto the 3D printing platform layer by layer. The platform is the printing surface. Just like DED, MEX is a family of AM processes with many members. The most common MEX AM process is fused filament fabrication, also known as FDM. In FDM, the typical feedstock is a continuous filament of a thermoplastic polymer. This filament could be entirely made of polymer or be made from a multitude of materials, but the filament must be thermoplastic for the FDM process to work. This filament is used to print layers of the filament material. The filament is heated at the printer's nozzle to reach a semiliquid state and then extruded on the print platform or on top of previously printed layers. The platform and the previous layers can both function as the print surface. In FDM, thermoplasticity is an essential filament property because this property allows the filaments to soften when heated, to fuse together during printing, and to solidify after printing. Key parameters concerning FDM include layer thickness, air gaps, filament width, and filament orientation, all of which could affect the mechanical properties of the printed object. The main advantages of FDM are low cost, high speed, and process simplicity. The main disadvantages of FDM include weak mechanical properties, poor surface quality, and layered appearance (i.e., highly visible layer lines on the printed product). Figure 2.5 illustrates the FDM.<sup>112,113,119–122</sup>

FDM has been used to create many different types of magnets in the form of hybrid magnets. Typically, the filament comprises a magnet material powder mixed into a polymer. Because no known magnetic material is a polymer, the FDM process cannot print magnets exclusively. Thus, all attempted AM of magnets via FDM have been hybrid magnets. Because the polymer in these hybrid magnets is not magnetic and does not contribute to magnetization, these hybrid magnets' magnetic properties are inferior to those of the nonbonded magnets. However, the magnets'

properties could be superior to those of the conventionally made bonded magnets because those magnets are also hybrid magnets. Magnetic materials are often orders of magnitude denser than polymers. Therefore, increasing the hybrid magnet's density increases the composition of magnetic materials within the hybrid magnet while decreasing the composition of the polymer. Thus, the key to improving the magnetic properties of hybrid magnets is to increase its density by reducing or eliminating its polymer components. A permutation of FDM, a process known as big area additive manufacturing (BAAM), could achieve this improvement. Figure 2.6 illustrates the BAAM process.<sup>113</sup>

#### **2.4.3.1 Big Area Additive Manufacturing**

BAAM is a gantry-driven extrusion-based AM process developed at DOE's Oak Ridge National Laboratory (ORNL). It is like an enlarged version of FDM. The BAAM system deposits thermoplastics and customized thermoplastic composites via melt extrusion processing, which enables rapid manufacturing of objects completely unbound by size. Unlike FDM, the BAAM system uses pellets instead of pre-extruded filament feedstock. The BAAM system accepts pellets—magnetic material powder mixed with a polymer—and extrudes them into filament during printing. This in-system compression and extrusion of filament allows a much higher density than that of pre-extruded filaments. The BAAM printing process can also be conducted within a magnetic field, thereby improving the magnetic properties of the resultant magnet because the magnetic field aligns the magnetic domains within the printed object, increasing its anisotropy. These advantages of BAAM have allowed the creation of neodymium bonded magnets of high magnetic quality. BAAM has been used to produce isotropic near-net shaped NdFeB nylon bonded magnets, with magnetic and mechanical properties comparable to or better than those of traditional injection-molded magnets. BAAM has also been utilized to print hybrid magnets with multiple



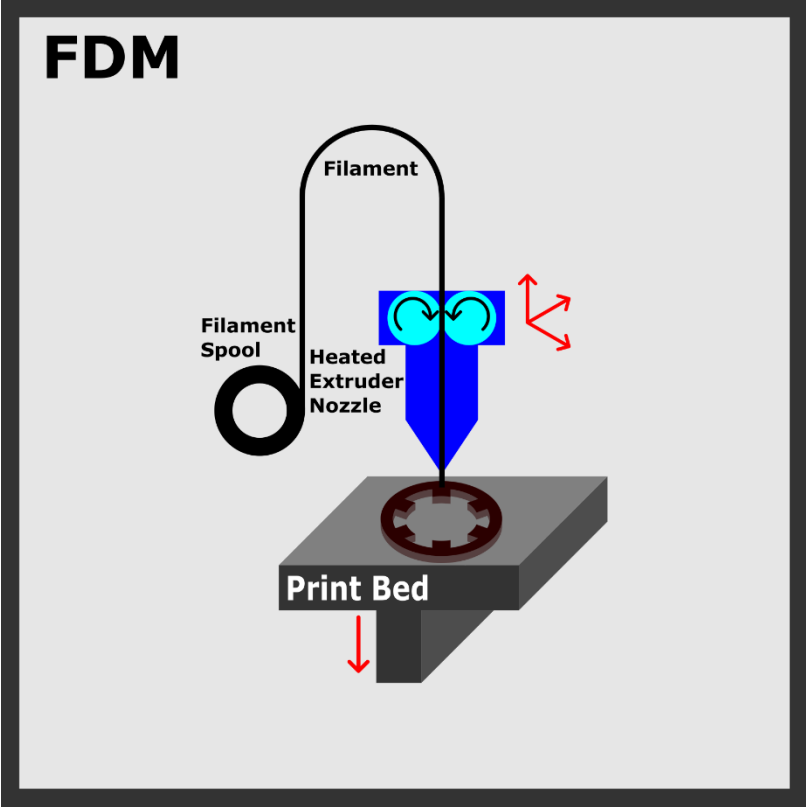


Figure 2.7: The fused deposition modeling AM process.

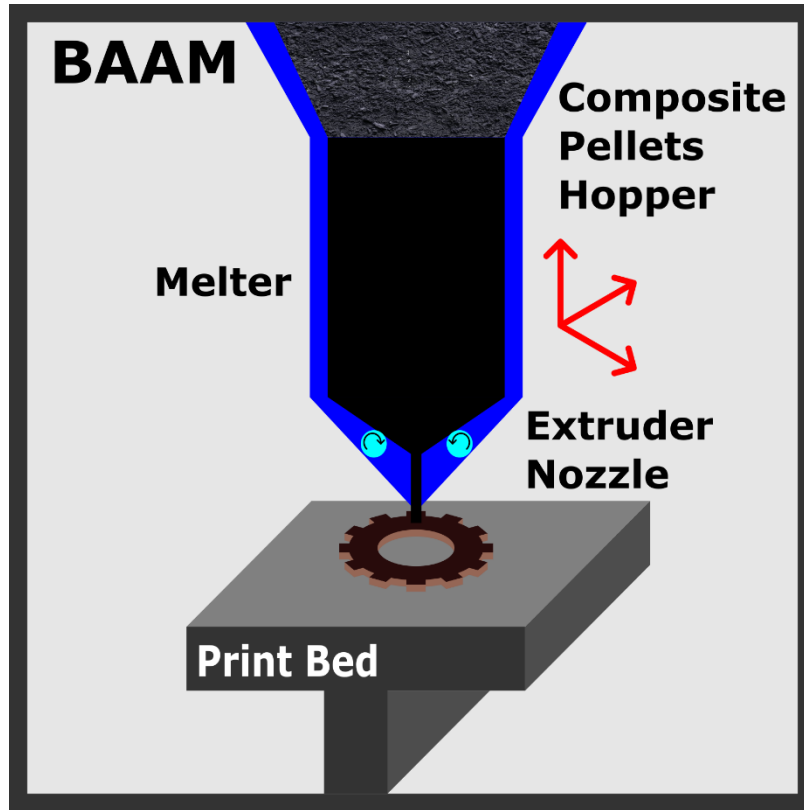


Figure 2.8: The big area additive manufacturing (BAAM) process.<sup>113</sup>

magnetic materials. SmFeN and NdFeB in nylon bonded magnets have been created with BAAM, and aligned in magnetic field to improve magnetic properties. The polymer need not to be nylon. The NdFeB polypropylene sulfide (PPS) bonded PMs have also been created using the BAAM method.<sup>113,123–125</sup>

In the printing of magnets, BAAM has several drawbacks. One drawback is that BAAM is designed to print large objects at a large scale and thus has limited resolution when printing smaller objects. The material density of the magnets produced via BAAM is a major improvement over FDM: the volume percentage of the magnet powder exceeds 70%, but improvements can still be made. The initial ratio of magnet powder to polymer in the feedstock could be further improved and optimized. BAAM allows unprecedented low percentages of polymer in the resultant magnet, but the polymer has not been fully eliminated. Currently, no good process or postprocess exists for removing more of the polymer binder from the printed magnets. Furthermore, rare earth-free magnets have yet to be attempted via BAAM. BAAM reduces the consumption of critical rare earth materials but does eliminates their usage.<sup>113</sup>

BAAM also has many advantages in printing magnets. The large scale at which BAAM is designed to print could be useful for applications involving large magnets. Wind turbine generators are large and are becoming even more massive. BAAM could be used to print massive wind turbine magnets on-site, eliminating the risks and costs of transporting such large magnets. BAAM could also reduce waste of critical materials and eliminate tooling costs for such large magnets. To improve bonded magnets' magnetic properties, density must be increased, and BAAM already offers higher magnetic density than FDM. BAAM also offers further avenues to improve density. BAAM can produce multimaterial hybrid magnets, which are bonded magnets with multiple types of magnetic material powders. Average powder diameters of different magnetic materials often have dissimilar

magnitudes. Powders of different diameters can be packed more densely than powders of homogenous size: the smaller powders fit into the interstitial spaces of the larger powders. Therefore, BAAM multimaterial magnets have the potential for higher densities and consequently stronger magnetic properties. A magnet's energy density is directly proportional to the square of the loading fraction of the magnet. BAAM can offer a better loading fraction than FDM, and it can exceed the loading fraction of the conventional IM process, which has a limit of 0.65. BAAM has the capacity for loading fractions of 0.7 and higher, so BAAM can create magnets of higher energy product than those created via the IM conventional process. Magnets with high energy density are more efficient than those with lower energy products and can offer savings in both energy and raw material consumption. Lower material consumption can mean reductions in environmental emissions and impact. It could also mean huge savings because of the reduced consumption of critical materials such as rare earth elements, especially in times of global economic disruptions, such as those caused by the COVID-19 pandemic, which resulted in price spikes for critical materials. Other advantages of BAAM include fast printing speeds and the ability to produce parts of unlimited size with high shape complexity. Magnets produced via BAAM exhibit similar performance in small motors to sintered ferrites, indicating that these magnets are suitable for small-motor applications. The continued development, improvement, and optimization of energy product of magnets produced via BAAM will allow for further electrical machine applications for BAAM-produced magnets, especially as they near and exceed the properties of sintered NdFeB.<sup>113,126-128</sup>

#### **2.4.4 Powder Bed Fusion**

PBF is a family of AM processes in which thermal energy selectively fuses regions of a powder bed. In the context of powder bed, a bed is flat surface or base upon which anything rests. A powder bed is a bed on which powder rests. The powder bed is the location in an AM system where the

feedstock is deposited and either fused via heat such as the case of PBF or bonded via adhesives such as the case of BJT. The thermal heat source of PBF can be laser beams, electron beams, or infrared light. The PBF process that uses electron beams is known as the electron beam melting (EBM) process. The PBF processes that use laser beams are selective laser sintering (SLS) and selective laser melting (SLM). In SLS, the laser is used to sinter the powder without reaching the melting point of the feedstock powder. In SLM, the laser is used to melt the powder by exceeding the melting temperature of the feedstock powder. The most recent ASTM International (ASTM) standard classifies both SLS and SLM to be laser sintering. SLS, SLS, and EBM are the three most common PBF processes. Figure 2.7 illustrates these three processes. Figure 2.7 is an amalgamation of the three processes. The following differences are indicated via text in the image: EBM uses an electron beam, whereas SLS and SLM use laser beams; EBM and SLM melt the powder feedstock, whereas SLS sinters it.<sup>112,113,129</sup>

All PBF processes offer very high shape complexity and dimensional resolution. The printed object could be made fully dense with mechanical properties that are near that of the bulk material. PBF and can work directly with metal powders to fuse them together. It can produce magnets without bonding the magnet material within a polymer, which does not contribute to the magnet's magnetic properties. Therefore, many attempts have been made to manufacture magnets via PBF.<sup>113</sup>

SLS has been used to produce NdFeB and SmCo PMs. SLM has been used to produce NdFeB PMs. EBM has been used to produce AlNiCo PMs. Some of these attempts have successfully produced high-density magnets. For example, Kolb et al. have successfully produced NdFeB of up to 0.93 relative density to its fully dense sintered variant. PBF has produced magnets with the highest density among all the AM processes. However, this density does not translate to high

magnetic properties. In fact, the magnetic properties of PBF magnets are quite poor. All PBF processes use thermal energy to fuse the feedstock powder, but this high-temperature environment often destroys or severely damages the microstructure of the magnetic alloy powders and can prevent the formation of microstructures that support strong magnetic properties. Despite full or nearly full density magnets being achieved via PBF, the strong magnetic properties associated with those high densities have yet to appear because of the lack of microstructure phases desirable for magnets.<sup>113,130</sup>

PBF has also been used to create alternative magnets such as SmFeN and MnAl. Rare earth-free magnets such as MnAl and AlNiCo have been produced via PBF. Multimaterial hybrid magnets are also possible with PBF, such as nylon-bonded NdFeB. PBF can create many different types of magnets that are fully or near fully dense; however, significant thermodynamic issues regarding the formation of the correct microstructure must be resolved before magnets of high magnetic strength can be produced via PBF.<sup>113</sup>

In addition to producing PMs, AM has also been used to produce soft magnets. BJT, FDM, and SLM are the most popular methods for the AM of soft magnetic material for electrical machines. SLM has been used to print rotor cores. The most common SLM core materials are Fe-Si and Fe-Co alloys. FDM has been used to produce NiFe<sub>2</sub>O<sub>4</sub> ferrite soft magnets. BJT has been used to produce highly dense Fe-6.5Si alloys via postprocessing with thermal debinding of the polymer. These processes all have advantages and drawbacks unique to soft magnets. For SLM, the main drawback is that the produced soft magnets have high eddy current loss in electrical cores. The advantage of SLM is that it can produce parts with high saturation magnetization. For the FDM printing of soft magnets, advantages include the ability to use the high resistivity of polymers to reduce eddy current loss. Furthermore, magnetic properties are preserved because the process does

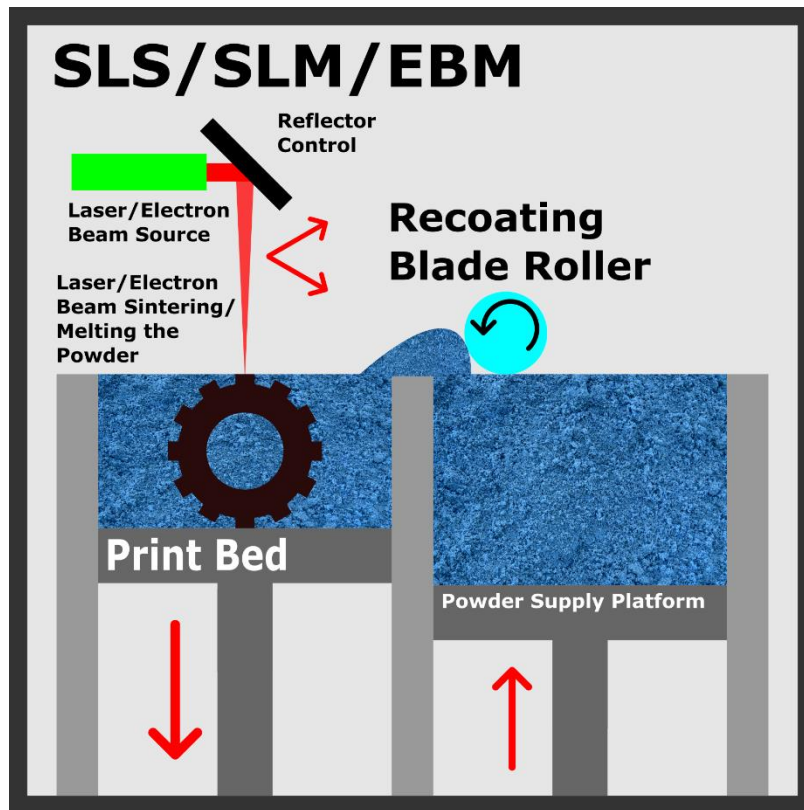


Figure 2.9: The powder bed fusion AM processes.<sup>113</sup>

not require excessively high temperatures. Unfortunately, the saturation magnetization can be ruined because of the nonmagnetic polymer binder. BJT provides the freedom to debind or inject additional material after printing. This technique enables magnet densification, but the magnetic properties could be degraded by porosity or remnants of sacrificial material in the magnet. Furthermore, the magnet undergoes significant size changes during debinding, and thus tolerance is difficult to maintain.<sup>77</sup>



## **CHAPTER 3 : MATERIALS CHARACTERIZATION AND TESTING**

### **3.1 Material Characterization and Testing**

Characterization describes those features of composition and structure (including defects) of a material that are significant for a particular preparation, study of properties, or use, and suffice for reproduction of the material. This definition limits the characterization methods to those that provide information about the material, but not information about the material's material properties. Material testing provides the latter, and in this paper, is performed via mechanical and magnetic tests to determine those material properties. This section introduces selected material characterization techniques that have been used to analyze 3D printed magnets. This section also presents example results and figures for each technique. The characterization and testing methods used include tensile testing, DSC, TGA, SEM, XRPD, and magnetic field testing.<sup>131,132</sup>

### **3.2 Mechanical Testing**

Within the context of materials science, mechanical properties are described as the relationship between stresses or forces acting upon a material and the resistance of the material to strains, deformation, and fracture. The testing of a material for such properties is known as mechanical testing. Mechanical testing is conducted via mechanical testing machines, the most common of which are universal testing machines, which are designed to test specimens in tension, compression, or bending. The testing machines are designed to apply a force to a material to determine its strength and resistance to deformation. These testing machines are designed to drive a crosshead or platen at a controlled rate, thus applying a tensile or compressive load to a specimen. Mechanical testing machines measure, indicate, and record the load to the specimen and the strain of the specimen throughout the test. This paper focuses on tension testing.<sup>133,134</sup>

Uniaxial tension testing, or the tension test, is one of the most common tests for evaluating materials. It is accomplished by gripping the opposite ends of the test specimen within the load

frame of a test machine. The test machine applies a tensile force, resulting in the gradual elongation and eventual fracture of the test specimen. During this process, force-extension data, a quantitative measure of how the test specimen deforms under the applied tensile force, is usually monitored and recorded. When properly conducted, the tension test provides force-extension data that can quantify several important mechanical properties of a material. Mechanical properties that tension tests can determine include yield strength, ultimate tensile strength (UTS), Young's modulus (the modulus of elasticity), Poisson's ratio, ductility properties, and strain-hardening characteristics.<sup>135</sup> An example of the tensile test results—the stress–strain curve—for 3D printed magnets is presented in Figure 3.1. The strain data from the mechanical testing are plotted on  $x$ -axis, and the corresponding stress data are plotted on the  $y$ -axis. This type of graph can be generated by spreadsheet software such as Microsoft Excel or any data analysis software such as OriginLab's Origin. Figure 3.1 was generated by the Origin software using tensile testing data from a 3D printed NdFeB magnet. Figures 3.2 and 3.3 show screenshots of the user interface of Origin and Excel, respectively.

### **3.3 Thermogravimetric Analysis**

TGA is a thermal analysis technique that measures the amount and rate of change in the weight of a material as a function of temperature or time in a controlled atmosphere. The weight of the evaluated material can be changed by the elevated temperature provided by the TGA instrument. This change in weight (or lack of thereof) is measured and recorded by the TGA instrument, and the results are usually presented in the form of a TGA thermogram, also known as a TGA curve. On such a curve, the  $y$ -axis is usually the sample weight in percent of the original weight of the sample at the start of the TGA evaluation. The  $x$ -axis can be time but is usually temperature. TGA instruments usually consist of two primary components: the microbalance and the furnace. The

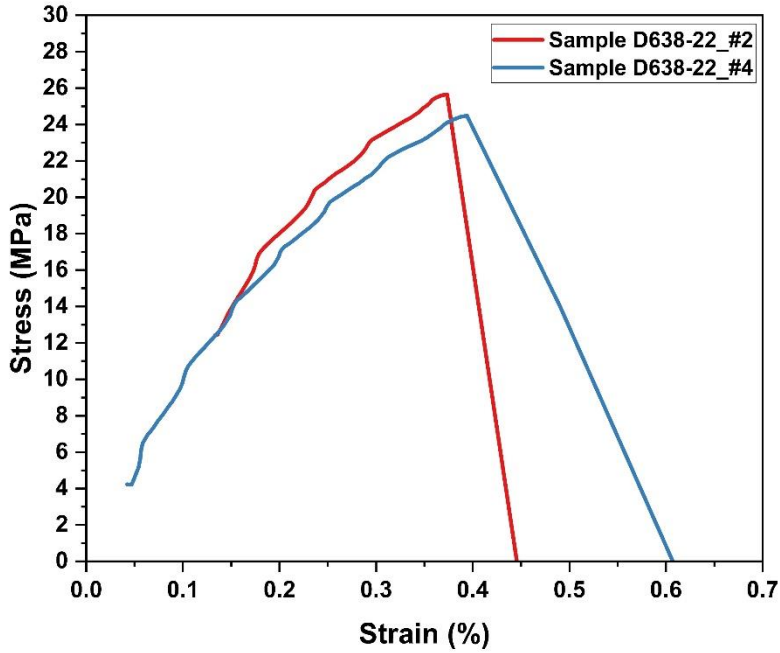


Figure 3.1: Example of the stress–strain curve resulting from mechanical testing.

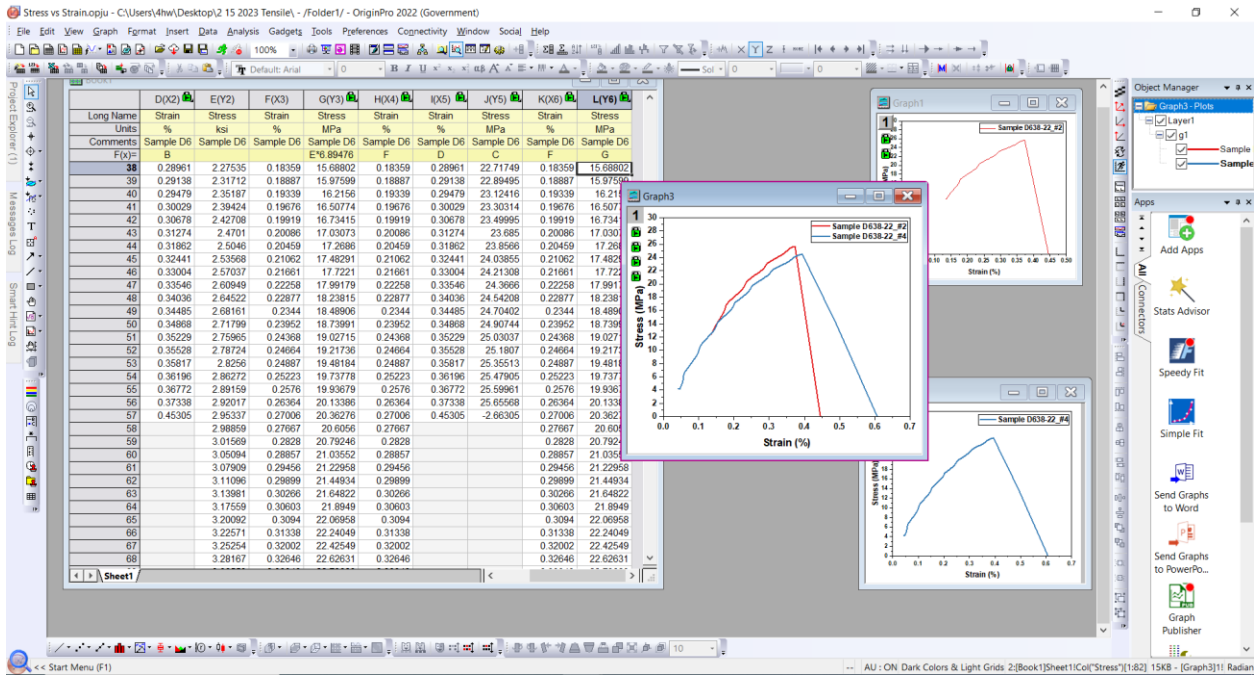


Figure 3.2: Screenshot of Origin's user interface.

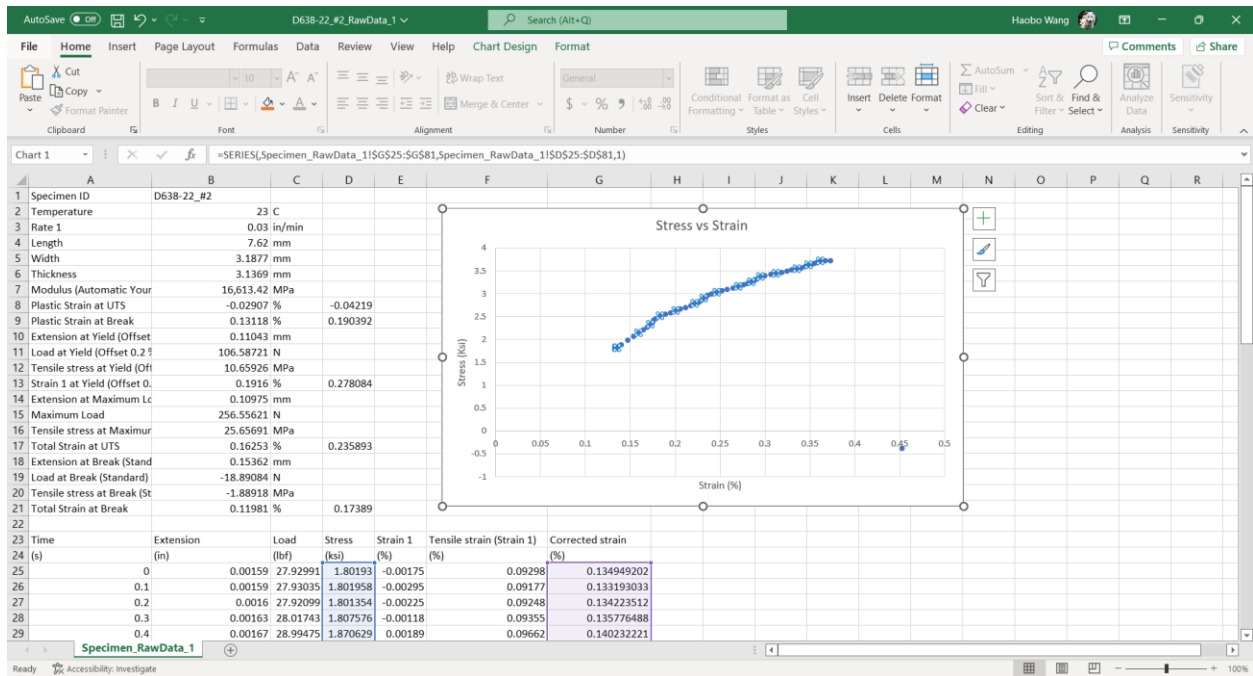


Figure 3.3: Screenshot of Excel’s user interface.

The material being evaluated is loaded into a sample pan—usually ceramic or platinum that can withstand the high-temperature conditions of the TGA experiment. The loaded sample pan is suspended on the microbalance, which measures and records the weight of the sample throughout the experiment. The furnace applies heat to the sample. The sample is usually heated from room temperature to a very high temperature in a nitrogen gas (or air) environment.<sup>136</sup> TGA evaluations of 3D printed magnets are typically performed to determine the magnet's composition. Bonded 3D printed magnets comprise the magnetic material and the polymer binding. The high temperatures in the TGA instrument burn away the polymer, leaving the magnetic material behind, allowing the determination and confirmation of the composition of the 3D printed magnet. An example of a TGA curve is shown in green in Figure 3.4. Figure 3.5 is a TGA curve of SLM 3D printed Hiperco. This curve, made using Origin, portrays the decline of the sample mass with increasing temperature.

### **3.4 Differential Scanning Calorimetry**

DSC is a common thermal technique for the characterization of polymers. It measures the difference in heat flow between a sample and a reference as the material is heated or cooled. It measures the heat flow associated with sample transitions as a function of temperature (or time) under controlled atmospheric conditions. DSC can be used to study thermodynamic processes and kinetic events. DSC can also be used to evaluate any thermal transitions within a material that involve a change in the heat content of the material. Such thermal transitions include melting, solidification, evaporation, oxidation, decomposition, crystallization, cross linking, and chemical reactions. DSC results are presented via a DSC thermogram. On a typical DSC thermogram, the *y*-axis shows the heat flow in energy units or energy per mass units. The *x*-axis shows the temperature or time. Because endothermic transitions require heat to proceed, whereas exothermic

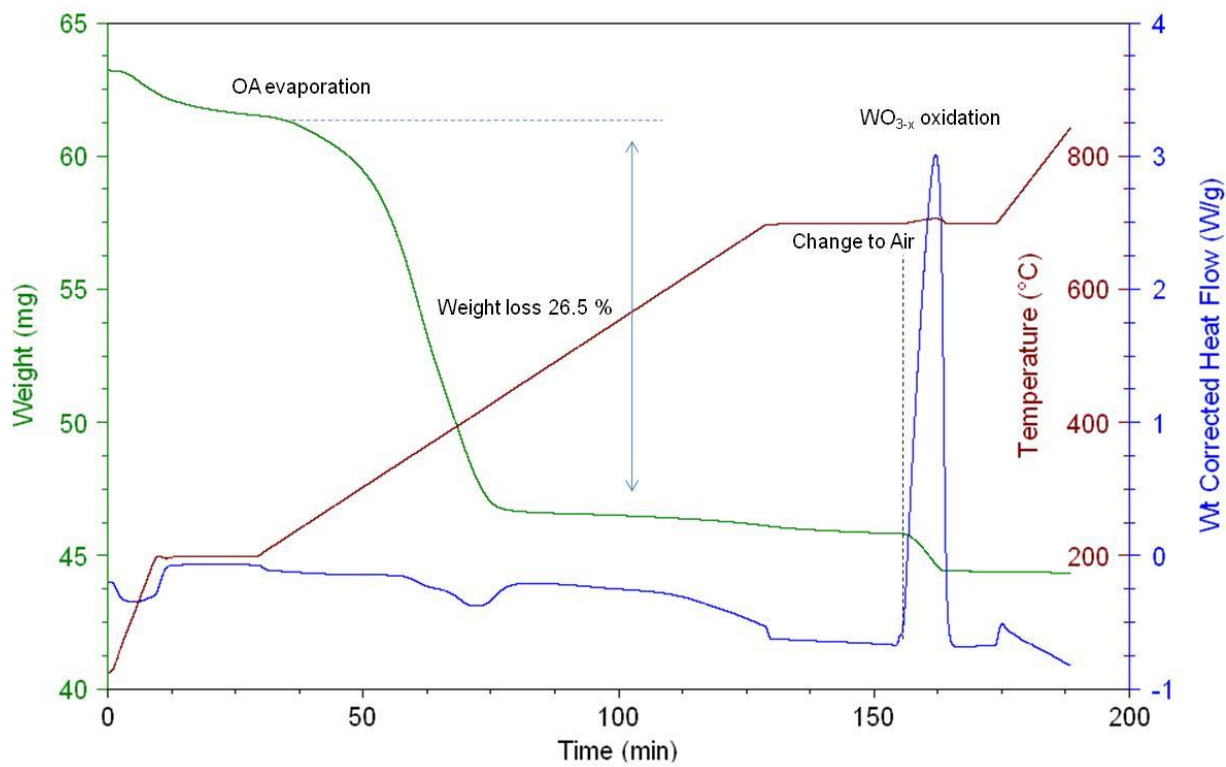


Figure 3.4: Example of TDG/DSC curves. Here TGA is shown in green.<sup>137</sup>

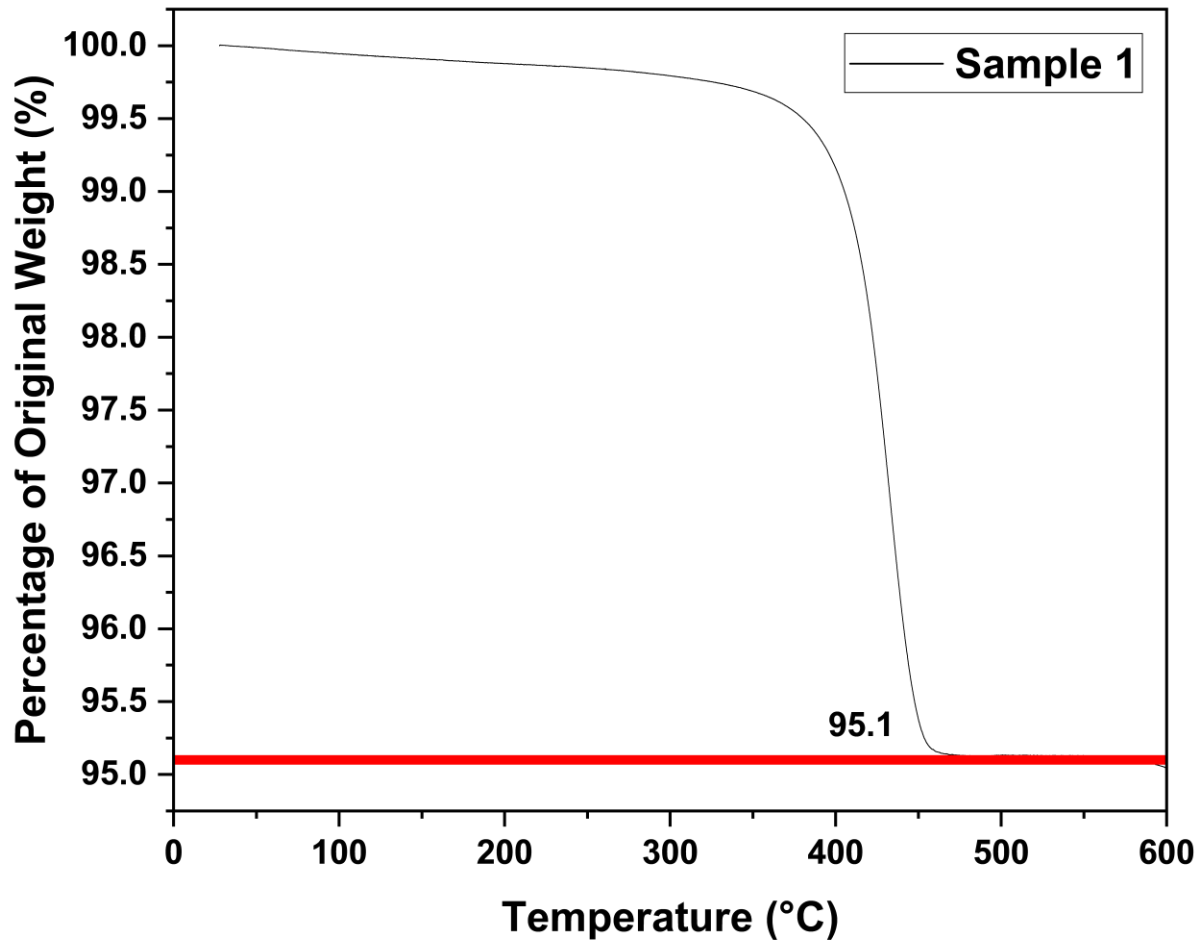


Figure 3.5: Example of TGA curve made via Origin using data from 3D printed SLM Hipercer.



reactions gives off heat, they leave their mark on the DSC curve, which is often unique and identifiable. In DSC, the specimen is placed within a metal pan. Often, this pan is then hermetically sealed. The sample pan is then weighed. A reference pan with weight as close to the sample pan as possible is then selected. DSC measurement is done in two ways. One method involves measuring the energy provided to the heaters below the pans to maintain both pans at the same temperature. The second method involves measuring the heat flow as a function of the sample temperature. DSC specimen mass sizes are quite small, typically between 1 and 10 mg. The sample chamber is flushed with a purge gas, often nitrogen gas. Typically, DSC is used to identify key temperature points, such as the melting temperature ( $T_m$ ) and the glass transition temperature ( $T_g$ ). This use of DSC was employed on the 3D printed magnets in this project. The melting temperature is revealed as the peaks on crystalline DSC curves. On semicrystalline DSC curves, the glass transition phase change appears as a change in slope on the curve. The inflection point on the curve is the glass transition temperature.<sup>138,139</sup> An example of an idealized DSC curve is shown in Figure 3.6. Figure 3.7 serves as another example of a DSC graph and was generated using Origin with data from DSC measurements of NdCuCo and PrCuCo. These alloys are used to infiltrate 3D printed NdFeB.<sup>140</sup>

### **3.5 Scanning Electron Microscopy**

A scanning electron microscope is a type of instrument that magnifies and images the surfaces of the sample specimen via the controlled rastering of a highly focused electron beam across the area of interest. This process produces a variety of signals, particularly backscattered and secondary electrons, as the electron beam interacts with the sample surface. These signals provide local topographic and compositional information regarding the specimen. SEM is primarily used to

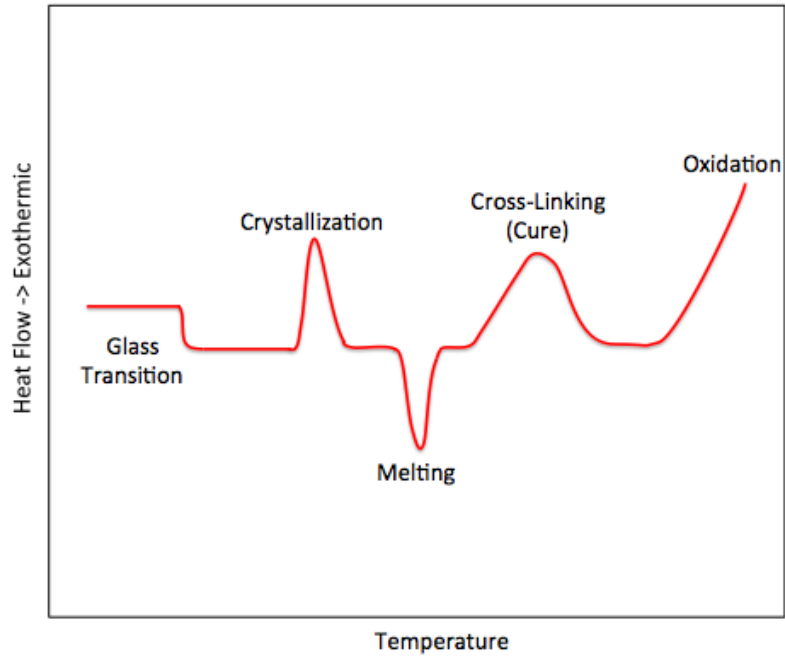


Figure 3.6: Example of an idealized DSC curve.<sup>137</sup>

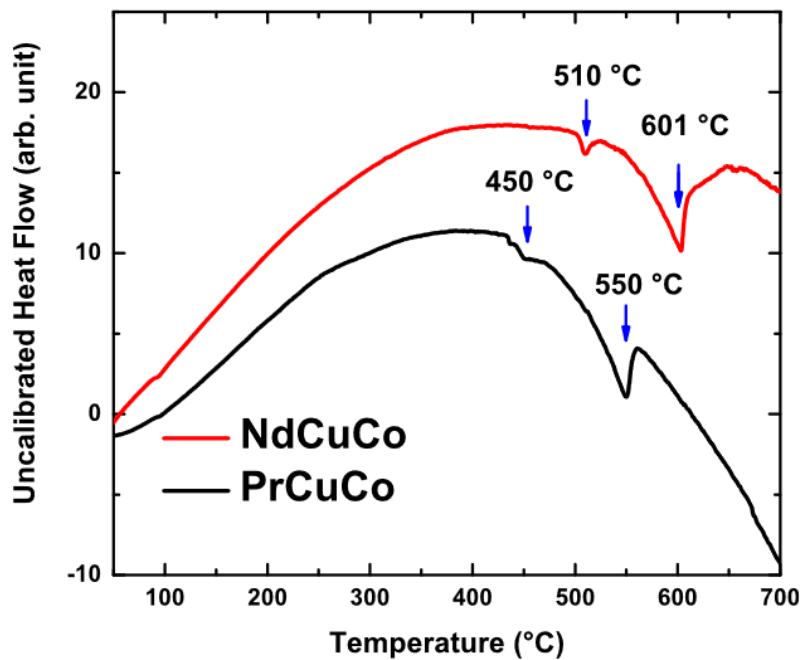


Figure 3.7: DSC graph made with Origin, using data from NdCuCo and PrCuCo, alloys used to infiltrate 3D printed NdFeB magnets.<sup>140</sup>

obtain high-resolution images of the specimen at magnifications unattainable by optical microscopy. SEM can also provide direct compositional and topographic information. Magnifications of up to 100,000× or more are possible by modern SEM instruments. Scanning electron microscopes can produce such images of nanoscale resolution and high magnifications because the electron beam is focused to a nanometer-scale probe of 1–10 nm. A special technique of SEM is Electron backscatter diffraction (EBSD). EBSD is an SEM-based approach that can be used to determine the local crystal structure, including the identity of the phase and its orientation, to map the microstructure of the sample surface. EBSD is used to produce a variety of maps that provide valuable insight on the crystallographic properties of materials. Such crystallographic properties include grain size, grain boundaries, texture, dislocations, plastic deformation, and elastic strain.<sup>141,142</sup> In this project, SEM was used to image the surfaces of 3D printed magnet samples at high magnifications, mapping and identifying their microstructures. SEM was also used to identify the composition of the 3D printed magnet sample. An example of an SEM image is shown in Figure 3.8. It depicts a magnified image of a 3D printed SmFeN magnet.

### **3.6 X-Ray Powder Diffraction**

X-ray diffraction techniques are used to characterize crystalline materials, such as metals, intermetallics, ceramics, and polymers. It is primarily used to identify the phases present within the samples and can provide information on the physical state of the sample, such as texture and grain size. Most X-ray diffraction techniques are nondestructive and are rapid in procuring results. There are two main types of X-ray diffraction techniques: single-crystal X-ray diffraction, and XRPD. This project used XRPD to investigate 3D printed magnets. XRPD is used to characterize samples in the form of loose powders. XRPD characterization involves placing the sample within a collimated monochromatic X-ray beam. X-rays follow the Bragg equation,  $n\lambda = 2d\sin\theta$ . This

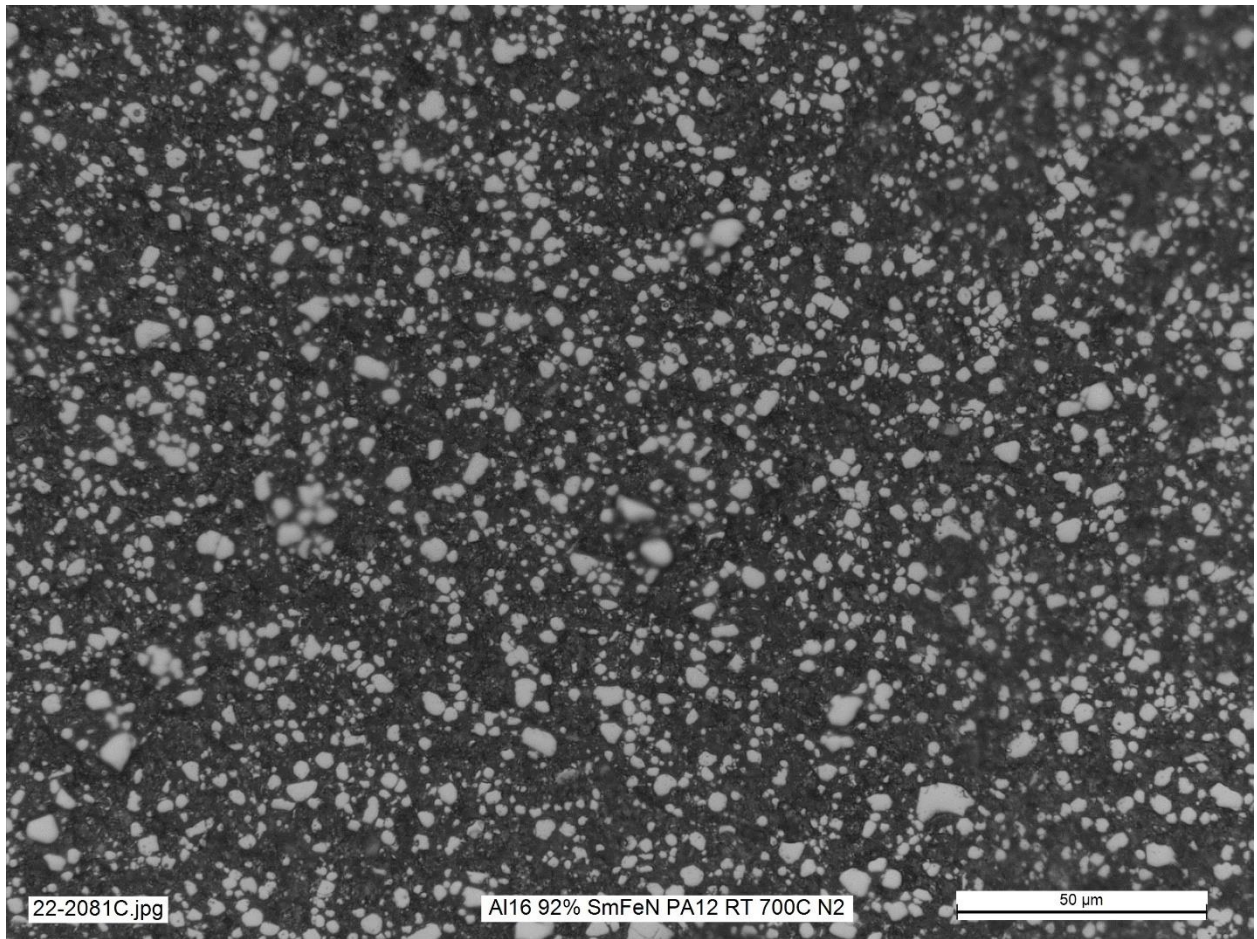


Figure 3.8: SEM image of 3D printed SmFeN magnet.

equation states that the angular position ( $\theta$ ) of the diffracted X-ray beam maxima depends on the spacing ( $d$ ) between planes of atoms in a crystalline phase and on the X-ray wavelength ( $\lambda$ ). The sample material's crystal structure determines the angle of X-ray diffraction. Working backward, the sample material's crystal structure can be determined by analyzing the angular information of the diffracted X-rays. XRPD characterization usually requires some sample preparation, typically crushing the material being investigated into powder and packing it into the sample holder of the X-ray powder diffractometer. The output of such a machine is a diffractogram, also known as an XRPD graph. It is a plot of intensity, in terms of X-ray counts, versus the diffraction angle, in terms of  $\theta$ . Diffractograms include several peaks, each corresponding to a particular set of crystallographic planes and its characteristic  $d$ -spacing. Phase identification utilizing XRPD is based on the fact that every crystalline phase produces a unique pattern. Just like a fingerprint is unique for each person, the X-ray diffraction pattern can act as an empirical fingerprint for a crystalline phase. XRD patterns have been collected and stored in databases, such as the Powder Diffraction File maintained by the International Centre for Diffraction Data. By comparing pattern of the material being investigated to those in a XRD database, the phase of the material can be identified.<sup>143–147</sup> XRPD is used to identify the phases of the 3D printed magnets in this paper. Figure 3.9 shows a simulated image of the XRPD pattern for  $\text{Nd}_2\text{Fe}_{14}\text{B}$  using data from the Crystallography Open Database. Figure 3.10 depicts the XRD patterns for a 3D printed  $\text{SmFeN}$  magnet.<sup>148</sup>

### **3.7 Superconducting Quantum Interference Device Magnetometer**

Magnetic field testing is a nondestructive evaluation method used (1) to inspect magnetic materials for defects such as cracks, voids, and inclusions and (2) to assess magnets' material properties, especially magnetic properties. This project used magnetic field testing for magnetic properties

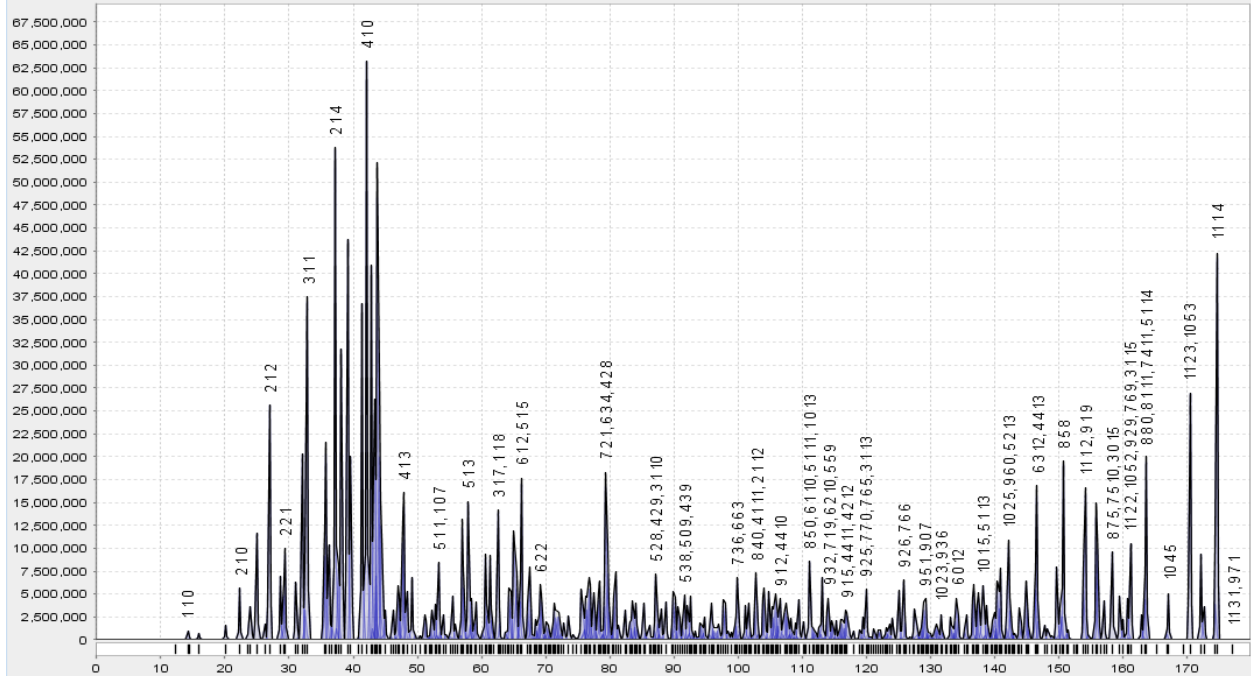


Figure 3.9: Simulated Nd<sub>2</sub>Fe<sub>14</sub>B XRPD pattern. Data from Crystallography Open Database.<sup>149</sup>

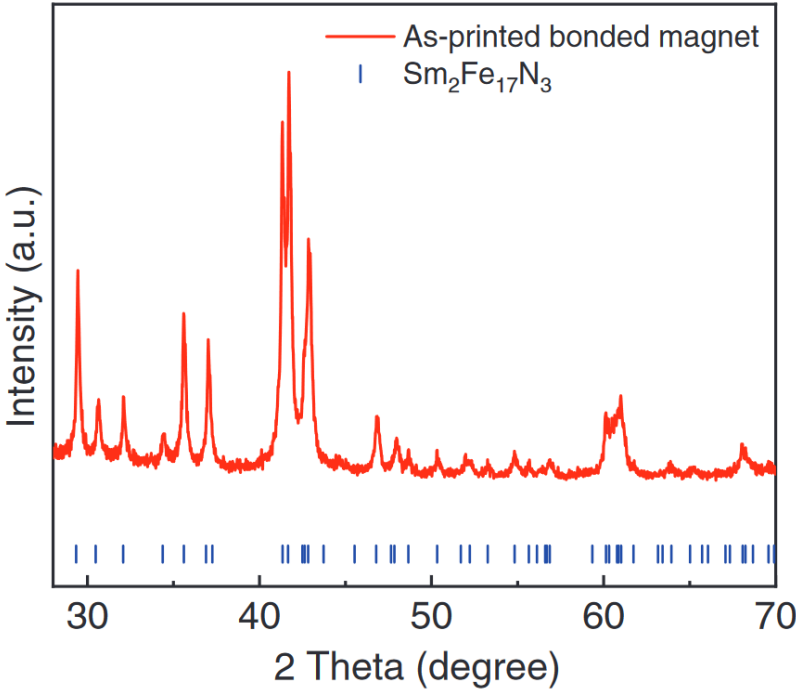


Figure 3.10: XRPD results of a 3D printed SmFeN magnet.<sup>148</sup>

characterization based on bulk measurements of the hysteretic properties of material magnetization. More specifically, this project focused on magnetometry. Magnetometry is the measurement of the magnetization ( $M$ ) or the magnetic moment ( $m$ ) of a sample. The resultant data can be used to determine the magnetic properties of the sample material. A common lab-based magnetometry device is the SQUID magnetometer. The commercially available SQUID magnetometers allow a fully automated measurement of the magnetization of a specimen as a function of the magnetic field and/or temperature.<sup>150-154</sup> SQUID can output data in the form of an Excel spreadsheet that can be imported to Origin to generate graphs. These graphs can be hysteresis curves or  $B/(BH)_{\max}$  vs.  $H$  curves. Examples of such Origin graphs are provided in Figures 3.11 and 3.12.

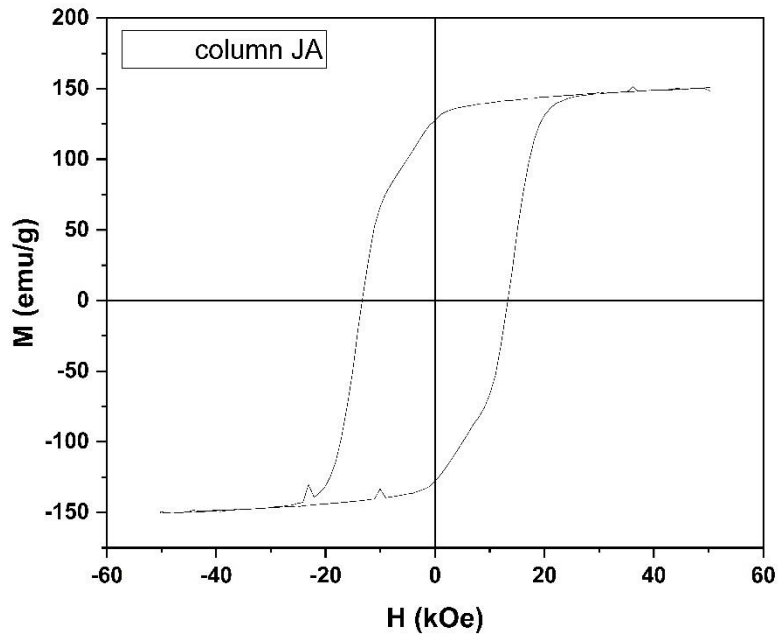


Figure 3.11: Hysteresis graph generated with Origin using data from SQUID of 3D printed NdFeB.

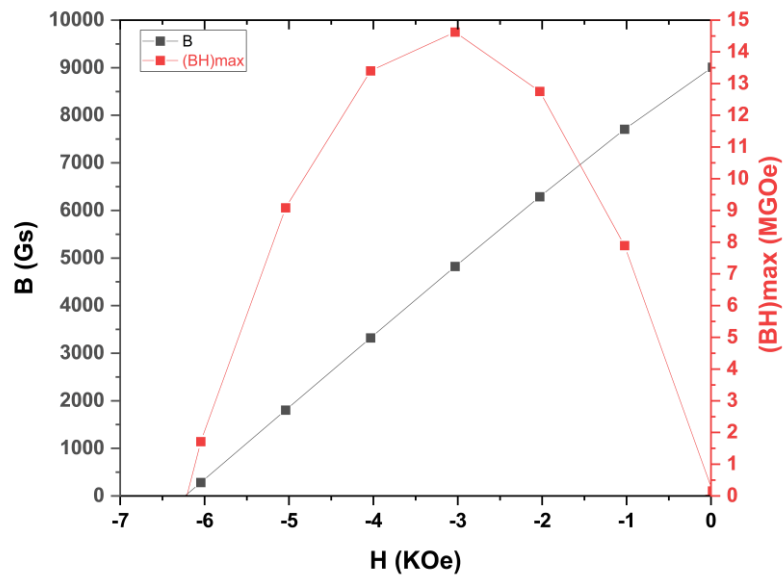


Figure 3.12:  $B$  and  $(BH)_{max}$  vs.  $H$  curves generated with Origin using data from SQUID of 3D printed NdFeB.



## **CHAPTER 4 : SOFT MAGNETS**

#### **4.1 On the Important Material Properties Concerning Soft Magnets**

Soft magnetic materials, also known as soft magnets or temporary magnets, are magnetic materials that have low coercivity and thus a narrow hysteresis loop. Soft magnets have high magnetic permeability, which allows the material to produce large magnetic flux changes with only small fields. A key indicator of magnetic permeability is relative permeability ( $\mu_r$ ). Soft magnets with high magnetic permeability have high relative permeabilities. Soft magnets are very easy to reverse and are ideal for high-frequency applications. Magnetization,  $M$ , is a measure of the magnetic polarization that occurs when a material is placed in a magnetic flux. It is defined as magnetic moment per unit volume. The remanent magnetization, or remanence ( $B_r$  or  $M_r$ ), is the magnetization remaining in the material when the driving field is reduced to zero. Soft magnets have negligible remanence and thus exhibit negligible hysteresis. Soft magnets should also have high saturation magnetization ( $M_s$ ), the value of  $M$  when all the dipoles are aligned. Soft magnets have both static and alternating-current (AC) applications. Typical applications of soft magnets include electromagnets, transformers, inductors, motors, generators, and microwave ovens.<sup>77,155,156</sup> In summary, high permeability, low remanence, and high saturation magnetization are features of an excellent soft magnet. Some of the most common, important, or interesting soft magnets are introduced in the following subsections.

#### **4.2 Important Soft Magnets and their Properties**

The major material families of soft magnets include soft ferrites, Fe–Ni alloys, Fe–Si alloys, Fe–Co alloys, soft material composites (SMCs), and amorphous nanocrystalline soft magnets. Important soft magnetic properties include saturation magnetization ( $M_s$ ) and relative permeability ( $\mu_r$ ). The specific materials with the strongest soft magnetic properties of the major soft material families are listed in Table 4.1 and compared in Figure 4.1.<sup>77,155–157</sup>

Table 4.1: Soft magnetic material families and their magnetic properties.

Material families	Specific materials	Saturation magnetization $M_s$ (T)	Relative permeability $\mu_r$ (maximum)
Soft ferrites	MnZnFe <sub>2</sub> O <sub>4</sub>	0.545	200,000
Fe–Ni alloys	Permalloy	0.8	600,000
	Supermalloy	0.82	1,200,000
Fe–Si alloys	6.5 wt.% Si Steel	1.27	58,000
Fe–Co alloys	Permendur	2.2	15,000
SMC	Somaloy	2.45	950
Amorphous nanocrystalline soft magnets	FINEMET	1.23	100,000

Sources: 76,158–159

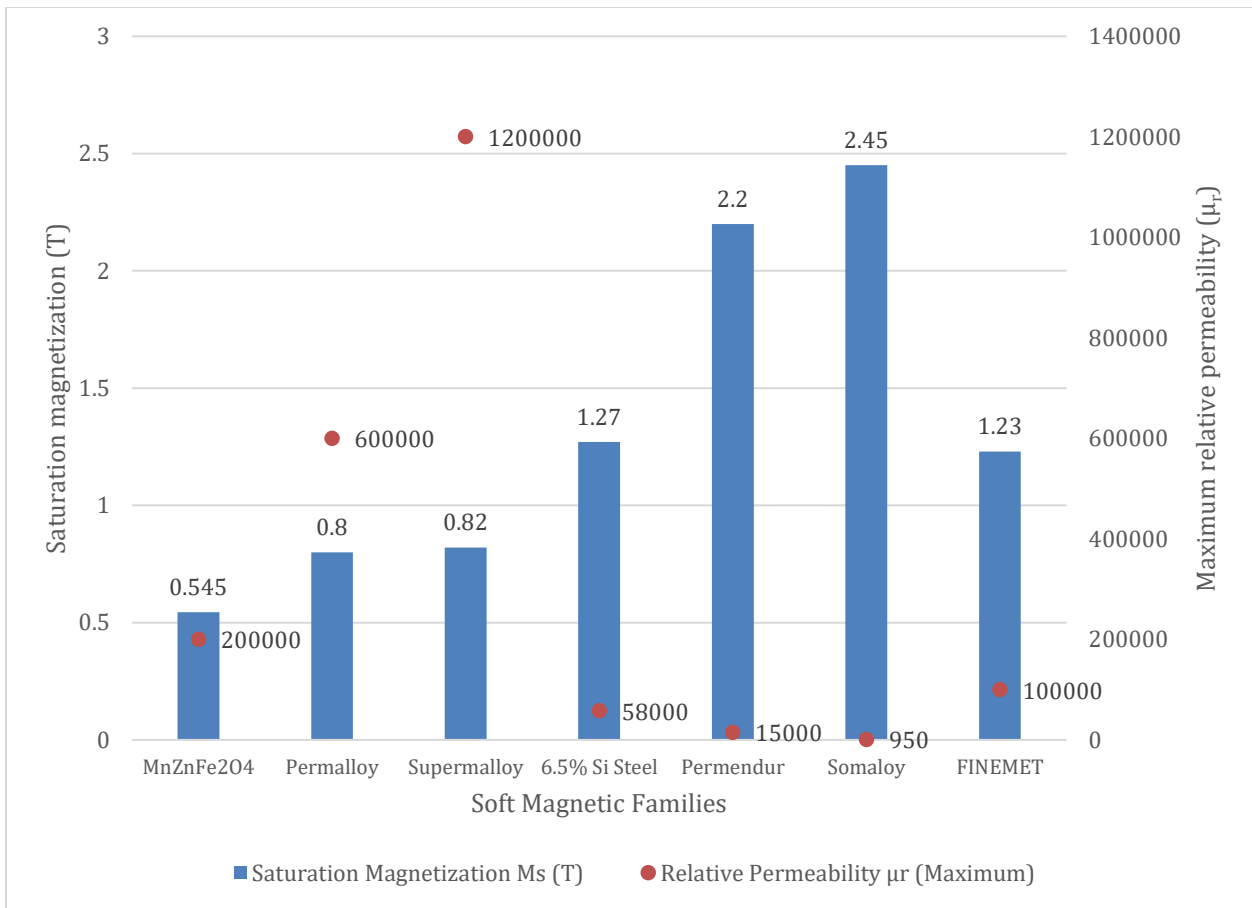


Figure 4.1: Soft magnetic materials and their properties.

Table 4.1 and Figure 4.1 reveal that soft magnetic materials with excellent permeabilities often have poor saturation magnetization. The opposite is also true: soft magnetic materials with superb saturation magnetizations often have poor permeabilities. Only silicon steel has both great permeability and saturation magnetization; therefore, it is the dominant soft magnetic material for electrical machine applications. By tonnage, 95% of all soft magnet used in electrical machine applications are silicon steel. FINEMET offers better permeability at slightly lower saturation magnetization but has not challenged the dominance of silicon steel because FINEMET is more expensive than silicon steel. FINEMET requires more varieties of raw materials, including the critical material niobium. FINEMET also has a much more complex manufacturing process. These reasons contribute to the higher cost and lower availability of FINEMET. Thus, the primary challenge in the AM of soft magnets is to offer a superior alternative to silicon steel, primarily by achieving better overall material properties and without using expensive nor critical materials.<sup>76,155</sup>

### **4.3 On the Additive Manufacturing of Soft Magnets and the Material Properties of these Magnets**

This project involved attempts to 3D print soft magnets, primarily using permutations of silicon steel, but also using the Fe–Co soft magnetic alloy Hiperco 50. BJT and SLM were used to print silicon steel, and Hiperco was printed with SLM.

#### **4.3.1 Binder Jetting Fe-6.5Si**

An advantage of AM is that it can produce electrical steels with high silicon content. High silicon content electrical steel can be used in electrical machine applications, offering superior magnetic and electrical properties. However, it is difficult to manufacture via conventional methods. Bender jetting successfully produced 6.5 wt% silicon, highly dense electrical steels.<sup>160</sup>

Most soft magnetic applications prefer materials with high magnetic permeability and low core losses. Soft magnetic silicon steel fits this description and thus is widely used in many electrical applications, such as motors, generators, transformers, and magnetic shielding. Silicon steel has a microstructure called the Goss texture that is responsible for its superior soft magnetic properties. Higher quantities of silicon within the steel increases electrical resistance and further improves magnetic properties. At 6.5 wt% silicon, the magnetostriction of the silicon steel becomes zero, and low eddy current losses are achieved. However, the Goss texture is more difficult to achieve at higher silicon content. Silicon increases the brittleness of the material, and at more than 4 wt%, the material becomes too brittle to be stamped or rolled without cracking during the production of thin sheets. Because silicon steels are brittle above about 3.5 wt% silicon, conventional cold rolling is not possible with higher silicon contents. AM is a solution to this problem. BJT has been used successfully to produce 6.5 wt% silicon steel. The major steps of the process are as follows. First the Fe–6.5Si powders are procured and dried at 100°C in an oven in air. Then the powder is transferred to the printer, and the piece is produced via BJT. Next, the piece is cured in air at 200°C. Then the piece undergoes thermal debinding at very high temperatures (603°C–900°C in argon gas). This debinding removes most of the polymer binder. Last, the parts are solid-state sintered in a vacuum oven at extremely high temperatures under vacuum (up to 1,300°C for 2 h under vacuum). This process successfully produced soft magnetic materials with very high densities. The relevant densities of the printed material are listed in Table 4.2.<sup>160–166</sup>

These densities prove that BJT can produce near-net shape, fully dense silicon steel. Furthermore, no crack defects occurred because cracking was mitigated by solid-state sintering. The magnetic properties are also quite impressive. The material properties of the BJT silicon steel soft magnetic

material are summarized in Table 4.3. Comparisons of these properties with standard soft magnetic materials are discussed in Section 4.4.<sup>160</sup>

The BJT printed Fe–6.5Si soft magnetic material has several advantages such as high resistivity and good magnetic permeability. Moreover, the printed material demonstrated reduction in core loss at low, medium, and high frequencies compared with standard silicon steel. This AM method shows great promise for fabricating parts for electrical machine applications that have improved efficiencies.<sup>160</sup>

#### **4.3.2 Selective Laser Melting Fe–3Si**

SLM was used to manufacture 3 wt% silicon steel. Thin laminations were then made from the printed material and successfully integrated into an electric motor, and performance results were obtained. EDM is a machining process in which material is removed from an object immersed in a dielectric liquid by a series of electrical discharges between the object and the electrode. This type of machining is often employed on metals and alloys that are difficult to machine via conventional methods. The main steps for the work on 3D printed Fe–3Si laminates are as follows. First, a CAD model of a motor stator design is procured. Second, selective laser melting is used to create the Fe–3Si stator. Cylinders and cubes are also created in the same batch for material properties measurement. Then, the stator is cut into thin laminate sheets via EDM. The cut laminates are heat-treated under hydrogen gas at high temperatures (750°–800°C) and then insulated separately by epoxy coating. Finally, they are assembled to form the stator core. The rotor PMs in this work were made via FDM with NdFeB powder and PPS polymer, magnetized post-print in a 5 T magnetization field. The material properties of the SLM Fe–3Si steel laminate are summarized in Table 4.4. The material properties of a conventionally processed Fe–3Si steel laminate are also listed in the table for comparison.<sup>125,167–169</sup>

Table 4.2: Densities of BJT silicon steel.

<b>Property</b>	<b>Measured value (g/cm<sup>3</sup>)</b>	<b>Percentage of theoretical density (%)</b>
Theoretical density	7.48	100
Green density	4.2	58
Final density	7.31	99

Source: <sup>160</sup>

Table 4.3: Material properties of the BJT Fe–6.5Si soft magnetic material.

<b>Material property</b>	<b>Value</b>
Tensile strength	434 MPa
Electrical resistivity	98 $\mu\Omega\cdot\text{cm}$
Saturation magnetization	1.83 T
Maximum relative permeability	10,700
Coercivity	0.4 Oe

Source: <sup>160</sup>

Table 4.4: Material properties of the conventional and SLM Fe–3Si steel.

<b>Properties</b>	<b>Conventional Fe–3Si Steel</b>	<b>AM/EDM Fe–3Si Steel</b>
Lamination thickness (mm)	0.65	0.6
Saturation magnetization (T)	2.03	2.1
Coercivity (Oe)	1.256	0.5
Resistivity ( $\mu\Omega\cdot\text{cm}$ )	50	50
Maximum permeability	3,000–9,000	7,494
Tensile strength (MPa)	400	555.57

Source: <sup>167</sup>

The data in Table 4.4 reveal that the SLM material exhibits higher saturation magnetization and lower coercivity than the conventional equivalent, indicating superior performance in soft magnetic applications. The SLM material also has permeability toward the high end of the range for silicon steel. The tensile strength of the SLM sample is also superior to that of the conventional version. Consequently, SLM is suitable for applications that demand higher mechanical loading, such as high-mechanical-stress electrical machine applications. The 3D printed soft and hard magnets were assembled into a working electric motor, demonstrating that such a feat is possible.<sup>167</sup>

### **4.3.3 Selective Laser Melting FeCoV (Hiperco 50)**

Hiperco 50 soft magnet stators were produced via SLM. Bimetallic iron–cobalt alloys are known as permendur. Permendur is the brand name for an alloy of this type, but over time this type of alloy came to be known as permendur. Supermendur, which has improved soft magnetic properties, is Permendur with 2 wt.% addition of vanadium. Hiperco is Supermendur with the addition of small amounts of niobium and has even better soft magnetic properties. All Hiperco alloys exhibit high magnetic saturation, high maximum permeability, low coercive force, and low core loss. In fact, the Hiperco alloys exhibit the highest magnetic saturation of any commercially available soft magnetic alloys. Because of these material properties, Hiperco50 alloy is used as rotor and stator laminations for high-performance motors and generators for achieving maximum torque density and minimum losses. Hiperco can help improve the motor power density and efficiency and can also reduce the overall size of the motor.<sup>170–173</sup>

The main steps in the fabrication of SLM Hiperco 50 stator is as follows. First the CAD model of the stator is created. Then the Hiperco 50 parts are produced via SLM. Additional geometries are co-produced for material characterization purposes. Next, the 3D printed parts are subjected to hot



isostatic pressing at high temperatures under high pressure to densify the printed parts and to relieve their internal stresses. The printed stator and some of the additional geometries are then subjected to wire EDM and are sliced into thin laminations. Some of the pieces are used for material characterization. Last, the stator laminations are assembled into a stator, which is also characterized for material properties. This research successfully demonstrates the viability and proof of concept of 3D printed Hiperco stators.

Table 4.5 lists the material properties of the printed Hiperco 50 stator. It is compared with baseline conventional Hiperco material in Section 4.4.

#### **4.4 Comparison of the Materials Properties of 3D printed Soft Magnets and their Baseline Counterparts**

This section compares the various 3D printed soft magnets with their baseline conventional counterparts. The material properties of the 3D printed magnets and their baseline counterparts are listed in Table 4.6. Figure 4.2 illustrates their magnetic properties in a comparative way, highlighting their differences.

Figure 4.2 displays the bars for the 3D printed soft magnets in red, and the bars for the conventional magnets are in blue. The 3D printed magnets are displayed to the right of their conventional equivalent. This strategy facilitates distinguishment and comparison between the two categories of soft magnets.

All the 3D printed soft magnetic materials have higher saturation magnetization than their conventional counterparts. Magnetization is a measure of the magnetic polarization that occurs when a material is placed in a magnetic flux and is defined as magnetic moment per unit volume. All materials have a limit to their magnetization, and this limit is the saturation magnetization  $M_s$ . At this upper limit, increasing the magnitude of the applied magnetic field  $H$  no longer increases

Table 4.5: Material properties of the SLM Hiperco 50 stator.

<b>Material property</b>	<b>Value</b>
Saturation magnetization (T)	2.25
Coercivity (Oe)	1.9
Relative permeability	3,900
Electrical resistivity ( $\mu\Omega\cdot\text{cm}$ )	33
Yield strength (MPa)	917
Ultimate tensile strength (MPa)	1,013.53
Elastic modulus (MPa)	17,257.58

Table 4.6: Material properties of conventional and 3D printed soft magnetic material.

<b>Specific materials</b>	<b>Saturation magnetization <math>M_s</math> (T)</b>	<b>Relative permeability <math>\mu_r</math> (maximum)</b>
MnZnFe <sub>2</sub> O <sub>4</sub>	0.545	200000
Permalloy	0.8	600000
Supermalloy	0.82	1200000
6.5 wt% Si Steel	1.27	58000
BJT Fe-6Si	1.83	10700
SLM Fe-3Si	2.1	7494
Permendur	2.2	15000
SLM Hiperco 50	2.25	3900
Somaloy	2.45	950
FINEMET	1.23	100000

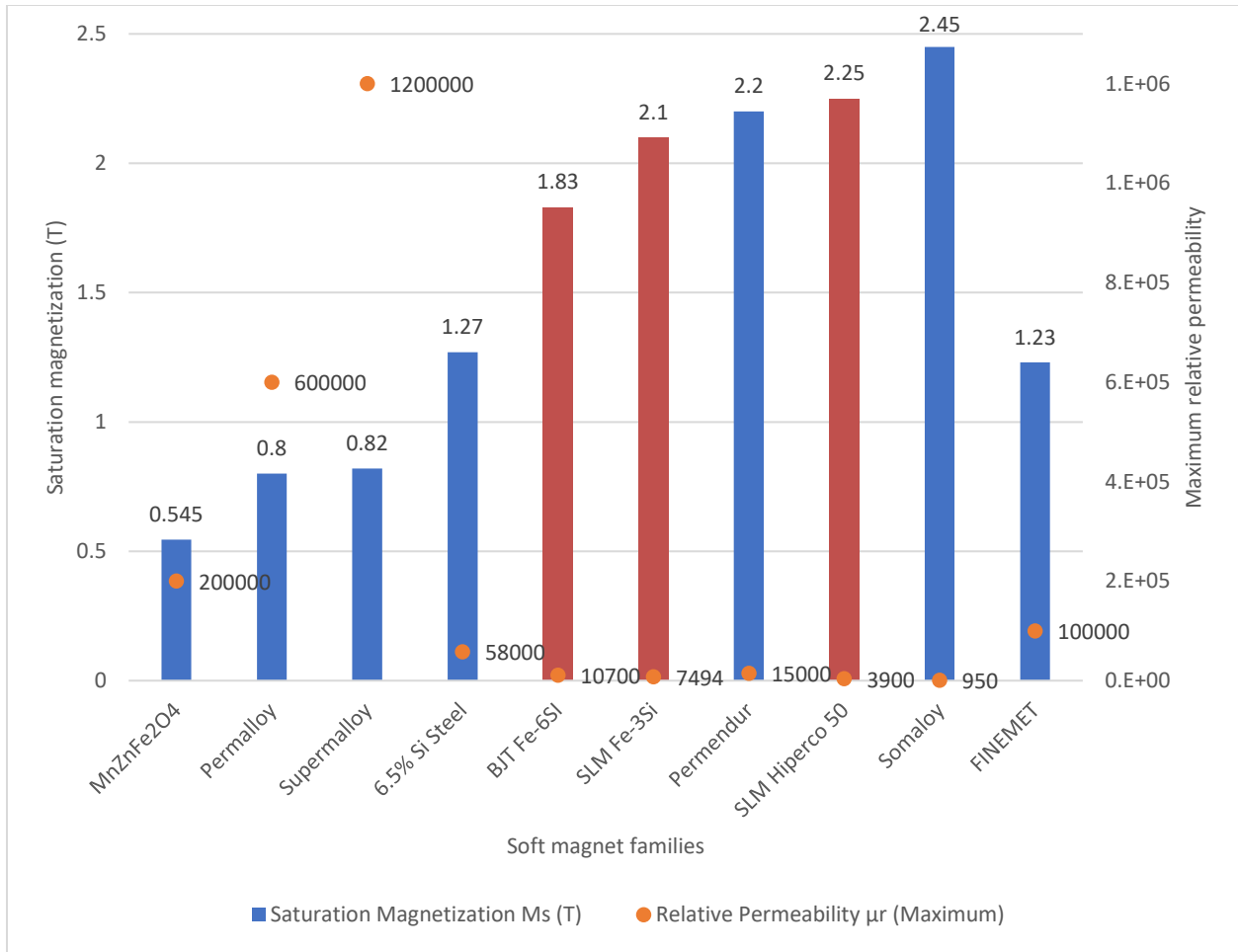


Figure 4.2: Material properties of conventional and 3D printed soft magnetic material.

the magnitude of the magnetization. Saturation magnetization exists when all the magnetic domains have completed orientation and have aligned to the direction of the applied field. Saturation magnetization exists because only a finite number of magnetic domains within a magnetic material orient to the direction of the applied field. Because 3D printed magnets have higher saturation magnetization, these materials can contain higher magnetic moments per volume than their conventional counterparts. Consequently, less volume of the soft magnetic material is needed to conduct the large amounts of magnetic flux necessary for the required application. Therefore, applications such as motors, generators, or transformers no longer need to be so physically large. The 3D printed soft magnetic materials can enable the miniaturization of the magnetic cores of such applications. This miniaturization should be especially useful for applications in which weight minimization is critically important, such as in electric aircraft motors or transformers. Reducing the size of wind turbine generators can ease the installation of new turbines because smaller parts would be much easier and cheaper to transport to the on-site location. Alternatively, it could generate more power at the same size, resulting in more efficient wind generators. For EVs, smaller magnetic cores reduce the weight of the electric motor and improve efficiency. With such weight savings more batteries could be aboard the vehicle, further improving its range and efficiency. The 3D printed magnets have lower relative maximum permeability than their conventional counterparts, so they require a stronger magnetic field (i.e., more energy) to magnetize. Therefore, 3D printed soft magnets are less energy efficient in their applications than conventional soft magnets. Heat-based postprocessing such as sintering and hot isostatic pressing dramatically affect the densification of certain 3D printed soft magnets and could result in near fully dense soft magnets. Such densification significantly improves the magnetic properties of 3D printed soft magnets.

## **CHAPTER 5 : HARD OR PERMANENT MAGNETS**

## 5.1 On Important Material Properties Concerning Hard Magnets

Hard magnetic materials, also known as hard magnets or PMs, have high coercivity, and thus have a wide, square hysteresis loop. As a result, PMs require large fields to switch, and their applications mainly take advantage of the remanent induction. PMs also have high remanence and high energy products. The energy product, or  $(BH)_{\max}$ , is the maximum value of the product of the  $B$  and  $H$  in the second quadrant of a magnetic material's hysteresis curve. The energy product represents the density of magnetic energy within the material and indicates the material's magnetic strength. The Curie temperature,  $T_c$ , is the temperature below which spontaneous magnetization owing to the alignment of the magnetic moments may occur, and it governs the magnet's operational temperature range. Thus, a high  $T_c$  is desirable for most magnets. Common applications of PMs include MRI, motors, generators, loudspeakers, bearings, and breaks.<sup>155,156,174–176</sup> Some of the most common, important, or interesting hard magnets will now be introduced.

## 5.2 List of Important Hard Magnets and their Properties

The four major types of hard magnets are NdFeB, SmCo, AlNiCo, and hard ferrites. The most common hard ferrites are barium carbonite or strontium carbonite. Alternative PMs include SmFeN, Fe<sub>16</sub>N<sub>2</sub>, MnBi, Mn-Al(-C), L<sub>10</sub>-FeNi, L<sub>10</sub>-FeCo, HfCo<sub>7</sub>, Zr<sub>2</sub>Co<sub>11</sub>, and Co<sub>3</sub>C. Only the four major types are commercially successful and have widespread adoption. For PMs, the saturation magnetization and the remanent magnetization are often very similar. This similarity is due to PMs' defining feature: the ability to hold magnetization in the absence of a magnetic field. This section gives remanent magnetization for PMs (or saturation magnetization if unavailable). Curie temperature is given (or a working temperature or close equivalent if unavailable).<sup>156,174,177</sup> The hard magnetic material families and properties are listed in Table 5.1 and compared in Figure 5.1.

The size of the circles in Figure 5.1 represents the magnitude of the energy product of the hard magnetic materials. Hard ferrites are represented in Figure 5.1 by  $\text{SrFe}_{12}\text{O}_{19}$ , one of the most common and widely used hard ferrites.<sup>75</sup>

Figure 5.1 and Table 5.1 reveal that only two materials have a larger energy product than NdFeB: the  $L1_0$  materials. Those nanoparticles have never been successfully created in bulk form and therefore have never been adopted for use in magnetic applications. The other alternative materials to the four mainstream magnets have energy densities much lower than that of NdFeB. Some of these alternative magnets use samarium, a less critical rare earth material than neodymium. The other alternative magnets do not use rare earth elements. The greatest advantage of these alternative magnets is that they do not rely on rare earth elements, meaning that a supply chain is easier to secure, and raw materials typically cost less, resulting in lower product prices. However, all the alternative magnets use some kind of critical material, as defined by the most recent critical materials list, but some are not rare earth elements and are much lower in criticality and market value. Consequently, these alternative materials have yet to displace the dominant four mainstream magnets. Furthermore, most of these alternative magnets can only be produced in thin films or particle form, not in bulk, making them impossible to use in magnetic applications. Figure 5.1 and Table 5.1 also show that NdFeB has the highest energy product of all four mainstream magnets, but also the lowest Curie temperature and a lower working temperature than the other mainstream magnets. Therefore, NdFeB is used for most applications that demand PMs of high magnetic strength. Of all the magnets listed here, AlNiCo and SmCo have the highest Curie temperatures, and SmCo has a higher energy product among all the magnets listed here. Thus for applications at higher temperature—quite common in electrical machine applications—SmCo is an alternative to NdFeB if the application demands high magnetic strength, and AlNiCo is used otherwise because

it is a much cheaper material. Hard ferrites have the lowest magnetic strength of all the mainstream magnets, but they are by far the cheapest materials. Thus, for everyday magnetic applications that do not demand high magnetic strength, hard ferrites are preferred. In fact, hard ferrites are the most utilized PM by weight demanded, while NdFeB is the most utilized PM by monetary value sold.<sup>12,113,177</sup>

Additively manufactured magnets must compete with NdFeB in magnetic quality or with hard ferrites in cost. The latter is unlikely: hard ferrites are already low in material price because they do not use expensive raw materials and are mass produced at high volumes. Furthermore, NdFeB's energy product is out of reach for most 3D printed magnets. Thus, AM research on PMs focuses on three major avenues: (1) competing with bonded NdFeB magnets with respect to high shape complexity, (2) reducing the amount of critical material within NdFeB, or (3) creating new types of NdFeB that have special properties that cannot be achieved via conventional methods.

### **5.3 On the Additive Manufacturing of Hard Magnets and the Material Properties of these Magnets**

Much work has already been done on the AM of PMs. This section explores the PMs that have been additively manufactured and laid the foundation for current work on 3D printed PMs.

#### **5.3.1 Beginning Steps**

This project began with using laser powder blown directed energy deposition to create NdFeB magnets. Magnetic properties were significantly reduced by the large fraction of new phases introduced by the AM process. The dramatic change in microstructure caused by the heat-based phase changes transformed the material into something resembling a soft magnet. At 35 kOe, the magnetization of the 3D printed material was 127.2 emu/g, whereas the feedstock isotropic powder reached only 113 emu/g. Despite this small improvement in saturation magnetization, the 3D



Table 5.1: Table of Hard Magnetic Material Families and Properties.

Material	Curie temperature (K)	Remanent magnetization (kG)	Energy product (MGOe)
NdFeB	585	16	56
SmCo	1190	12	34
AlNiCo	1260	14	7.2
Ferrite	723	3.85	5.2
SmFeN	749	15	14
Fe <sub>16</sub> N <sub>2</sub>	810	26.8	20
MnBi	633	9	16.3
Mn-Al(-C)	650	7.5	16.8
<b>L1<sub>0</sub>-FeNi</b>	820	16	56
<b>L1<sub>0</sub>-FeCo</b>	940	24	100
HfCo <sub>7</sub>	751	11.8	13.2
Zr <sub>2</sub> Co <sub>11</sub>	783	9.7	16.6
Co <sub>3</sub> C	510	2	2.51

Sources: 177-185

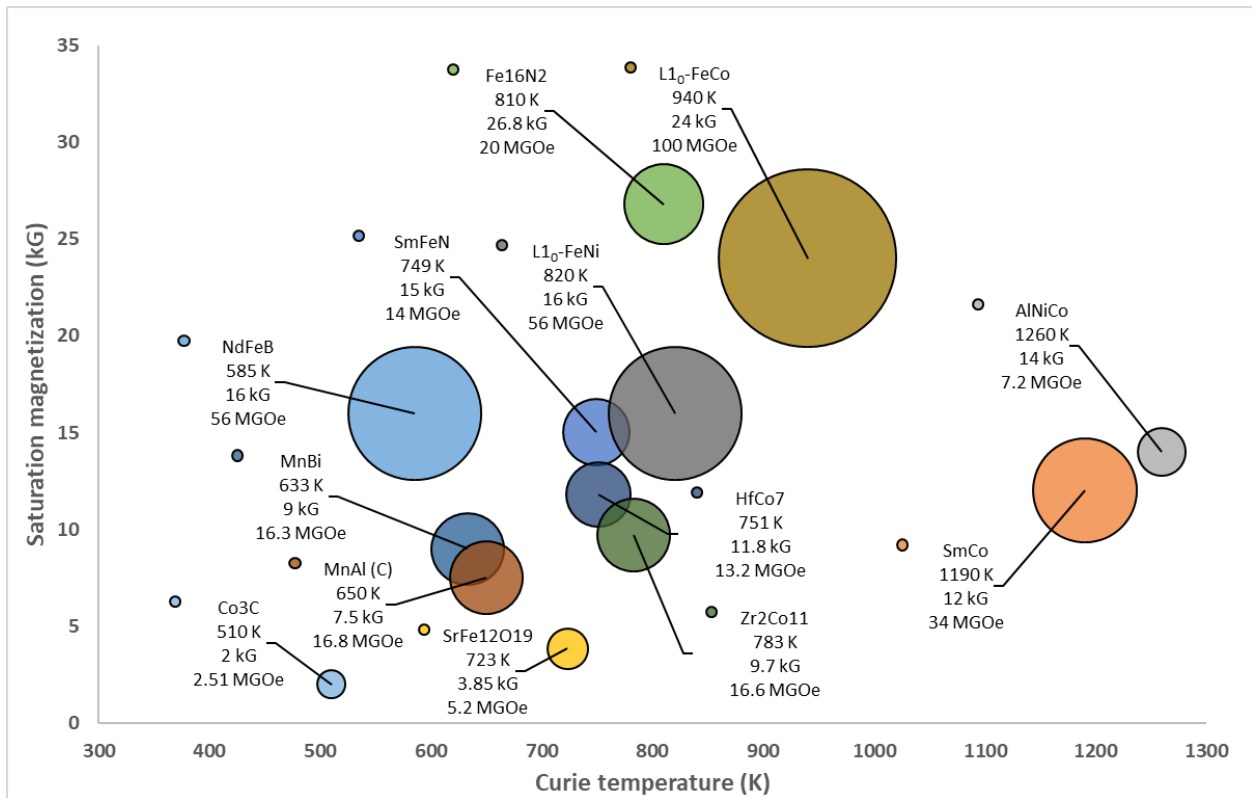


Figure 5.1: Plot of hard magnetic materials and their material properties.

printed material's coercivity collapsed to only 500 Oe, whereas the feedstock powder's coercivity was approximately 10,000 Oe. This report failed to state the density of the final product.<sup>186</sup> Assuming it was near the feedstock density of  $7.43 \text{ g/cm}^3$ , the saturation magnetization of the 3D printed material would be about 1.18 T, which is less than that of 6.5 wt% silicon steel ( $\sim 1.27 \text{ T}$ ). This material is unsuitable for soft magnetic use because of its unimpressive soft magnetic properties and because it requires critical materials such as neodymium, unlike silicon steel.<sup>186</sup>

### **5.3.2 Initial BAAM Permanent Magnets**

Subsequently, in 2016 BAAM was used to fabricate NdFeB/Nylon 12 composites. Magnetic and mechanical characterizations demonstrated that the BAAM-fabricated magnets can compete with or outperform conventional injection-molded magnets. The starting pellet compositions consisted of 65 vol% isotropic NdFeB powder and 35 vol% polyamide in the form of Nylon 12.<sup>123</sup> In 2017, this experiment was updated. The BAAM-fabricated magnets were coated with polymer-based coatings, yielding improved thermal stability. UTS increased with loading fraction of the magnet powder and decreased with temperature. BAAM was also shown provide extremely low eddy current loss and high resistivity. Electromotive force measurements for motors incorporating 3D printed NdFeB magnets exhibit similar performance to those with sintered ferrites.<sup>128</sup> The properties of the BAAM 3D printed magnets from these two studies are presented in Table 5.2. The data in Table 5.2 reveal that increasing the NdFeB content of the 3D printed bonded magnets yields noticeable improvements in the density, coercivity, remanence, and energy product. The closer the magnets get to full density, the higher those values will be.

### **5.3.3 Binder Jetting NdFeB Magnets with Low Melting Point Eutectic Alloy Infiltration**

In 2017, BJT was used to fabricate NdFeB magnets, which were then infiltrated by low-melting-point eutectic alloys. Resin-coated isotropic NdFeB powder was bound with aqueous solutions of diethylene glycol (DEG). The alloys were  $\text{Nd}_3\text{Cu}_{0.25}\text{Co}_{0.75}$  (NdCuCo) and  $\text{Pr}_3\text{Cu}_{0.25}\text{Co}_{0.75}$

Table 5.2: Material properties of the BAAM bonded NdFeB magnets.

<b>Material property</b>	<b>Initial feedstock (65 vol% isotropic NdFeB powder/35 vol% Nylon 12)</b>	<b>Revised product (70 vol% isotropic NdFeB powder/30 vol% Nylon 12)</b>
Density	4.8 g/cm <sup>3</sup>	5.15 g/cm <sup>3</sup>
Intrinsic coercivity	688.4 kA/m	708.2 kA/m
	8,650.7 Oe	8,900 Oe
Remanence	0.51 T	0.58 T
		5,800 G
Energy product	43.49 kJ/m <sup>3</sup>	58.1 kJ/m <sup>3</sup>
	5.47 MGOe	7.3 MGOe
Ultimate tensile strength	6.60 MPa	10 MPa
Average failure strain	4.18%	3%

Source: <sup>123,128</sup>

(PrCuCo). The weight ratio of the infiltration alloy to the magnet is approximately 0.46. The infiltration improved the mechanical strength and increased the density of the BJT magnets. Coercivity was also dramatically enhanced. The intrinsic coercivity of the printed sample was enhanced from 732 to 1,345 kA/m (an approximate 83.7% increase) and 1,233 kA/m (an approximate 68.5% increase) after diffusion of NdCuCo and PrCuCo, respectively, at an expense of remanence reduction from 0.35 to 0.31 T (NdCuCo) and 0.25 T (PrCuCo). A high quantity of the eutectic alloys were in the final product, but such alloys are not ferromagnetic, and thus do not contribute to the net magnetization. Therefore, remanence and magnetization are both reduced after infiltration. Infiltration with ferromagnetic alloys could be a fascinating future avenue of research.<sup>140,187</sup> The density and magnetic properties of the as-printed sample and the infiltrated samples are presented in Table 5.3.

Table 5.3 shows that infiltration increased the density, but magnetization did not increase along with it. Magnetic properties can only increase with density if the reason for the increase in density is the increased magnetic material content. Nevertheless, coercivity dramatically increased. The BJT NdFeB magnet is very hard and difficult to magnetize/demagnetize; however, its magnetic strength is not very high.

### **5.3.4 Initial Experiments on Bimodal Powder BAAM Magnets**

In 2018, BAAM was used to print anisotropic hybrid NdFeB–SmFeN nylon-composite bonded magnets. These magnets comprised 65 vol% Magfine anisotropic composite dysprosium-free NdFeB and SmFeN mixed powders and 35 vol% Nylon 12. Post-print alignment in magnetic field can tune the magnetic properties of the bonded magnet without impairing the shape of the printed magnet. Remanence and energy product can both be improved via magnetic alignment. The SmFeN powders were chosen because they show good hard magnetic properties and high oxidation resistance. The SmFeN powders exhibit good saturation magnetization (1.54–1.57 T),

Table 5.3: Material properties of the BJT NdFeB and its alloy-infiltrated variants.

Sample	Density (g/cm <sup>3</sup> )	Intrinsic coercivity (kA/m) / (Oe)	Remanence (T)	Magnetization at 4 T (T)
As Printed	3.3	732	0.35	0.53
		9,198.6		
NdCuCo	4.3	1345	0.31	0.5
		16,901.8		
PrCuCo	4.3	1,233	0.25	0.39
		15,494.3		

Source: <sup>140</sup>

Table 5.4: Magnetic properties of as-printed and post-aligned BAAM NdFeB and SmFeN hybrid bonded magnets.

Sample	Coercivity (kOe)	Remanence (kG)	Energy Product (MGOe)
As-Printed	10.8	3.7	2.8
		0.37 (T)	
Post-Alignment	11	7.2	11.0
		0.72 (T)	

Source: <sup>188</sup>

high anisotropy field (14 T), and impressive Curie temperature (750 K). The SmFeN powders are available at much smaller particle sizes and lower powder diameters than the NdFeB powder particles. Consequently, the fine SmFeN particles fill in the voids between the larger NdFeB particles, thereby improving the density of the magnets and increasing the magnetic material content of the magnet, which improves its magnetic properties. Combining two magnet powders of vastly different particle diameters in AM is termed bimodal powder 3D printing.<sup>188</sup> The magnetic properties of the as-printed magnet as well the post magnetic field alignment magnet are presented in Table 5.4.

Table 5.4 shows that the magnetic alignment dramatically boosts the remanence as well as the energy product of the magnet. The coercivity also improved slightly. Comparing Tables 5.2 and 5.4 reveals that even the as-printed hybrid magnet has higher coercivity than the NdFeB-only BAAM magnets. Once the hybrid magnets are fully aligned magnetically, their remanence and energy product far exceed that of the NdFeB-only BAAM magnets. Therefore, the bimodal packing of two types of magnet powders improves the magnetic properties of the 3D printed magnet. However, the bimodal magnets are made from anisotropic magnet powders, whereas the 3D printed magnets are made from isotropic magnet powders. Anisotropic powders tend to create better magnets than isotropic powders, so the results are not conclusive because the bimodal magnet's magnetic properties are not impressive compared with other anisotropic 3D printed magnets. Nevertheless, this initial result is promising, and future bimodal magnets will be much more impressive.

### **5.3.5 Initial Anisotropic BAAM Magnets**

In 2019, BAAM anisotropic nylon-bonded NdFeB magnets were demonstrated to be viable for PM motors, allowing up to 40% reduction in critical material when replacing conventional isotropic PMs in this application. The 3D printed magnet material in this case was composed of

65 vol% NdFeB and 35 vol% Nylon 12. The motor in this case was a 20 W brushless direct current (DC) surface PM motor. The study demonstrated sufficient alignment of anisotropic bonded magnets for PM motor applications at applied magnetic fields as low as 0.25 T. This work illustrated the economic potential of employing magnetic alignment for 3D printed bonded NdFeB magnets as well as the potential of using aligned anisotropic bonded magnets to address the criticality of rare earth and strategic materials.<sup>189</sup>

### **5.3.6 Recycling of BAAM Magnets**

In 2019, recycling of BAAM printed magnets was successfully demonstrated. The process is mechanical rather than chemical. Remanent magnetization and saturation magnetization can be slightly improved compared with the original BAAM magnets via this method. The initial 3D printed magnets contained 65 vol% isotropic NdFeB powder and 35 vol% Nylon 12. The 3D printed bonded NdFeB magnets were cryomilled at liquid nitrogen temperatures ( $-196^{\circ}\text{C}$ ) for 30 min. This process rapidly pulverizes the bonded magnets into composite powder containing NdFeB particles and polymer binder powder. After cryomilling, the powder mixture was compression molded at  $200^{\circ}\text{C}$  and 10 MPa uniaxial pressure.<sup>39</sup> The material properties of the starting 3D printed bonded magnet, the cryomilled powder, and the recycled bonded magnet are listed in Table 5.6.

The data in Table 5.5 show that the magnetic properties of the material before and after cryomilling change only slightly. Both remanence and saturation magnetization improved slightly, possibly owing to the slight increase in density enabled by CM. However, the energy product did not change and coercivity decreased slightly. Because cryomilling does not affect the material properties of the magnetic material, it is possible to recycle bonded 3D printed magnets. Furthermore, the recycled magnet's compressive strength was 85.4 MPa. This result is comparable to commercially available compression-bonded NdFeB, which has compression strength in the range of 80 to 120

Table 5.5: Material properties of the starting BAAM magnets, the cryomilled powder, and the recycled bonded magnet.

<b>Magnet type</b>	<b><math>B_r</math> (kG)</b>	<b><math>M_s</math> (kG)</b>	<b><math>H_c</math> (kOe)</b>	<b><math>(BH)_{max}</math> (MGOe)</b>	<b>Density (g/cm<sup>3</sup>)</b>
<b>Starting BAAM Bonded magnet</b>	5.2	7.5	8.8	5.7	4.8
<b>Cryomilled powder</b>	4.9	7.5	8.5	-	-
<b>Recycled bonded magnet</b>	5.4	8.0	8.2	5.7	5.1

Source: <sup>39</sup>



MPa. The recycling process also did not affect the magnet material's mechanical properties. Although bonded AM processes such as BAAM produce little to no waste during production, some waste could be produced during the pre-print purging process. Moreover, the printed magnet, like any product, has a life cycle of use; at the end of life, the battery would have been disposed of as waste. This work enables recycling these wastes, thereby reducing the criticality of rare earth materials. This recycling process did not use any harsh chemicals, nor does it require an inert atmosphere. Thus, the recycling process is eco-friendly in addition to ensuring sustainability in materials for PM production.

### **5.3.7 High Mechanical Strength PPS BAAM Magnets**

In 2020, isotropic NdFeB PPS-bonded PMs were successfully created by the BAAM process. The PPS magnets have nearly double the mechanical strength of nylon magnets. When coated with a resin protective coating, the high temperature stability as well as the corrosion resistance improved over the nylon BAAM magnet. The magnetic properties are also an improvement over the nylon magnets: little degradation in magnetic properties occurs during the BAAM process. The composition of magnets are approximately 63 vol% isotropic NdFeB powders and 37 vol% PPS.<sup>125</sup> The magnetic properties and density of the 3D printed NdFeB-PPS bonded PM are presented in Table 5.6.

Experiments revealed that protective resin coatings can reduce the flux loss of 3D printed PMs at high temperatures and limit such flux loss to under 4% at 175°C and under 9% at 200°C. This capability is beneficial because NdFeB is limited in its working temperature by its low Curie temperature, whereas most efficient electrical machine applications favor higher working temperatures for the magnet. Increasing the working temperature of PMs allows them to be used in more efficient electrical machine applications. Experiments also demonstrated that the protective resin coatings can protect the 3D printed magnets from corrosion from both highly

acidic (pH 1.35) and high-humidity (95% relative humidity) conditions. The 3D printed magnets without such coatings suffered dramatic decreases in magnetic properties after being in such adverse environments, whereas 3D printed magnets with the coatings barely experienced any decrease.<sup>125</sup> The mechanical properties of such BAAM NdFeB PPS magnets were also measured and are presented in Table 5.7.

The data in Table 5.7 show that the mechanical properties of the PPS 3D printed magnets are much stronger than that of the Nylon 12 3D printed magnets. (See table 5.2 for the material properties of the Nylon 12 3D printed magnets.) In fact, the PPS 3D printed magnets' tensile strength is twice that of Nylon 12 3D printed magnets. Thus, PPS is an attractive binding polymer for binder-based AM systems, allowing for better mechanical properties in BAAM magnets and enabling the use of such magnets in more mechanically demanding applications.<sup>125,128</sup>

### **5.3.8 Anisotropic BAAM Magnets with Magnetic Field Alignment**

In 2020, BAAM was used to print NdFeB magnets. A high loading fraction was achieved (>70 vol%). The printed magnets exhibited better thermal stability and superior magnetic properties compared with commercial injection-molded magnets. The magnet feedstock composite pellets comprised 70 vol% Magnequench anisotropic (MQA) powder and 30 vol% Nylon 12. Some of the BAAM printed magnets were post-aligned in magnetic fields of different magnitudes. The magnet aligned at 2.0 T had the highest energy product of all the magnets in this work.<sup>124</sup> The magnetic properties of the as-printed magnet and the magnet aligned at 2.0 T are presented in Table 5.8. These data show that magnetic field alignment improved the properties of the 3D printed magnet—significantly so for remanence and energy product. High density owing to increased magnetic material content and magnetic field alignment are responsible for this outcome.<sup>124</sup> The magnetic properties of the 3D printed magnet and its commercial equivalent were also compared.

Table 5.6: Material properties of the BAAM NdFeB-PPS bonded permanent magnet.

<b>Material property</b>	<b>Value</b>
Residual magnetization (kG)	5.0
Saturation magnetization (kG)	7.3
Coercivity (kOe)	11.4
Energy product (MGOe)	5.4
Density (g/cm <sup>3</sup> )	4.85

Source: <sup>125</sup>

Table 5.7: Mechanical properties of BAAM NdFeB PPS permanent magnets.

<b>Material property</b>	<b>Value</b>
Tensile strength (MPa)	20.37
Tensile strain (%)	0.09
Young's modulus (GPa)	21.53

Source: <sup>125</sup>

The magnetic properties of a 54 vol% NdFeB injection-molded in PPS magnet and of a BAAM printed 70 vol% NdFeB in Nylon-12 magnet are listed in Table 5.9. The BAAM printed magnet was magnetically aligned at approximately 2 T.<sup>124</sup> These data show that the high-density BAAM magnet has significantly higher remanence and energy product values than that of its commercial injection-molded equivalent. The BAAM magnet's coercivity is less than that of the commercial magnet, but the difference is negligible: BAAM magnets can already compete with certain commercial magnets in magnetic performance and applications.<sup>124</sup>

The mechanical properties of these BAAM magnets were also measured and are listed in Table 5.10. These data show that the high-density BAAM NdFeB magnet's tensile stress is slightly less than that of the PPS BAAM NdFeB magnet (20.37 MPa), but it is much more than that of the less-dense BAAM NdFeB magnet (10 MPa). Mechanical properties improved with density increased by NdFeB content.<sup>124,125,128</sup>

### **5.3.9 Printing Bimodal and Recycled Magnets with Magnetic Field Alignment**

In 2020, the integration of a magnetic field during the AM process was demonstrated and verified to result in the magnetic alignment of the magnetic particles while ensuring the other advantages of AM are retained. Two types of composite magnetic material were successfully printed. The first material is 65 vol% anisotropic NdFeB and SmFeN powder mixtures bonded in Nylon 12. The second material is 15 vol% recycled SmCo powder bonded in PLA. An electromagnet field source device was installed into a fused-filament commercial 3D printer. This device is responsible for the in situ alignment of the magnetic particles during printing. The concept of in situ alignment mechanism for additively manufactured magnets is based on the rotation of magnetic particles within the nozzle of an AM machine as the result of an applied magnetic field. Magnetic characterization after printing indicates that the extent of alignment of the magnetic material powders increased with both the alignment field strength and the printing temperature. Coercivity

Table 5.8: Magnetic properties of the as-printed magnet and the 2.0 T aligned magnet.

<b>Alignment Field</b>	<b>Remanence</b>	<b>Coercivity</b>	<b>Energy product</b>
As-printed	0.48 T	962.88 kA/m	35 kJ/m <sup>3</sup>
	4800 G	12099.9 Oe	4.398 MGOe
2.0 T	0.98 T	978.8 kA/m	148.81 kJ/m <sup>3</sup>
	9800 G	12300.0 Oe	18.7 MGOe

Source: <sup>124</sup>

Table 5.9: Magnetic properties of the high-density aligned BAAM magnets and its injection-molded commercial equivalent.

<b>Material property</b>	<b>Unit</b>	<b>MQA-38-14 NdFeB, injection-molded, 54 vol% NdFeB, in PPS</b>	<b>MQA-38-14 NdFeB, BAAM printed, 70 vol% NdFeB, in Nylon-12</b>
<b>Remanence</b>	T	0.635	0.94
	kG	6.35	9.4
<b>Coercivity</b>	kA/m	1082.2	1034.5
	kOe	13.6	13
<b>Energy product</b>	kJ/m <sup>3</sup>	70.0	140.0
	MGOe	8.796	17.593

Source: <sup>124</sup>

Table 5.10: Mechanical properties of the high-density BAAM NdFeB magnet.

<b>Sample</b>	<b>Max load</b>	<b>Max stress</b>
<b>Sample 1</b>	41.06 N	14.77 MPa
<b>Sample 2</b>	39.68 N	14.28 MPa
<b>Sample 3</b>	36.48 N	13.12 MPa
<b>Sample 4</b>	36.34 N	13.08 MPa
<b>Average</b>	38.39 N	13.81 MPa

Source: <sup>124</sup>

and remanence were both found to strongly depend on degree of alignment, with the exception being printing performed at below but near the Curie temperature. High temperatures near or above the Curie point severely damage the microstructure of the material responsible for magnetic properties. Under an applied magnetic field of 0.15 kOe, the SmCo sample achieved 83% degree of alignment, while the NdFeB/SmFeN hybrid magnet was able to obtain 65% degree of alignment. The magnetic alignment produced magnetic anisotropy in the printed magnet and is reflected in the coercivity values of the magnet. For example, the anisotropic SmCo PLA composite magnet was measured to have 12.2 kOe. The aligned version of this magnet is measured to have 9.3 kOe if measured parallel to the direction of alignment and 13.2 kOe if measured perpendicular to the direction of alignment.<sup>190</sup>

#### **5.3.10 Mathematical Model on Degree of Alignment of the Magnetic Field Alignment of 3D Printed Magnets**

A mathematical framework and multiphysics model on the phenomenon of the degree of alignment in an in situ aligned 3D printed bonded magnet was successfully developed in 2021. This model can predict the degree of magnetic alignment in an in situ aligned 3D printed bonded magnet. The multiphysics model was developed to simulate the alignment of magnetic particles in the presence of an externally applied field for a 3D printed magnetic sample. This simulation predicts the particle distribution and the degree of alignment of the magnetic particles based on the magnetic and hydrodynamic interactions of the magnetic material particles with the molten polymer matrix under an applied magnetic field. The model made several fascinating predictions. One such prediction was that the contribution of the magnetophoretic force is insignificant compared with the drag force experienced by the particle in the flow, resulting in no significant nonuniformity in the particle distribution. Magnetophoresis is the motion induced by a magnetic field on a magnetizable particle in a fluid. Magnetospheric force is the force causing such a motion. Another

prediction is that the degree of alignment of the particles within the magnet increases with the magnetic field strength because of the larger magnetic torque. The model also predicted the effects of the loading fraction on the degree of alignment. Increasing the loading fraction reduces the overall alignment for very high and very low alignment field owing to the repulsion between the nearest neighbors. However, at moderate fields, an increase in alignment was observed to a maximum, followed by a decay, owing to particle-to-particle interactions. These interactions accentuated the effects of the magnetic torque at low loading fractions and attenuated the effects of the magnetic torque at high loading fractions. The printing speed was predicted to have an inverse effect on the degree of alignment because of the reduced exposure time of the particles in the external magnetic field. The alignment model was validated against experimental measurements and was found to be within 8% of measured data. This model can be used to optimize the parameters of the 3D printers to produce 3D printed bonded magnets with the maximum degree of alignment, thus ensuring that magnets with the best magnetic properties are produced.<sup>191,192</sup> The experimental and model data for the degree of alignment of 3D printed magnets before and after alignment under magnetic field are presented in Table 5.11. M1 refers to NdFeB and SmFeN bonded in Nylon 12, and M2 refers to SmCo in PLA.

### **5.3.11 BAAM Halbach Arrays**

In 2021, BAAM produced PPS-bonded NdFeB magnets that were used to produce concentric Halbach array rings. Halbach arrays are a special arrangement of PMs that augments the magnetic field on one side of the array while cancelling the field to near zero on the other side. Such arrays are very efficient closed structures for generating directed magnetic fields and gradients. They are widely used in numerous electrical machine applications. The 3D printed magnet in this case was 63 vol% NdFeB and 37 vol% PPS, manufactured via BAAM. The magnet was manufactured into a disk shape, sliced into eight equal segments, and magnetized based on the orientation needed for

the Halbach array. After magnetization, the pieces were assembled into the Halbach array. Concentric Halbach rings are made this way for polarized neutron reflectometry applications. The Halbach rings could generate a magnetic field between 0 and 0.3 T while preserving 90% polarization of the axial neutron beam.<sup>193,194</sup> This study demonstrates another application for 3D printed magnets: AM could produce Halbach magnets faster and cheaper than conventional subtractive machining.

### **5.3.12 Optimizing Feedstock: Increased Magnetic Material Loading via Premixing**

In 2021, CM of anisotropic NdFeB magnets in a polycarbonate (PC) matrix was successfully achieved. By using a lab-scale batch mixer for melt processing and compounding, followed by CM, weight fraction of NdFeB in PC of up to 95% can be achieved. The 95 wt% NdFeB magnet exhibits excellent magnetic and tensile properties. Its intrinsic coercivity is 942.99 kA/m, its remanence is 0.86 T, and its energy product is 120.96 kJ/m<sup>3</sup>.<sup>195</sup> Although CM is not AM, this extrusion-based process is similar to BAAM and could be adapted for AM-related work in the future and employed to produce 3D printed magnets of higher density and better magnetic and mechanical properties. The 95 wt% NdFeB magnet's material properties are presented in Table 5.12. SEM images of the PC bonded NdFeB magnet are presented in Figures 5.2 through 5.5.

Improving AM does not necessarily mean improving what happens during the process itself; sometimes improvement can be achieved before the process even begins by optimizing the feedstock material. The term premixing refers to the mixing of raw materials into the AM feedstock before mixing is done on any AM machine that has the capability to mix its feedstock (e.g., the extruder in BAAM). The premixed PC–NdFeB here has superior magnetic properties than anything previously used in this project for BAAM and will produce BAAM magnets of even greater magnetic quality.



### **5.3.13 Optimizing Feedstock: Bimodal Powder Mixing for Higher Packing Density**

The previous premixing technique could be modified to use on bimodal powders. A mixture of 60 vol% anisotropic NdFeB and 40 vol% anisotropic SmFeN powders was chosen. The particle diameter of the SmFeN powder is much smaller than that of NdFeB powder, enabling bimodal packing. These magnetic materials totaled 96 wt% of the overall bonded magnet. The remaining 4 wt% came from PPS pellets. These raw materials were batch mixed, screw extruded, and then compression molded. After CM, the magnets were magnetically aligned under a magnetic field. This process yielded a hybrid bonded magnet with an 81 vol% magnet loading fraction and a density of 6.15 g/cm<sup>3</sup>. The bimodal bonded magnet has excellent magnetic properties. Its remanence is 10,500 G. Its coercivity is 10,820 Oe. Its energy product is 20.0 MGOe. This bimodal magnet has the best magnetic properties ever obtained during this project. This material could be used as feedstock to create 3D printed magnets of great magnetic quality.<sup>196</sup>

## **5.4 The Eddy Current Behavior, Working Temperatures, and Material Properties Summary of the 3D Printed Permanent Magnets**

### **5.4.1 On Electrical Resistivity and Eddy Current Behavior of 3D Printed Permanent Magnets**

Core loss, or iron loss, refers to the total energy dissipation in the ferromagnetic core of an inductor or transformer. It is the energy loss in the core of electrical machines. It is the energy lost from the core when the core is subjected to a changing magnetic field, such as from AC. Core loss primarily comprises two types of energy loss: the eddy current loss and the magnetic hysteresis loss.<sup>111</sup> Hysteresis loss is the energy dissipated from a ferromagnetic material in one complete magnetization cycle when it is subjected to an alternating magnetic field. This form of loss usually comes in the form of heat. Hysteresis loss results from the change in the direction of the magnetizing field. This change in direction forces the molecules within the magnetic material to

Table 5.11: Model prediction and experimental data of the degree of alignment of 3D printed bonded magnets.

<b>Degree of alignment</b>	<b>Experimental</b>		<b>Model</b>	
	M1	M2	M1	M2
Pre-alignment	55.0%	66.0%	56.8%	63.2%
Post-alignment	63.0%	83.0%	63.6%	86.2%

Source: <sup>191</sup>

Table 5.12: Material Properties of 95 wt% NdFeB Compression-Molded Magnet

<b>Material property</b>	<b>Value</b>
<b>Magnetic loading fraction</b>	95%
<b>Density</b>	5.34 g/cm <sup>3</sup>
<b>Young's modulus</b>	43.91 GPa
<b>Intrinsic coercivity</b>	942.99 kA/m
	11.85 kOe
<b>Remanence</b>	0.86 T
	8.6 kG
<b>Energy product</b>	120.96 kJ/m <sup>3</sup>
	15.2 MGOe

Source: <sup>195</sup>

Sample No. 66: MQA-PC, Surface

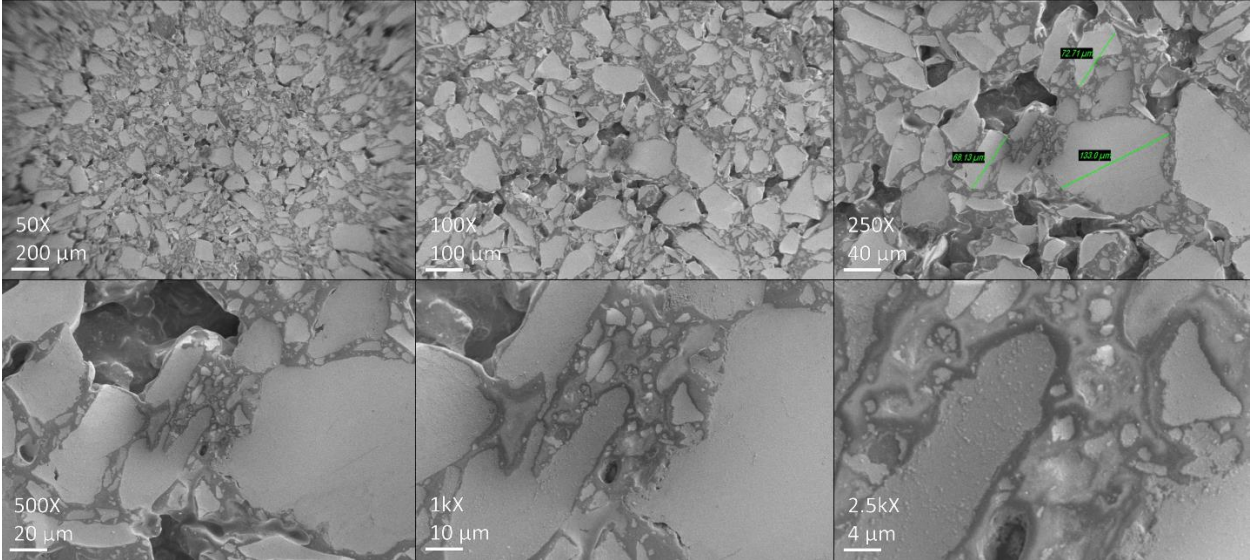


Figure 5.2. Sample 66: MQA-PC, surface.

Sample No. 66: MQA-PC, Surface

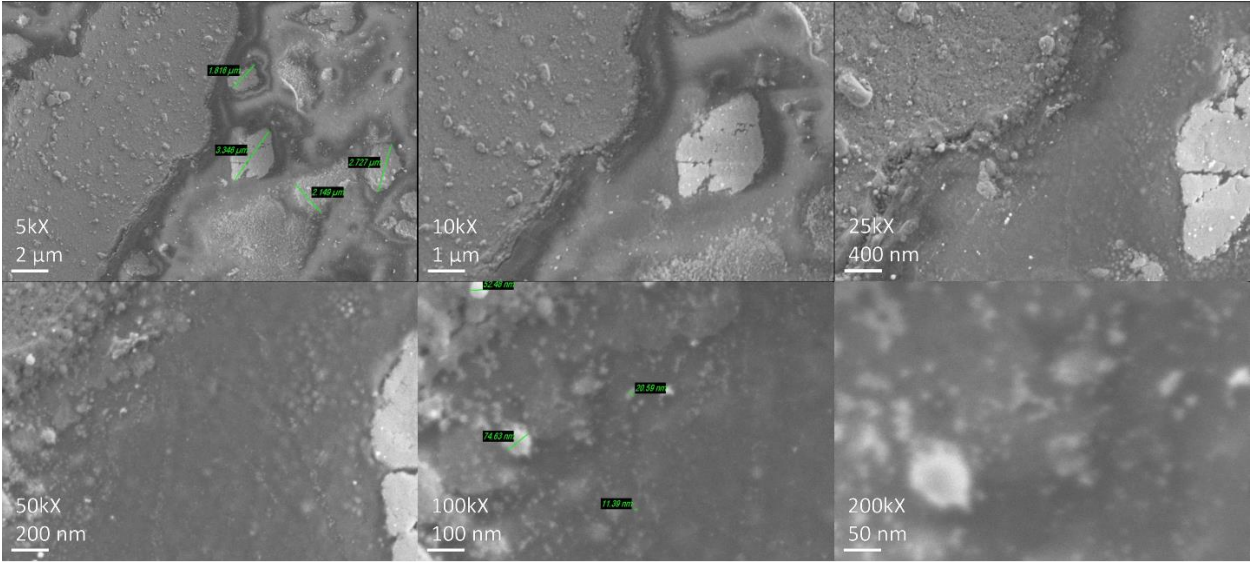


Figure 5.3. Sample 66: MQA-PC, surface.

### Sample No. 67: MQA-PC, Cross Section

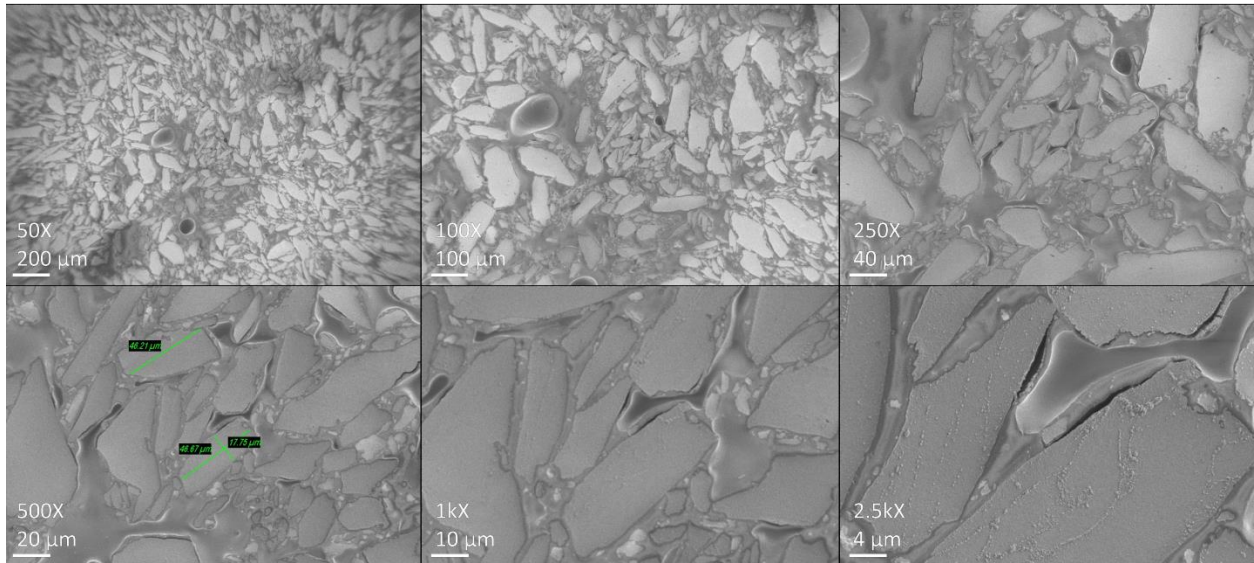


Figure 5.4. Sample 67: MQA-PC, cross section.

### Sample No. 67: MQA-PC, Cross Section

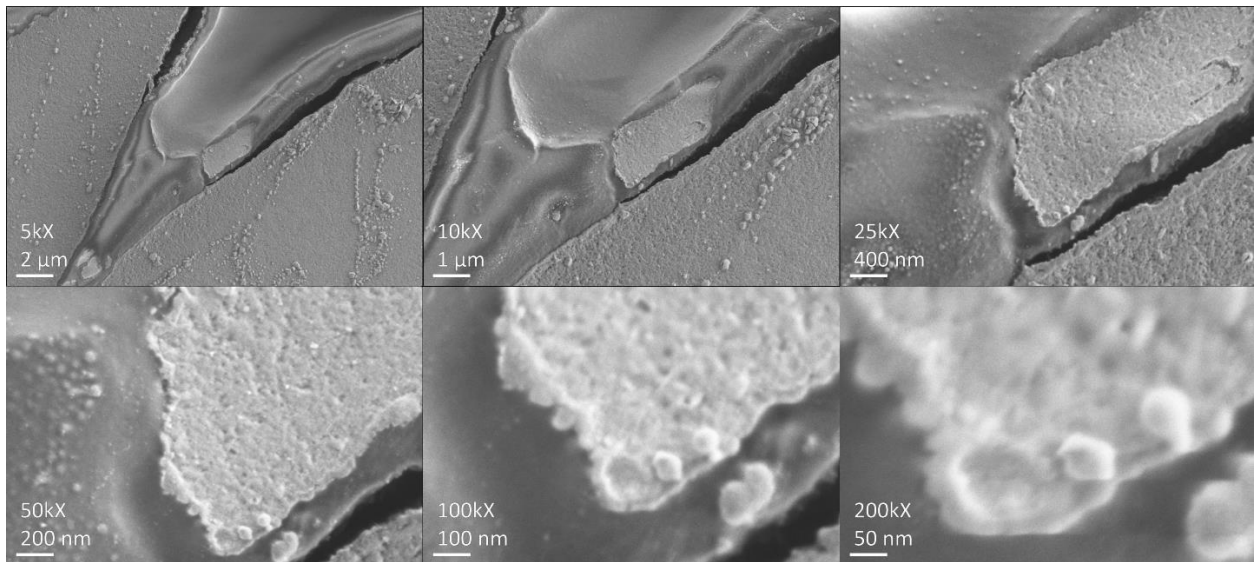


Figure 5.5. Sample 67: MQA-PC, cross section.

reorient to align with the new field direction. During this process, these molecules often collide with each other, causing friction and heat, which cause hysteresis loss.<sup>85</sup> Eddy current loss is energy dissipated by eddy currents and usually comes in the form of heat. Eddy currents are electric currents that are induced when a conductor is subjected to a varying magnetic field. Eddies are the loops of electric currents induced in the conductor by the magnetic field. Eddy currents are induced whenever relative motion occurs between the magnetic field and the conductor. Eddy currents flow in circular loops within the conductor, perpendicular to the magnetic field. Len's law states that the direction of the electric current induced in a conductor by a changing magnetic field is such that the magnetic field created by the induced current opposes changes in the initial magnetic field. Thus, the induced eddy currents generate a magnetic field that counters the initial magnetic field of the magnet. Consequently, the conductor produces a drag force on the magnet owing to the interaction of the two fields. Kinetic energy is consumed to overcome this drag force and is dissipated as heat by the currents flowing through the resistance of the conductor, and this loss of energy as heat is the eddy current loss. Thus, eddy current loss is the result of interactions between the conductor and the magnetic field.<sup>197-202</sup> Therefore, core loss can be thought of as a measure of the heat generated within the material as a result of AC. High core losses reduce the overall efficiency of the electrical machine and should be mitigated and minimized to improve efficiency. Eddy current loss can be mitigated. Eddy current loss depends on many factors. Eddy current loss is proportional to the square of the thickness of the lamination and is inversely proportional to the electrical resistivity of the magnetic material. Consequently, two methods can reduce the energy loss from eddy currents. One method is to decrease the thickness of the lamination. In electrical machine applications, decrease is usually accomplished by splitting the core through lamination. The core is cut into multiple thin sheets insulated from each other. This process transforms the

thick core magnet into many thinner magnets. The other method is to increase the electrical resistivity of the core. Electrical resistivity is a fundamental material property, so this method involves replacing magnetic materials in the core with new types of material that have higher electrical resistivity.<sup>199,203–206</sup>

AM can create magnets that lose less energy from eddy currents. Creating 3D printed bonded magnets involves mixing magnetic particles within a polymer material. The polymer itself is not magnetic and is not conductive. This mixing diminishes the magnet properties of the 3D printed bonded magnet. However, a great portion of the bonded magnet is nonconductive polymer, so the overall bonded magnet material has greater electrical resistivity than that of a fully dense sintered magnet made of the same magnetic material. Thus, 3D printed bonded magnets have much lower eddy current loss and higher energy conversion efficiency than sintered magnets. These bonded magnets are suitable for electrical machine applications that have a lesser demand for magnetic performance and a greater emphasis on energy efficiency.<sup>128</sup>

The capability of 3D printed magnets to have lower eddy current loss is demonstrated by magnetic susceptibility measurements. Such testing indicates that BAAM bonded isotropic NdFeB magnets has a much lower eddy current energy loss than sintered anisotropic NdFeB magnets. The eddy current loss of the BAAM magnet remained near zero even at high frequencies, whereas the sintered magnet exhibited much higher eddy current loss at low frequencies. These losses increased near linearly with increased frequency. The energy product of the magnet is sacrificed by incorporating nonmagnetic polymer binder. However, the reduced eddy current loss yields higher energy efficiency, thereby enabling weight reduction for the application, which is very important in many electrical machine applications, such as for automotive motors.<sup>128</sup>

The choice of the polymer binder material significantly affects the capability of the 3D printed magnet to mitigate eddy current loss. Eddy current losses are inversely proportional to the electrical resistivity: higher resistivity implies lower energy losses from eddy currents. Table 5.13 lists the electrical resistivity of a state-of-the-art commercial sintered NdFeB and 3D printed versions.<sup>125,128</sup>

The data in Table 5.13 show that the PPS BAAM magnet has much greater resistivity than the Nylon 12 BAAM magnet, and both are better than the commercial sintered magnet. PPS BAAM magnets have much lower eddy current losses than Nylon 12 BAAM magnets, which are already lower than those of the sintered magnet. Eddy current loss is also proportional to the AC magnetic loss fraction  $M''/M'$ , where  $M''$  is the imaginary part of the magnetization, and  $M'$  is the real part of the magnetization. The loss fractions of the sintered and 3D printed magnets have been measured at a wide range of frequencies; the result is illustrated by Figure 5.6.<sup>125</sup>

Both 3D printed magnets have loss fractions of less than 1%, whereas that of the sintered magnet ranges from 15% to 20%. The 3D printed magnets have much better eddy current loss mitigation capabilities than the sintered magnets. Because the Nylon 12 magnet already has a very low loss fraction, the difference between it and the PPS magnet is apparent in Figure 5.6.<sup>125</sup>

#### **5.4.2 On Flux Loss Behavior of 3D Printed Permanent Magnets and the Influence of Coatings**

The Curie temperature is the temperature above which ferromagnetic materials become paramagnetic materials and lose their ferromagnetic properties. A material's permanent magnetic properties are completely destroyed at the Curie temperature. Usually, a PM's magnetic properties are severely degraded well before its Curie point is reached; therefore, PMs usually have working temperatures well below their Curie temperature. Electrical machine applications often require working environments of elevated temperatures, and thus the magnet's working



Table 5.13: Electrical resistivity of conventional and 3D printed magnets.

Material	Electrical resistivity ( $\text{m}\Omega\cdot\text{cm}$ )
Sintered NdFeB	0.15
BAAM isotropic NdFeB + Nylon 12	170
BAAM isotropic NdFeB + PPS	2,580

Source: <sup>125,128</sup>

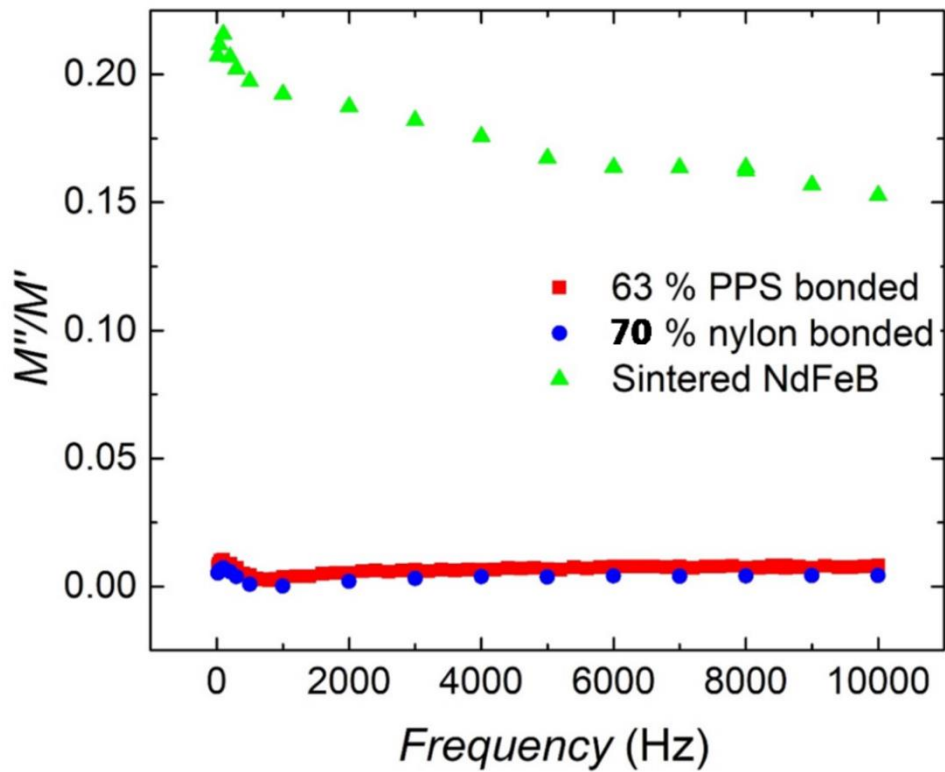


Figure 5.6: AC loss fraction of sintered and 3D printed magnets.<sup>125</sup>



temperature limits the number of applications it can serve. Furthermore, design limitations on the temperature environment of electrical machine applications often hamper their efficiency. Thus, the thermal stability of PMs is very important. Flux loss (%) can be used to evaluate the environmental stability of magnets. Flux loss is defined as the change in flux density of the material before and after the material experiences a certain duration of elevated temperature exposure, as a percentage of the value of the initial flux density of the material before temperature exposure. In other words, flux loss is  $100\% \times (B_f - B_i)/B_i$ , where  $B_f$  is the flux density of the material after a certain duration of elevated temperature exposure, and  $B_i$  is the initial flux density of the material before such exposure. The flux loss behavior of BAAM NdFeB magnets has been measured, and is presented in Figure 5.7.<sup>123</sup>

Figure 5.7 shows that the BAAM magnet remains quite stable at 350 K. It can endure long durations at that temperature with very small flux loss. At 400 K, the magnet can still endure for quite a long time without major changes in magnetic properties, with flux loss between 5% and 7%. However, major decrease in magnetic properties starts to occur when the aging time nears 1,000 h. At 450 K, flux loss is large at the start, and magnetic properties decrease rapidly with time. The flux losses of the BAAM magnet after 200 h exposure at 350 K, 400 K, and 450 K, are 2.3%, 7.1%, and 13.3%, respectively. Thus, the working temperature of the BAAM magnets is between 350 and 400 K. Another study demonstrated that, for 70 vol% NdFeB BAAM magnets, the temperature coefficients of the remanence, the intrinsic coercivity, and the energy product, are  $-0.18\%/^{\circ}\text{C}$ ,  $-0.33\%/^{\circ}\text{C}$ , and  $-0.36\%/^{\circ}\text{C}$ , respectively.<sup>128</sup> The magnetic properties of unprotected BAAM magnets decrease with increasing temperature.

This loss of magnetic properties from increased temperatures can be mitigated by coating the BAAM magnets with protective materials. Figure 5.8 shows the flux loss behavior of BAAM

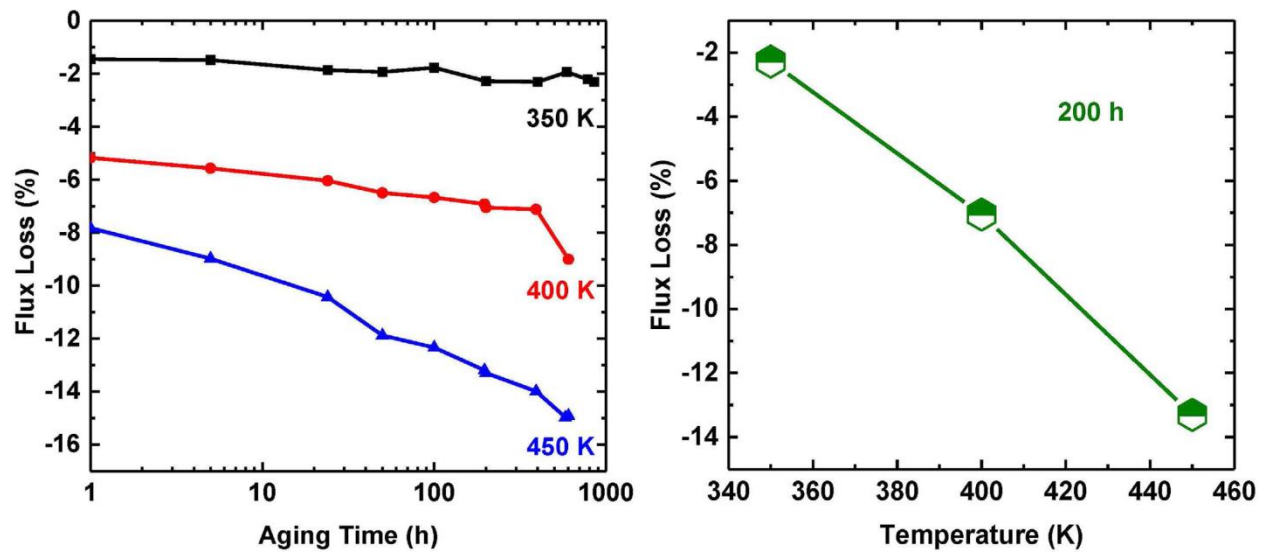


Figure 5.7: Flux loss behavior of BAAM NdFeB Nylon 12 bonded magnets.<sup>123</sup>

magnets with and without protective coatings. Process I denotes the BAAM magnet coated with a 3M Scotch-Weld DP100 two-part epoxy. Process II denotes the BAAM magnet coated with a VHT high-temperature silica ceramic coating.<sup>128</sup> Both coatings successfully mitigate the BAAM magnets' loss of magnetic properties from increasing temperatures. Without protective coating, the BAAM magnet exceeds 5% flux loss at 127°C (400.15 K). Process I prevented the BAAM magnet from reaching 5% flux loss at that temperature, and process II mitigated the flux loss to around 5%. The working temperature of such BAAM magnets without coating is 102°C (375.15 K), whereas coating increases the working temperature to around 127°C (400.15 K).<sup>128</sup>

The flux loss of BAAM magnets could be further improved by changing the binder polymer material. PPS offers much better thermal protection than Nylon 12. BAAM-fabricated NdFeB PPS-bonded PMs were heated to various temperatures with and without coating, and their magnetic flux was measured before and after heating. The results of these measurements are presented in Figure 5.9.<sup>125</sup>

In Figure 5.9, coating 1 refers to the 3M Scotch-Weld DP100 resin coating, and coating 2 refers to the J-B weld epoxy coating. Without coatings, the PPS magnet reached 5% flux loss at 150°C (423.15 K) and does not exceed 6% at 175°C (448.15 K). Coating 1 prevented the magnet from reaching 5% flux loss at 175°C (448.15 K). The effect of coating 2 is less clear and does not seem to offer any thermal advantage to the magnet. Thus, without coating, the working temperature of the PPS magnet is approximately 150°C (423.15 K), and coating 1 improves this temperature to approximately 175°C (448.15 K). Both working temperatures are higher than their equivalents in the Nylon 12 BAAM magnet.<sup>125</sup>

Another way to measure the thermal stability of a material is via the  $\alpha$  and  $\beta$  of the material. Here,  $\alpha$  refers to the reversible temperature coefficients of remanence, and  $\beta$  refers to the reversible

thermal coefficient of coercivity. The  $\alpha$  and  $\beta$  values of a high-density BAAM 70 vol% NdFeB Nylon 12 magnet were measured and compared with corresponding values for a commercial injected molded equivalent and are presented in Table 5.14. The data in Table 5.14 show that the two magnets' thermal stability performances are nearly equivalent.<sup>124</sup>

### **5.4.3 On the Mechanical Properties of 3D Printed Permanent Magnets**

Important mechanical properties concerning 3D printed PMs include the modulus of elasticity, UTS, and the strain at UTS.

Strain is the per-unit change in the size or shape of a body with respect to its original size or shape. It is a nondimensional quantity and is often expressed in percent. In the context of mechanical testing, strain refers to changes in size or shape associated with the application of force. Engineering strain is a dimensionless value that is the change in length per unit length of original linear dimension along the loading axis of the specimen. An increase in strain is usually considered positive.<sup>207</sup>

Stress is the intensity at a point in a body of the force, or components of force, which acts on a given plane through the point. It is usually expressed in force per unit of area, such as megapascals, gigapascals, or pounds-force per square inch. In the context of mechanical testing, such as tension or compression testing, stress is calculated based on the original dimensions of the specimen's cross section and is also known as engineering stress. It is expressed in units of applied force per unit of original cross-sectional area. Tensile stress is the normal stress caused by forces directed away from the plane on which they act. Tensile strength is the maximum tensile stress that a material is capable of sustaining. Tensile strength is also known as UTS. It can be calculated by dividing the maximum load by the original cross-sectional area of the specimen. In a ductile material, the UTS is defined as the stress at which necking begins. In a brittle material, the UTS is defined as the stress at fracture.<sup>207–209</sup> In this paper, the terms ultimate strain and tensile strain refer

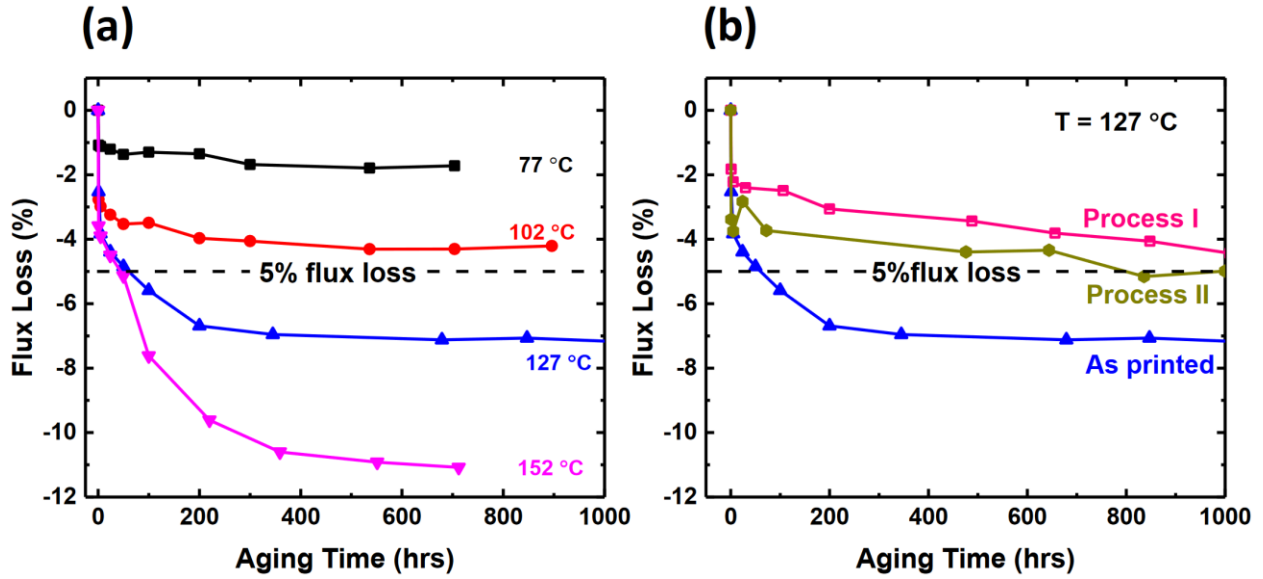


Figure 5.8: Flux loss behavior of BAAM NdFeB Nylon 12 bonded magnets. (a) Without and (b) with protective coatings.<sup>128</sup>

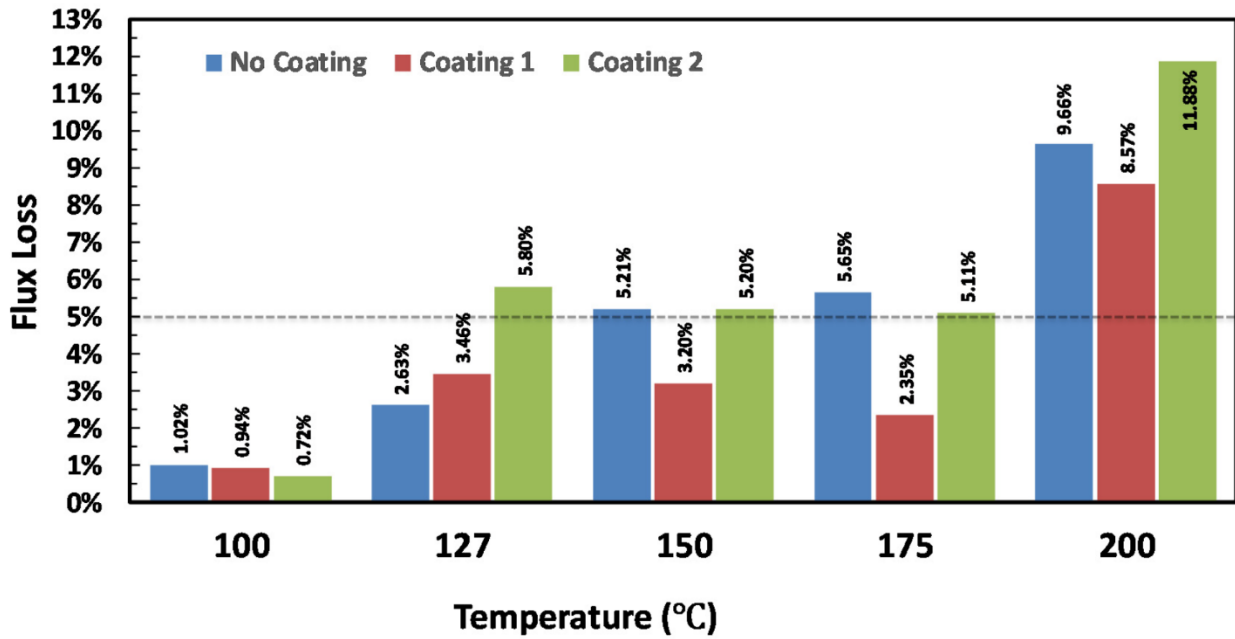


Figure 5.9: Flux loss behavior of BAAM NdFeB PPS bonded magnets with and without protective coating.<sup>125</sup>

Table 5.14: Thermal stability of BAAM NdFeB magnet and commercial injection-molded NdFeB magnet.

<b>Material Property</b>	<b>MQA-38-14 NdFeB, Injection-Molded, 54 vol% NdFeB, in PPS</b>	<b>MQA-38-14 NdFeB, BAAM Printed, 70 vol% NdFeB, in Nylon</b>
<b><math>\alpha</math> to 373 K (100°C)</b>	-0.09%	-0.09%
<b><math>\beta</math> to 373 K (100°C)</b>	-0.66%	-0.53%

Source: <sup>124</sup>

to the strain at the UTS of a material, and modulus refers to Young's modulus.

The modulus of elasticity is the ratio of stress to corresponding strain below the proportional limit.

The stress can be tensile stress or compressive stress. The modulus of elasticity is also known as the elastic modulus, or Young's modulus. It is expressed in force per unit area, usually in gigapascal.<sup>207</sup> Figure 5.10 shows the blueprint for a tensile specimen for one of the tensile testing standards used to determine the mechanical properties of 3D printed magnets. The dimensions for the Type V variant, which has been used to test 3D printed magnets, are listed in Table 5.15.

The mechanical properties of the commercial and 3D printed PMs are summarized in Table 5.16. The properties of the compression-molded, high-density, anisotropic NdFeB in PC magnet are also included.

Tensile testing revealed that the UTS increases with the loading fraction of the magnet powder and decreases with increasing temperature.<sup>128</sup> The choice of the binder polymer matters in the mechanical properties of 3D printed magnet. PPS 3D printed magnets have much better mechanical properties than those of Nylon 12. However, PPS 3D printed magnets are also significantly less flexible and more brittle than Nylon 12 magnets.<sup>125</sup> The PC CM magnet has twice the modulus as that of the PPS BAAM magnet. Perhaps if PC is used in an AM process, then BAAM PC magnets with similar superior mechanical properties could be produced. Anisotropy might influence the magnet's UTS, given that the anisotropic BAAM magnets have a slight increase in UTS compared with their isotropic equivalent. BAAM magnets with high magnetic material loading fraction, strong binder polymer material, and anisotropic magnet material have the best performance in terms of mechanical properties.

None of the 3D printed magnets have superior mechanical properties compared with the commercial sintered NdFeB. The CM PC magnet did have higher modulus than the commercial

compression- and injection-molded magnets. The BAAM PPS magnet has higher modulus than the injection-molded Nylon 12 magnet but lower tensile strength. Overall, the BAAM magnets have poorer mechanical properties compared with commercial NdFeB magnets.

The density and magnetic properties of the 3D printed PMs are summarized in Table 5.17. The properties of the compression-molded, high-density, anisotropic NdFeB in PC magnet are also included.

The data in Table 5.17 show that magnets with higher densities are usually associated with better magnetic performance. This trend holds for magnets of the same process and material but different densities. Infiltrating BJT magnets with alloys seems to dramatically increase the magnets' coercivity and slightly increase the density. However, the remanence decreased after infiltration, no evidence indicates that infiltration improved the energy product. Introducing SmFeN to the magnet in addition to NdFeB does not seem to improve the magnetic properties. Although the SmFeN magnets seem to have improved properties compared with the isotropic NdFeB magnets, the SmFeN magnets use anisotropic NdFeB, so this comparison is unfair. Compared with the anisotropic NdFeB BAAM magnets, all three of the key magnetic properties of the SmFeN magnet have lower values. Further complicating this comparison is the density of the SmFeN magnet, which was not reported in the original paper. The SmFeN magnet is less dense than the anisotropic NdFeB magnet, possibly leading to the disappointing magnetic performance. Nevertheless, SmFeN contains less critical materials than NdFeB, so it could be used as a filler to make magnets with reduced criticality and price than magnets that contain only NdFeB as the magnetic material. Although the CM PC demonstrated much higher loading fraction and modulus than the post-aligned BAAM anisotropic NdFeB magnet, as well as slightly higher density, the magnetic properties of the CM PC magnet are slightly inferior to the BAAM magnet. CM PC could be an




**D638 – 22**

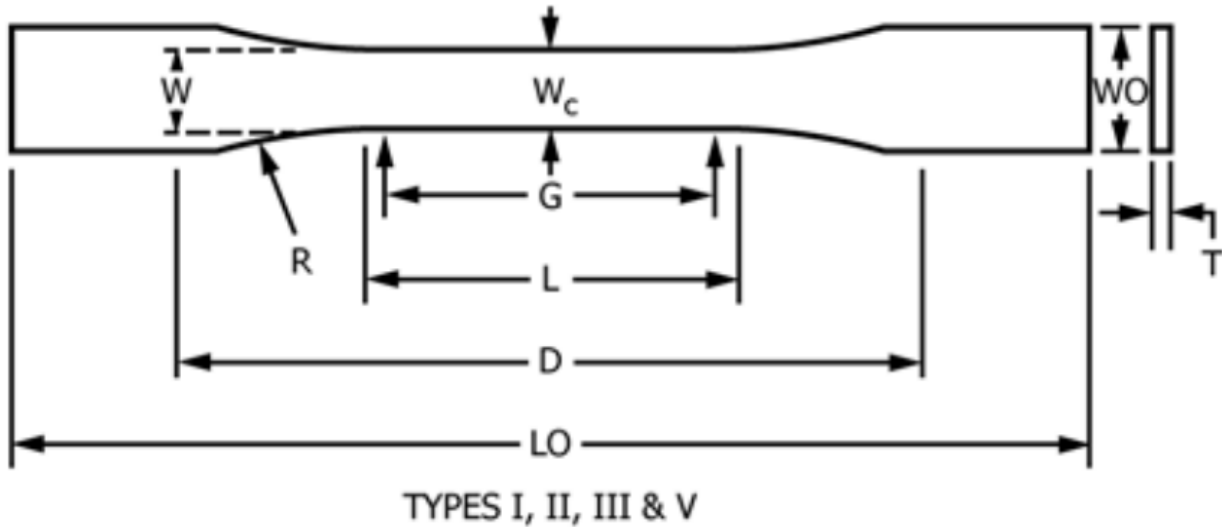


Figure 5.10: Specimen blueprint for the ASTM D638-22, “Standard Test Method for Tensile Properties.”<sup>210</sup>

Table 5.15: Dimensions for the Type V variant of the ASTM D638-22 specimen.

Dimension	Type V (mm [in.])
W – Width of narrow section	3.18 (0.125)
L – Length of narrow section	9.53 (0.375)
WO – Width overall, min	9.53 (0.375)
LO – Length overall, min	63.5 (2.5)
G – Gage length	7.62 (0.3)
D – Distance between grips	25.4 (1.0)
R – Radius of fillet	12.7 (0.5)

Note: Source: ASTM<sup>210</sup>

Table 5.16: Mechanical properties of 3D printed and CM magnets.

<b>Reference</b>	<b>Material</b>	<b>Magnet loading fraction (vol%)</b>	<b>Modulus (GPa)</b>	<b>UTS (MPa)</b>	<b>Ultimate strain (%)</b>
211	Commercial sintered NdFeB	100	152	82.7	—
212	Commercial compression-molded NdFeB + Epoxy	—	28	33	—
213	Commercial injection-molded isotropic NdFeB + Nylon 12	—	11	27.5	2
213	Commercial injection-molded isotropic NdFeB + PPS	—	22	48	1
123	BAAM isotropic NdFeB + Nylon 12	65	4.29	6.60	4.18
128	BAAM isotropic NdFeB + Nylon 12	70	—	10	3
125	BAAM isotropic NdFeB + PPS	63	21.53	20.37	0.09
124	BAAM anisotropic NdFeB + Nylon 12	70	—	13.81	—
195	Compression-molded anisotropic NdFeB + PC, post aligned	95	43.91	-	—

alternative binder material for improved mechanical properties at the cost of slightly lower magnetic properties. The PPS magnet exhibits improved coercivity compared with the Nylon 12 magnet, and the other two magnetic properties are equivalent. The PPS magnet also demonstrated improved mechanical properties. PPS is also a valid alternative polymer binder to Nylon 12, offering improved mechanical properties and slightly improved magnetic properties. In conclusion, post-aligned BAAM anisotropic NdFeB magnets with Nylon 12 polymer binder offered the best magnetic properties. High magnetic material content, the use of anisotropic magnetic materials, and the alignment of the magnets under magnetic fields all contributed to this outcome. Alternative polymer binders could improve the mechanical properties of the BAAM magnet but do not greatly improve its magnetic properties.

### **5.5 Comparison of the Materials Properties of 3D Printed Hard Magnets and their Baseline Counterparts**

The data from Table 5.1 and Table 5.17 can be combined to form Table 5.18, the magnetic properties of commercial and 3D printed PMs.

The data in Table 5.18 show that none of the 3D printed magnets have superior magnetic properties than sintered NdFeB or sintered SmCo. Most of the 3D printed magnets have better magnetic properties than hard ferrite. Although none of the 3D printed magnets have superior remanent magnetization than cast AlNiCo, the post-aligned anisotropic 3D printed magnets have superior energy products than cast AlNiCo. The post-aligned anisotropic NdFeB BAAM magnets have superior magnetic properties than commercial compression-molded and injection-molded NdFeB magnets. The compression-molded magnets could be used as future feedstock for the BAAM process. These feedstocks have some of the best magnetic properties ever obtained and could result in 3D printed magnets with even better magnetic properties.

Table 5.17: Magnetic properties of 3D printed and CM magnets.

<b>Material</b>	<b>Density (g/cc)</b>	<b>Intrinsic coercivity (kOe)</b>	<b>Remanence (kG)</b>	<b>Energy product (MGOe)</b>
BAAM isotropic NdFeB + Nylon 12	4.8	8.65	5.1	5.47
BAAM isotropic NdFeB + Nylon 12	5.15	8.9	5.8	7.3
BJT isotropic NdFeB + DEG	3.3	9.20	3.5	-
BJT isotropic NdFeB + DEG + NdCuCo	4.3	16.90	3.1	-
BJT isotropic NdFeB + DEG + PrCuCo	4.3	15.50	2.5	-
BAAM anisotropic NdFeB + anisotropic SmFeN + Nylon 12, as printed	-	10.8	3.7	2.8
BAAM anisotropic NdFeB + anisotropic SmFeN + Nylon 12, post aligned	-	11	7.2	11
BAAM isotropic NdFeB + PPS	4.85	11.4	5.0	5.4
BAAM anisotropic NdFeB + Nylon 12, as printed	5.15	12.1	4.8	4.4
BAAM anisotropic NdFeB + Nylon 12, post aligned	5.15	12.3	9.8	18.7
CM anisotropic NdFeB + PC, post aligned	5.34	11.85	8.6	15.2

Source: <sup>123,124,125,128,140,188,195</sup>

Table 5.18: Magnetic properties of commercial and 3D printed permanent magnets.

<b>Material</b>	<b>Remanent Magnetization (kG)</b>	<b>Energy product (MGOe)</b>
Sintered NdFeB	16	56
Sintered SmCo	12	34
Cast AlNiCo	14	7.2
Hard ferrite	3.85	5.2
Compression-molded NdFeB + epoxy <sup>212</sup>	5	5
Injection-molded NdFeB + Nylon 12 <sup>213</sup>	5.89	7.44
BAAM isotropic NdFeB + Nylon 12	5.1	5.47
BAAM isotropic NdFeB + Nylon 12	5.8	7.3
BJT isotropic NdFeB + DEG	3.5	-
BJT isotropic NdFeB + DEG + NdCuCo	3.1	-
BJT isotropic NdFeB + DEG + PrCuCo	2.5	-
BAAM anisotropic NdFeB + SmFeN + Nylon 12, as-printed	3.7	2.8
BAAM anisotropic NdFeB + anisotropic SmFeN + Nylon 12, post-aligned	7.2	11
BAAM isotropic NdFeB + PPS	5.0	5.4
BAAM anisotropic NdFeB + Nylon 12, as-printed	4.8	4.4
BAAM anisotropic NdFeB + Nylon 12, post-aligned	9.8	18.7
CM anisotropic NdFeB + PC, post aligned	8.6	15.2
CM anisotropic NdFeB + anisotropic SmFeN + PPS, post-aligned	10.5	20.0

**CHAPTER 6 : ON THE EVOLUTION AND IMPROVEMENT OF THE  
ENERGY PRODUCT OF 3D PRINTED HARD MAGNETS**

## 6.1 On Utilizing Sacrificial Polymers for 3D Printed Permanent Magnets

Bonded magnets are composite materials comprising both polymeric and magnetic materials. These composites sacrifice magnetic strength for enhanced shape complexity by replacing some of the magnetic material with polymeric material. The higher the content of the polymeric material within the bonded magnet, the weaker the overall magnetic strength. Increasing the loading of magnetic material within bonded magnets increases the magnetic strength of the bonded magnet. However, because of the bonding polymer's high viscosity, there is a hard limit to the magnetic material loading in bonded magnets achievable via conventional processes. This hard limit is approximately 70 vol% of magnetic materials in injection-molded magnets, and 80 vol% of magnetic materials in compression-molded magnets.<sup>101,214</sup>

A workaround to this hard limit involves using sacrificial polymers. The final product need not contain the binding polymer. An ideal sacrificial polymer in this case is one that does not react besides undergoing thermal decomposition when the need and the heat for it to do so arises. The sacrificial polymer would be employed in the same way as in normal bonded processes, such as IM, CM, or bonded AM processes, but after the bonded magnet is produced, it would undergo heat treatment to remove the sacrificial polymer via thermal decomposition. Then, with the sacrificial polymer removed from the magnet, a much higher loading of magnetic materials would be achieved. An ideal case would be to use entirely sacrificial polymer, and completely remove it via thermal treatment. Realistically, the sacrificial polymer is only a portion of the polymer mixture used to make bonded magnets. The other portion is a so-called permanent polymer that remains in the bonded magnet from start to finish. The two portions make up the dual-binder polymer system of the sacrificial polymer–bonded magnet process. The permanent polymer maintains the structural integrity of the bonded magnet because, currently, the sacrificial polymer cannot

perform this function alone. Furthermore, the sacrificial polymer currently cannot be completely removed via thermal treatment; trace quantities of it remain within the magnet.<sup>214</sup> The relationship between the magnetic material, the permanent polymer, the sacrificial polymer, and the composite magnet, is defined by the following equation:

$$\text{Magnetic material} + \text{Permanent polymer} + \text{Sacrificial polymer} = \text{Composite magnet}$$

For example, a composite magnet could comprise of 94 mass% magnetic material, 3 mass% permanent polymer, and 3 mass% sacrificial polymer. The goal is to remove the sacrificial polymer eventually via postprocessing, ensuring a higher composition of magnetic material within the composite magnet.

During this project, some sacrificial polymers have been investigated for magnet manufacturing. The permanent and sacrificial polymers are listed in Table 6.1.<sup>214–218</sup>

Three pairs of permanent and sacrificial polymers were studied: PC and POM, which both contain oxygen, Nylon and ABS, which contain oxygen in the permanent polymer but not the sacrificial polymer, and PPS and ABS, which are both oxygen free. When the study, the reactivity of oxygen was expected to play a crucial role in degrading the magnetic properties of the bonded magnet.<sup>214</sup> For the PC–POM pairing, the bonded magnet suffered a dramatic decrease in magnetic properties after heat treatment. Coercivity of the sample was entirely lost; the saturation magnetization also significantly decreased. This result indicates that the oxygen contained within the polymers reacted and damaged the magnetic quality of the bonded magnet sample.<sup>214</sup> Figure 6.1 shows the hysteresis curve of this sample before and after heat treatment.

For the Nylon–ABS pairing, heat treatment significantly decreased coercivity, but not to the extent



Table 6.1: Permanent and sacrificial polymers.

<b>Polymer</b>	<b>Abbreviation</b>	<b>Melting temperature (°C)</b>	<b>Role</b>
Polyphenylene sulfide	PPS	280	Oxygen-free permanent polymer
Nylon 12	Nylon	268.8	Oxygen-containing permanent polymer
Polycarbonate	PC	288–316	Oxygen-containing permanent polymer
Polyoxymethylene	POM	175	Oxygen-containing sacrificial polymer
Polystyrene	PS	270	Oxygen-free sacrificial polymer
Acrylonitrile Butadiene Styrene	ABS	105	Oxygen-free sacrificial polymer
Polyvinyl Butyral	PVB	165–185	Oxygen-containing sacrificial polymer
Styroflex	—	170–240	Oxygen-free sacrificial polymer

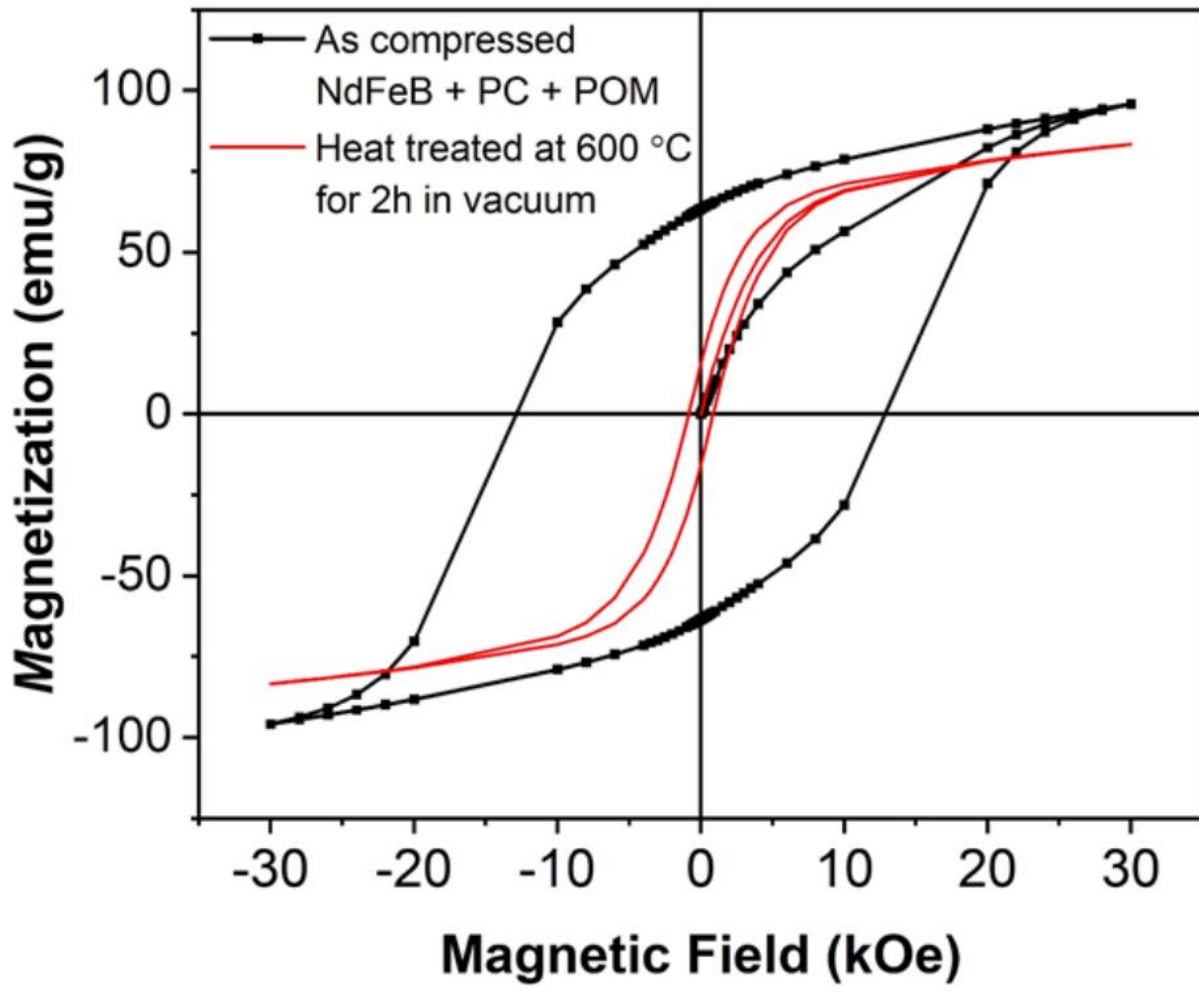


Figure 6.1: Hysteresis curve of NdFeB with PC–POM. (black) Before and (red) after high-temperature heat treatment.<sup>214</sup>

of the PC–POM pairing. Moreover, negligible saturation magnetization loss occurred. When the sample was heat-treated within an applied magnetic field, the saturation magnetization improved, and the coercivity loss with an applied field was minor. This result demonstrates the ability of magnetic fields to align the magnetic domains of the composite magnet and increase the degree of alignment of such magnets. By using an oxygen-free sacrificial polymer, the damaging effects of reacting oxygen were curtailed, and decreases in the magnetic properties of the sample were mostly mitigated.<sup>214</sup> The testing conditions and magnetic properties of the Nylon–ABS NdFeB samples are listed in Table 6.2. The hysteresis curves of samples without and with applied magnetic fields are presented in Figure 6.2.

A strange occurrence was observed in the PPS–ABS pairing. Neither polymer contained oxygen. If the magnetic properties were preserved only by mitigating oxygen content, then this pair should have produced the smallest reduction in magnetic properties. Instead, heat treatment drastically decreased coercivity despite no oxygen content in PPS nor ABS. Some fluctuations in the saturation magnetization occurred, depending on the heat treatment temperature, but those test results are inconclusive. This result casts a shadow of doubt on the presence of oxygen being detrimental to magnetic properties of bonded magnets.<sup>214</sup> The testing conditions and magnetic properties of the PPS–ABS NdFeB samples are listed in Table 6.3. Figure 6.3 shows the hysteresis curves of samples without and with applied magnetic fields.

Nevertheless, the Nylon–ABS pairing provided the smallest decrease in magnetic properties. The heat treatment temperature should not be above 300°C because beyond that temperature the magnetic properties are greatly degraded by the heating. The heat treatment time should be between 5 and 10 h because almost no coercivity was lost at 5 h, and a minor coercivity loss occurred at 10 hours. The sample mass loss was 0.32% at 2 h, 0.61% at 5 h, and 0.81% at 10 h,

Table 6.2: NdFeB with Nylon–ABS sample testing conditions and magnetic properties.

Sample conditions	Coercivity (kOe)	Sample mass loss (%)	Saturation magnetization (emu/g)
Nylon+ABS-300 °C-2h-1T	12.2	0.32	154.0
Nylon+ABS-300 °C-5h-1T	12.2	0.61	153.4
Nylon+ABS-300 °C-10h-1T	10.8	0.81	151.4
Nylon+ABS as compounded	12.2	—	141.0

Source: <sup>214</sup>

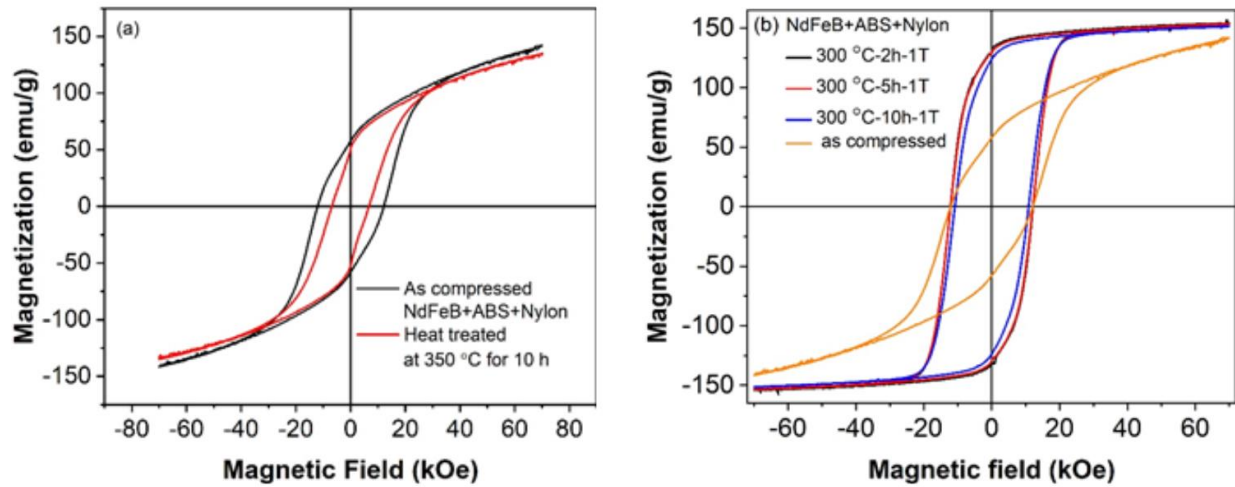


Figure 6.2: Hysteresis curves of Nylon–ABS NdFeB samples under various heat-treatment conditions. (left) Without applied field and (right) with applied field.<sup>214</sup>

Table 6.3: NdFeB with PPS–ABS sample testing conditions and magnetic properties.

Sample conditions	Coercivity (kOe)	Sample mass loss (%)	Saturation magnetization (emu/g)
PPS+ABS as compounded	11.4	—	141.6
PPS+ABS-300 °C-1T	9.4	0.4	141.9
PPS+ABS-350 °C-1T	6.19	0.5	138.2
PPS+ABS-400 °C-1T	5.1	1.48	141,0

Source: <sup>214</sup>

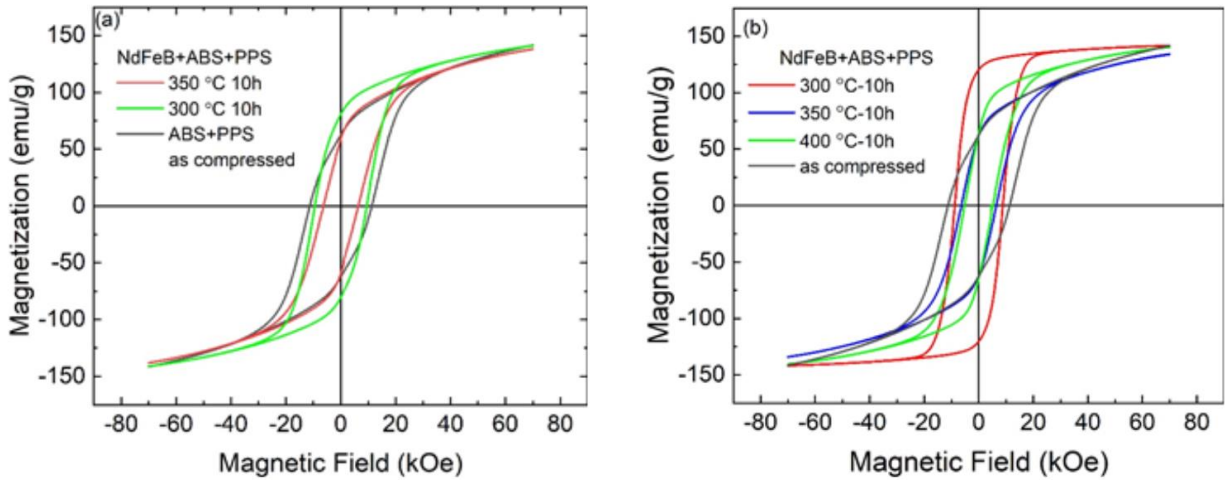


Figure 6.3: Hysteresis curves of PPS–ABS NdFeB samples under various heat-treatment conditions. (left) Without applied field and (right) with applied field. <sup>214</sup>

suggesting that mass loss increases with heat treatment time. The melting temperature of ABS is only 105°C, and the testing was conducted at 300°C. Heat treatment of Nylon–ABS at 200°C for longer than 10 h may lead to more significant mass loss and less loss of magnetic quality. Alternatively, increasing the sacrificial polymer content and decreasing the permanent polymer content could have the same effect. This dual-polymer system has not yet been employed to 3D print magnets. Other potential sacrificial/permanent polymer pairs could be employed. These potential future avenues of research could improve the quality of 3D printed magnets.<sup>214</sup>

The ABS and Nylon dual-binder system was the best at maintaining the magnetic properties of the magnets, so this system was chosen to be 3D printed via the BAAM process. Previous work indicates that 300°C is the best temperature, so it was selected as the heating temperature. Furthermore, previous work suggested that the heat treatment time significantly influences mass loss, so this variable was investigated in the present study. Samples were under an applied magnetic field because previous results suggest this condition is best for the magnetic properties of the test samples. The hysteresis curves of the samples are presented in Figure 6.4. The testing conditions and magnetic properties of the BAAM Nylon–ABS samples are provided in Table 6.4. These results demonstrate that it is possible to use sacrificial polymer in AM. As predicted, sample loss increases with time. Saturation magnetization remained unchanged even at 10 h. Coercivity did not degrade at 5 h but had minor degradation by 10 h. This result suggests it might be inadvisable to add heat-treatment time because it could erode magnetic properties. Mass loss of magnetic material remained below 1% at 10 h. Because of the low mass loss, a negligible change occurred in the sample density. However, the quantity of sacrificial polymer within the samples was low to begin with. The sample was composed of 95 mass% MQA NdFeB, 3 mass% Nylon, and only 2 mass% ABS. Assuming most of the mass loss was due to removed ABS, a large portion

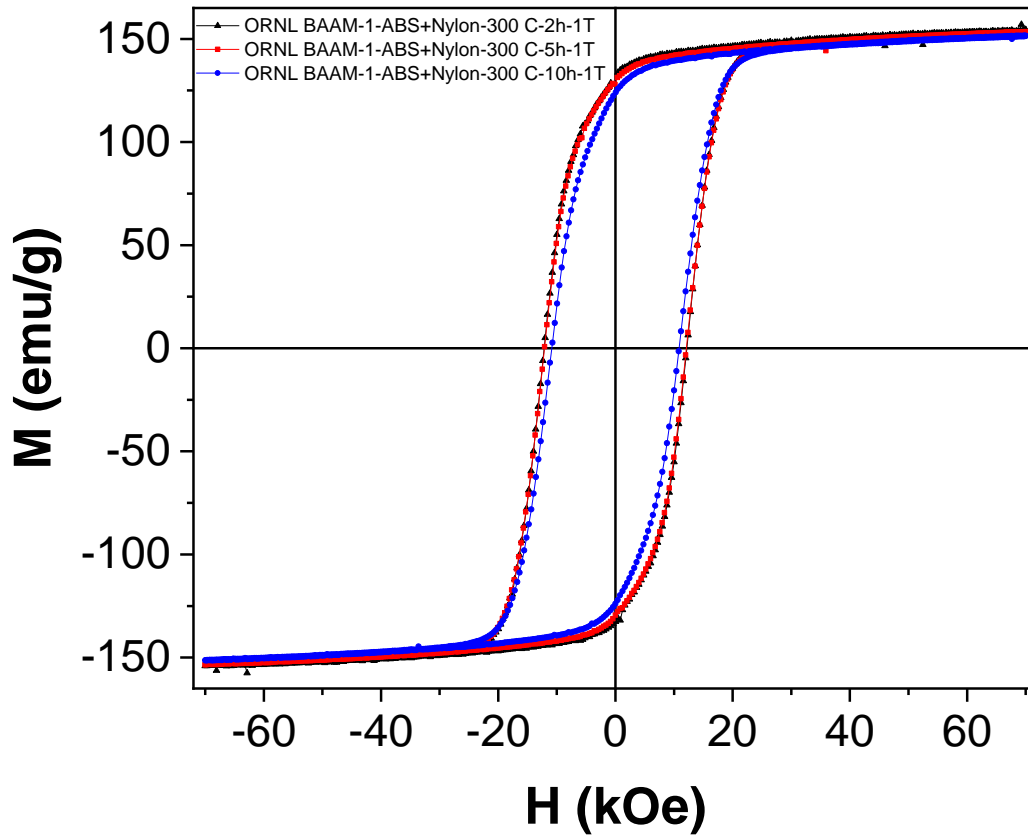


Figure 6.4: Hysteresis curves of BAAM Nylon-ABS NdFeB samples under various heat-treatment conditions.

Table 6.4: NdFeB with Nylon-abs sample testing conditions and magnetic properties.

Sample conditions	Coercivity (kOe)	Sample mass loss (%)	Saturation magnetization (emu/g)
BAAM-Nylon+ABS-300 C-2h-1T	12.2	0.32	154
BAAM-Nylon+ABS-300 C-5h-1T	12.2	0.61	153.4
BAAM-Nylon+ABS-300 C-10h-1T	10.8	0.81	151.4

of the sacrificial polymer decomposed. Increased sacrificial polymer content within the magnets should result in more mass loss.

This investigation began with the creation of MQA–ABS magnets, without a permanent polymer like Nylon. The composition of these magnets is 97 wt% MQA and 3 wt.% ABS. These magnets were made via the CM process, and the product had a density of 5.91 g/cm<sup>3</sup>.<sup>214</sup> The samples were measured as made and after heat treatment under an applied magnetic field. All magnetic measurement were made via the MicroSense Vibrating Sample Magnetometer (VSM).<sup>219</sup> Test results showed that heat treatment under magnetic field improves the magnetic properties of the magnet. Hysteresis curves of the samples are shown in Figure 6.5. The testing conditions and magnetic properties of the BAAM MQA–ABS samples are listed in Table 6.5. The test temperature was at 250°C rather than 300°C as in the mass degradation tests. The MQA–ABS system is stable and can be enhanced magnetically via an applied field.

The magnetization, energy product, and magnetic induction of the 97% MQA 3% ABS samples are illustrated in Figure 6.6. This sample was aligned under a 2 T magnetic field at 250°C. The energy product of this sample peaked at approximately 21 MGOe, indicating that sample has good magnetic properties after magnetic alignment under a 2 T field and 250°C heat treatment.

SEM images of the MQA–ABS composite magnet are shown in Figures 6.7 through 6.10.

Potential sacrificial polymers—polystyrene (PS), polyvinyl butyral (PVB), and Styroflex (a styrene-butadiene block copolymer with the properties of a thermoplastic elastomer)—were investigated via simultaneous thermogravimetric analysis (STA), a thermal analysis technique that combines TGA and DSC in a single instrument for simultaneous measurement.<sup>215,217,220</sup> The STA test involved increasing the temperature to 250°C at 20°/min and holding at 250°C for 2 h. The STA results are summarized in Table 6.6. These results suggest that all three potential sacrificial



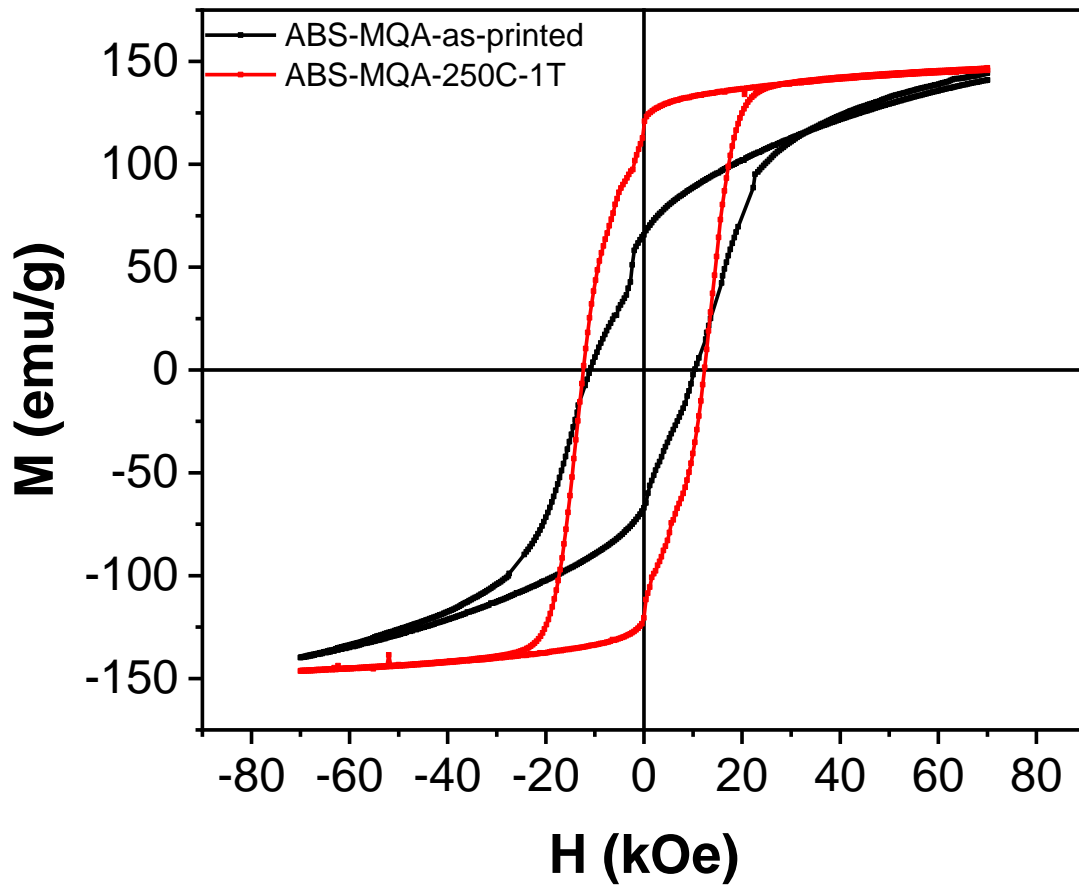


Figure 6.5: Hysteresis curves of the BAAM MQA-ABS samples with and without heat treatment under an applied magnetic field.

Table 6.5: MQA-ABS sample testing conditions and magnetic properties.

Sample conditions	Coercivity (kOe)	Saturation magnetization (emu/g)
1-ABS-MQA-as printed	11	139.7
1-ABS-MQA-250 C-1T	12.4	146.8

polymers are stable at temperatures below 250°C and exhibit low mass loss. PVB and Styroflex seem to have a melting range rather than a melting point. These potential future sacrificial polymers require more testing at higher temperatures to determine their suitability for such a role. In conclusion, sacrificial polymers were developed for bonded magnets produced via CM. These sacrificial polymers were successfully removed by heat-based postprocessing. The bonded magnets' magnetic properties were not degraded by the heating. Currently, the mass percentage of the sacrificial polymer in the raw material mixture is low. Increasing this mass percentage and decreasing that of the permanent polymer could significantly increase the mass removed by heat-based postprocessing, thereby achieving bonded magnets with high magnetic material loading and better magnetic properties. This strategy could be applied to AM feedstocks, enabling 3D printed magnets containing less polymer, thereby improving magnetic performance and recyclability.

## **6.2 History of the Development of Energy Products of 3D Printed Permanent Magnets**

Figure 6.11 illustrates the history of the development of energy product of this project's 3D printed NdFeB PMs. BAAM Nylon 12 bonded NdFeB PMs were first successfully produced in 2016 using isotropic magnetic material powder. These magnets had an energy product of about 5.5 MGOe. The magnets were not aligned under a magnetic field. In 2018, magnetic alignment of the 3D printed magnets under a magnetic field occurred for the first time. Additionally, anisotropic magnetic material powder was used for the first time. To reduce critical material usage, SmFeN—an alternative to NdFeB—was used in conjunction with NdFeB. The SmFeN has less magnetic strength than NdFeB. Nevertheless, the anisotropic nature of the powders in addition to the magnetic alignment yielded magnets with stronger energy product: approximately 11 MGOe, about double the energy product of the 2016 3D printed magnets. In 2020, anisotropic NdFeB without SmFeN was used to 3D print magnets. These magnets were aligned under a magnetic field.

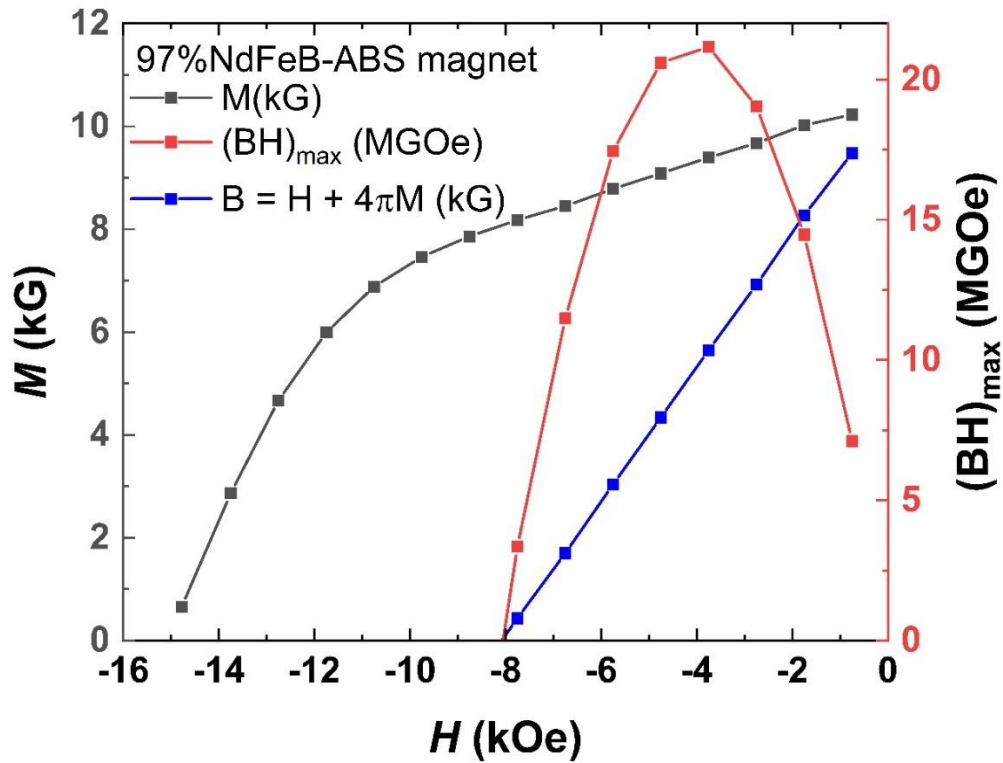


Figure 6.6: Magnetization ( $M$ ), energy product ( $(I)_{\max}$ ), magnetic induction ( $B$ ) of the 97% MQA 3% ABS magnet.

Sample No. 68: MQA-ABS, Surface

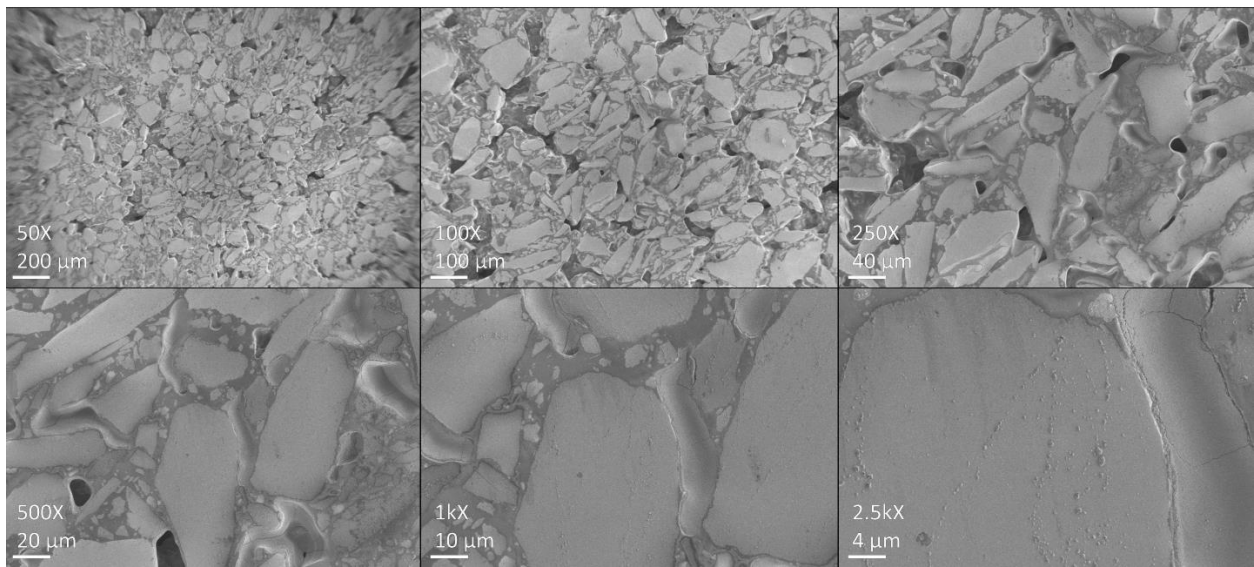


Figure 6.7. Sample 68: MQA-ABS, surface, low magnification.

### Sample No. 68: MQA-ABS, Surface

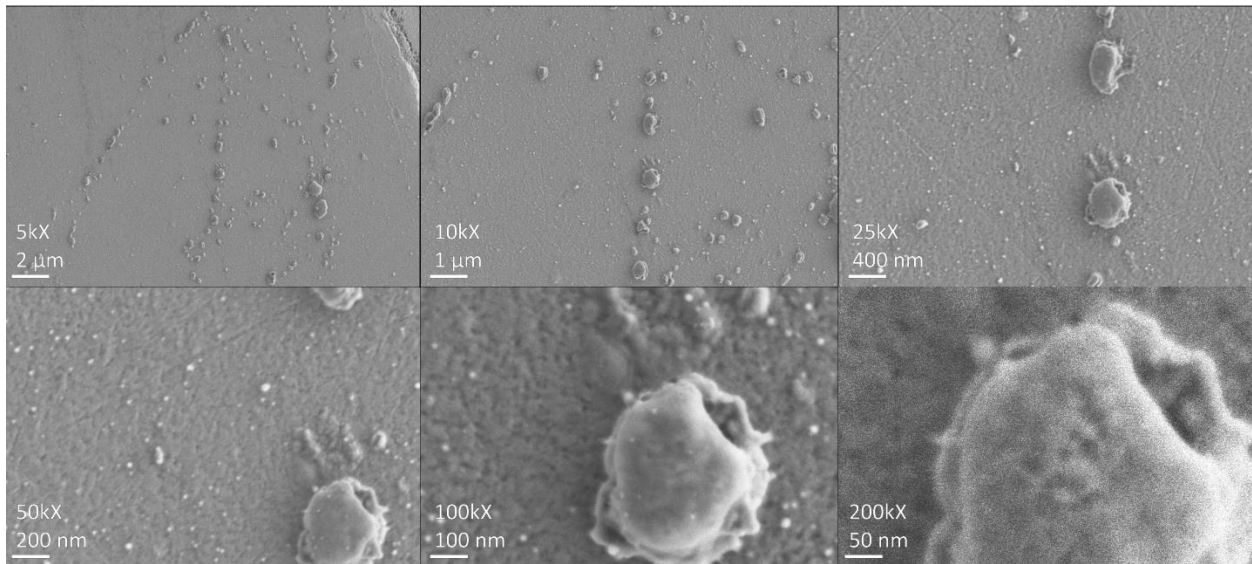


Figure 6.8. Sample 68: MQA-ABS, surface, high magnification.

### Sample No. 69: MQA-ABS, Cross Section

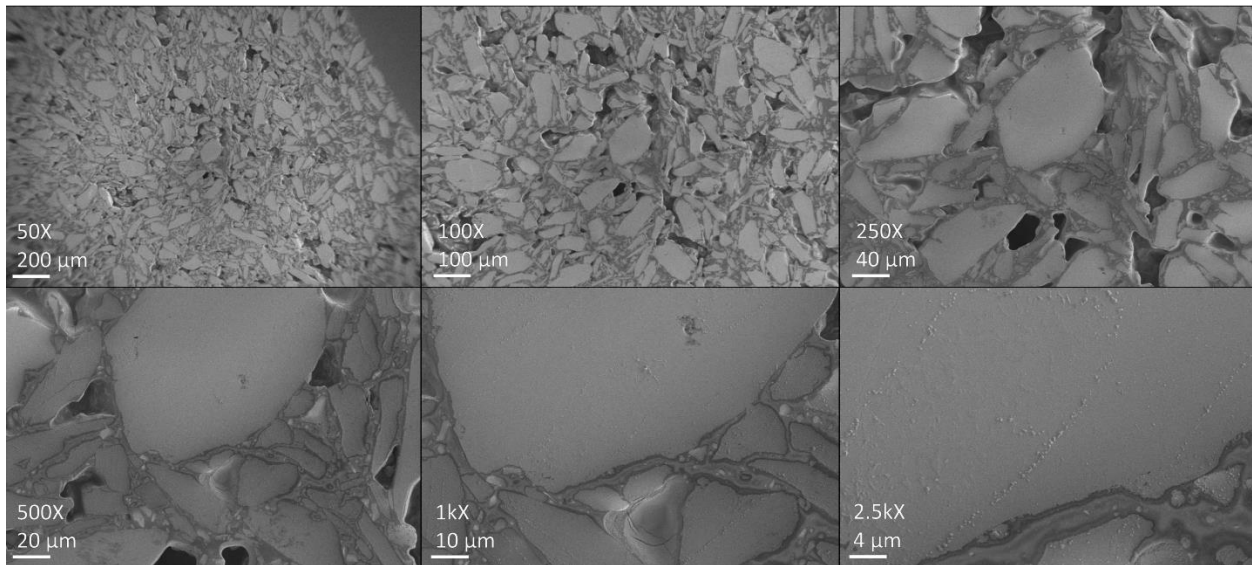


Figure 6.9: Sample 69: MQA-ABS, cross section, low magnification.

## Sample No. 69: MQA-ABS, Cross Section

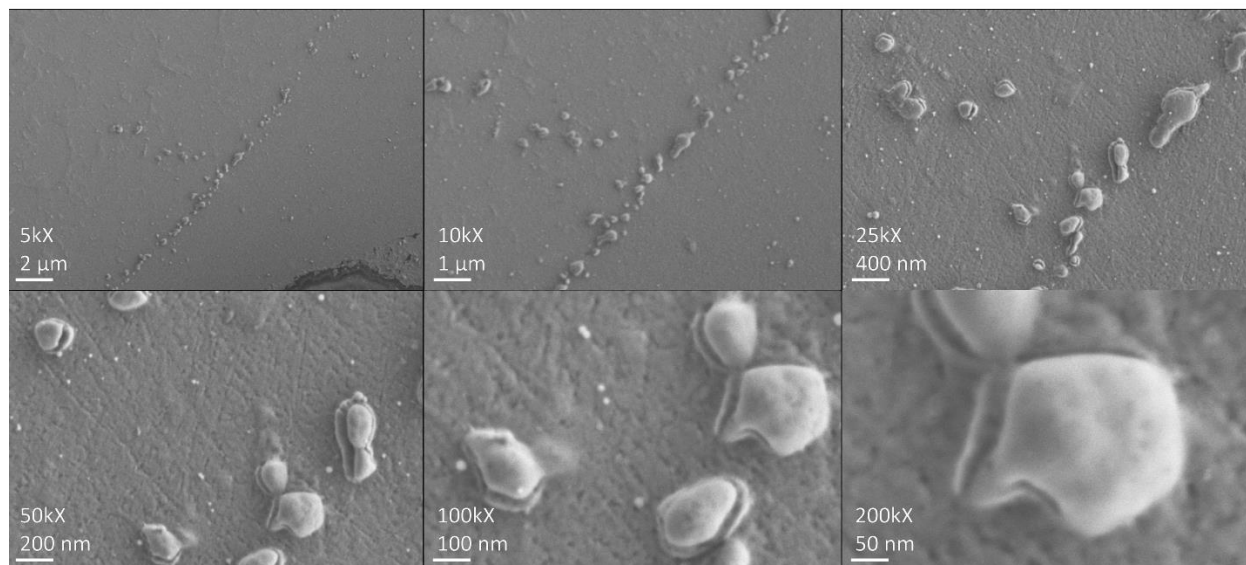


Figure 6.10. Sample 69: MQA-ABS, cross section, high magnification.

Table 6.6: STA results of possible new sacrificial polymers.

<b>Polymer</b>	<b>Sample mass loss (%)</b>	<b>Crystallization temperature (°C)</b>	<b>Melting temperature (°C)</b>
PS	0.92	104	240
PVB	1.11	70.5	—
Styroflex	0.65	—	—

As expected, without the magnetically weaker SmFeN, magnets with higher energy product values—18.7 MGOe—were produced. The use of anisotropic magnetic materials, magnetic alignment of the magnets under magnetic field, and the use of magnetic materials of high magnetic quality are all important factors in improving the energy product of 3D printed PMs.<sup>123,124,188</sup>

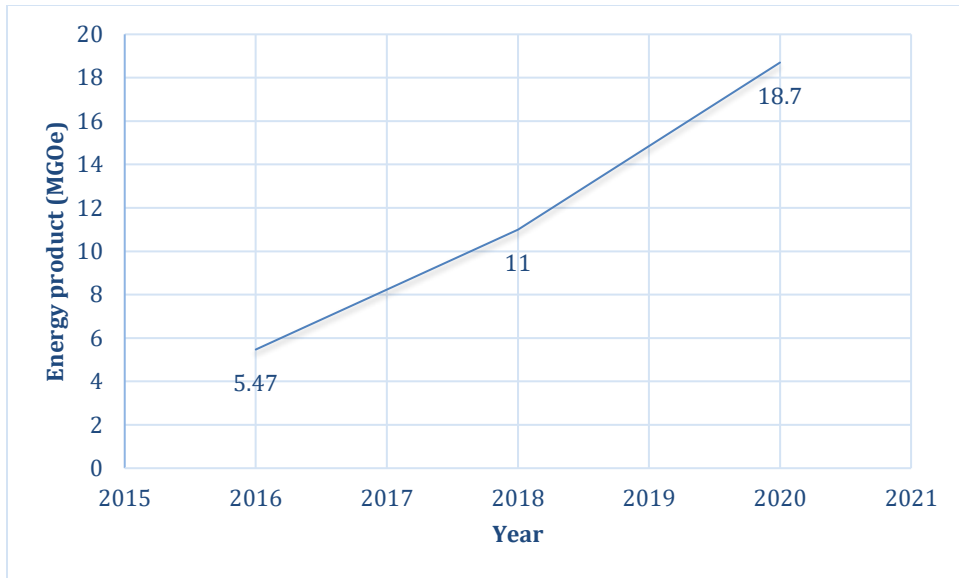


Figure 6.11: History of the development of the energy product of 3D printed NdFeB magnets.<sup>123,124,188</sup>

## **CHAPTER 7 : THE IMPLEMENTATION OF 3D PRINTED SOFT AND HARD MAGNETS IN ELECTRIC MACHINES**



## **7.1 On the Design and Fabrication of an Electric Motor Incorporating 3D Printed Soft and Hard Magnets**

This section details the fabrication of the electric motor that employs additively manufactured soft and hard magnets. The silicon steel 3D printed soft magnets function as the magnet's stator laminations. The BAAM NdFeB 3D printed hard magnets are built into the rotor and function as rotor magnets.

The creation of the electric motor began with the search for a suitable motor design. A simple electric motor design by Arnold Magnets was chosen as the 3D printed magnet motor. The motor uses PMs in the rotor and soft magnets in the stator. Figures 7.1 and 7.2 illustrate the electric motor's stator design and rotor shape.

The motor designs are proprietary, so the exact design and dimensions of stator and rotor are not provided here. However, the outer diameter of the stator is 55 mm, and the outer diameter of the rotor is 20.5 mm. The cylindrical rotor core is entirely 3D printed NdFeB. This motor design is a two-pole surface PM. The 3D printed NdFeB is a cylindrical filling within a hollow steel tube, which is the magnet's rotor housing. A data sheet of the Arnold motor is provided via Table 7.1. Figures 7.3 and 7.4 are screenshots of the Arnold motor's CAD model.

Figure 7.5 shows the 3D printed PM rotor assembly after construction. The magnet material is in the center, surrounded by the steel rotor housing. The stator and rotor designs were both adapted into computer models using CAD software. These CAD models were uploaded to the 3D printers, which then fabricated the magnet components.

The soft magnet and hard magnet are made using different AM processes. For the soft magnetic material, silicon steel (Fe-3Si) powders were chosen to the feedstock for 3D printing. These powders have an average particle size distribution of less than 45  $\mu\text{m}$ . The aim is to 3D print a

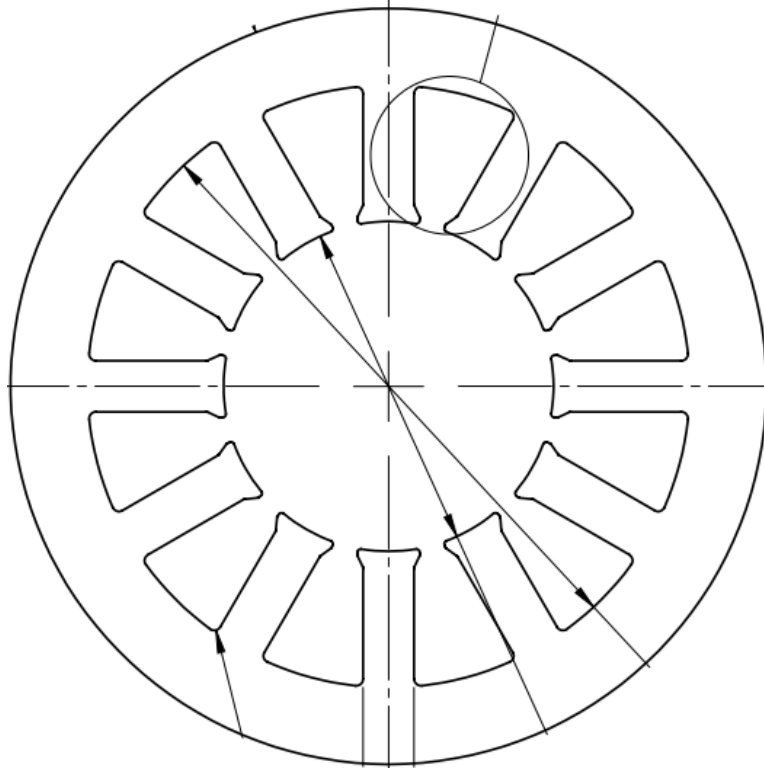


Figure 7.1: Stator design of the motor.

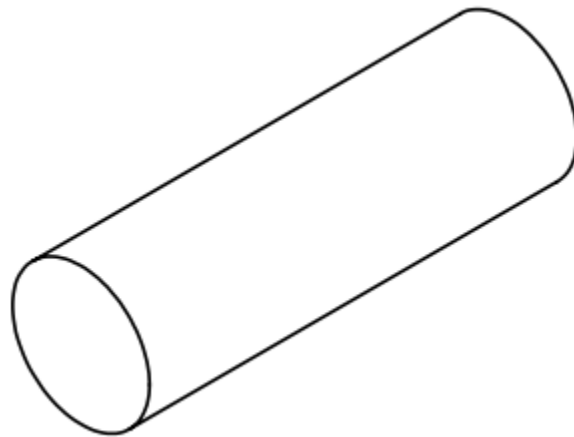


Figure 7.2: Rotor shape of the motor.

Table 7.1: Data sheet of the Arnold motor.

<b>Arnold motor data sheet</b>	
Air cooled at 320 V	
Peak torque (N·m)	1.53
Peak current (A)	52.9
Rated speed (rpm)	60,000
Rated torque (N·m)	1.45
Shaft power at rated speed (kW)	8.4
Current at rated speed (A)	37.4
Voltage constant ( $V_{\text{rms}}/\text{rad}/\text{sec}$ )	0.022
Torque constant (N·m/A)	0.044
Resistance (line to line) ( $\Omega$ )	0.4
Max DC bus voltage (V)	320
Max AC phase voltage (V)	147.5
Rotor inertia ( $\text{kg}\cdot\text{m}^2$ )	4.15E-05
Motor weight (kg)	1.734
Rated input power (W)	159
Efficiency at rated operating point (%)	98.7

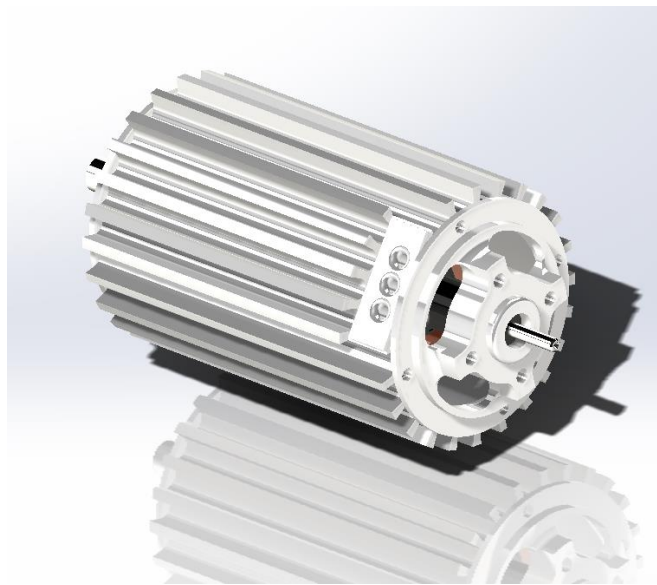


Figure 7.3: Screenshot of the CAD model of the Arnold motor.

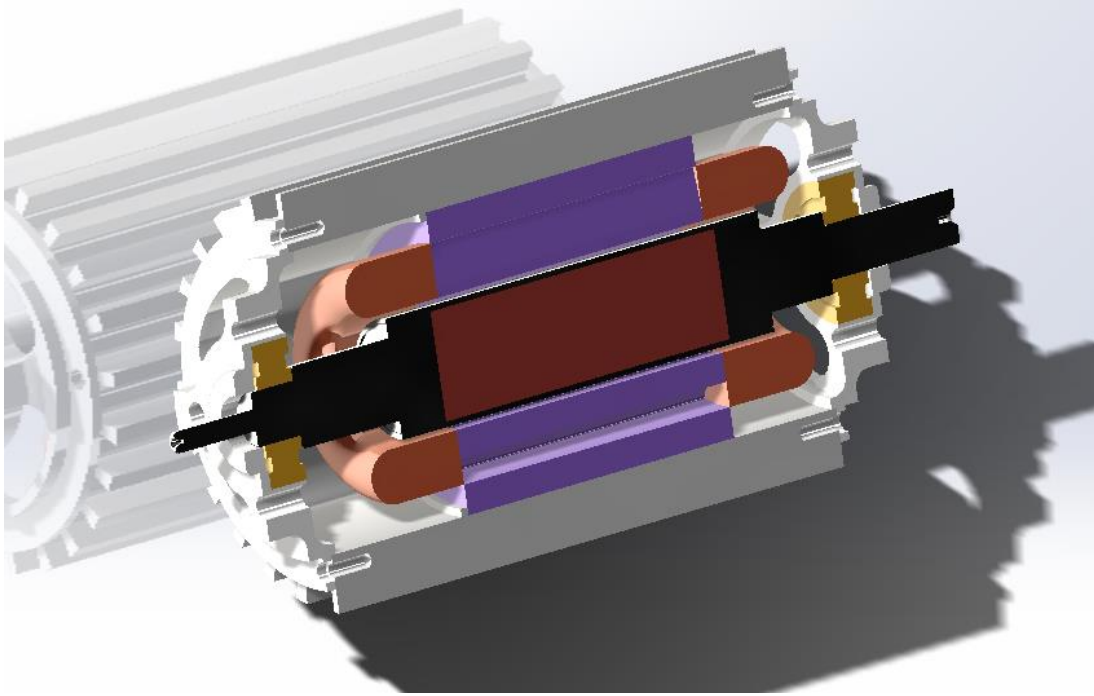


Figure 7.4: Screenshot of the CAD model of the Arnold motor, cross-sectional view.



Figure 7.5: The 3D printed rotor magnet cylinder in magnet housing.



Figure 7.6: Renishaw AM250 SLM printer.<sup>221</sup>

material with a composition close to that of the conventional E33 silicon steel alloy lamination material. The printer used was the Renishaw AM250 selective laser melting printer, shown in Figure 7.6. The main 3D printing parameters are listed in Table 7.2. These parameters are adapted from the reference work of Plotkowski et al.<sup>222</sup>

The motor stator CAD design was adjusted into the form of hollow cylinders. The hole of the ring-like stator faces upward in the  $z$ -direction, which is the print direction. Figure 7.7 provides examples of what the stator cylinders look like during and after SLM printing.

The printed Fe<sub>3</sub>Si parts were then subjected to hot isostatic pressing at 1,150°C for 2 h at 200 MPa, with a heating rate of 30°C/min and a cooling rate between 40°C/min and 50°C/min. This annealing densified the material and yielded nearly 100% dense parts with densities measured at 7.62 g/cm<sup>3</sup> via the Archimedes density method. The heat treatment also relieved the internal stresses within the parts. The AM laminate process differs from the conventional process in that a bulk is formed and then cut, instead of the material being rolled thin and then punched. Internal stresses are unfortunately inherent within the bulk, and the conventional rolling process eliminates the structural resistance to these stresses, liberating them to warp and deform the material. EDM was used to slice the printed Fe<sub>3</sub>Si columns into laminations. Hydrogen gas annealing was used to remove carbon and oxide in the parts cut by EDM. Each sliced laminate had a thickness of approximately 1.4 mm. The design called for the laminate thickness to be 0.18 mm. Common commercial electrical steels have thickness ranging from 0.2 to 0.65 mm.<sup>223</sup> The 3D printed laminates were thicker to avoid warping the sliced part. The laminates were then stacked again for the next step in the manufacturing process. The EDM sliced and stacked 3D printed Fe<sub>3</sub>Si laminates are pictured in Figure 7.8. The estimated printing time of the SLM printing of the monolithic stator core is approximately 280 h. By contrast, the postprocessing, including

machining and EDM slicing, took only 2 h. As previously mentioned, the hot isostatic pressing took about 2 h at the process temperature, and the heating and cooling time totaled approximately 1 h. FDM took most of the overall processing time. Although the 280 h printing time is long, several factors that mitigate the disadvantage of the long print time should also be considered. First, AM is capable of great concurrency. As shown in Figure 7.7, many parts can be printed concurrently, thereby reducing the time per part printed. Second, AM processes such as SLM are capable of multimaterial printing. An end goal of applying AM to stators is to 3D print a multimaterial that has a nonconducting phase and a conducting phase, with the former insulating the latter. Having insulators already within the material eliminates the necessity to create lamination creation and insulation, saving time and resources that would have been committed to these processes. The Paranthaman group has already successfully printed such multimaterials, and results will be published in the near future. (Late 2023 to early 2024) Third, future improvement, development, and optimization of commercial printers will likely reduce the print times.

The next step of the motor fabrication process is to apply electrical insulation to the printed laminates. The laminates were bonded using a mixture of 30  $\mu\text{m}$  glass spheres and Dolph's CC-1105 resin. These insulation materials ensured electrical insulation between the laminates, thereby reducing eddy current loss by reducing the thickness of the conductor. To electrically insulate the laminates from the housing, 3D printed nylon laminates were attached to the top and bottom of the laminate stack. These nylon parts are the gray pieces attached to the stator stack pictured in Figure 7.8. The stators' winding slots were further insulated using DuPont Nomex Kapton tape. This insulating tape is commonly used on electrical motors. Nomex is a type of meta-aramid fiber. Kapton refers to Kapton polyimide film. This tape is the white material folded between the stator teeth in Figure 7.9.

Table 7.2: Nominal process parameters for the printing of the Fe<sub>3</sub>Si stator and induction rings for magnetic property measurements.

Parameters	Value
Power (W)	200
Hatch spacing (μm)	100
Point spacing (μm)	75
Exposure time (μs)	110
Layer thickness (μm)	50

Source: <sup>222</sup>

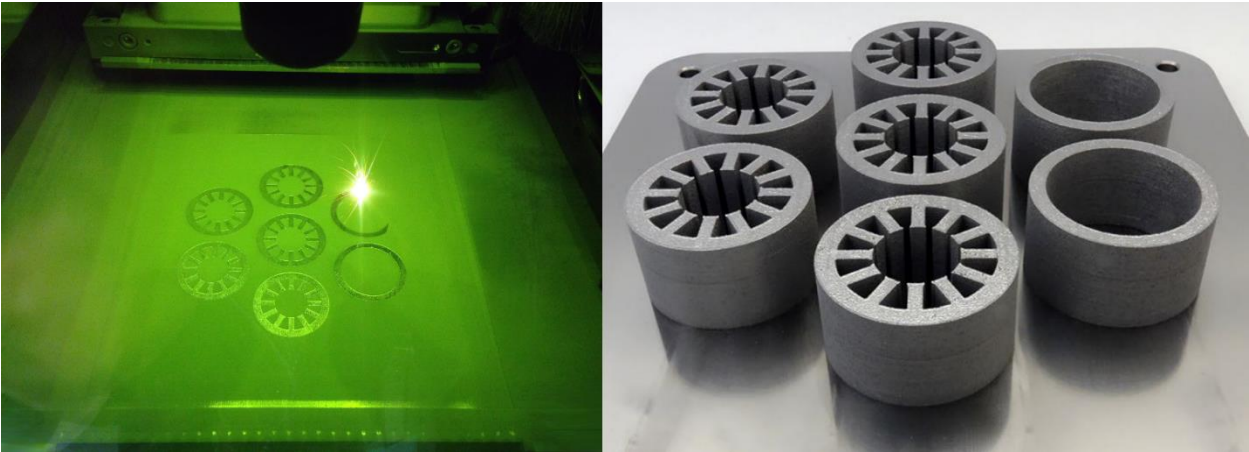


Figure 7.7: Photo of the first layer being printed during the SLM process (left); Completed build of the seven Fe-3Si stator samples in a single run (right).



The next step of electric motor construction is winding. For this motor, 26 American wire gauge (AWG) round copper magnet wire was chosen as the electric wiring. This motor is a three-phase design, so three-phase coils were wound using the aforementioned wiring. Each of these phases consists of 16 eight-turn coil in series using eight parallel strands of wire, which resulted in 128 wires in each of the stator slots, as illustrated in Figure 7.10.

The wound coils were positioned into the core slots and held in place using a top stick made from Nomex Kapton Nomex tape. Nomex Kapton Nomex is like Nomex Kapton, with an additional layer of Nomex, and the two Nomex layers sandwich the polyamide Kapton layer. The tail ends of the phase leads were soldered to a single neutral connection, forming a Wye configuration. The endwindings were compressed with a custom tool so that the stator would fit into the motor housing envelope. The stator windings were vacuum-impregnated with CC-1105 varnish resin to consolidate the insulation and prepare the stator for the motor assembly. A Smartsyn brushless resolver was used to control the motor. After the insulation processing, the stator assembly was placed into the stator housing.

Figure 7.11 shows pictures of the stator being insulated. Figure 7.12 shows the picture of the stator within the stator housing.

The hard magnet of the motor is made via a different process than the soft magnet. The motor hard magnet is a bonded magnet made via the BAAM process. The bonding polymer is PPS. The volume percentage of PPS is 67%, and 33% isotropic NdFeB powder. BAAM is used to print the NdFeB-PPS in a cylinder shape. The cylinder was then installed into the rotor housing, and then magnetized, creating a dipolar rotor core. The remanence, coercivity and energy product of the printed magnets were:  $B_r > 5$  kG and  $H_C > 11$  kOe and  $BH(\max) > 5.7$  MGOe. In the case of the rotor assembly, a single-pole BAAM-printed NdFeB-PPS magnet was installed in the Arnold

magnetic benchmark rotor housing and magnetized. Then, the rotor was assembled into its final state.

A photo of the cross section of the rotor core is provided in Figure 7.13. Note the 3D printed magnet center, surrounded by the steel of the housing. A picture of the completed rotor assembly is provided in Figure 7.14. The important magnetic properties of the rotor magnet after magnetization are provided in Table 7.3.

After both the stator and rotor components have been fabricated, they are assembled together into the final electric motor. Pictures of the fully assembled electric motor are provided via Figures 7.15 to 7.17.

## **7.2 On the Material Characterization of 3D Printed Stator Laminates**

After the EDM process, microscopy samples were made from certain pieces of the 3D printed silicon steel. Optical and scanning electron microscopy were both employed to analyze the samples. Four pieces of the 3D printed laminate were mounted on epoxy and polished to ensure surface smoothness. Two samples were mounted facing the print layers (i.e., the plane of the sample layers). The corresponding images show the flat surface of the sample, parallel to the AM scan direction. Thus, these samples were the scan-direction samples. The other two samples were mounted facing the cross section, perpendicular to the print layers. These images show the lateral view of the samples, and the surface being shown is parallel to the AM build direction ( $z$ -direction). Thus, these samples were the build-direction samples. One scan-direction sample and one build-direction sample were subjected to etching with 4% Nital (a solution of nitric acid and alcohol) to better manifest the sample microstructure for observation under microscopy. The four samples then underwent optical microscopy.

In Figure 7.18, panels (a) and (c) show the as-polished and unetched 3D printed Fe<sub>3</sub>Si in the scan



Figure 7.8: Stacked EDM sliced 3D printed Fe<sub>3</sub>Si laminates.



Figure 7.9: The motor undergoing the winding process.

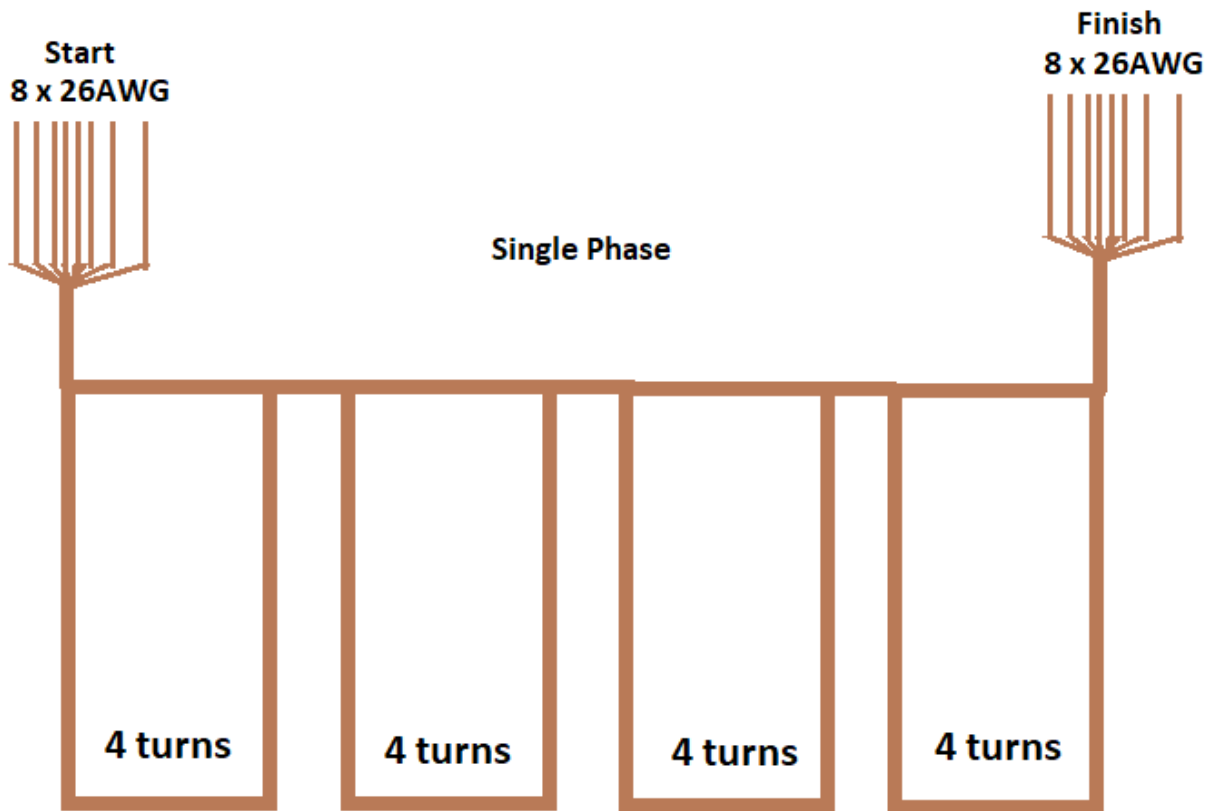


Figure 7.10: Illustration of the winding of a single phase of the three-phase 3D printed motor.



Figure 7.11: The stator assembly submerged in varnish (left); the stator assembly coated in varnish.



Figure 7.12: Stator assembly within its housing.





Figure 7.13: Cross section of the permanent magnet rotor core.



Figure 7.14: The completed rotor assembly.

Table 7.3: Magnetic properties of the 3D printed permanent magnet rotor core.

<b>Material</b>	63 vol% NdFeB, 33 vol% PPS bonded 3D printed magnet
<b>Remanence</b>	5,000 G
<b>Coercivity</b>	11,000 kOe
<b>Energy Product</b>	5.7 MGOe



Figure 7.15: The fully assembled electric motor.





Figure 7.16: Side view of the fully assembled electric motor.

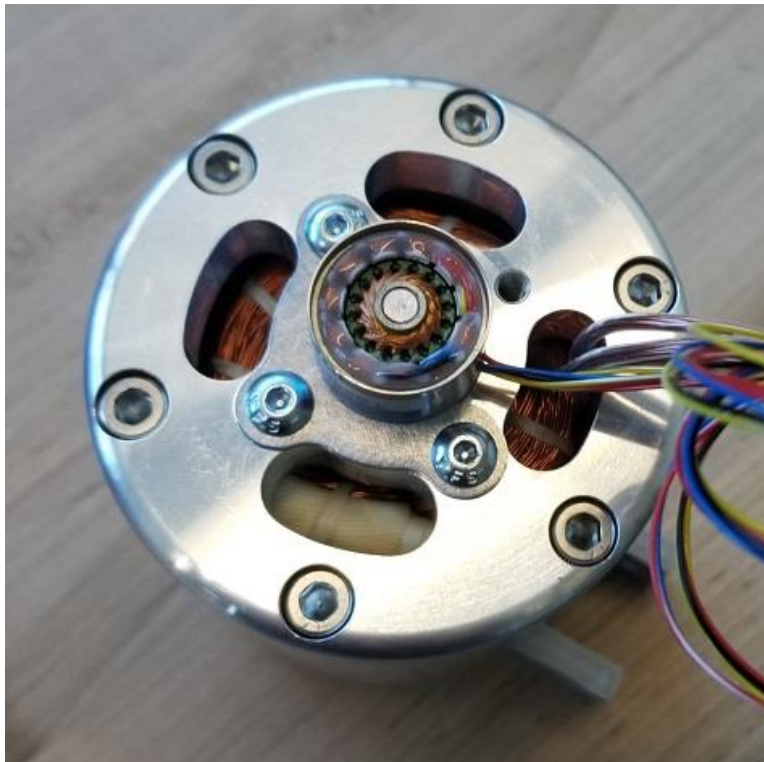


Figure 7.17: Top view of the fully assembled electric motor.

direction and build direction, respectively. The unetched sample surfaces—in the scan direction and build direction—are uniform, indicating the high quality of the samples. Panels (b) and (d) show the corresponding etched versions. The etching yielded more apparent microstructure. The microstructures in the two directions are different. The planar microstructure of the etched scan-direction sample (b) is irregular in shape and size, and some of the grains appear to be equiaxed. The cross-sectional microstructure of the etched build-direction sample (d) looks predominantly columnar. After optimal microscopy, SEM and EDX were performed on the 3D printed Fe<sub>3</sub>Si samples, and the results are shown in Figure 7.19. The SEM was performed on the build-direction sample.

Figure 7.19(a) shows an SEM image of the 3D printed soft magnet laminate. The image is of the area corresponding to the rectangular section highlighted in Figure 7.18(d). The image is parallel to the build direction. A 5kV excitation potential was used to obtain this SEM image. Figure 7.19(b) shows the EDX spectra of the laminate. Panel (c) shows the sample's carbon mapping, panel (d) shows the silicon mapping, panel (e) shows the iron mapping, and panel (f) shows the iridium mapping. The sample did not contain iridium; rather, iridium film was coated on top of the samples to avoid electrostatic charging by the probing electron beam. These elemental mapping images show the uniform distribution of carbon, iron, and silicon and demonstrate the high quality of the printed parts. Analysis of the microstructures observed in the optical microscope and SEM images indicate that the columnar grains are oriented perpendicular to the AM laser scanning direction and parallel to the build direction.

The 3D printed laminates also underwent mechanical materials characterization. Some of the 3D printed material was cut into ORNL SS3 standard sized dog-bone samples for tensile measurements. The samples' average gauge dimensions were  $0.3 \times 0.035 \times 0.065$  in. A servo

hydraulic testing machine (MTN model 810; Eden Prairie, Minnesota) was used to determine the samples' mechanical properties. The machine had hydraulically actuated grips and used a clip-on extensometer with a gauge length of 25 mm. The tensile testing was conducted with a constant crosshead displacement rate of 5 mm/min. Figure 7.20 shows the blueprint of the ORNL SS-3 test sample, the tensile curve obtained from the mechanical testing, and photos of several of the test samples in a horizontal row.

Table 7.4 lists the samples' measured mechanical properties. Mechanical measurements were obtained from 7 samples. The samples averaged 555.6 MPa in yield tensile strength, 624.3 MPa in UTS, and 27.15 GPa in Young's modulus. For reference, commercial grain-oriented electrical steel has yield points ranging from 285 to 358 MPa and tensile strength ranging from 310 to 411 MPa. Commercial grain non-oriented electrical steels have yield points ranging from 256 to 453 MPa, and tensile strength ranging from 358 to 576 MPa.<sup>223</sup> The yield point and the UTS of the 3D printed laminates are both higher than those of the commercial electrical steels. Furthermore, the 3D printed laminate's Young's modulus is typically an order of magnitude higher than that of commercial electrical steels: the 3D printed laminate's modulus is around tens of gigapascals, whereas that of the commercial electrical steels are less than 10 GPa.

In conclusion, mechanical testing results shows 3D printed Fe<sub>3</sub>Si laminates having higher mechanical strength than commercial electrical steel. The 3D printed material has higher yield strength, UTS, and Young's modulus than that of commercial electrical steels.

Some of the printed Fe<sub>3</sub>Si were tested for magnetic and electrical properties. DC and AC properties are different and have differing yet similar measurement methods. DC properties measurement will be discussed first. First, some of the Fe<sub>3</sub>Si feedstock material is printed into a hollow cylinder. Figure 7.21(a) shows a photograph of this cylinder. Then, thin induction rings (with the following

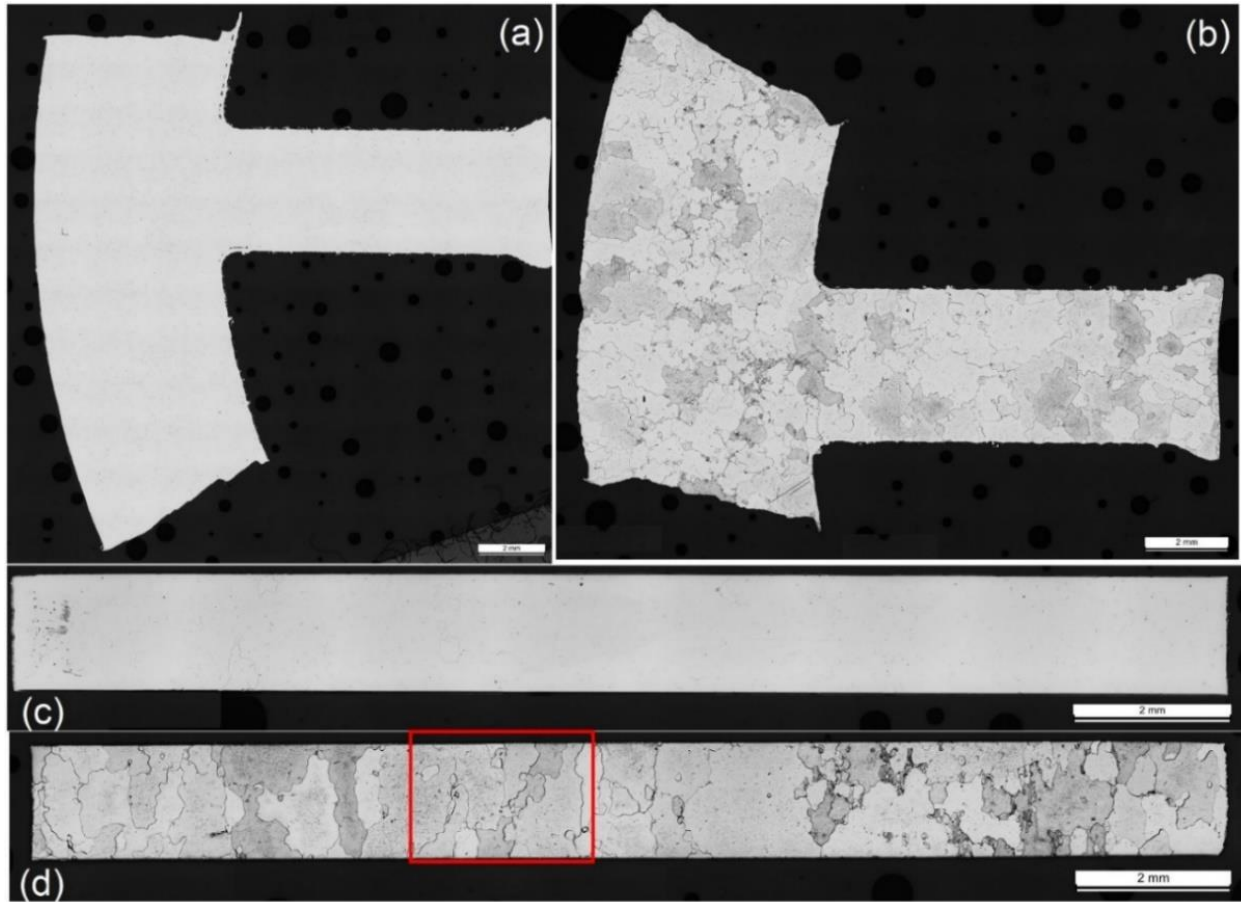


Figure 7.18: Optical microscope images of the 3D printed Fe<sub>3</sub>Si laminate samples.

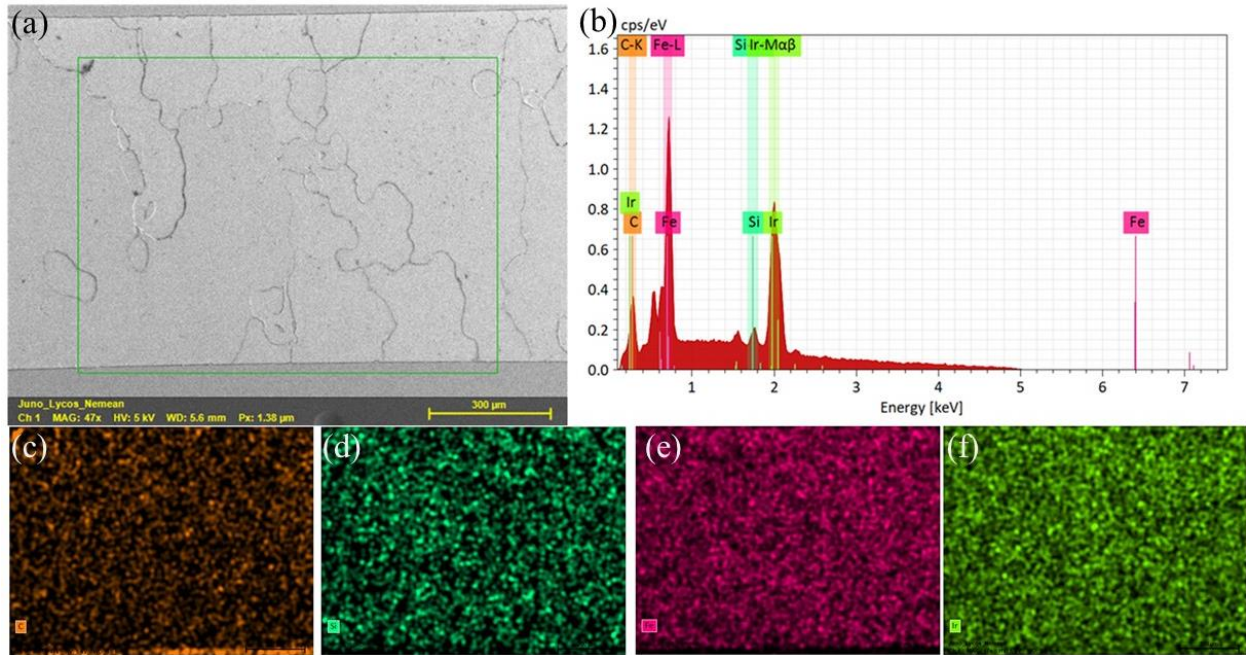


Figure 7.19: SEM/EDX results of 3D printed silicon steel laminate.

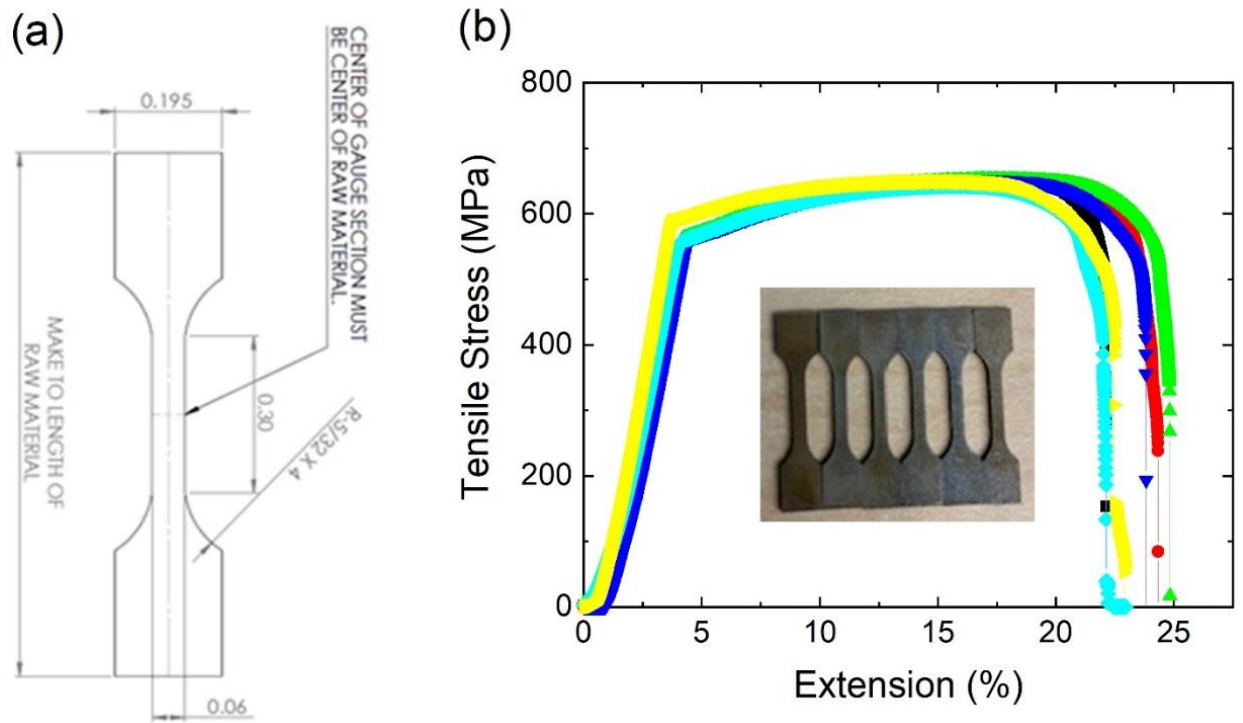


Figure 7.20: (a) ORNL SS-3 standard sample specification; (b) tensile curve chart and picture of the tensile samples.

dimensions: inner diameter:1.757 in., outer diameter: 2.158 in., thickness: 0.05512 in.) were machined from the cylinder to measure DC magnetic and electrical properties. Figure 7.21(b) shows one of these induction rings. Some of these rings will be used for both high- and low-field DC magnetic measurements, as well as to study the influence of heat treatment on the magnetic properties of the 3D printed Fe<sub>3</sub>Si material.

One set of rings was left as printed. Two other sets of rings were annealed under a 4% hydrogen/argon atmosphere at 750°C and 800°C, respectively, in a horizontal furnace, for 2 h. Each ring was then wound with Litz wire. Figure 7.21(c) shows one of these wound rings.

In addition to these induction rings, some of the as-printed Fe<sub>3</sub>Si material was cut into sample pieces for high-field DC magnetization testing. One randomly chosen sample piece was subjected to high-field DC magnetization and was measured in this state via a SQUID. The result of this measurement is presented in Figure 7.22. The right image of Figure 7.22 shows the high-field DC magnetization measured in a randomly chosen cut piece equivalent to an isotropic direction using a SQUID magnetometer at room temperature. The measured saturation induction value of 2.1 T is consistent with conventional Fe-3Si steel products. The left image of Figure 7.22 shows the DC electrical resistivity measured using a conventional four-probe resistance measurement system. The room-temperature resistivity is approximately 50 μΩ·cm, which is comparable to cold-rolled, non-grain-oriented Fe-3Si resistivity.<sup>224</sup>

The previously mentioned and prepared wounded induction rings were then subjected to a low applied magnetic field for further magnetic properties characterization. The magnetic hysteresis loops were measured for the ring samples magnetized up to a low in magnitude DC applied field of approximately 32 Oe, as shown in Fig. 7.23 (left). The corresponding low-field, DC-relative permeability is presented in Fig. 7.23 (right). The coercivity is approximately 0.5 Oe, which is



Table 7.4: Measured mechanical properties of the 3D printed Fe-3Si alloy using ORNL SS-3 standard samples.

Sample number	Yield Tensile Strength (MPa)	Yield Tensile Strain (%)	Ultimate Tensile Strength (MPa)	Ultimate Tensile Strain (%)	Young's Modulus (MPa)
1	573.6	2.157	613.5	17.9	29317.1
2	518.8	2.270	598.7	14.9	25068.1
3	629.2	2.361	638.3	11.0	29117.1
4	553.3	2.326	645.5	15.8	26019.6
5	550.3	2.292	631.9	16.3	26303.4
6	524.2	2.185	611.5	16.3	26404.3
7	539.6	2.100	630.5	24.7	27836.6
Average	555.6	2.200	624.3	16.7	27152.3

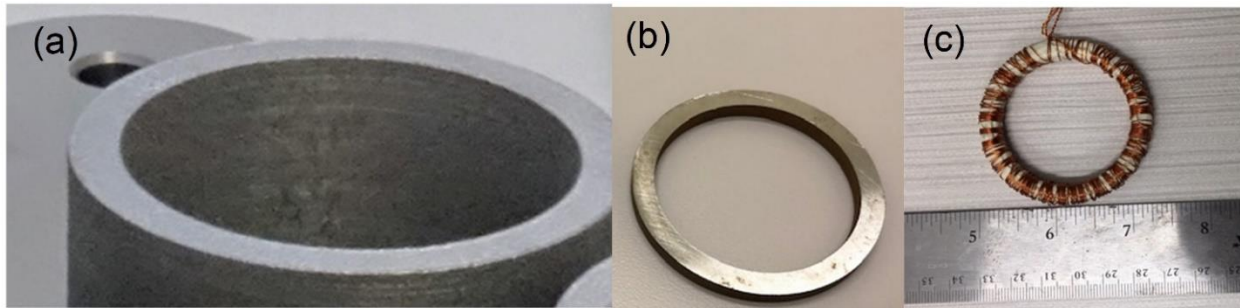


Figure 7.21: Measuring DC properties of a printed Fe<sub>3</sub>Si cylinder. (a) The as-printed Fe<sub>3</sub>Si cylinder, which will be cut into laminates for low magnetic field and AC properties studies. (b) Cylinder laminate that has been machined into a thin induction ring for DC and AC magnetic property measurements. (c) One of the induction rings that has been wound with Litz wire for the induction study.

the range of conventional laminations (25 to 50 A/m, or 0.314 to 0.628 Oe). The maximum relative permeability of 7479 at an applied field of approximately 1 Oe is comparable to that of the rolled, non-oriented electrical steel.<sup>225</sup>

Figure 7.24 presents the comparison of the saturation magnetization and relative permeabilities of the as-printed and annealed samples. The saturation magnetization and maximum relative permeability both increase with heat-treatment temperatures under low applied magnetic field (0–60 Oe). The annealed samples were heated for 2 h in hydrogen gas at high temperatures. Some of the samples were heated at 750°C, and others were heated at 800°C. The left graph of Figure 7.24 compares the magnetic induction curves of the three sample types. The right graph of Figure 7.24 compares the relative permeability curve of the three sample types. The permeability of the three sample types is highly divergent at low magnetic field strength values but converges as the magnitude of the magnetic field strength increases. At 1 Oe, the 800°C samples' permeability is 325.72% that of the as-printed sample. By 20 Oe, the 800°C sample's permeability is only 106.19% that of the as-printed sample. At 50 Oe, the difference is less than 2%: the 800°C sample's permeability is only 101.53% that of the as-printed sample. Nevertheless, high-temperature heat treatment is clearly beneficial for the soft magnetic properties of 3D printed Fe-3Si, especially at low magnetic field strength conditions, which are the typical working conditions for most soft magnetic laminate applications.

The hysteresis loop and permeability of the 3D printed magnets could also be characterized at room temperature via a Hysteresisgraph. The AMH-500 Hysteresisgraph was used to characterize the DC magnetic properties of the 3D printed Fe<sub>3</sub>Si<sup>226</sup> and a 3D printed Fe<sub>6</sub>Si magnet from an earlier experiment.<sup>160</sup> To compare the two materials, Figure 7.25 combines the results of both measurements. The 3D printed Fe<sub>3</sub>Si is superior to 3D printed Fe<sub>6</sub>Si in saturation magnetization,



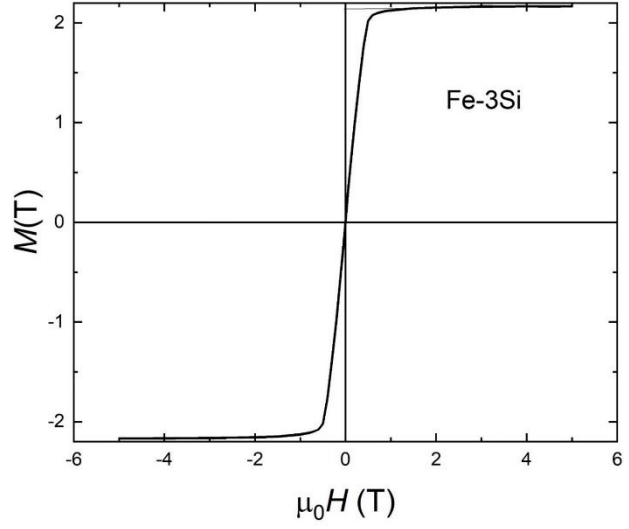
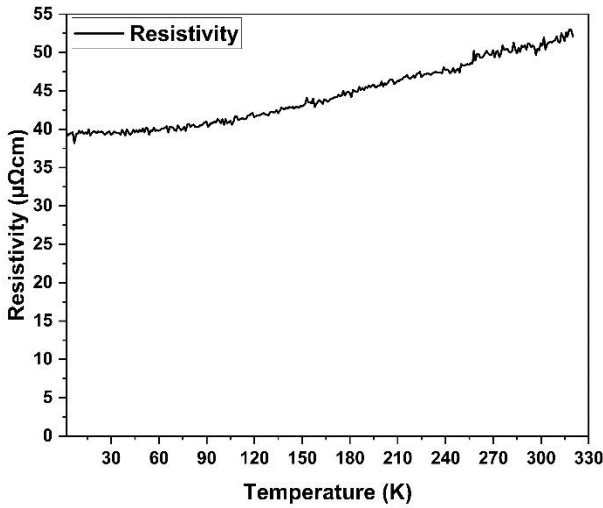


Figure 7.22: Resistivity of AM Fe-3Si vs. temperature (left) ; Hysteresis loop of AM Fe-3Si, under DC magnetization up to a high magnitude of 6 T (right); Saturation induction of approximately 2.1 T is achievable at high magnetizing field values.

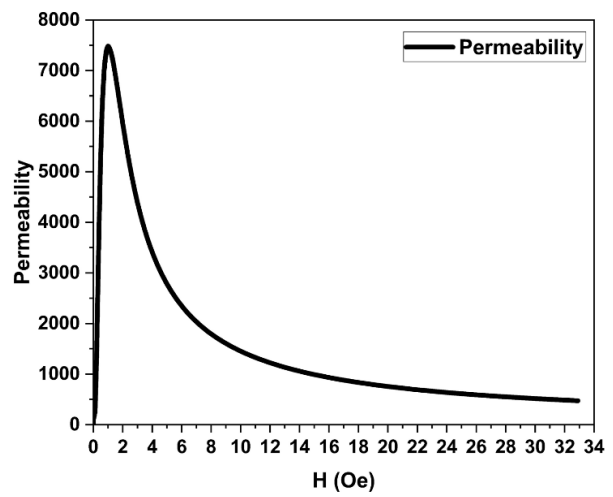
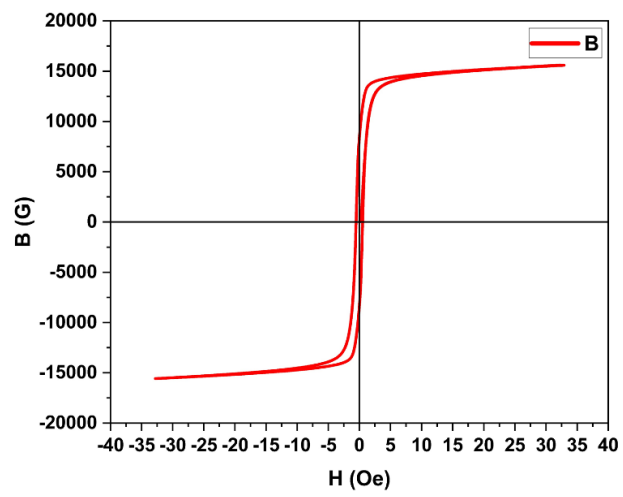


Figure 7.23: Low DC magnetic field hysteresis curve of 3D printed Fe-3Si induction ring (left); relative permeability of the ring across initial magnetization  $H$  field values.

measurements. The 3D printed Fe<sub>3</sub>Si is superior to 3D printed Fe<sub>6</sub>Si in saturation magnetization, whereas 3D printed Fe<sub>6</sub>Si is superior to 3D printed Fe<sub>3</sub>Si in maximum permeability.

The AC properties were measured on as-printed and annealed Litz wire-wound induction ring samples at various combinations of excitation frequencies and magnetic induction. The core losses were measured via an AMH-200K-S permeameter, pictured in Figure 7.26.<sup>227</sup>

The losses were measured using an AMH-20K-S AC hysteresis graph. Table 7.5 shows the results for the as-printed samples, the 750°C samples, and the 800°C samples. The core loss results are in watts per pound (W/lb). Table 7.5 can be split into two sections. The upper section contains the three 60 Hz tests at varying induction levels. The lower level contains the data from tests at 400 Hz and above. At low frequencies, core losses in the samples were low. Core loss increases with frequency and peaks at around 5,000 Hz. At higher frequencies, core loss begins to decrease. Fixing frequency at 60 Hz and varying induction reveals that core loss increases with increasing induction. The difference in core loss between the two annealed samples at the fixed frequency is small across all induction values. At all combinations of frequency and induction, under the same test conditions, the as-printed sample exhibits more loss than the 750°C sample, which exhibits more loss than the 800°C sample. This trend holds except for two cases in Table 7.5. In the 60 Hz 15,000 G case, the core loss values of the three sample types are extremely close, but measurement inaccuracies could explain this result. The same explanation can be applied to the 1,000 Hz 5,000 G results. Post-hydrogen annealing was performed to remove carbon or oxide impurities present on the printed parts, and 750°C and 800°C temperature annealing was chosen based on the Fe<sub>3</sub>Si data sheet available from Carpenter. The data in Table 7.5 suggest that annealing reduces core loss in 3D printed FeSi. The higher the annealing temperature, the lower the core loss. In addition to boosting saturation magnetization and relative permeability, heat treatment could also

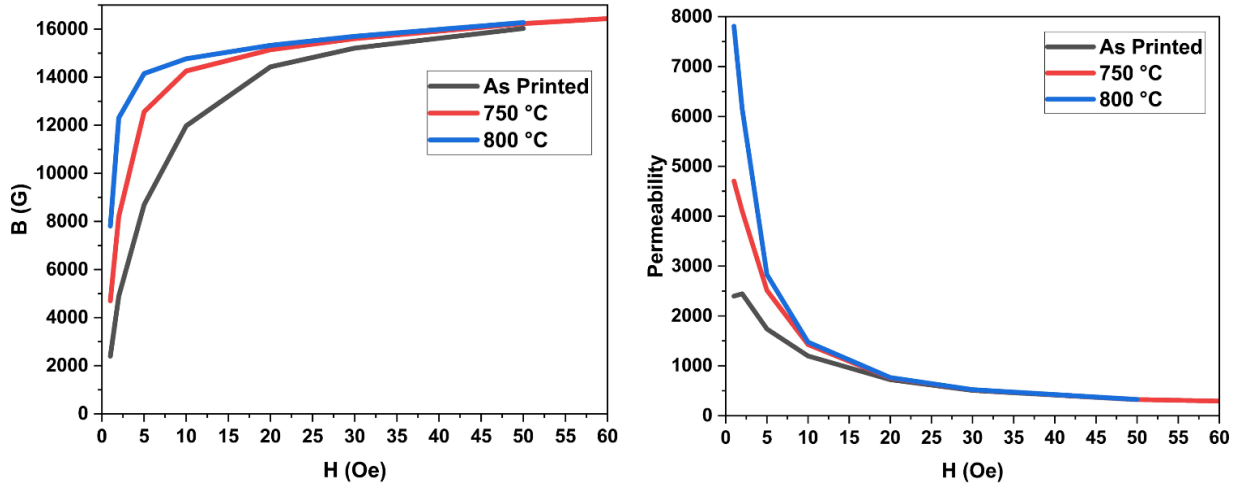


Figure 7.24: Effect of heat treatment on the magnetic induction (left) and Relative permeability (right) of the as printed and heat-treated Fe-3Si laminates; Higher the annealing temperature, higher the B or permeability values.

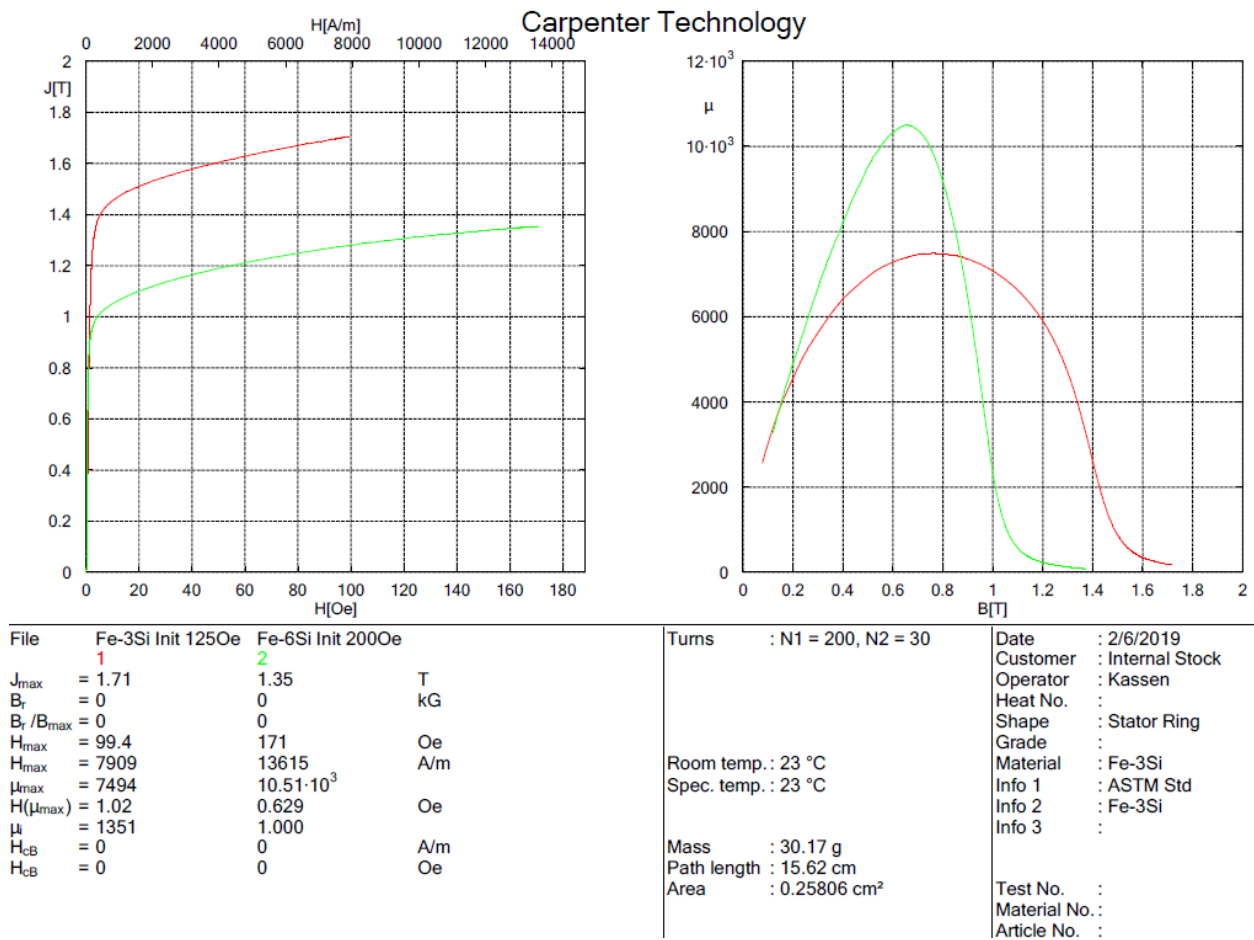


Figure 7.25: Comparison of 3D printed Fe3Si vs. 3D printed Fe6Si.<sup>160</sup>

reduce core losses in 3D printed Fe<sub>3</sub>Si.

The results of the core loss measurements at a fixed 60 Hz frequency are illustrated in Figure 7.27. The annealed samples have lower core loss at all induction values. However, the core loss differences between the two annealed samples are very small and are vulnerable to measurement inaccuracies.

The DC and AC magnetic properties of the 3D printed Fe<sub>3</sub>Si, the previously obtained data for 3D printed Fe-3Si, and data from commercial electrical steel sheets from JFE Steel are listed in Table 7.6.<sup>223</sup>

The 3D printed laminates could be cut to only 1.4 mm because the EDM machine's cutting capabilities were limited. By contrast, the thickest laminate on JFE Steel's electrical steel sheet catalogue is 0.65 mm, and thinner options are available. This discrepancy explains the higher core loss from the 3D printed samples compared with the commercial laminate. The 3D printed laminate's other properties are all similar to, or exceed, those of the commercial laminate. If the 3D printed laminate could be sliced thinner, or if multimaterial printing with the insulating layer printed between conducting layers were possible, then the core loss disadvantage could be resolved, and 3D printed Fe-3Si laminate could become a legitimate competitor to commercial electrical steel.<sup>223</sup>

Electrical motors convert electrical energy into mechanical energy. These motors work by sending a current through a loop of wire in a magnetic field. This loop generates another magnetic field that interacts with first magnetic field, and the magnetic field that is not fixed in place rotates and is the field of the motor's rotor. The rotor rotates with the motor's shaft, thereby creating mechanical work. When the motor's two magnetic fields are in relative motion to each other (e.g., when one field is rotating relative to the other), the wiring (an electrical conductor) is in a changing

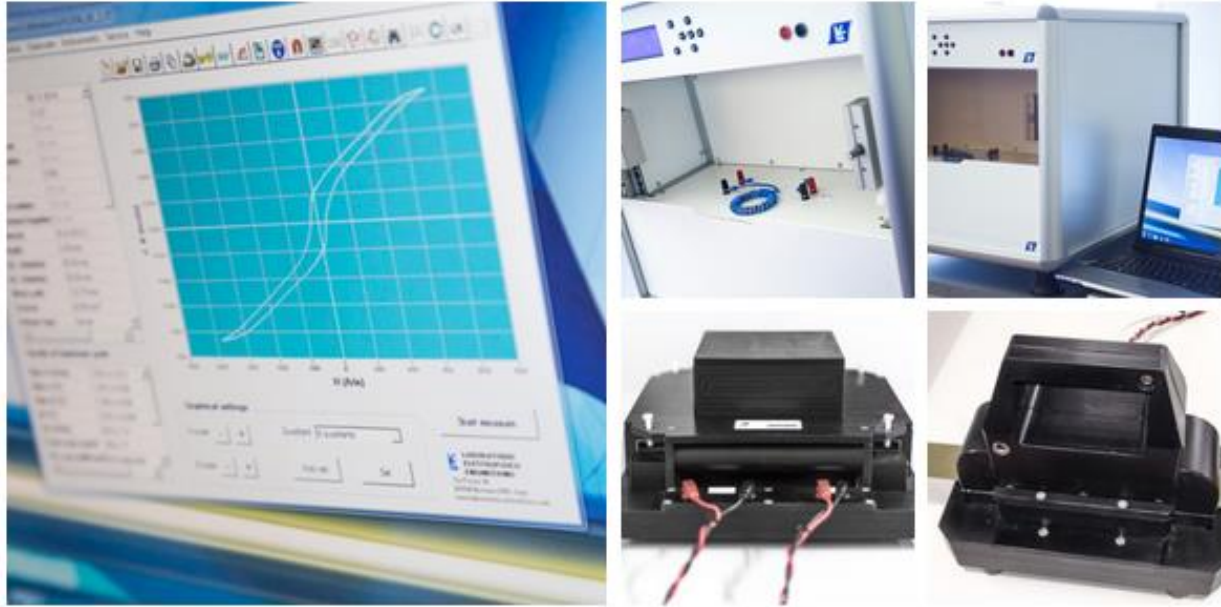


Figure 7.26: The Laboratorio Elettrofisico AMH-200K-S permeameter system.<sup>227</sup>

Table 7.5: AC magnetic properties of as-printed and 4% hydrogen–argon atmosphere annealed 3D printed Fe-3Si rings.

<b>Fe-3Si test freq (Hz)</b>	<b><math>B_m</math> (G)</b>	<b>As-printed core loss (W/lb)</b>	<b>750°C-2h core loss (W/lb)</b>	<b>800°C-2h core loss (W/lb)</b>
60	5000	1.72	1.11	0.911
60	10000	8.65	6.22	5.76
60	15000	21.5	19.6	20.3
400	5000	40.2	30.1	28.3
1000	5000	173	166	166
5000	2000	336	268	254
10000	1000	222	149	134

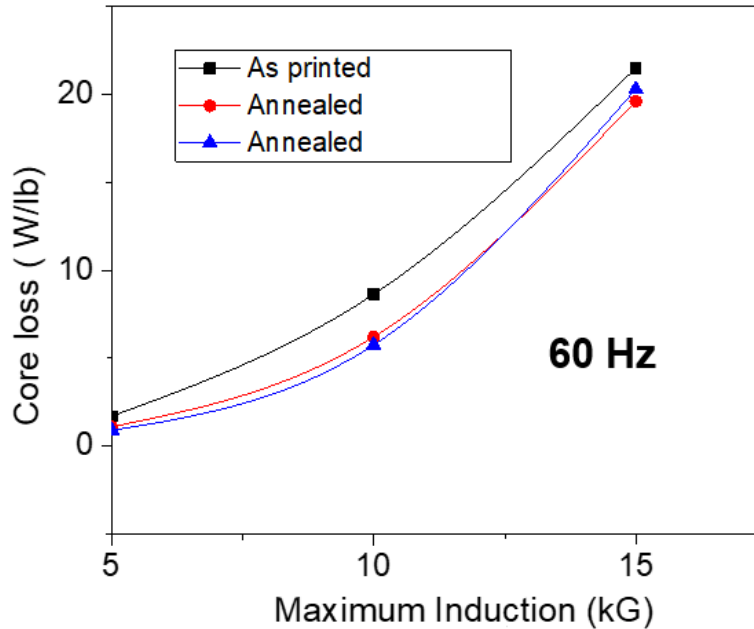


Figure 7.27: Core loss vs. induction of the 3D printed Fe3Si at 60 Hz.

Table 7.6: Comparison of magnetic and Electrical properties of conventionally processed electrical steel and SLM 3D printed Fe3Si laminates.

Properties	Conventionally processed	SLM-printed and EDM-cut ring samples
Lamination thickness	0.65 mm	1.4 mm
Measured induction, $B_m$ , and saturation magnetization, $M_s$ (T)	$M_s$ : 1.46–1.98 <sup>223</sup>	$B_m$ : 1.72 at 100 Oe field $B_m$ : 1.57 at 30 Oe field $M_s$ : 2.1 at higher field
Coercivity, $H_c$ (Oe)	25–50 Am <sup>-1</sup> (0.314–0.628 Oe) <sup>228</sup>	0.5
Resistivity, $\rho$ ( $\mu\Omega\cdot\text{cm}$ )	~50 <sup>229</sup>	50
Maximum permeability (non-oriented)	3,000–9,000 <sup>225</sup>	7,494
AC core loss, (W/lb)	4.6–9.22 (60 Hz, 1.5 T) at 0.65 mm thickness <sup>223</sup>	~20 (60 Hz, 1.5 T) at 1.4 mm thickness
Tensile strength (MPa)	>400 <sup>230</sup>	555.57

magnetic field. Faraday's law of induction implies that the wiring produces an electromotive force (EMF). Lenz's law implies that this induced EMF will oppose the initial input EMF that powers the motor. Thus, this induced EMF is the back EMF of the motor. The generator output of the motor is the difference between the supply voltage and the back EMF. The back EMF is zero when the motor is first turned on because rotation has not begun. When the coil receives full driving voltage, the current is at the maximum, and the motor is on but not yet turning. As the motor turns faster, the back EMF increases, reducing the overall voltage and current of the motor. Back EMF needs energy to overcome it, thus EMF reduces the motor's energy efficiency, and therefore should be minimized to reduce energy usage.<sup>231</sup> The assembled 3D printed motor was subjected to back EMF testing. The 3D printed motor was rotated by an external drive and without any excitation current into the 3D printed motor. The 3D printed motor therefore acts as a generator, and rotating PMs produce only the induced back EMF on the stator coils. The back EMF manifests as voltage in the measurement results. The results of the back EMF measurement of the assembled brushless 3D printed PM motor are illustrated in Figure 7.28.

The back EMF is very low for a motor of such size, possibly owing to the polymer content of the 3D printed PMs. Back EMF is caused by the interaction between the electromagnetic field of the stator and the permanent magnetic field of the rotor. The 3D printed PM has PPS filler polymer content, which does not contribute to magnetic field formation and is electromagnetically inert. Thus, the permanent magnetic field is quite weak, and cannot offer enough resistance to the stator field; therefore, the assembled motor has low back EMF. Nevertheless, the low back EMF is attributable to the low permanent magnetic field, thereby resulting in a low-efficiency motor. Better 3D printed PMs of higher energy product must be created for an energy efficient motor. Current research is constantly improving the energy product of 3D printed PMs, so energy

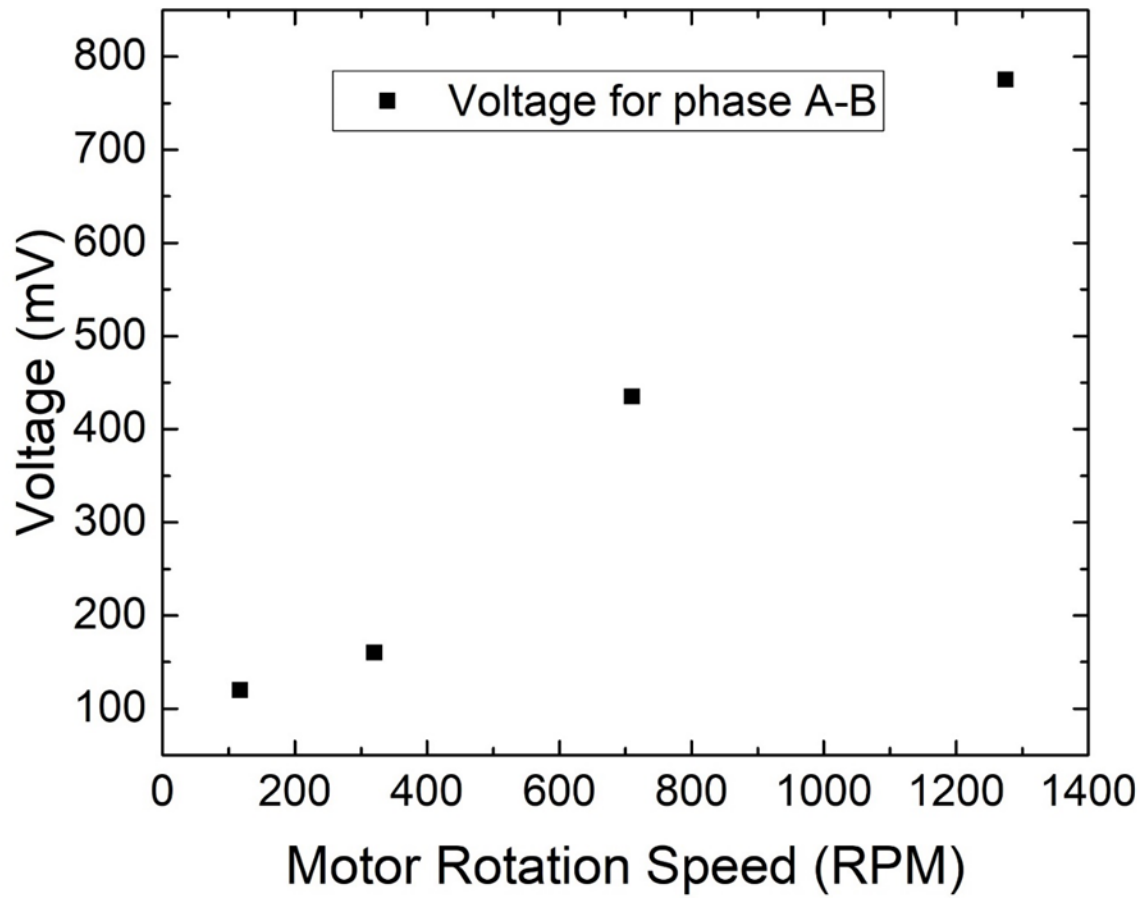


Figure 7.28: Measured back EMF for the 3D printed motor at various RPMs.



efficiency of 3D printed motors will continue to improve.

## **CHAPTER 8 : FUTURE RESEARCH DIRECTIONS**

## **8.0 Future Research Directions for 3D Printed Magnetic Materials**

This chapter presents future research directions of the AM of magnetic materials. Although the research of 3D printed magnetic materials has made tremendous progress, major research goals ahead remain to be sufficiently investigated. By hitting these future research targets, the materials properties, commercial viability, and applicability of 3D printed magnets could be further improved. Research on 3D printed magnets is still in its early stages, and the best is yet to come!

### **8.1 On the Additive Manufacturing of Multimaterial Stators for Electrical Machines**

Laminations in electrical steel cores reduce eddy current loss. The smaller the surface area facing (and perpendicular to) the magnetic flux direction, the less eddy current is induced, and the lower the energy loss from heat from the eddy currents. Reducing energy loss from eddy current allows for more efficient electrical machines. Traditionally, laminating the electrical steel is the only method of reducing eddy current loss. With AM, by combining the conducting material with a second insulating material, eddy current loss could be reduced without laminating the electrical steel core. This strategy saves capital and time from the lamination process, allowing single-piece solid electrical steel cores, thereby expanding the design possibilities of electrical machines. Two main processes can achieve this goal with AM. One is to distribute the insulating material evenly within the conducting material. The other method is to employ dual-feed AM to print alternating layers of conducting and insulating material. Both methods are described in the subsequent subsections.

#### **8.1.1 Premixing Aluminum Alloy with Fe-3Si and made via SLM**

By distributing an insulating material within the silicon steel, the insulating material can subdivide the silicon steel, yielding smaller pieces of conducting material in which the eddy current can flow. Two AM methods could achieve this result. The first AM method is to premix aluminum alloy

powder with Fe-3Si powder into feed for SLM. Figure 8.1 shows photographs of this process. After SLM, the 3D printed pieces are annealed to oxidize the aluminum alloy into the insulator alumina. This process causes the insulating material to subdivide the conducting material, eliminating the need for laminations.

Figure 8.2 is an Ellingham diagram of several relevant materials. In the diagram, the lower a material's line is along the vertical axis, the more the material is preferentially oxidized. These materials oxidize before other materials in that test condition. Figure 8.2 shows that aluminum will always have preferential status over the silicon and iron materials in the range of temperature and atmospheric condition covered by the diagram. Aluminum was chosen as the insulating material because so it oxidizes first during heat-based postprocessing.

Several pieces of the 3D printed multimaterial stator samples were annealed at various atmospheric and temperature conditions. In Figure 8.3, the table on the left states the experimental conditions of the samples and includes a picture of the sample after the annealing. The right side of Figure 8.3 shows the change in the resistivity of the samples after annealing, relative to the as-printed sample. Annealing at 800°C in a dry argon–hydrogen environment offered the best increase in resistivity. Optimizing the annealing conditions for the 3D printed multimaterial stator remains an ongoing research subject.

### **8.1.2 Premixing Alumina with FeSi and Made via BJT**

The second AM process is to premix alumina powder with FeSi powder into feed for BJT. After BJT, the 3D printed pieces can be sintered to increase their density. This strategy also causes the insulating material to subdivide the conducting material, eliminating the need for laminations. Initial steps have been taken in this research direction.

BJT was employed to print four FeSi samples: (1) Fe<sub>3</sub>Si; (2) Fe<sub>3</sub>Si premixed with alumina, the Fe<sub>3</sub>Si multimaterial composite; (3) Fe<sub>6</sub>Si; and (4) Fe<sub>6</sub>Si premixed with alumina, the Fe<sub>6</sub>Si

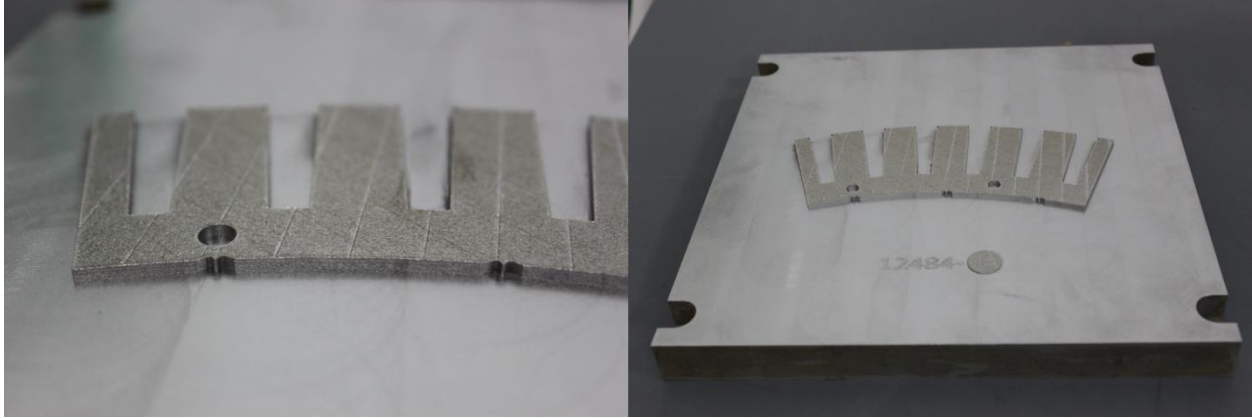


Figure 8.1: Multimaterial 3D printed stators; FeSi premixed with 1–2 wt% AlSi10Mg and printed via SLM.

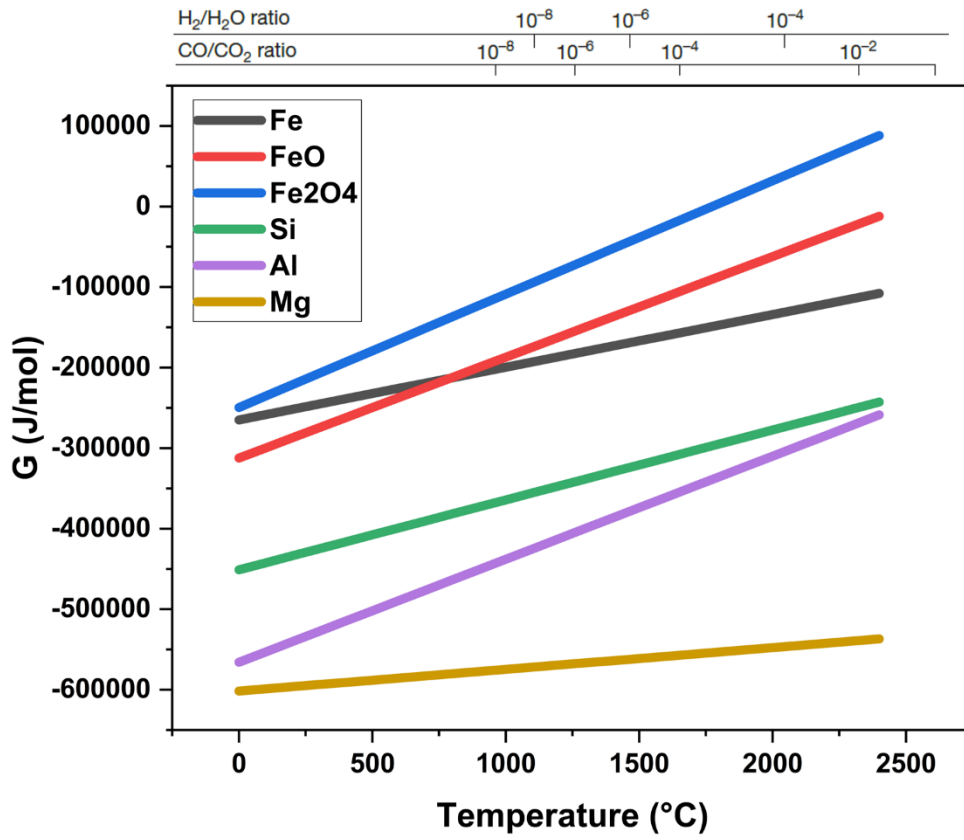







Figure 8.2: Ellingham diagram of various materials.

Annealing Temperature Conditions	Atmosphere	Picture of Sample
As-printed	Ar/H <sub>2</sub>	
600°C, hold 2 hrs	Ar/H <sub>2</sub>	
800°C, hold 2 hrs	Ar/H <sub>2</sub>	
800°C, hold 2 hrs	Ar/H <sub>2</sub> , Wet gas	
600°C, hold 2 hrs	Pure Ar	

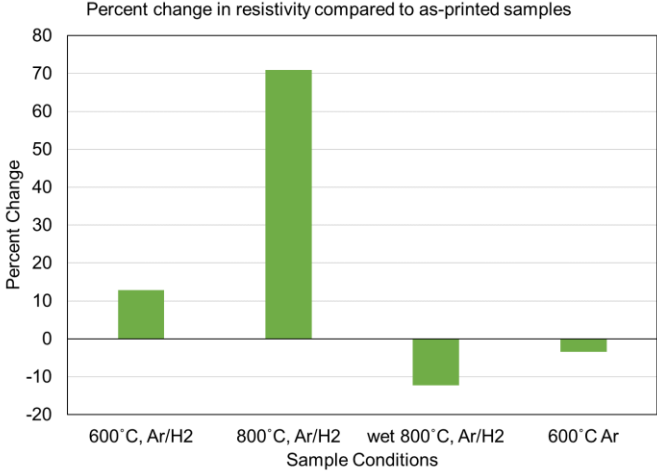


Figure 8.3: Several 3D printed multimaterial stator samples underwent annealing. (left) Annealing conditions of 3D printed multimaterial stator samples and (right) change in percentage of resistivity caused by annealing compared with as-printed samples.

multimaterial composite. All four were printed and then annealed at 300 K in an argon atmosphere. Then, their material properties were measured. These properties are listed in Table 8.1.

These test results were unexpected. The alumina was expected to help increase the material's resistivity. Instead, resistivity decreased compared with the sample without alumina. Permeability results were also quite strange. Alumina Fe<sub>3</sub>Si had half the maximum relative permeability than that of Fe<sub>3</sub>Si, but alumina Fe<sub>6</sub>Si had a higher maximum relative permeability than that of Fe<sub>6</sub>Si. Addition of alumina has an uncertain effect on permeability. The alumina addition did not seem to affect the saturation magnetization of Fe<sub>3</sub>Si, but it significantly decreased that of Fe<sub>6</sub>Si.

These initial experiments have not yielded conclusive results. Work on this research direction has only just begun. More printing and testing of the material, as well as optimization of the heating conditions, premix compositions, and printing settings, are needed.

Figure 8.4(left) compares the magnetization of the four samples, and Figure 8.4(right) compares the permeability of the four samples.

### **8.1.3 On the Layer-by-Layer Dual-Feed Approach**

Existing 3D printers with dual-feed capability could be employed to print alternating layers of conducting and insulating material. The first feed could be the conducting material such as silicon steel. The second feed could be insulating material such as alumina or other insulating metals/alloys. This process prints insulating layers between conducting layers, eliminating the need for laminations.

## **8.2 Future Direction of the Additive Manufacturing of Permanent Magnets**

This subsection describes the future research targets of the 3D printing of PMs. Although much progress has been made toward improved magnetic strength of 3D printed PM, the energy products of the 3D printed PMs are still not as high as that of sintered NdFeB. To further improve the energy

Table 8.1: Material properties of the four 3D printed FeSi samples.

Samples	Max relative permeability	Theoretical density (g/cc)	Measured density (g/cc)	Resistivity at 300K ( $\mu\Omega\cdot\text{cm}$ )	Saturation magnetization at 3T field (T)
1. Fe <sub>3</sub> Si	21.39	7.6	6.97	50	1.55
2. Fe <sub>3</sub> Si-Al <sub>2</sub> O <sub>3</sub>	10.92	7.55	6.78	33	1.55
3. Fe <sub>6</sub> Si	6.15	7.34	6.87	93	1.44
4. Fe <sub>6</sub> Si-Al <sub>2</sub> O <sub>3</sub>	9.75	7.3	6.84	70	1.34

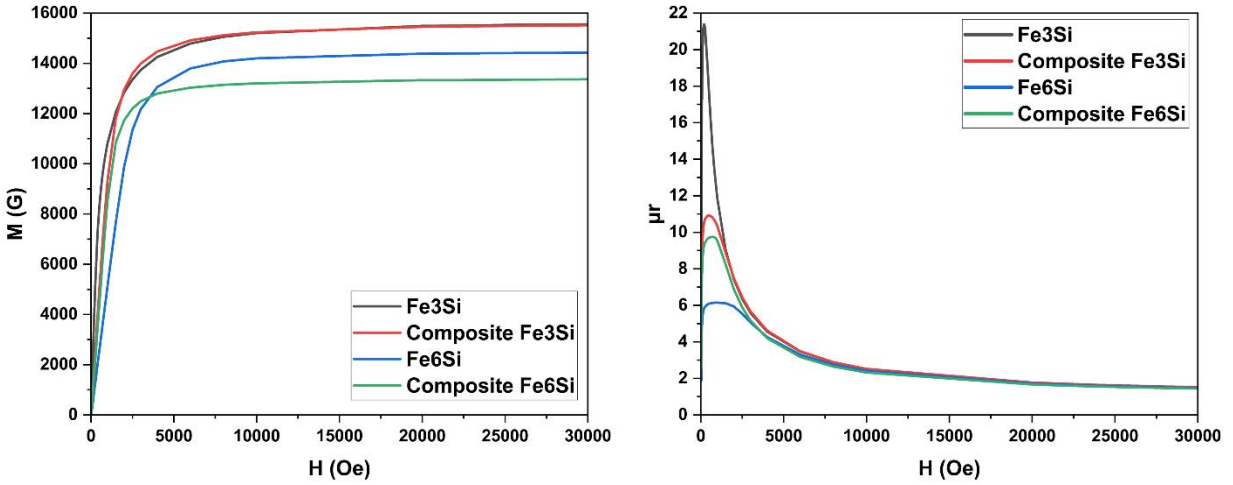


Figure 8.4: Comparing magnetic properties of the four samples. (left) H vs. M and (right) H vs.  $\mu_r$ .



product of 3D printed PMs, magnetic alignment techniques will be explored. Currently, the magnetic material powders are distributed evenly within 3D printed magnets. However, the magnetic material is often not needed everywhere within an application. By tailoring the distribution of magnetic materials with an 3D printed PM, critical materials could be conserved.

### **8.2.1 Magnetic Alignment of 3D Printed Permanent Magnet to Further Improve their Magnetic Properties**

This subsection describes a recent experiment in high-temperature magnetic alignment. First, an 3D printed NdFeB was made via BAAM. Immediately after fabrication, this premade 3D printed magnet was not magnetized. The premade 3D printed magnet was then put inside a superconducting magnet machine with heating facility. Throughout the heating process, from the start of heating to the ambient cooling to room temperature, the premade magnet was within a 5 T field created by the superconducting magnet machine. The premade magnet was heated from room temperature to 220°C (493.15 K) in 2 h. The magnet was kept at this temperature for 1 h. Then the premade magnet was ambient-cooled to room temperature. Then, the 5 T field was shut off, and the premade magnet was the “as-received” state of Step I.

The next phase begins with aluminum alignment fixtures. These fixtures hold the 3D printed PM pieces. Premade 3D printed PMs are cut into pieces that can be inserted into the fixture, and then the fixture is heated to a high temperature while within a magnetic field. Heating makes the grains within the 3D printed PM easier to align, and the magnetic field aligns the grains of the 3D printed PM. In this phase, the magnetic alignment and heating are done via SQUID machine instead of the superconducting magnet machine of the previous phase. Figure 8.5(a,b) shows photographs of the aluminum alignment fixtures. Different shapes can be machined into the aluminum block for insertion of 3D printed PMs. Figure 8.5(c) shows a fixture with 3D printed NdFeB inserted into it.

Figure 8.5(d) shows the superconducting magnet that generates the magnetizing field and can heat the 3D printed PM.

Table 8.2 lists the five major steps in a magnetic alignment experiment that was performed according to the aforementioned alignment method. In Step I, premade as-received 3D printed NdFeB was inserted into a fixture. The fixture was then heated to 300 K and underwent a hysteresis cycle at that temperature. The magnetizing field was provided by the SQUID machine. In Step II, the magnet samples were brought under a fixed 2 T magnetizing field. The magnets were heated from 300 K to around 525 K and then cooled to 300 K. The red arrows in Figure 8.6(left) indicate the direction of experiment. The magnetization vs. temperature curve is shown in Figure 8.6(left). The heating action resulted in high magnetization when the sample returned to 300 K. The magnet was already highly aligned, but the heating further increased the magnetization. In Step III, the temperature was kept at 300 K, and the magnets underwent another hysteresis cycle. In Step IV, the temperature was kept at 400 K, and the magnets underwent another hysteresis cycle. In Step V, the temperature was kept at 300 K, and the magnets underwent another hysteresis cycle. The hysteresis loops of Steps I, II, III, IV, and V are shown in Figure 8.6(right). The loops of the 300 K steps (I, II, V) are nearly identical, whereas the 400 K step (IV) has a much smaller and narrower loop. Heating the magnets to 400 K significantly degrades their magnetic properties; however, this damage can be reversed by reducing the temperature to 300 K.

The second quadrant of the hysteresis loop of Step III is enlarged and presented in Figure 8.7. The magnetic induction curve and the energy product curve are both provided. This image reveals that, at Step III, the coercivity of the samples are approximately 6.3 kOe, the remanence 9,007.51 G, and the energy product 14.057 MGOe.

The key magnetic properties of the magnets are Steps I, III, IV, V are listed in Table 8.3. The magnetic properties of the 300 K steps (I, III, and V) are nearly identical. The 400 K step (IV) has much lower magnetic properties. Step III has a small improvement in magnetic properties compared with Step I. The heating action improved the magnetic properties by increasing the magnet's degree of alignment. Future work involves further optimization of the alignment of additively manufactured PMs.

### **8.2.2 The 3D Printed Permanent Magnet with Tailorable Gradient Concentrations of Critical Materials**

Another goal of 3D printing PMs is control over the concentration of critical materials within the 3D printed PM. PMs are often composed of light rare earth elements, such as neodymium or samarium, or the even more critical heavy rare earth elements, such as dysprosium. Dysprosium, for example, plays two critical roles within PMs. It increases the working temperature of the PM and allows it to maintain its magnetic properties at higher temperatures without degradation. Dysprosium also improves the PM's coercivity. Coercivity is a measure of the PM's resistance to demagnetization from another magnetizing field. Figure 8.8 shows photographs of 3D printed PMs, some with a film covering them. The film manifests the magnetic field of the PMs. Magnetic field intensity is indicated by brightness on the film. The surface of the magnet experiences the highest magnetic flux. Dysprosium need not be distributed throughout the entire magnet to accomplish this goal. Dysprosium can accomplish its main functions by just being on the PM's surface and does not need to be present in the interior of the magnet. Concentrating dysprosium on the magnet's surface allows it to form a protective shell for the PM against high temperature or magnetic field demagnetization. Thus, it is possible to create a PM that uses less dysprosium by concentrating it on the PM's surface. This PM can have equivalent or better magnetic performance than PMs with dysprosium distributed evenly within. Using this so-called dysprosium armor can

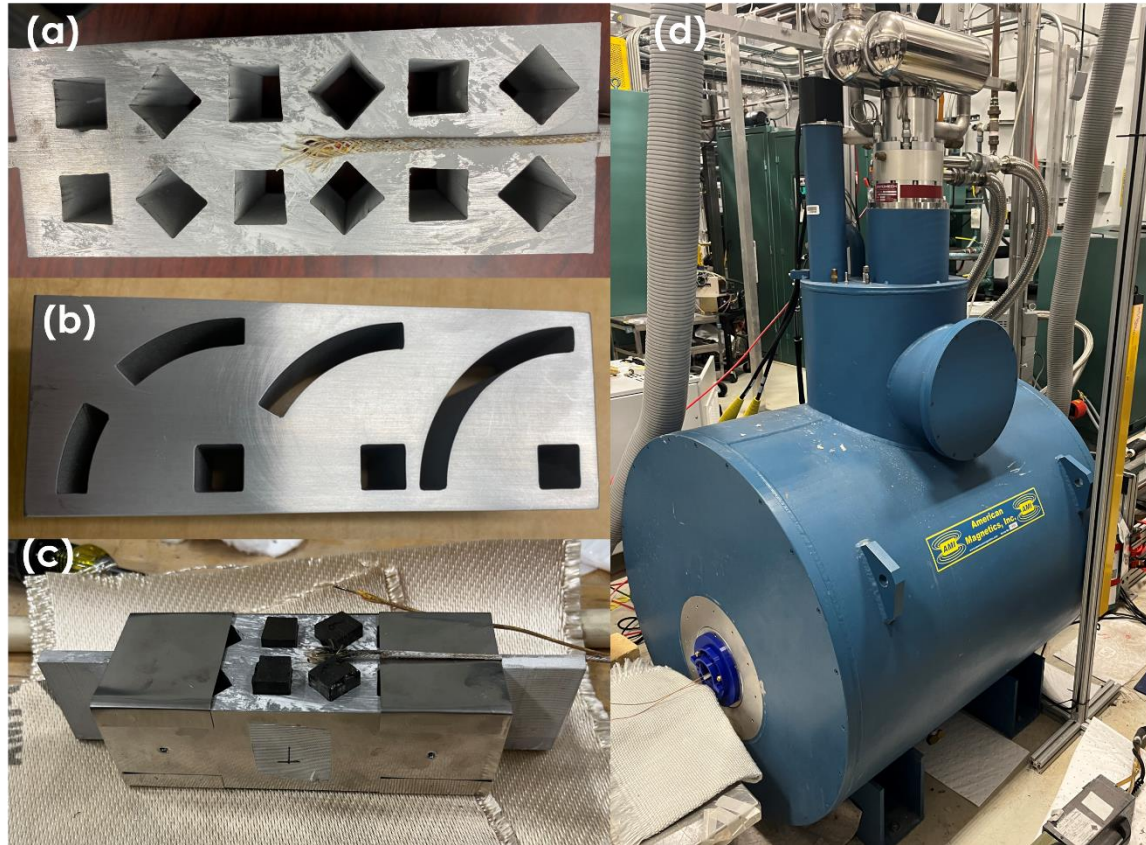


Figure 8.5: Magnetic alignment of 3D printed permanent magnets. (a) and (b) the aluminum alignment fixtures. (c) A fixture with 3D printed NdFeB within it. (d) A superconducting magnet with heating capability.

Table 8.2: The five steps of the magnetic alignment experiment.

Step	Temperature (K)	Magnetizing field $H$ (T)	Notes
I	300	Variable	As-received
II	Variable	2	$H$ constant at 2 T
III	300	Variable	-
IV	400	Variable	-
V	300	Variable	-

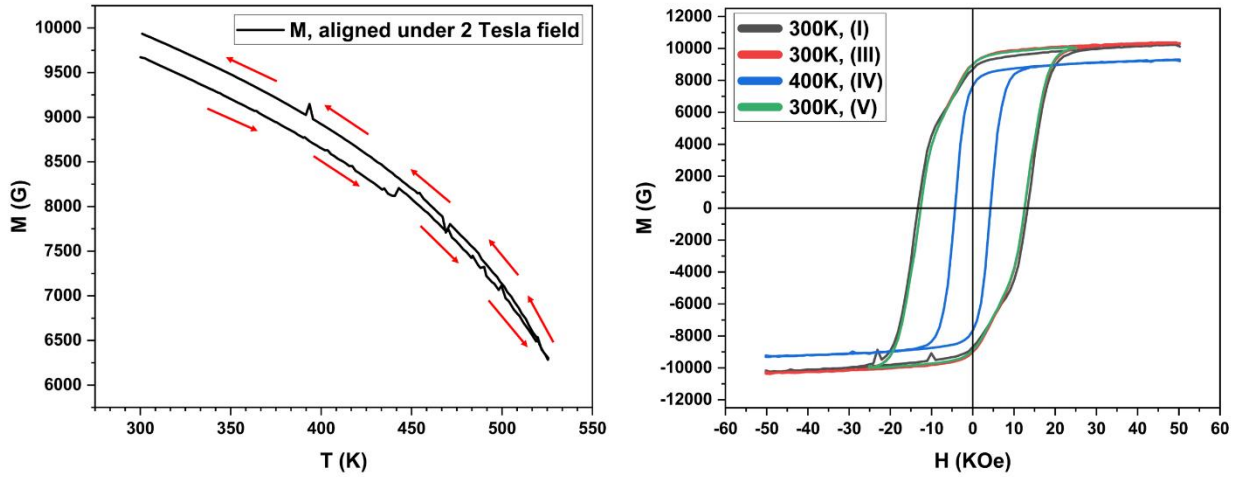


Figure 8.6: Magnetic alignment experiment results. (left) The magnetization vs. temperature curve of Step II of the experiment; the red arrows indicate the direction of the experiment. (right) The hysteresis loops of Steps I, III, IV, V of the experiment.

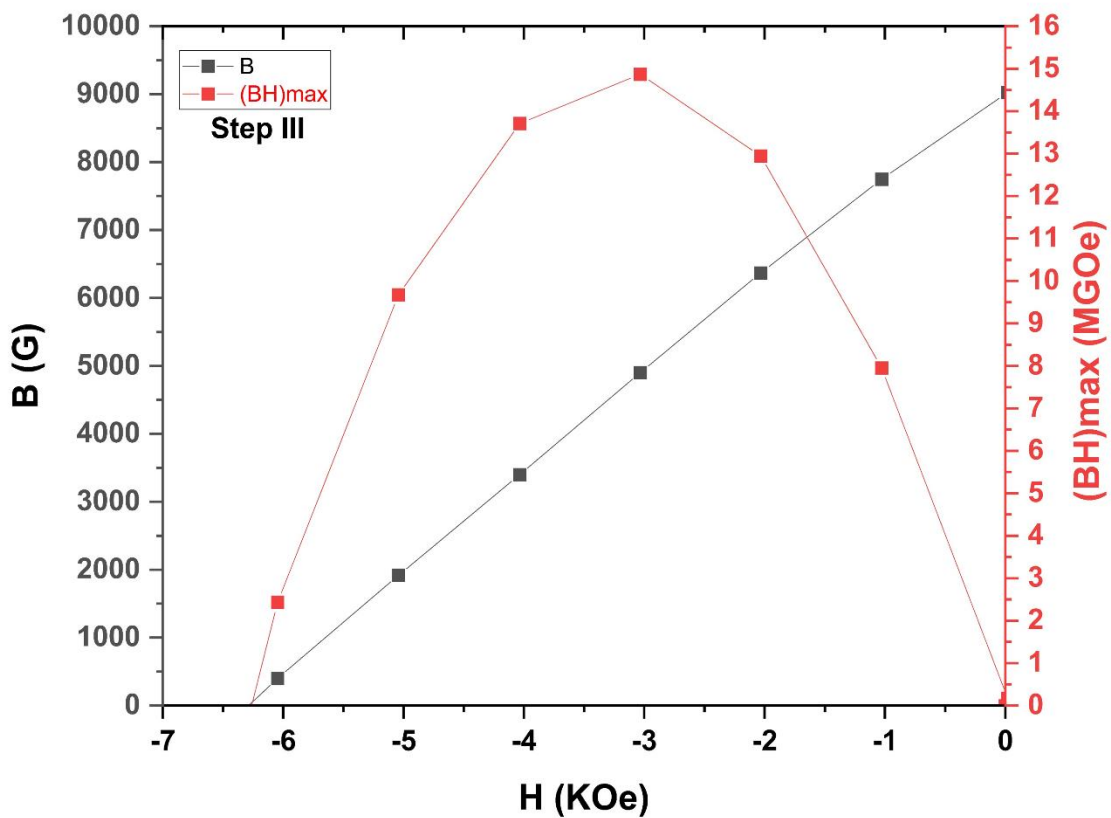


Figure 8.7: Second quadrant of the Step III hysteresis loop. The magnetizing field  $H$  vs. the magnetic induction  $B$  and the energy product  $(BH)_{max}$ .

Table 8.3: Key magnetic properties of the aligned 3D printed permanent magnet at the various steps.

<b>Steps</b>	<b>Coercivity (kOe)</b>	<b>Remanence (G)</b>	<b>Energy product (MGOe)</b>
I	6.3	8,692.16	14.057
III	6.3	9,007.51	14.869
IV	3.25	7,659.62	7.865
V	6.22	8,993.21	14.621

conserve significant quantities of critical materials. To create magnets with dysprosium armor, dual-feed AM with separate feeds for critical materials can be employed. The first feed would be NdFeB with high concentrations of dysprosium. The second feed would be NdFeB without dysprosium. The first feed would be the base layer and surface of the 3D printed PM. The second feed would be the bulk of the 3D printed PM. AM of PMs with tailorable concentrations of critical materials remains a future goal of 3D printed magnet research.<sup>232</sup>

### **8.3 On the Additive Manufacturing of Cu Coils for Electric Motors and Generators**

The copper windings of electrical machines are not magnets. However, they magnetize the soft magnet electrical steel cores of the electrical machines. Traditionally, these windings are composed of coils of copper wiring. Copper wiring is difficult to automate in production and takes up a lot of space. Newer copper winding designs such as the so-called hairpin windings use copper pieces instead of copper wiring and are designed to be easier to automate in production and to be more space efficient. Figure 8.9 shows a pair of newer copper winding designs.

Copper wiring is difficult (nearly impossible) to 3D print in a timely and cost-efficient manner. However, copper pieces of the new designs have high shape complexity that could be difficult to fabricate via conventional processes. It is possible to 3D print such copper pieces. Figure 8.10 shows photographs of a 3D printed copper winding component part. AM of the copper winding is another step toward the full AM of electrical machines.

### **8.4 Concluding Remarks on the Implementation of Future Research on Electric Motors and Generators**

Figure 8.11 illustrates the main components of a commercial electric motor. The writing in red describes the technologies discussed in this chapter in the form of alternative components. Each of these red 3D printed component writings are next to their black conventional versions in the



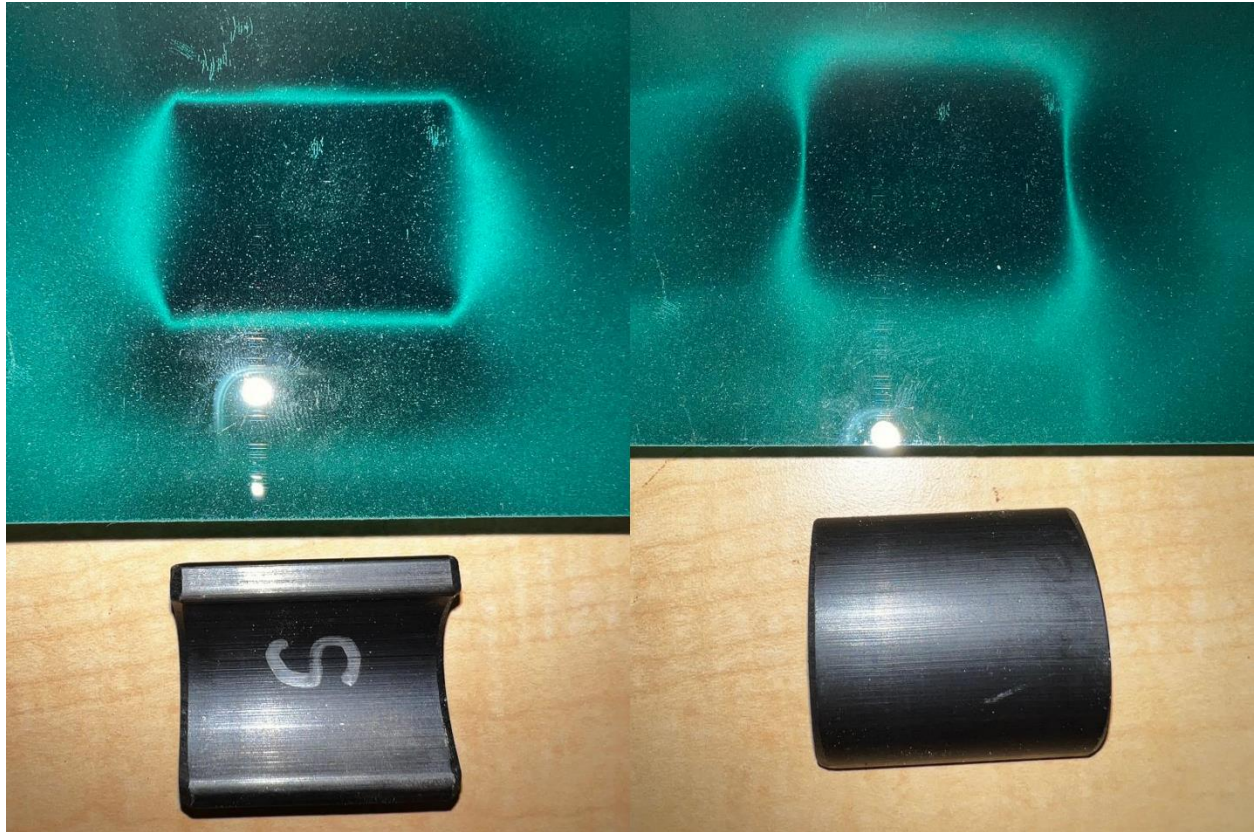


Figure 8.8: A film that manifests the magnetic field of objects covering 3D printed NdFeB magnets. (top) The magnetic field appears as bright regions in the film. (bottom) The 3D printed NdFeB magnets without the film.



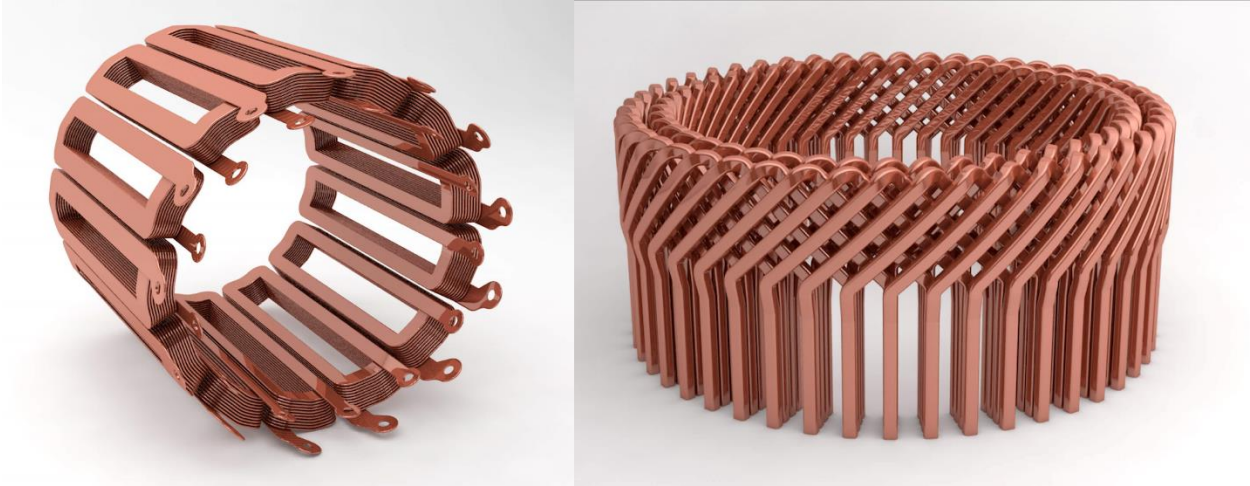


Figure 8.9: A pair of advanced copper motor winding designs.

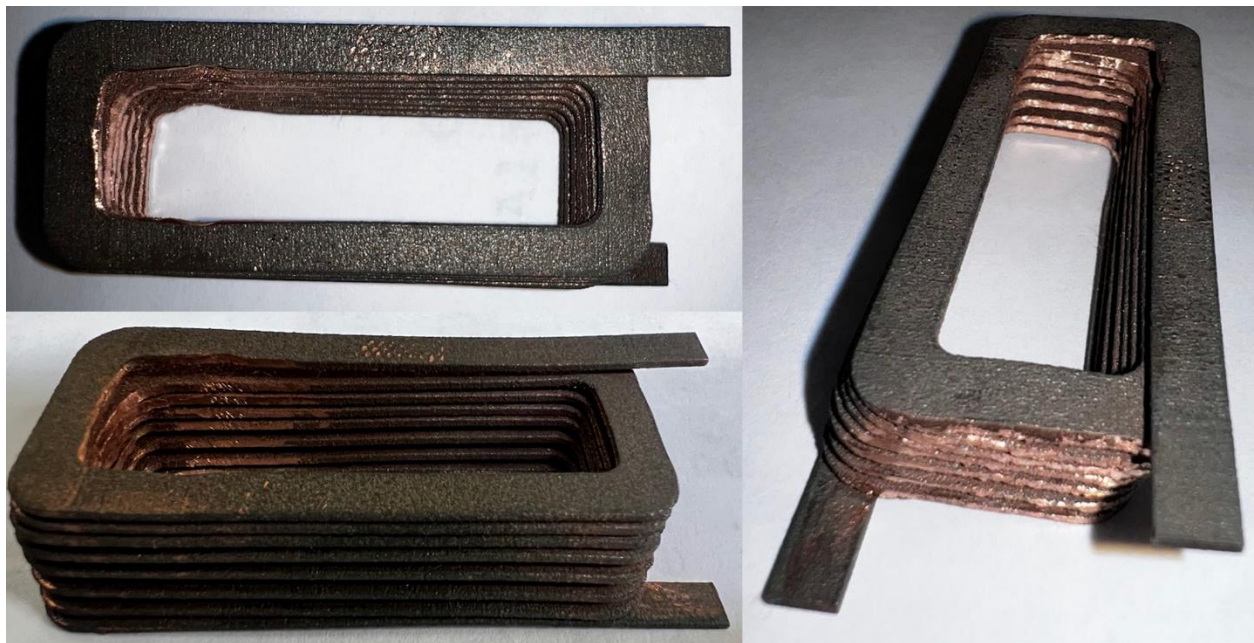


Figure 8.10: A 3D printed copper winding component.

illustration. The 3D printed rotor magnets could replace the conventional rotor magnets. The 3D printed multimaterial FeSi with alumina could be made into single-piece rotor and stator cores that do not need to be laminated because the insulation is printed within the material. The wound wire could be replaced with 3D printed copper hairpin-type windings. These technologies enable most components on the electrical motor to be made via AM. Should these technologies be successfully developed, a fully 3D printed commercial electrical motor will be close to realization.



# General Motors

## Permanent Magnet Electric Motor

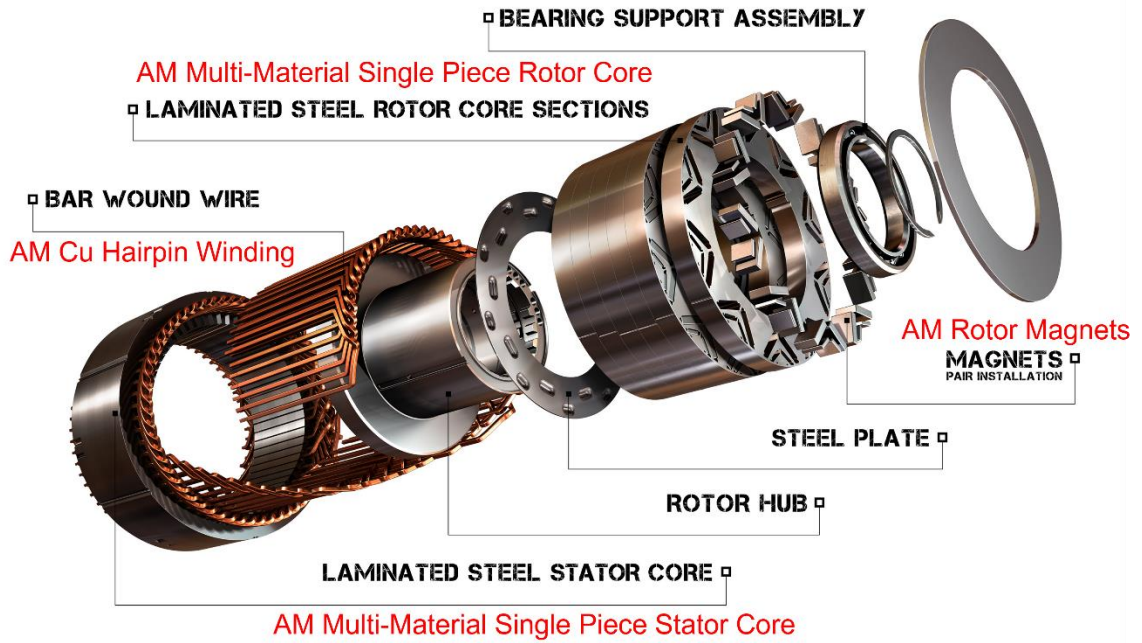


Figure 8.11: The technologies of Chapter 8 in an electric interior permanent magnet motor.<sup>233</sup>

## REFERENCES:

1. Butterfield, A. & Szymanski, J. electric vehicle. in *A Dictionary of Electronics and Electrical Engineering* (Oxford University Press, 2018).
2. Rennie, R. R. & Law, J. L. wind power. in *A Dictionary of Physics* (eds. Rennie, R. & Law, J.) (Oxford University Press, 2019).
3. Jelley, N. wind turbine. in *A Dictionary of Energy Science* (Oxford University Press, 2017).
4. electric motor. in *A Dictionary of Physics* (Oxford University Press, 2009).
5. Butterfield, A. & Szymanski, J. generator. in *A Dictionary of Electronics and Electrical Engineering* (Oxford University Press, 2018).
6. Wallace, J., Uberti, D., Kantchev, G. & Boston, W. European Manufacturers Reel From Russian Gas Shutoff. *WSJ* (2022).
7. Chapman, S. J. *Electric Machinery Fundamentals*. (McGraw-Hill, 1985).
8. Delogu, M., Berzi, L., Dattilo, C. A. & Del Pero, F. Definition and sustainability assessment of recycling processes for bonded rare earths permanent magnets used on wind generators. *Adv. Mater. Process. Technol.* **0**, 1–47 (2022).
9. Wang, H., Lamichhane, T. N. & Paranthaman, M. P. Review of additive manufacturing of permanent magnets for electrical machines: A prospective on wind turbine. *Mater. Today Phys.* **24**, 100675 (2022).
10. Patil, A. B., Paetzel, V., Struis, R. P. W. J. & Ludwig, C. Separation and Recycling Potential of Rare Earth Elements from Energy Systems: Feed and Economic Viability Review. *Separations* **9**, 56 (2022).
11. Farina, A. & Anctil, A. Material consumption and environmental impact of wind turbines in the USA and globally. *Resour. Conserv. Recycl.* **176**, 105938 (2022).

12. U.S. Geological Survey Releases 2022 List of Critical Minerals | U.S. Geological Survey.  
<https://www.usgs.gov/news/national-news-release/us-geological-survey-releases-2022-list-critical-minerals>.
13. Daniel, J. C. Rare Earths Statistics and Information | U.S. Geological Survey. *USGS*  
<https://www.usgs.gov/centers/national-minerals-information-center/rare-earths-statistics-and-information> (2022).
14. rare earth. *Oxford Reference* [https://www-oxfordreference-com.utk.idm.oclc.org/view/10.1093/acref/9780195392883.001.0001/m\\_en\\_us1283046](https://www-oxfordreference-com.utk.idm.oclc.org/view/10.1093/acref/9780195392883.001.0001/m_en_us1283046).
15. *BUILDING RESILIENT SUPPLY CHAINS, REVITALIZING AMERICAN MANUFACTURING, AND FOSTERING BROAD-BASED GROWTH*. <https://www.whitehouse.gov/wp-content/uploads/2021/06/100-day-supply-chain-review-report.pdf> (2021).
16. MacDonald, A. U.S. Faces Uphill Climb to Rival China’s Rare-Earth Magnet Industry. *WSJ* (2021).
17. Zhai, K. WSJ News Exclusive | China Set to Create New State-Owned Rare-Earths Giant. *Wall Street Journal* (2021).
18. Subin, S. The new U.S. plan to rival China and end cornering of market in rare earth metals. *CNBC*  
<https://www.cnn.com/2021/04/17/the-new-us-plan-to-rival-chinas-dominance-in-rare-earth-metals.html> (2021).
19. Carson, N. Highlightable Periodic Table. Approved for Reuse. *Nessa Carson website*  
<http://www.supersciencegrl.co.uk/periodictable.html> (2019).
20. A Federal Strategy To Ensure Secure and Reliable Supplies of Critical Minerals. *Federal Register*  
<https://www.federalregister.gov/documents/2017/12/26/2017-27899/a-federal-strategy-to-ensure-secure-and-reliable-supplies-of-critical-minerals> (2017).
21. The Defense Department’s Strategic and Critical Materials Review. *U.S. Department of Defense*  
<https://www.defense.gov/News/Releases/Release/Article/2649649/the-defense-departments-strategic-and-critical-materials->

- review/[https%3A%2F%2Fwww.defense.gov%2FNews%2FReleases%2FRelease%2FArticle%2F2649649%2Fthe-defense-departments-strategic-and-critical-materials-review%2F](https://www.defense.gov/News/Releases/Release/Article/2649649/the-defense-departments-strategic-and-critical-materials-review) (2021).
22. User:michbich, G. B. H., Sara Boore, and Susan Mayfield from USGS; vectorized by. *English: Relative abundance of elements in the Earth's upper crust.* (2003).
  23. Schnebele, E. Manganese Statistics and Information | U.S. Geological Survey. *USGS*  
<https://www.usgs.gov/centers/national-minerals-information-center/manganese-statistics-and-information>.
  24. Neodymium today | Rare Earth | SMM - China Metal Market. <https://www.metal.com/Rare-Earth-Metals/201102250470>.
  25. Dysprosium today | Rare Earth | SMM - China Metal Market. <https://www.metal.com/Rare-Earth-Metals/201102250389>.
  26. The London Metal Exchange. LME Cobalt | London Metal Exchange. *LME*  
<https://www.lme.com/Metals/EV/LME-Cobalt>.
  27. The London Metal Exchange. LME Nickel | London Metal Exchange. *Lme*  
<https://www.lme.com/Metals/Non-ferrous/LME-Nickel>.
  28. The London Metal Exchange. LME Copper | London Metal Exchange. *Lme*  
<https://www.lme.com/Metals/Non-ferrous/LME-Copper>.
  29. EMM today | Minor Metals | SMM - China Metal Market.  
<https://www.metal.com/Manganese/201102250594>.
  30. The London Metal Exchange. LME Steel HRC FOB China (Argus) | London Metal Exchange. *Lme*  
<https://www.lme.com/Metals/Ferrous/LME-Steel-HRC-FOB-China-Argus>.
  31. Shedd, K. Cobalt Statistics and Information | U.S. Geological Survey. *USGS*  
<https://www.usgs.gov/centers/national-minerals-information-center/cobalt-statistics-and-information>.
  32. Garside, M. Praseodymium oxide price globally 2030. *Statista*  
<https://www.statista.com/statistics/450148/global-reo-praseodymium-oxide-price-forecast/> (2022).

33. OECD. *Global Material Resources Outlook to 2060: Economic Drivers and Environmental Consequences*. (OECD, 2019). doi:10.1787/9789264307452-en.
34. Tuck, C. C. Iron and Steel Statistics and Information | U.S. Geological Survey. *USGS* <https://www.usgs.gov/centers/national-minerals-information-center/iron-and-steel-statistics-and-information>.
35. Kramer, M. J., McCallum, R. W., Anderson, I. A. & Constantinides, S. Prospects for Non-Rare Earth Permanent Magnets for Traction Motors and Generators. *JOM* **64**, 752–763 (2012).
36. Cui, J. Manufacturing Processes for Permanent Magnets: Part 7 I—Sintering and Casting. *JOM* (2022) doi:<https://doi.org/10.1007/s11837-022-05156-9>.
37. European Commission. Joint Research Centre. *The role of rare earth elements in wind energy and electric mobility: an analysis of future supply/demand balances*. (Publications Office, 2020).
38. Lee, Y.-K. & Han, J. Current opinion in medium manganese steel. *Mater. Sci. Technol.* **31**, 843–856 (2015).
39. Gandha, K. *et al.* Recycling of additively printed rare-earth bonded magnets. *Waste Manag.* **90**, 94–99 (2019).
40. Chen, M. *et al.* Recycling End-of-Life Electric Vehicle Lithium-Ion Batteries. *Joule* **3**, 2622–2646 (2019).
41. Emil, E., Kaya, O., Stopić, S., Gurmen, S. & Friedrich, B. NdFeB Magnets Recycling Process: An Alternative Method to Produce Mixed Rare Earth Oxide from Scrap NdFeB Magnets. *Metals* **11**, 716 (2021).
42. Chandra, M., Yu, D., Tian, Q. & Guo, X. Recovery of Cobalt from Secondary Resources: A Comprehensive Review. *Miner. Process. Extr. Metall. Rev.* **43**, 679–700 (2022).
43. Wind Vision. *Energy.gov* <https://www.energy.gov/eere/wind/wind-vision-1>.
44. Wind Market Reports: 2022 Edition. *Energy.gov* <https://www.energy.gov/eere/wind/wind-market-reports-2022-edition>.

45. Woodward, M., Walton, B. & Hamilton, J. Electric Vehicles, Setting a Course for 2030. *Deloitte* <https://www2.deloitte.com/us/en/insights/focus/future-of-mobility/electric-vehicle-trends-2030.html> (2020).
46. Joint Research Centre (European Commission), Alves Dias, P., Pavel, C., Plazzotta, B. & Carrara, S. *Raw materials demand for wind and solar PV technologies in the transition towards a decarbonised energy system*. (Publications Office of the European Union, 2020).
47. Annual Energy Outlook 2022 - U.S. Energy Information Administration (EIA). *Energy Information Administration* <https://www.eia.gov/outlooks/aeo/narrative/consumption/sub-topic-01.php> (2022).
48. IEA. The Role of Critical Minerals in Clean Energy Transitions. *International Energy Agency (IEA)* <https://www.iea.org/reports/the-role-of-critical-minerals-in-clean-energy-transitions> (2021).
49. The White House. FACT SHEET: President Biden’s Economic Plan Drives America’s Electric Vehicle Manufacturing Boom. *The White House* <https://www.whitehouse.gov/briefing-room/statements-releases/2022/09/14/fact-sheet-president-bidens-economic-plan-drives-americas-electric-vehicle-manufacturing-boom/> (2022).
50. Mackrael, K. & Boston, W. EU Lawmakers Vote to Ban Sale of New Gasoline-Powered Cars From 2035. *Wall Street Journal* (2023).
51. Butterfield, A. & Szymanski, J. magnet. in *A Dictionary of Electronics and Electrical Engineering* (Oxford University Press, 2018).
52. Cresswell, J. magnet. in *Oxford Dictionary of Word Origins* (Oxford University Press, 2021).
53. magnet, n. *OED Online*.
54. dipole, n. *OED Online*.
55. Butterfield, A. & Szymanski, J. magnetic moment. in *A Dictionary of Electronics and Electrical Engineering* (Oxford University Press, 2018).
56. induce, v. *OED Online*.
57. induction, n. *OED Online*.
58. vector, n. *OED Online*.



59. flux, n. *OED Online*.
60. Rennie, R. R. & Law, J. L. magnetic field. in *A Dictionary of Physics* (eds. Rennie, R. & Law, J.) (Oxford University Press, 2019).
61. Sung, H. W. F. & Rudowicz, C. Physics behind the magnetic hysteresis loop—a survey of misconceptions in magnetism literature. *J. Magn. Magn. Mater.* **260**, 250–260 (2003).
62. permeate, v. *OED Online*.
63. permeable, adj. *OED Online*.
64. permeability, n. *OED Online*.
65. permeability. in *World Encyclopedia* (Philip's).
66. magnetism, n. *OED Online*.
67. Cammack, R. C. *et al.* magnetism. in *Oxford Dictionary of Biochemistry and Molecular Biology* (Oxford University Press, 2006).
68. Rennie, R. R. & Law, J. L. magnetism. in *A Dictionary of Physics* (eds. Rennie, R. & Law, J.) (Oxford University Press, 2019).
69. Escudier, M. & Atkins, T. magnetic materials. in *A Dictionary of Mechanical Engineering* (Oxford University Press, 2019).
70. Allaby, M. magnetic domain. in *A Dictionary of Geology and Earth Sciences* (Oxford University Press, 2020).
71. Butterfield, A. & Szymanski, J. magnetism. in *A Dictionary of Electronics and Electrical Engineering* (Oxford University Press, 2018).
72. Ravat, D. Curie temperature. in *The Oxford Companion to the Earth* (Oxford University Press, 2000).
73. Allaby, M. Curie temperature. in *A Dictionary of Geology and Earth Sciences* (Oxford University Press, 2020).
74. Home, R. W. magnetism. in *The Oxford Companion to the History of Modern Science* (Oxford University Press, 2003).

75. Sugimoto, M. The Past, Present, and Future of Ferrites. *J. Am. Ceram. Soc.* **82**, 269–280 (1999).
76. Nanocrystalline Soft Magnetic Material FINEMET® | Hitachi Metals, Ltd. [https://www.hitachi-metals.co.jp/e/products/elec/tel/p02\\_21.html](https://www.hitachi-metals.co.jp/e/products/elec/tel/p02_21.html).
77. Lamichhane, T. N. *et al.* Additive manufacturing of soft magnets for electrical machines—a review. *Mater. Today Phys.* **15**, 100255 (2020).
78. Rennie, R. R. & Law, J. L. soft iron. in *A Dictionary of Physics* (eds. Rennie, R. & Law, J.) (Oxford University Press, 2019).
79. electromagnet, n. *OED Online*.
80. Rennie, R. R. & Law, J. L. electromagnet. in *A Dictionary of Physics* (eds. Rennie, R. & Law, J.) (Oxford University Press, 2019).
81. Butterfield, A. & Szymanski, J. electromagnet. in *A Dictionary of Electronics and Electrical Engineering* (Oxford University Press, 2018).
82. hysteresis, n. *OED Online*.
83. Escudier, M. & Atkins, T. hysteresis. in *A Dictionary of Mechanical Engineering* (Oxford University Press, 2019).
84. Butterfield, A. & Szymanski, J. magnetization. in *A Dictionary of Electronics and Electrical Engineering* (Oxford University Press, 2018).
85. Butterfield, A. & Szymanski, J. magnetic hysteresis. in *A Dictionary of Electronics and Electrical Engineering* (Oxford University Press, 2018).
86. Brandon. B-H vs M-H Hysteresis Loops: Magnetic Induction vs Magnetization (Similarities, Differences, and Points on the Graph). *Materials Science & Engineering Student* <https://mstudent.com/b-h-vs-m-h-hysteresis-loops-magnetic-induction-vs-magnetization-similarities-differences-and-points-on-the-graph/>.
87. remanence, n. *OED Online*.
88. susceptibility, n. *OED Online*.

89. Butterfield, A. & Szymanski, J. susceptibility. in *A Dictionary of Electronics and Electrical Engineering* (Oxford University Press, 2018).
90. Butterfield, A. & Szymanski, J. permeability. in *A Dictionary of Electronics and Electrical Engineering* (Oxford University Press, 2018).
91. Moosbrugger, C. & Cverna, F. *ASM ready reference Electrical and magnetic properties of metals*. (ASM International, 2000).
92. Goldfarb, R. B. & Fickett, F. R. Units for Magnetic Properties. *National Institute for Standard and Technology (NIST)* <https://www.nist.gov/system/files/documents/2017/05/09/UnitsChart.pdf> (1985).
93. Escudier, M. & Atkins, T. powder metallurgy. in *A Dictionary of Mechanical Engineering* (Oxford University Press, 2019).
94. Law, J. L. & Rennie, R. R. powder metallurgy. in *A Dictionary of Chemistry* (eds. Law, J. & Rennie, R.) (Oxford University Press, 2020).
95. Law, J. L. & Rennie, R. R. sintering. in *A Dictionary of Chemistry* (eds. Law, J. & Rennie, R.) (Oxford University Press, 2020).
96. Escudier, M. & Atkins, T. casting. in *A Dictionary of Mechanical Engineering* (Oxford University Press, 2019).
97. Makino, N. & Kimura, Y. Techniques to Achieve Texture in Permanent Magnet Alloy Systems. *J. Appl. Phys.* **36**, 1185–1190 (1965).
98. White, E. M. H. *et al.* Net Shape Processing of Alnico Magnets by Additive Manufacturing. *IEEE Trans. Magn.* **53**, 1–6 (2017).
99. Arnold Magnetic Technologies. Cast Alnico Permanent Magnets. *Arnold Magnetic Technologies* <https://www.arnoldmagnetics.com/wp-content/uploads/2017/10/Cast-Alnico-Permanent-Magnet-Brochure-101117-1.pdf> (2003).
100. Ireland, R. & Yeung, C. A. Y. A. casting. in *A Dictionary of Dentistry* (ed. Yeung, C. A.) (Oxford University Press, 2020).

101. Ormerod, J. & Constantinides, S. Bonded permanent magnets: Current status and future opportunities (invited). *J. Appl. Phys.* **81**, 4816–4820 (1997).
102. metallurgy - Alloying | Britannica. <https://www.britannica.com/science/metallurgy/Alloying>.
103. Davis, J. R. *Alloying: Understanding the Basics*. (ASM International, 2001).
104. alloy, v. *OED Online*.
105. alloy, n. *OED Online*.
106. electrical, adj. and n. *OED Online*.
107. stamp, v. *OED Online*.
108. punch, n.1. *OED Online*.
109. punch, v.1. *OED Online*.
110. Goll, D. *et al.* Additive manufacturing of soft magnetic materials and components. *Addit. Manuf.* **27**, 428–439 (2019).
111. Butterfield, A. & Szymanski, J. core loss. in *A Dictionary of Electronics and Electrical Engineering* (Oxford University Press, 2018).
112. American Society for Testing and Materials (ASTM). *ISO/ASTM 52900:2021*. <https://www.iso.org/cms/render/live/en/sites/isoorg/contents/data/standard/07/45/74514.html> (2022).
113. Wang, H., Lamichhane, T. N. & Paranthaman, M. P. Review of additive manufacturing of permanent magnets for electrical machines: A prospective on wind turbine. *Mater. Today Phys.* **24**, 100675 (2022).
114. Escudier, M. & Atkins, T. additive-layer manufacturing. in *A Dictionary of Mechanical Engineering* (Oxford University Press, 2019).
115. Escudier, M. & Atkins, T. subtractive manufacturing. in *A Dictionary of Mechanical Engineering* (Oxford University Press, 2019).
116. D, n. *OED Online*.

117. Paranthaman, M. P. *et al.* Binder Jetting: A Novel NdFeB Bonded Magnet Fabrication Process. *JOM* **68**, 1978–1982 (2016).
118. White, E. *et al.* Processing of Alnico Magnets by Additive Manufacturing. *Appl. Sci.* **9**, 4843 (2019).
119. Jones, R. *et al.* RepRap – the replicating rapid prototyper. *Robotica* **29**, 177–191 (2011).
120. N. Turner, B., Strong, R. & A. Gold, S. A review of melt extrusion additive manufacturing processes: I. Process design and modeling. *Rapid Prototyp. J.* **20**, 192–204 (2014).
121. Ngo, T. D., Kashani, A., Imbalzano, G., Nguyen, K. T. Q. & Hui, D. Additive manufacturing (3D printing): A review of materials, methods, applications and challenges. *Compos. Part B Eng.* **143**, 172–196 (2018).
122. thermoplastic, adj. and n. *OED Online*.
123. Li, L. *et al.* Big Area Additive Manufacturing of High Performance Bonded NdFeB Magnets. *Sci. Rep.* **6**, 36212 (2016).
124. Gandha, K. *et al.* Additive manufacturing of highly dense anisotropic Nd–Fe–B bonded magnets. *Scr. Mater.* **183**, 91–95 (2020).
125. Paranthaman, M. P. *et al.* Additive Manufacturing of Isotropic NdFeB PPS Bonded Permanent Magnets. *Materials* **13**, 3319 (2020).
126. Bai, Y., Wagner, G. & Williams, C. B. Effect of Particle Size Distribution on Powder Packing and Sintering in Binder Jetting Additive Manufacturing of Metals. *J. Manuf. Sci. Eng.* **139**, (2017).
127. Kulkarni, S., Zhao, F., Nlebedim, I. C., Fredette, R. & Paranthaman, M. P. Comparative Life Cycle Assessment of Injection Molded and Big Area Additive Manufactured NdFeB Bonded Permanent Magnets. *Journal Manuf. Syst.* (2022).
128. Li, L. *et al.* Fabrication of highly dense isotropic Nd-Fe-B nylon bonded magnets via extrusion-based additive manufacturing. *Addit. Manuf.* **21**, 495–500 (2018).
129. bed, n. *OED Online*.

130. Kolb, T. *et al.* Laser Beam Melting of NdFeB for the production of rare-earth magnets. in *2016 6th International Electric Drives Production Conference (EDPC)* 34–40 (2016).  
doi:10.1109/EDPC.2016.7851311.
131. McCauley, J. W. Materials Characterization: Definition, Philosophy and Overview of Conference. in *Materials Characterization for Systems Performance and Reliability* (eds. McCauley, J. W. & Weiss, V.) 1–11 (Springer US, 1986). doi:10.1007/978-1-4613-2119-4\_1.
132. ASM International. Introduction to Materials Characterization. *ASM Handb.* **10**, (2019).
133. Osman, T. M. & Rigney, J. D. Introduction to the Mechanical Behavior of Metals. *ASM Handb.* **8**, (2000).
134. House, J. W. & Gillis, P. P. Testing Machines and Strain Sensors. *ASM Handb.* **8**, (2000).
135. Holt, (Tim) & M, J. Uniaxial Tension Testing. *ASM Handb.* **8**, (2000).
136. ASM International. Thermogravimetric Analysis. *ASM Handb.* **10**, (2019).
137. Barron, A. R. 2.8: Thermal Analysis. *Chemistry LibreTexts*  
[https://chem.libretexts.org/Bookshelves/Analytical\\_Chemistry/Physical\\_Methods\\_in\\_Chemistry\\_and\\_Nano\\_Science\\_\(Barron\)/02%3A\\_Physical\\_and\\_Thermal\\_Analysis/2.08%3A\\_Thermal\\_Analysis](https://chem.libretexts.org/Bookshelves/Analytical_Chemistry/Physical_Methods_in_Chemistry_and_Nano_Science_(Barron)/02%3A_Physical_and_Thermal_Analysis/2.08%3A_Thermal_Analysis)  
(2016).
138. Burt, V. Differential Scanning Calorimetry. *ASM Handb.* **10**, (2019).
139. Escudier, M. & Atkins, T. differential scanning calorimetry. in *A Dictionary of Mechanical Engineering* (Oxford University Press, 2019).
140. Li, L. *et al.* A novel method combining additive manufacturing and alloy infiltration for NdFeB bonded magnet fabrication. *J. Magn. Magn. Mater.* **438**, 163–167 (2017).
141. Picard, Y. N. Scanning Electron Microscopy. *Handbook* **10**, (2019).
142. Escudier, M. & Atkins, T. scanning electron microscope. in *A Dictionary of Mechanical Engineering* (Oxford University Press, 2019).
143. Leoni, M. Introduction to Diffraction Methods. *ASM Handb.* **10**, (2019).
144. Leoni, M. X-Ray Powder Diffraction. *ASM Handb.* **10**, (2019).

145. Ameh, E. S. A review of basic crystallography and x-ray diffraction applications. *Int. J. Adv. Manuf. Technol.* **105**, 3289–3302 (2019).
146. Ali, A., Chiang, Y. W. & Santos, R. M. X-ray Diffraction Techniques for Mineral Characterization: A Review for Engineers of the Fundamentals, Applications, and Research Directions. *Minerals* **12**, 205 (2022).
147. Warren, B. E. *X-ray Diffraction*. (Courier Corporation, 1990).
148. Gandha, K. *et al.* 3D printing of anisotropic Sm–Fe–N nylon bonded permanent magnets. *Eng. Rep.* **3**, (2021).
149. Isnard, O., Yelon, W. B., Miraglia, S. & Fruchart, D. Neutron-diffraction study of the insertion scheme of hydrogen in Nd<sub>2</sub>Fe<sub>14</sub>B. *Crystallography Open Database* <http://www.crystallography.net/cod/1008718.html> (1995).
150. Davis, J. R. Magnetic Field Testing. *ASM Met. Handb. 2nd Ed.* (1998)  
doi:10.31399/asm.hb.mhde2.a0003233.
151. Buchner, M., Höfler, K., Henne, B., Ney, V. & Ney, A. Tutorial: Basic principles, limits of detection, and pitfalls of highly sensitive SQUID magnetometry for nanomagnetism and spintronics. *J. Appl. Phys.* **124**, 161101 (2018).
152. Fagaly, R. L. Superconducting quantum interference device instruments and applications. *Rev. Sci. Instrum.* **77**, 101101 (2006).
153. Kleiner, R., Koelle, D., Ludwig, F. & Clarke, J. Superconducting quantum interference devices: State of the art and applications. *Proc. IEEE* **92**, 1534–1548 (2004).
154. Granata, C. & Vettoliere, A. Nano Superconducting Quantum Interference device: A powerful tool for nanoscale investigations. *Phys. Rep.* **614**, 1–69 (2016).
155. Coey, J. M. D. *Magnetism and magnetic materials*. (Cambridge University Press, 2009).
156. Laughlin, D. E. & Hono, K. *Physical Metallurgy: 3-Volume Set*. (Elsevier, 2014).

157. Ouyang, G., Chen, X., Liang, Y., Macziewski, C. & Cui, J. Review of Fe-6.5 wt%Si high silicon steel—A promising soft magnetic material for sub-kHz application. *J. Magn. Magn. Mater.* **481**, 234–250 (2019).
158. Download-Ferrocube. <https://www.ferrocube.com/en-global/download/index>.
159. Soft Magnetic Composites | Höganäs. <https://www.hoganas.com/en/powder-technologies/soft-magnetic-composites/products/coated-powders-for-electromagnetic-applications/>.
160. Cramer, C. L. *et al.* Binder jet additive manufacturing method to fabricate near net shape crack-free highly dense Fe-6.5 wt.% Si soft magnets. *Heliyon* **5**, (2019).
161. Mishra, S., Därmann, C. & Lücke, K. On the development of the goss texture in iron-3% silicon. *Acta Metall.* **32**, 2185–2201 (1984).
162. Liu, X. *et al.* Goss Texture Evolution in a Grain-Oriented Fe-6.5wt%Si Steel Processed by Strip-Casting. *Mater. Sci. Forum* **1016**, 1653–1658 (2021).
163. Jain, V., Modak, P., Patra, S. & Ghosh, A. Origin of Goss texture in grain oriented electrical steel: Role of shear bands. *Materialia* **22**, 101398 (2022).
164. Goss, N. P. New Development in Electrical Strip Steels Characterized by Fine Grain Structure Approaching the Properties of a Single Crystal. *Trans. Am. Soc. Met.* **23**, 511–531 (1935).
165. Goss, N. P. Electrical sheet and method and apparatus for its manufacture and test. (1934).
166. Nam, W. J. & Choi, H. C. Effect of Si on mechanical properties of low alloy steels. *Mater. Sci. Technol.* **15**, 527–530 (1999).
167. Lamichhane, T. N. *et al.* Additively Manufactured Fe-3si Stator for High-Performance Electrical Motor. SSRN Scholarly Paper at <https://doi.org/10.2139/ssrn.4086824> (2022).
168. Escudier, M. & Atkins, T. electric-discharge machining. in *A Dictionary of Mechanical Engineering* (Oxford University Press, 2019).
169. Ho, K. H. & Newman, S. T. State of the art electrical discharge machining (EDM). *Int. J. Mach. Tools Manuf.* **43**, 1287–1300 (2003).



170. Mohapatra, J., Xing, M., Elkins, J. & Liu, J. P. Hard and semi-hard magnetic materials based on cobalt and cobalt alloys. *J. Alloys Compd.* **824**, 153874 (2020).
171. Gould, H. L. B. & Wenny, D. H. Supermendur: A new rectangular-loop magnetic material. *Electr. Eng.* **76**, 208–211 (1957).
172. Carpenter Hiperco® 50 Fe-Co-V Soft Magnetic Alloy, 0.15 mm Strip Heat Treated 843°C.  
<https://www.matweb.com/search/datasheet.aspx?matguid=373bd24bddd641a19c21de9409a9b90a&ckck=1>.
173. Carpenter Technology. Hiperco® 50 - Specialty Alloys | Carpenter Technology.  
<https://www.carpentertechnology.com/alloy-finder/hiperco-50>.
174. Coey, J. M. D. Perspective and Prospects for Rare Earth Permanent Magnets. *Engineering* **6**, 119–131 (2020).
175. Skomski, R. & Coey, J. M. D. Giant energy product in nanostructured two-phase magnets. *Phys. Rev. B* **48**, 15812–15816 (1993).
176. Sort, J. *et al.* Improving the energy product of hard magnetic materials. *Phys. Rev. B* **65**, 174420 (2002).
177. Cui, J. *et al.* Current progress and future challenges in rare-earth-free permanent magnets. *Acta Mater.* **158**, 118–137 (2018).
178. Alliance LLC. Neodymium Magnets | Alliance LLC. *Alliance LLC Industrial Permanent Magnets* <https://allianceorg.com/magnetic-materials/> (2022).
179. Alliance LLC. Samarium Cobalt Magnets | Alliance LLC. *Alliance LLC Industrial Permanent Magnets* <https://allianceorg.com/magnetic-materials/samarium-cobalt-magnets/> (2022).
180. Alliance LLC. Alnico Magnets | Alliance LLC. *Alliance LLC Industrial Permanent Magnets* <https://allianceorg.com/magnetic-materials/alnico-magnets/> (2022).
181. Alliance LLC. Hard Ferrite Ceramic Magnets | Alliance LLC. *Alliance LLC Industrial Permanent Magnets* <https://allianceorg.com/magnetic-materials/ceramic-magnets/> (2022).

182. Constantinides, S. Market Outlook for Ferrite, Rare Earth and other Permanent Magnets. *Arnold Magnetic Technologies* <https://www.arnoldmagnetics.com/wp-content/uploads/2017/10/Magnetics-2016-Market-Outlook-Constantinides-160119-opt8.pdf> (2016).
183. Morii K. & Hasegawa F. Data Sheet of Sm-Fe-N Isotropic Bonded Magnet. *DENKI-SEIKOELECTRIC Furn. STEEL* **79**, 149–155 (2008).
184. Jiang, Y. *et al.* Synthesis of Fe<sub>16</sub>N<sub>2</sub> compound Free-Standing Foils with 20 MGOe Magnetic Energy Product by Nitrogen Ion-Implantation. *Sci. Rep.* **6**, 25436 (2016).
185. Sankar, S. G. & Kecskes, L. J. *Consolidation of Fe-N Magnets Using Equal Channel Angular Extrusion*: <http://www.dtic.mil/docs/citations/AD1006013> (2016) doi:10.21236/AD1006013.
186. Paranthaman, M. P. *et al.* *Additive Manufacturing of Near-net Shaped Permanent Magnets*. ORNL/TM-2016/340, 1311265 <http://www.osti.gov/servlets/purl/1311265/> (2016) doi:10.2172/1311265.
187. Lores, A., Azurmendi, N., Agote, I. & Zuza, E. A review on recent developments in binder jetting metal additive manufacturing: materials and process characteristics. *Powder Metall.* **62**, 267–296 (2019).
188. Gandha, K. *et al.* Additive manufacturing of anisotropic hybrid NdFeB-SmFeN nylon composite bonded magnets. *J. Magn. Magn. Mater.* **467**, 8–13 (2018).
189. Khazdozian, H. A. *et al.* Low-Field Alignment of Anisotropic Bonded Magnets for Additive Manufacturing of Permanent Magnet Motors. *JOM* **71**, 626–632 (2019).
190. Sarkar, A. *et al.* Functionalizing magnet additive manufacturing with in-situ magnetic field source. *Addit. Manuf.* **34**, 101289 (2020).
191. Sarkar, A., Paranthaman, M. P. & Nlebedim, I. C. In-situ magnetic alignment model for additive manufacturing of anisotropic bonded magnets. *Addit. Manuf.* **46**, 102096 (2021).
192. Cammack, R. C. *et al.* magnetophoresis. in *Oxford Dictionary of Biochemistry and Molecular Biology* (Oxford University Press, 2006).

193. Lamichhane, T. N. *et al.* Additively Manufactured NdFeB Polyphenylene Sulfide Halbach Magnets to Generate Variable Magnetic Fields for Neutron Reflectometry. *3D Print. Addit. Manuf.* (2021) doi:10.1089/3dp.2020.0340.
194. Halbach, K. Design of permanent multipole magnets with oriented rare earth cobalt material. *Nucl. Instrum. Methods* **169**, 1–10 (1980).
195. Mungale, K. *et al.* Compression molding of anisotropic NdFeB bonded magnets in a polycarbonate matrix. *Materialia* **19**, 101167 (2021).
196. Liu, X. B. *et al.* Packing bimodal magnetic particles to fabricate highly dense anisotropic rare earth bonded permanent magnets. *RSC Adv.* **13**, 17097–17101 (2023).
197. Butterfield, A. & Szymanski, J. eddy current. in *A Dictionary of Electronics and Electrical Engineering* (Oxford University Press, 2018).
198. Rennie, R. R. & Law, J. L. Lenz's law. in *A Dictionary of Physics* (eds. Rennie, R. & Law, J.) (Oxford University Press, 2019).
199. Krings, A. & Soulard, J. Overview and Comparison of Iron Loss Models for Electrical Machines. *J. Electr. Eng.* **10**, 162–169 (2010).
200. Bertotti, G. Physical interpretation of eddy current losses in ferromagnetic materials. I. Theoretical considerations. *J. Appl. Phys.* **57**, 2110–2117 (1985).
201. Bertotti, G. Physical interpretation of eddy current losses in ferromagnetic materials. II. Analysis of experimental results. *J. Appl. Phys.* **57**, 2118–2126 (1985).
202. Bertotti, G., Schino, G., Milone, A. & Fiorillo, F. On the effect of grain size on magnetic losses of 3% non-oriented SiFe. <http://dx.doi.org/10.1051/jphyscol:1985671> **46**, (1985).
203. Steentjes, S., Leßmann, M. & Hameyer, K. Advanced iron-loss calculation as a basis for efficiency improvement of electrical machines in automotive application. in *Railway and Ship Propulsion 2012 Electrical Systems for Aircraft* 1–6 (2012). doi:10.1109/ESARS.2012.6387502.

204. Yamazaki, K. & Fukushima, N. Iron-Loss Modeling for Rotating Machines: Comparison Between Bertotti's Three-Term Expression and 3-D Eddy-Current Analysis. *IEEE Trans. Magn.* **46**, 3121–3124 (2010).
205. Bertotti, G. *et al.* An improved estimation of iron losses in rotating electrical machines. *IEEE Trans. Magn.* **27**, 5007–5009 (1991).
206. Fiorillo, F. *Characterization and Measurement of Magnetic Materials*. (Academic Press, 2004).
207. ASTM. ASTM E6-15e4 Standard Terminology Relating to Methods of Mechanical Testing. *ASTM Compass* <https://compass.astm.org/document/?contentCode=ASTM%7CE0006-15E04%7Cen-US> (2021).
208. Dieter, G. E. Mechanical Behavior Under Tensile and Compressive Loads. *ASM Handb.* **8**, (2000).
209. Kuhn, H. A. Overview of Mechanical Properties and Testing for Design. *ASM Handb.* **8**, (2000).
210. ASTM. ASTM D638-22 Standard Test Method for Tensile Properties of Plastics. *ASTM Compass* <https://compass.astm.org/document/?contentCode=ASTM%7CD0638-22%7Cen-US> (2022).
211. MatWeb. Alliance N-55 Sintered NdFeB Neodymium Magnet. *MatWeb Material Property Data* <https://www.matweb.com/search/DataSheet.aspx?MatGUID=567a142f9ed94ead97bd28e97fadbd44> (2023).
212. MatWeb. Alliance BCN-29-5 Compression Bonded Neodymium Iron Boron Magnet. *MatWeb Material Property Data* <https://www.matweb.com/search/DataSheet.aspx?MatGUID=64e10e431bc64ff095373bf6d01a7d34> (2023).
213. Arnold Magnetic Technologies. Injection Molded Magnets Catalog. *Arnold Magnetic Technologies* <https://www.arnoldmagnetics.com/products/injection-molded-magnets/> (2023).
214. Lamichhane, T. N. *et al.* Challenges in Postprocessing of Hybrid Manufacturing of Magnet Polymer Composites to Enhance the Energy Product of NdFeB Bonded Magnets. *Res. Dev. Mater. Sci.* **16**, 1802–1808 (2021).

215. Polymer Properties Database. PVB. *Polymer Properties Database*  
<https://polymerdatabase.com/Polymer%20Brands/PVB.html>.
216. A2B Chem. 63148-65-2 | MFCD00084458 | Polyvinyl butyral. *A2B Chem*  
<https://www.a2bchem.com/63148-65-2.html> (2019).
217. INEOS Styrolution Group. Styroflex® - Transparent Specialties favorable buying at our shop.  
*INEOS Styrolution* [https://www.ineos-styrolution.com/Product/Styroflex\\_ID40090025.html](https://www.ineos-styrolution.com/Product/Styroflex_ID40090025.html).
218. CAS Common Chemistry. Butadiene-styrene copolymer. *CAS Common Chemistry. CAS, a division of the American Chemical Society, n.d* [https://commonchemistry.cas.org/detail?cas\\_rn=9003-55-8](https://commonchemistry.cas.org/detail?cas_rn=9003-55-8)  
(2023).
219. Vibrating Sample Magnetometer (VSM), Magnetic Moment Measurement, Magnetic Coercivity Measurement - MicroSense, LLC. <http://www.microsense.net/products-vsm.htm>.
220. The Editors of Encyclopaedia Britannica. Polyvinyl alcohol | chemical compound | Britannica.  
*Encyclopaedia Britannica* <https://www.britannica.com/science/polyvinyl-alcohol>.
221. 3Dnatives. Renishaw AM250 Renishaw 3D printer: Price, Features, Videos.... *Comparator*  
<https://www.3dnatives.com/3D-compare/en/3d-printers/renishaw-am250/>.
222. Plotkowski, A. *et al.* Influence of scan pattern and geometry on the microstructure and soft-magnetic performance of additively manufactured Fe-Si. *Addit. Manuf.* **29**, 100781 (2019).
223. JFE Steel Corporation. JFE's Electrical Steel Sheets. *JFE Steel Corporation* <https://www.jfe-steel.co.jp/en/products/electrical/index.php>.
224. Lyudkovsky, G., Rastogi, P. K. & Bala, M. Nonoriented Electrical Steels. *JOM* **38**, 18–26 (1986).
225. Iordache, V. & Hug, E. Effect of mechanical strains on the magnetic properties of electrical steels.  
*J. Optoelectron. Adv. Mater.* (2009).
226. Dell'Acqua, F. Hysteresisgraph AMH-500 BH tracer. *Laboratorio Elettrofisico*  
<https://www.laboratorio.elettrofisico.com/measuring-equipment/hard-magnetic-materials/hysteresisgraph-amh-500-bh-tracer/> (2015).

227. Dell'Acqua, F. AMH-200K Permeameter. *Laboratorio Elettrofisico*  
<https://www.laboratorio.elettrofisico.com/measuring-equipment/soft-magnetic-materials/amh-200k-permeameter/> (2015).
228. Fe-Si steel. transformer steel, electrical steel, soft magnetic, inhibition, Goss texture, microstructure, EBSD, texture. <http://www.dierk-raabe.com/electrical-steels-fe-3-si/>.
229. Bas, J. A., Calero, J. A. & Dougan, M. J. Sintered soft magnetic materials. Properties and applications. *J. Magn. Magn. Mater.* **254–255**, 391–398 (2003).
230. Gargalis, L. *et al.* Additive Manufacturing and Testing of a Soft Magnetic Rotor for a Switched Reluctance Motor. *IEEE Access* **8**, 206982–206991 (2020).
231. Ling, S., Moebs, W. & Sanny, J. 13.7: Electric Generators and Back Emf. *Physics LibreTexts*  
[https://phys.libretexts.org/Bookshelves/University\\_Physics/Book%3A\\_University\\_Physics\\_\(OpenStax\)/Book%3A\\_University\\_Physics\\_II\\_-\\_Thermodynamics\\_Electricity\\_and\\_Magnetism\\_\(OpenStax\)/13%3A\\_Electromagnetic\\_Induction/13.07%3A\\_Electric\\_Generators\\_and\\_Back\\_Emf](https://phys.libretexts.org/Bookshelves/University_Physics/Book%3A_University_Physics_(OpenStax)/Book%3A_University_Physics_II_-_Thermodynamics_Electricity_and_Magnetism_(OpenStax)/13%3A_Electromagnetic_Induction/13.07%3A_Electric_Generators_and_Back_Emf) (2016).
232. Paranthaman, M. P. *et al.* Neodymium-iron-boron magnet with selective surface modification, and method of producing same. (2017).
233. Chevrolet Showcases Spark EV Electric Motor. *media.gm.com*  
[https://media.gm.com/media/us/en/chevrolet/news.detail.html/content/Pages/news/us/en/2011/Oct/1026\\_spark\\_elec\\_mtr.html](https://media.gm.com/media/us/en/chevrolet/news.detail.html/content/Pages/news/us/en/2011/Oct/1026_spark_elec_mtr.html) (2011).

## APPENDIX:

### SUPPLEMENTAL SECTION

Table S1: US Geological Survey 2022 List of Critical Materials

<b>Number</b>	<b>Material</b>	<b>Number</b>	<b>Material</b>
1	Aluminum	26	Magnesium
2	Antimony	27	Manganese
3	Arsenic	28	Neodymium
4	Barite	29	Nickel
5	Beryllium	30	Niobium
6	Bismuth	31	Palladium
7	Cerium	32	Platinum
8	Cesium	33	Praseodymium
9	Chromium	34	Rhodium
10	Cobalt	35	Rubidium
11	Dysprosium	36	Ruthenium
12	Erbium	37	Samarium
13	Europium	38	Scandium
14	Fluorspar	39	Tantalum
15	Gadolinium	40	Tellurium
16	Gallium	41	Terbium
17	Germanium	42	Thulium
18	Graphite	43	Tin
19	Hafnium	44	Titanium
20	Holmium	45	Tungsten
21	Indium	46	Vanadium
22	Iridium	47	Ytterbium
23	Lanthanum	48	Yttrium
24	Lithium	49	Zinc
25	Lutetium	50	Zirconium

Source: US Geological Survey<sup>12</sup>

## HAOBO WANG PUBLICATION LIST

- 1. Packing Bimodal Magnetic Particles to Fabricate Highly Dense Anisotropic Rare Earth Bonded Permanent Magnets**  
Kinjal Gandha, Haobo Wang, Kaustubh Mungale, Xubo Liu, Ikenna C. Nlebedim, Uday Kumar Vaidya, M. P. Paranthaman  
*RSC Adv.* **13**, 17097–17101 (2023).  
<https://doi.org/10.1039/D3RA02349D>
- 2. Sintering-Based Metal Additive Manufacturing Methods for Magnetic Materials**  
Haobo Wang, A. M. Elliot, M. P. Paranthaman  
Submitted
- 3. Additively manufactured Fe-3Si stator for a high-performance electrical motor**  
Tej N. Lamichhane, Haobo Wang, Chins Chinnasamy, Latha Sethuraman, Fred A. List, Peeyush Nandwana, Jiaqiang Yan, Zheng Gai, M. Parans Paranthaman  
Submitted
- 4. Additive Manufacturing of Hiperco50 Alloy Stator for High-performance Electrical Motors**  
Haobo Wang, Tej N. Lamichhane, Chins Chinnasamy, Arjun Pathak, Peeyush Nandwana, Christopher Fancer, Mariappan Parans Paranthaman  
Submitted
- 5. Thermal Stability of Anisotropic Bonded Permanent Magnets Prepared by Additive Manufacturing**  
Kinjal Gandha, Mariappan Parans Paranthaman, Haobo Wang, Xubo Liu, Ikenna C. Nlebedim  
*J Am Ceram Soc.* 2023;106:166–171.  
<https://doi.org/10.1111/jace.18609>
- 6. Review of Additive Manufacturing of Permanent Magnets for Electrical Machines: A Prospective on Wind Turbine**  
Haobo Wang, Tej Nath Lamichhane, M Parans Paranthaman  
*Mater. Today Phys.* **24**, 100675 (2022).  
<https://doi.org/10.1016/j.mtphys.2022.100675>
- 7. Challenges in Postprocessing of Hybrid Manufacturing of Magnet Polymer Composites to Enhance the Energy Product of NdFeB Bonded Magnets**  
Tej Nath Lamichhane, Kaustubh Mungale, Haobo Wang, Kinjal Gandha, Xubo Liu, Ikenna C Nlebedim, Zhang Gai, Uday Kumar Vaidya and M Parans Paranthaman  
*Res. Dev. Mater. Sci.* **16**, 1802–1808 (2021).  
<http://dx.doi.org/10.31031/rdms.2021.16.000882>
- 8. 3D Printing of Anisotropic Sm-Fe-N Nylon Bonded Permanent Magnets**  
Kinjal Gandha, M. P. Paranthaman, Brian C. Sales, Haobo Wang, Adrian Dalagan, Tej N. Lamichhane, David S. Parker, Ikenna C. Nlebedim



Eng. Rep. 3, (2021).

<https://doi.org/10.1002/eng2.12478>

**9. Compression molding of anisotropic NdFeB bonded magnets in a polycarbonate matrix**

Kaustubh Mungale, Tej N. Lamichhane, Haobo Wang, Brian C. Sales, M. Parans Paranthaman, Uday Kumar Vaidya

Materialia 19, 101167 (2021).

<https://doi.org/10.1016/j.mtla.2021.101167>

**10. Additive manufacturing of soft magnets for electrical machines—a review**

T.N. Lamichhane, L. Sethuraman, A. Dalagan, H. Wang, J. Keller b, M.P. Paranthaman  
Mater. Today Phys. 15, 100255 (2020).

<https://doi.org/10.1016/j.mtphys.2020.100255>

**11. Photoactivated Structurally Tailored and Engineered Macromolecular (STEM) gels as precursors for materials with spatially differentiated mechanical properties**

Antoine Beziau, Andria Fortney, Liye Fu, Chiaki Nishiura, Haobo Wang, Julia Cuthbert, Eric Gottlieb, Anna Balazs, Tomasz Kowalewski, Krzysztof Matyjaszewski  
Polymer, 126, 224-230.

<https://doi.org/10.1016/j.polymer.2017.08.035>

## **VITA:**

Haobo Wang was born in 1993 in Beijing, China. He was raised there until 1999 when his father's work took the family to the United States. Haobo spent four years in Maryland and Washington, D.C., where he learned the language and culture of this exciting new country. He returned to China when his father's duty in the United States was done and was educated in Beijing until 2013, when he went to Carnegie Mellon University for college. Haobo received his bachelor's and master's degrees in materials science and engineering from Carnegie Mellon and graduated in 2018. In the same year, he joined the Bredesen Center for Interdisciplinary Graduate Education at the University of Tennessee, Knoxville, to pursue his doctorate in energy science and engineering with Dr. M. Parans Paranthaman at Oak Ridge National Laboratory. His research interest focused on the additive manufacturing of permanent and soft magnets for electric motor and generator applications. He has developed new materials and published numerous scientific papers on the topic.